UNIVERSITY OF BELGRADE
FACULTY OF MATHEMATICS

UNIVERSITÉ DE STRASBOURG
ÉCOLE DOCTORALE PHYSIQUE
ET CHIMIE-PHYSIQUE - ED182

Đorđe Savić

MEASURING BLACK HOLE MASSES IN ACTIVE GALACTIC NUCLEI USING THE POLARIZATION OF BROAD EMISSION LINES

Doctoral Dissertation

Belgrade, Strasbourg, 2019

Ђорђе Савић

ОДРЕЂИВАЊЕ МАСЕ ЦРНИХ РУПА КОД АКТИВНИХ ГАЛАКТИЧКИХ ЈЕЗГАРА ПОМОЋУ ПОЛАРИЗАЦИЈЕ У ШИРОКИМ ЕМИСИОНИМ ЛИНИЈАМА

Докторска дисертација

Београд, Стразбур, 2019

THÈSE

présentée par:

Đorđe SAVIĆ

soutenue le : **29 novembre 2019**

pour obtenir le grade de: **Docteur de l'université de Strasbourg**

Discipline/ Spécialité: Astrophysique

Détermination de la masse du trou noir central dans les noyaux actifs de galaxies par l'utilisation de la polarisation des raies larges

THÈSE dirigée par :
  Mr POPOVIĆ Luka   Professeur, Uiversity of Belgrade
  Mr GOOSMANN René[1]   Ancien Maitre de Conférence HDR, université de Strasbourg
  Mr HAMEURY Jean-Marie[2] Directeur de recherche au CNRS, université de Strasbourg

RAPPORTEURS :
  Mme ILIĆ Dragana   Associate professor, Faculty of mathematics, university of Belgrade
  Mr GRATADOUR Damien   Associate professor, LESIA, Observatoire de Paris

AUTRES MEMBRES DU JURY :
  Mme BOISSON Catherine   Astronome, LUTH, observatoire de Paris
  Mr STALEVSKI Marko   Assistant research prof., Belgrade astronomical observatory

---

[1] Jusqu'au 1er septembre 2017

[2] A compter du 1er septembre 2017

Đorđe SAVIĆ

Université de Strasbourg

de Strasbourg

ECOLE DOCTORALE
pcp

Détermination de la masse du trou noir central dans les noyaux actifs de galaxies par l'utilisation de la polarisation des raies larges

Résumé

Les trous noirs supermassifs (SMBH) se trouvent au cœur de presque toutes les galaxies massives dans l'Univers. La plupart sont en sommeil, mais lorsqu'il y a assez de gaz à proximité, ils entrent dans une phase active et forment ce qu'on appelle un noyau actif de galaxie (AGN). Ils ont alors un effet profond sur l'évolution de la galaxie hôte et jouent un rôle important sur leur environnement. La mesure fiable de la masse des SMBH est donc une tâche importante dans l'astronomie moderne. À cette fin, Afanasiev et Popovic (2015) ont récemment proposé une méthode qui utilise la rotation de l'angle de position du plan de polarisation sur le profil en fréquence des raies d'émission larges afin de tracer le mouvement Keplerien et de déterminer la masse du SMBH. Le but de la thèse est d'explorer théoriquement les possibilités de cette méthode. Pour ce faire, nous avons dans une première partie effectué de nombreuses simulations de transfert radiatif pour la modélisation de la diffusion équatoriale dans AGN à l'aide du code STOKES. Nous avons inclus les mouvements complexes présents dans le système sous forme d'accrétion et d'éjection, et nous avons également comparé nos résultats aux observations. Notre travail est important car nous avons démontré dans quelles circonstances cette méthode peut être utilisée pour mesurer la masse du trou noir de manière indépendante. La deuxième partie de ce travail consiste à prédire la polarisation des raies larges au cas où les AGN seraient alimentés par des trous noirs binaires supermassifs (SMBBH). Nous avons traité quatre cas différents avec des binaires de trous noirs séparés de moins d'un parsec, et modélisé à nouveau la diffusion équatoriale. Nous avons obtenu une signature de polarisation unique sur les raies larges. Nous avons montré que la spectropolarimétrie pouvait constituer un outil puissant et une première étape pour la recherche de SMBBH dans les futurs levés spectropolarimétriques systématiques.

Mots-clés: Noyaux actifs de galaxies - trous noirs supermassifs - polarisation - transfert radiatif.

Résumé en anglais

Supermassive black holes (SMBHs) reside in the heart of nearly every massive galaxy in the Universe. Most of them lie dormant, but when the nearby gas is abundant, it will enter an active phase and form an active galactic nucleus (AGN). When in their active phase, SMBHs have a profound effect on the host galaxy evolution and play an important role in shaping their environment. Reliable SMBH mass measuring is therefore an important task in modern astronomy. For that purpose, a method has been recently proposed by Afanasiev & Popovic (2015) that uses the rotation of the polarization plane position angle across the broad emission line profile in order to trace the Keplerian motion and determine the SMBH mass. The goal of the thesis is to theoretically explore the possibilities of this method. In order to do that, we performed numerous radiative transfer simulations for modeling equatorial scattering in AGNs using the code *STOKES*. We included complex motions present in the system in the form of inflows and outflows, and we also compared our results with observations. We have demonstrated under which circumstances this method can be used to measure the SMBH mass in a new independent way. The second part of this work involves predicting the broad lines polarization when AGNs are powered by supermassive binary black holes (SMBBHs). We treated four different cases with sub-pc SMBBHs, and again modeled equatorial scattering. We obtained a unique polarization signature across the broad lines. We have shown that spectropolarimetry could be a powerful tool and a first step for searching SMBBHs in the future systematic spectropolarimetric surveys.

Keywords: Active Galactic Nuclei – supermassive black holes – polarization – radiative transfer.

Advisors:

dr Luka Č. **Popović**, full research professor

    Astronomical Observatory Belgrade, Serbia

dr René **Goosmann**, former associate professor

    Université de Strasbourg, France

dr Jean-Marie **Hameury**, full research professor

    Université de Strasbourg, France

Jury members:

dr Dragana **Ilić**, associate professor

    University of Belgrade, Faculty of Mathematics, Serbia

dr Damien **Gratadour**, associate professor

    LESIA, Observatoire de Paris, France

dr Catherine **Boisson**, full research professor

    LUTH, Observatoire de Paris, France

dr Marko **Stalevski**, assistant research professor

    Astronomical Observatory Belgrade, Serbia

Date of defense: _____

Наслов дисертације: Одређивање масе црних рупа код активних галактичких језгара помоћу поларизације у широким емисионим линијама

Сажетак: Супермасивне црне рупе (СМЦР-е) се налазе у центру готово сваке масивне галаксије у свемиру. Већина су неактивне, али када у околини има доста гаса, започеће активна фаза у којој се формира активно галактичко језгро (АГЈ). У активној фази, СМЦР имају велики утицај на еволуцију галаксије која садржи АГЈ и њеног окружења. Поуздано мерење масе СМЦР је зато важан задатак савремене астрономије. У ту сврху, Афанасиев и Поповић (2015) су недавно предложили методу која користи ротацију позиционог угла поларизационе равни дуж профила широке емисионе линије како би детектовали кеплеровско кретање и одредили масу СМЦР-е. Ова метода претпоставља да су широке линије емитоване из пљоснатог дисколиког региона са кеплеровским кретањем, док је главни механизам поларизације расејање на унутрашњем зиду копланарног торуса прашине – тзв. екваторијално расејање. Циљ тезе је теоријски испитати могућности ове методе. Извршили смо бројне Монте Карло симулације за моделирање екваторијалног расејања код АГЈ-а користећи кôд за пренос зрачења STOKES (Goosmann & Gaskell 2007). Разматрали смо и утицај комплексног кретања емисионог региона које може бити у форми радијалног прилива и вертикалног одлива гаса, или услед присуства двојне супермасивне црне рупе (ДСМЦР-е). Такође, изабрали смо четири добро позната АГЈ-а која смо посматрали: NGC 4051, NGC 4151, 3C 273 и PG 0844+349. Спектрополариметрија је урађена користећи SCORPIO спектрограф монтираним на 6-метарском БТА телескопу Специјалне астрофизичке опсерваторије Руске академије наука (САО РАН-а). Моделирали смо сваки од ових АГЈ-а користећи податке из литературе и упоредили смо резултате наших модела са посматрачким подацима. Добили смо да се ова метода може користити за независно мерење маса СМЦР-а код АГЈ-а. Утицај прилива и отицања гаса се може игнорисати уколико су њихове брзине мање од брзина кеплеровског кретања. Додатно, када је расејавајући регион близу широколинијског региона, ова метода не зависи од инклинације посматрања. За систем ДСМЦР-е ова метода се не може користити, међутим, добили смо јединствене профиле које нису уобичајени за једну СМЦР-у, што може бити коришћено за одређивање могућих кандидата за ДСМЦР-е. Процењене масе СМЦР-а за четири посматрана АГЈ-а слажу се добро са масама које су процењене другим методама, пре свега методом реверберационог мапирања. Метода за независно мерење маса СМЦР-а је у овом раду теоријски и експериментално проверена, што је од изузетног значаја за будућа истраживања која се баве утицајем СМЦР-а на своју непосредну околину.

Dissertation title: Measuring black hole masses in active galactic nuclei using the polarization of broad emission lines

Abstract: Supermassive black holes (SMBHs) reside in the heart of nearly every massive galaxy in the Universe. Most of them lie dormant, but when the nearby gas is abundant, it will enter an active phase and form an active galactic nucleus (AGN). In their active phase, SMBHs have a profound effect on the host galaxy evolution and its environment. Reliable SMBH mass measuring is therefore an important task in modern astronomy. For that purpose, a method has been recently proposed by Afanasiev & Popović (2015) that uses the rotation of the polarization plane position angle across the broad emission line profile in order to trace the Keplerian motion and determine the SMBH mass. This method assumes that broad lines are emitted from a flattened disk-like region undergoing Keplerian motion, while the polarization is mainly due to the light scattering of the inner side of the coplanar dusty torus – the equatorial scattering. The goal of the thesis is to theoretically explore the possibilities of this method. We performed numerous Monte Carlo simulations for modeling equatorial scattering in AGNs using the radiative transfer code STOKES (Goosmann & Gaskell 2007). We included complex motion of the emitting region in the form of radial inflows, vertical outflows, or due to the presence of the supermassive binary black holes (SMBBHs). We also selected four well known AGNs for observations: NGC 4051, NGC 4151, 3C 273 and PG0844+349. Spectropolarimetry was done with the 6 m telescope BTA of the Special Astrophysical Observatory of the Russian Academy of Science (SAO RAS) with the focal reducer SCORPIO. We modeled each of these AGNs using observational data available from the literature, and we compared the results of our models with observational data. We find that this method can be used as a new independent way to measure the SMBH masses in AGNs. The influence of the inflows and the outflows can be ignored if they are much lower than the Keplerian velocity. Additionally, when the scattering region is close to the broad line region, this method becomes independent of the viewing inclination. For SMBBHs, this method cannot be used, however, we obtained unique polarization profiles which are not common for a single SMBH, which could be used for identifying possible SMBBH candidates. SMBH mass estimates for the four observed AGNs are in good agreement with the masses obtained using other methods, such as the method of reverberation mapping. Method for independent SMBH mass measurements has been theoretically and experimentally verified in this work, which is very important for the future research that is dealing with the SMBH influence on its immediate environment.

Acknowledgements

Contents

Abstract

Introduction

Supermassive black holes (SMBHs) reside in the heart of nearly every massive galaxy in the Universe. Their mass typically range between 10^6–$10^{9.5}\,M_\odot$ (Kormendy & Richstone 1995). Most of them lie dormant, but when the nearby gas is abundant, it will start the accretion process where the disk is formed. As the temperatures of the accreting matter increases, an immense amount of energy is radiated, triggering an active phase and forming an active galactic nucleus (AGN, Salpeter 1964; Zel'dovich & Novikov 1964; Lynden-Bell 1969). Whether they are dormant or active, SMBHs do not emit any light of their own; however, the gas and stars surrounding SMBHs are sensitive to their gravitational presence, allowing us to measure their mass.

The standard paradigm, or the so called unified model of AGNs (Antonucci 1993; Netzer 2015) assumes that the SMBH is surrounded by an accretion disk which, further away from the center, is fragmented into an optically thick dusty torus. This dusty torus collimates radiation in the polar direction and obscures the central region along the equatorial viewing direction. The broad line region (BLR) resides in the vicinity of the SMBH, at distances of a few to a few hundred light days, in which the gas is being photoionized by the radiation from the accretion disk. Most of the broad lines are emitted due to radiative recombination (Netzer 2013) and their width of a few thousand $\mathrm{km\,s^{-1}}$ is primarily due to Keplerian motion around the SMBH (Clavel et al. 1991). In the polar direction, highly ionized and modestly relativistic polar winds are emerging on scales smaller than $1\,\mathrm{pc}$ (Tombesi et al. 2012). Farther away, fueled by the polar wind, the outflows form a bi-conical structure of low density gas which emits forbidden narrow lines – the so called narrow line region (NLR). This region can have dimensions of the order of kpc (Bennert et al. 2002). Relativistic jets are sometimes formed in the polar axis direction, and thus produce strong radio emission. The observed dichotomy between type-1 AGNs, where the broad emission lines are visible, and type-2 AGNs, with only narrow emission lines in their optical spectra, is largely due to an orientation effect where type-1 AGNs are observed from close to pole-on view while type-2 AGNs are viewed at much higher inclinations, closer towards the edge on view. An illustration of the AGN structure is shown in Fig. 1.

The large majority of AGNs show weak optical continuum linear polarization $p < 3\,\%$, while circular polarization is a few magnitudes lower. Those AGNs with opti-
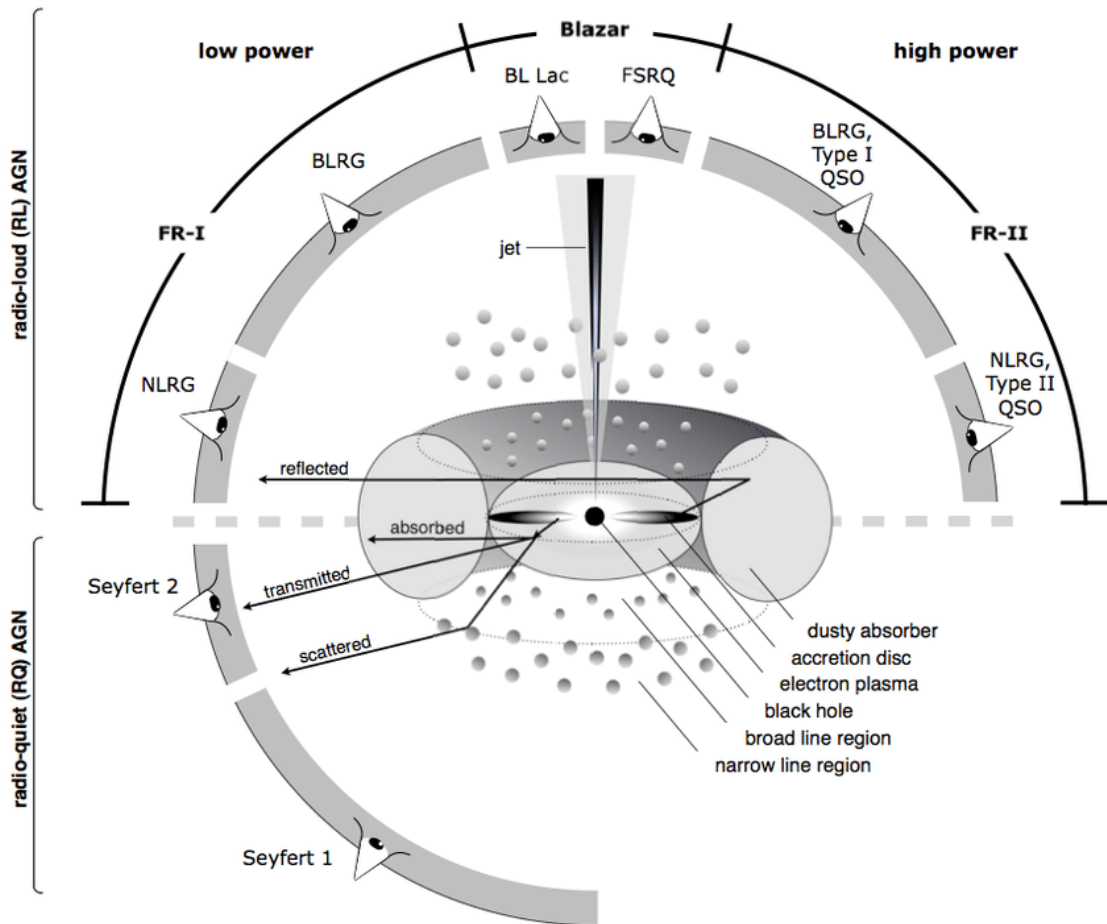
Figure 1: The unified model of AGNs. The black hole is residing in the center surrounded by an accretion disk. Farther away, past the sublimation radius, the accretion disk extends into the dusty torus. The broad line region is in the vicinity of the disk and is being obscured by the torus. Much farther away, on the kpc scales above and below the disk, lies the narrow line region. Relativistic jet is inside the narrow cone along the polar axis. Different AGN types are observed depending on the viewing inclination. Inclination is measured from the pole axis towards the equatorial plane where the accretion disk lies. Credits Beckmann & Shrader (2012).

cal polarization as high as 20 %, are predominantly blazars (Angel & Stockman 1980; Moore & Stockman 1981). Stockman et al. (1979) and Antonucci (1982) have shown that type-1 AGNs exhibit a strong tendency for the optical electric vector position angle to be closely aligned with the axis of the extended radio structure – a feature called parallel polarization. On the contrary, in type-2 AGNs, the polarization position angle is perpendicular to the radio axes – perpendicular (orthogonal) polarization (Antonucci 1982, 1983, 1984). Depending on the waveband, different physical processes are responsible for polarization. In X-rays, Compton and inverse Compton scattering are the dominant polarization mechanisms. From UV (ultraviolet) to near IR (infrared), it is Thomson (electron) and Mie (spherical particle) scattering. In the mid and far IR, dust alignment by large-scale magnetic fields (Lopez-Rodriguez et al. 2015) produce parallel polarization. In the radio domain, the electron scattered synchrotron emission is the dominant mechanism for polarization.

Optical spectropolarimetry of type-1 AGNs has shown that polarization of broad emission lines is caused by equatorial scattering (Smith et al. 2002). The observed polarization properties can be explained assuming a Keplerian disk-like BLR surrounded by a coplanar scattering region (SR, Smith et al. 2005). Along the line profile, the polarization plane position angle φ exhibits the so called S-shape profile: far away from the spectral line, φ follows the continuum value. At velocities corresponding to the blue wing, φ reaches a maximum, followed by a drop through the core until a minimum value is reached in the red wing. Equatorial scattering in AGNs is the main assumption we use in this work.

Measuring SMBH masses

When in their active phase, SMBHs play an important role in shaping its environment in a process called AGN feedback (Fabian 2012, and references therein). As a consequence of AGN feedback, numerous correlations of SMBH mass with the properties of the host galaxy have been found, among which the most notable is $\mathcal{M}_{bh} - \sigma_*$ relation (Ferrarese & Ford 2005; Kormendy & Ho 2013), implying that SMBH and the host galaxy co-evolve (Heckman & Kauffmann 2011). Therefore, reliable measurements of SMBH mass is an important task in modern astronomy. For that purpose, different techniques have been developed, both direct and indirect (Peterson 2014), with most methods targeting AGNs due to their high luminosity (up to $L_{bol} \approx 10^{48}\,\mathrm{erg\,s^{-1}}$, Padovani 2017a), which can be readily observed at different cosmological distances.

Over the past years, SMBH mass measurements most often come from the reverberation mapping of AGNs (Bentz & Katz 2015). By measuring the time delay between the variability of the ionizing continuum and the broad emission lines variability, we can obtain a photometric BLR radius. With a known photometric radius, and a velocity measured directly from the broad emission line, we can obtain the SMBH mass (Bahcall et al. 1972; Blandford & McKee 1982; Peterson 1993). The duration of a reverberation mapping experiment can be rather long. An individual galaxy needs to be observed over and over again for several months, while distant AGNs even require several years of successful monitoring (Shen et al. 2016; Grier et al. 2017, 2019). Hydrogen Balmer lines are the most commonly used; however, highly ionized broad emission lines like Mg II, C III] and C IV can also be used for AGNs at higher redshifts (Mejía-Restrepo et al. 2016).

Another method that has been recently proposed, uses the rotation of the polarization plane position angle across the broad emission line profile in order to trace the Keplerian motion and determine the SMBH mass (Afanasiev & Popović 2015, herafter AP15). It assumes that the BLR is flattened and that the light is dominantly being scattered from the inner side of the dusty torus (equatorial scattering, Smith et al. 2005), resulting in the broad line polarization. The relation between the rotational velocity across the emission line V and the polarization plane position angle φ is (Afanasiev & Popović 2015):

$$\log \frac{V}{c} = a - 0.5 \log\left(\tan\left(\varphi\right)\right), \tag{1}$$

where c is the speed of light. The constant a is related to the black hole mass by

$$a = 0.5 \log \frac{G\mathcal{M}_{\mathrm{bh}} \cos^2\theta}{c^2 R_{\mathrm{sc}}}, \tag{2}$$

where G is the gravitational constant, $\mathcal{M}_{\mathrm{bh}}$ is the BH mass, R_{sc} is the torus inner radius, and θ is the angle between the disc and the plane of scattering. The expected relation between velocity and φ is shown in Fig. 2 (right). In the case of a thin SR (scattering region), a good approximation would be to take $\theta \sim 0$. In this case, the relation between velocities and φ does not depend on the inclination since the BLR emission towards the SR is nearly edge-on. This method is in good agreement with the $\mathcal{M}_{\mathrm{bh}} - \sigma_*$ relation and reverberation mapping, and so far it has been applied to a dozen nearby AGNs (Afanasiev et al. 2019).
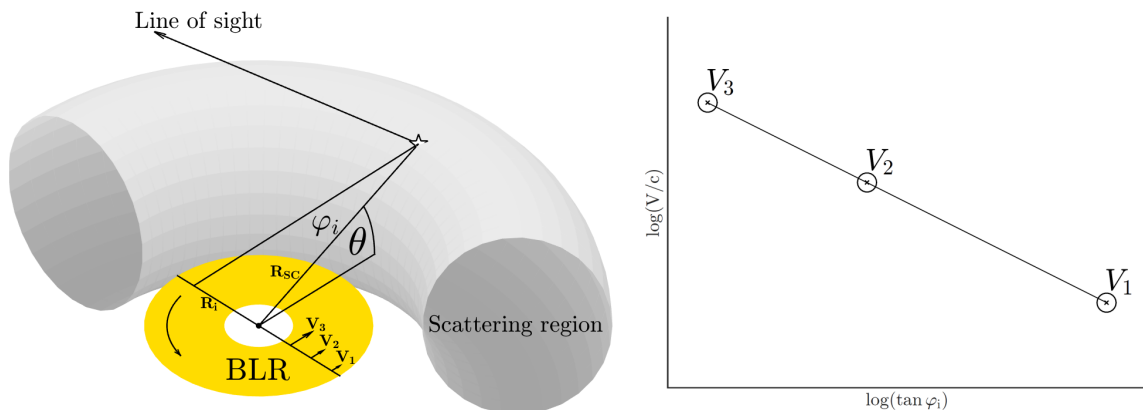
Figure 2: Schematic view of light scattered from the inner part of the torus (left). Expected relation between φ and velocity intensity (right). Credits: Savić et al. (2018).

This method offers a number of advantages over the reverberation mapping method. It requires only one epoch of observations and it is not telescope time consuming as compared to the reverberation mapping method. It can be applied to lines in different spectral ranges from near IR and optical (Balmer lines) to UV (Lyα, C III], C IV and Mg II), thus allowing black hole mass measurements for AGNs at different cosmological epochs (AP15). The virialization of the BLR is not a priori assumed, but it is reflected in the observed φ-profile. However, this method requires the inner radius of the torus to be known; $R_{\rm sc}$ is often found using dust reverberation or some other scaling relations (AP15). In addition, this method can only be used for a rotating disk-like BLR; in the case where the BLR is dominated by radial motion, it cannot be used. We also stress out that, in this method, we consider only one scattering event per line photon and the contribution of multiple scattering events is not taken into account. Since polarization is very sensitive to kinematics and geometrical setup (Goosmann & Gaskell 2007), the full treatment of 3D radiative transfer with polarization is required to test this method.

Methods

The main task of this thesis is to explore the possibilities and limitations of this method and to find in which conditions it can be used. This was done by performing numerous radiative transfer simulations with polarization for a set of generic models, taking into account important physical processes in the central part of AGNs. We heavily rely on the 3D Monte Carlo radiative transfer code STOKES for modeling scattering induced

polarization in AGNs, covering a broad spectral range around Hα line. In addition to generic models, using the data found in the literature, we made models for four AGNs: NGC 4051, NGC 4151, 3C 273 and PG0844+349. Input mass for each object was obtained applying AP15 method to our observations. Finally, we compared results of the models with observational data. All of our observations were carried out with the SAO RAS (Special Astrophysical Observatory of the Russian Academy of Science) 6 m alt-azimuthal telescope using the SCORPIO spectrograph (Afanasiev & Moiseev 2005). The work presented in this thesis is a further improvement of the Smith et al. (2005) equatorial scattering model. While Smith et al. (2005); Afanasiev & Popović (2015) have assumed a single scattering approximation, we have entirely based our simulations on a code allowing multiple scattering events for more general results.

We apply full 3D radiative transfer with polarization using the publicly available code STOKES (Goosmann & Gaskell 2007; Marin et al. 2012, 2015; Marin 2018b; Rojas Lobos et al. 2018). The program is suitable for dealing with the complex geometry and kinematics of the model and treats multiple reprocessing events such as electron and dust scattering as well as dust absorption. The luminosity of the source is divided into a large number of photon packets (typically more than 10^7 per wavelength bin) and follows the input SED (spectral energy distribution) that is a power-law for the continuum or a Lorentz-profile for the emitted broad line. For each emitted photon, the code follows its path and computes Stokes parameters I (total light intensity), Q (the amount of linear horizontal or linear vertical polarization), U (the amount of linear $+45°$ or $-45°$ polarization) and V (left or right circular polarization) after each scattering. Stokes parameters describe the polarization state of electromagnetic radiation and represent real measurable quantities. If there is no scattering region on its path, the photon with its polarization state is finally registered by one of the virtual detectors on the sky. The total (unpolarized) flux (TF), degree of polarization p and φ are computed by summing Stokes parameters of all detected photons for each spectral bin. The code was originally developed for modeling optical and UV scattering induced continuum polarization in radio-quiet AGNs, but it can be applied for studying the polarization of many astrophysical objects (Marin & Goosmann 2014). The default output of the code $\varphi = 90°$ corresponds to a polarization state where the electrical field vector E oscillates in the direction parallel to the axis of the symmetry of the system (z-axis). This is the opposite to the convention used by Smith et al. (2005).

In our model, a point-like continuum source is situated in the center, emitting isotropic unpolarized radiation for which the flux is given by a power-law spectrum
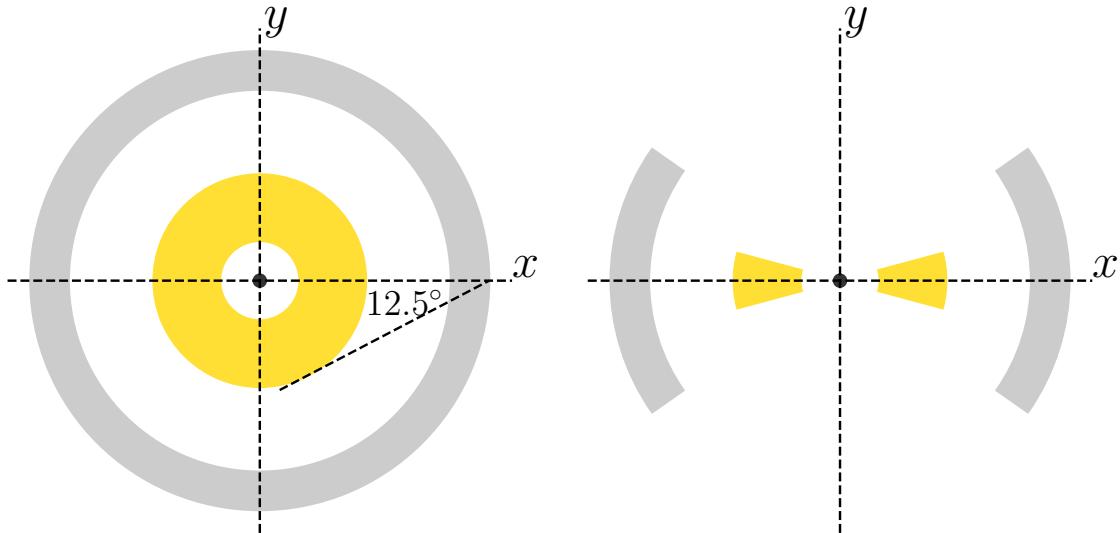
Figure 3: Cartoon showing the model geometry of the BLR (yellow) and the scattering disk (grey) in the face-on (left) and edge-on (right) view. The BLR and the SR half-opening angle is 15° and 35° respectively. Credits: Savić et al. (2018).

$F_C \propto \nu^{-\alpha}$ with $\alpha = 2$. This value corresponds to a flat spectrum when frequency is substituted by wavelength. The continuum source is surrounded by a BLR, and farther out by a SR. The BLR and the SR are modeled using a flared-disk geometry with a typical half-opening angle from the equatorial plane of 15° for the BLR and 35° for the SR (Marin et al. 2012). An illustration of the model geometry is shown in Fig. 3.

We generated four probe models for which the central SMBH has a mass of 10^6, 10^7, 10^8 and $10^9 \, M_\odot$. The size of the BLR and of the SR are scaled with the BH mass in the form of a power-law, for which the power index was obtained by compiling the known BLR and SR radii from the literature. First we performed simulations for different black hole masses with the assumption of a pure Keplerian motion; we then considered radial inflow and vertical outflow as additional components to the Keplerian gas motion caused by the black hole mass. We simulated both cases where the Keplerian motion is in anticlockwise (positive) and clockwise (negative) direction.

Additionally, the complex BLR kinematics could be due to the AGN central engine being driven by a supermassive binary black hole (SMBBH). We consider a model of sub-pc SMBBHs, where each of the BH components has its own accretion disk and BLR (Fig. 4). We also consider equatorial scattering of such a complex system on the inner part of the torus that surrounds the binary. We model the SMBBH system as two black holes orbiting around their common center of mass under the gravity
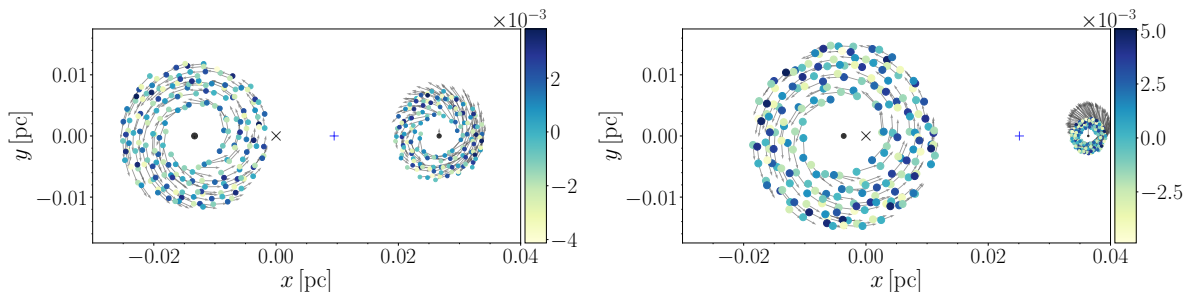
Figure 4: BLR geometry and kinematics for **distant** model with mass ratio $q = 0.5$ (left panel) and with $q = 0.1$ (right panel). Black $\times$ shows the center of mass, while the blue $+$ symbol marks the Lagrangian point L_1. Grey arrows denote the velocity of each BLR clump. Color bar is denoting the vertical offset from the xy-plane. Credits: Savić et al. (2019).

force. This is a well known problem for which it was shown that it is equivalent to the problem of a single body with reduced mass μ moving in an external gravitational field (Landau & Lifshitz 1969; Postnov & Yungelson 2014) which is determined by the mass of each component as $\mu = \mathcal{M}_1 \mathcal{M}_2 / (\mathcal{M}_1 + \mathcal{M}_2)$. We have made two assumptions in our model: one is that both SMBHs have their own accretion disk and corresponding BLR, and the second is that both the accretion disks and the scattering region are coplanar. Depending on the distance between black holes, we treated four different SMBBH cases: **distant**, **contact**, **mixed** and **spiral**. The scattering region is the same for all four binary models. We present here for the first time the polarization parameters across the broad lines in the case of an emission by a sub-pc scale SMBBH system.

We have also selected four AGNs with prominent changes of φ across the line profile: NGC 4051, NGC 4151, 3C273 and PG0844+349. These objects have been very well observed in the last few decades, both in polarized and unpolarized light. They all exhibit dominant equatorial scattering in their spectra. In 2014 and 2015 we carried out the spetropolarimetric observations of the four AGNs with the 6 m telescope BTA of SAO RAS with the focal reducer SCORPIO. We modeled each of these objects using observational data available from the literature and we compare the results of our models with our own observations.

Results

In Fig. 5, we show the simulated profiles of φ, polarized flux PF, degree of polarization p and total flux TF across the broad line profile for the case where the SMBH mass

is $10^6\,M_\odot$. From our models (Fig. 5, bottom right panel), we can see that the degree of polarization is sensitive to inclination. The p-profile peaks in the line wings and reaches its minimum in the line core just as it was shown by Smith et al. (2005). The polarized line (Fig. 5, middle right panel) is broader than the unpolarized line (Fig. 5, top right panel), as predicted by the equatorial scattering. In Fig. 5 (left panels), we show the simulated profiles of φ for three viewing inclinations. The φ-profiles show S-shape profiles. The rotation sign only affect φ, while TF, PF and p remains unaffected. For anticlockwise rotation, φ reaches its maximum in the blue part of the line and its minimum in the red part of the line. The φ swing occurs around the continuum level $\varphi_\mathrm{c} = 90°$. An important feature of φ is that it is symmetric with respect to the continuum polarization in such a way that for a given inclination i, it satisfies the equation:

$$\varphi(180° - i) = 180° - \varphi(i). \tag{3}$$

When performing AP15 method to the modeled data, one needs to consider polarization only in the broad line and for that, it was necessary to subtract the continuum polarization for all type-1 inclinations: $\Delta\varphi = \varphi - 90°$. In Fig. 6 (lower panels), we show the fit described by the AP15 method. We find that Keplerian motion can be traced across the φ-profile for type-1 viewing inclinations. The region inside the 1σ errors around the linear fit is becoming smaller as we go from face-on towards edge-on inclinations. For inclinations of 25° or lower, the simulated data show much a higher scatter around the straight line rather than for the cases with an intermediate inclination.

The distance between the BLR and the SR greatly affects the φ amplitude. In order to test this effect, we investigated different cases with various distances between the BLR and SR while keeping the same thickness and the optical depth of the SR. In Figs. 7 and 8, we show the influence of different distances between the two regions, and how it affects the parameter a and the SMBH mass estimates. Our models show that the distance between the BLR and the SR has a great influence on parameter a which consequently greatly affects our black hole mass estimates. One can see that parameter a shows the same profile and the same inclination dependence for all simulated cases. Only when the SR is adjacent to the BLR do we obtain inclination independence of the SMBH mass estimates. The SMBH mass estimates increase when the distance between the BLR and SR increases. For a given accuracy of 10%, we find that the best SMBH estimates for all four cases are obtained when the ratio of the inner radius of SR and
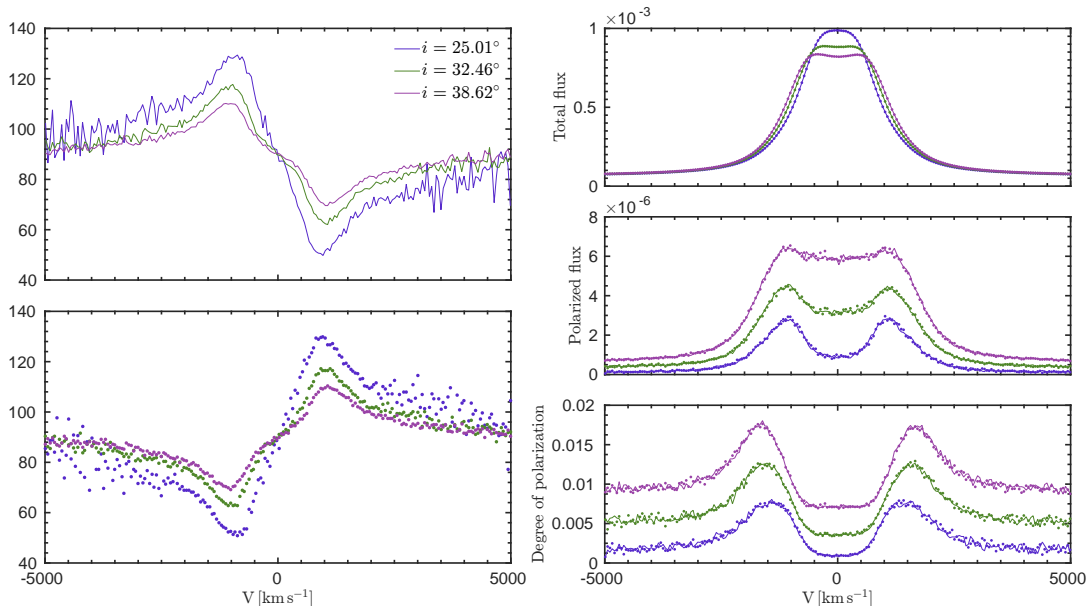
Figure 5: On the left panels, modeled polarization plane position angle φ is shown when the system is rotating anticlockwise (top) or when rotating in clockwise direction (bottom), total unpolarized flux (TF, top right), polarized flux (PF, middle right), degree of polarization p, bottom right. SMBH has mass of $10^6\,M_\odot$. We plot the results in solid lines for three viewing inclinations: $i = 25.01°$, $32.46°$, and $38.62°$ respectively, while dotted lines represent the results for the opposite direction of rotation. Note the symmetry of φ with respect to the continuum level due to the opposite direction of rotation. Opposite direction of rotation does not affect TF, PF and p. Total and polarized fluxes are given in arbitrary units. Credits: adapted from Savić et al. (2018).

the outer radius of the BLR is between 1.5 and 2.5 (Fig. 8). For an inclinations of 25° or less (face-on view), the contribution of equatorial scattering is low and we find that Keplerian motion cannot be recovered from the φ-profile. For additional BLR velocity components such as radial inflows or vertical outflows, we find that these effects can be neglected if the additional velocity components are not a significant fraction of the Keplerian velocity.

In Fig. 9 we show the results of φ, p and TF for two viewing inclinations i and for one azimuthal viewing angle ϕ. The profiles of φ are complex and differ much from the profiles obtained for the single black hole scenario. Very different φ-profiles are obtained when changing the azimuthal viewing angle. This is the result of different velocity projections towards the observer since the model is not azimuthally symmetric.
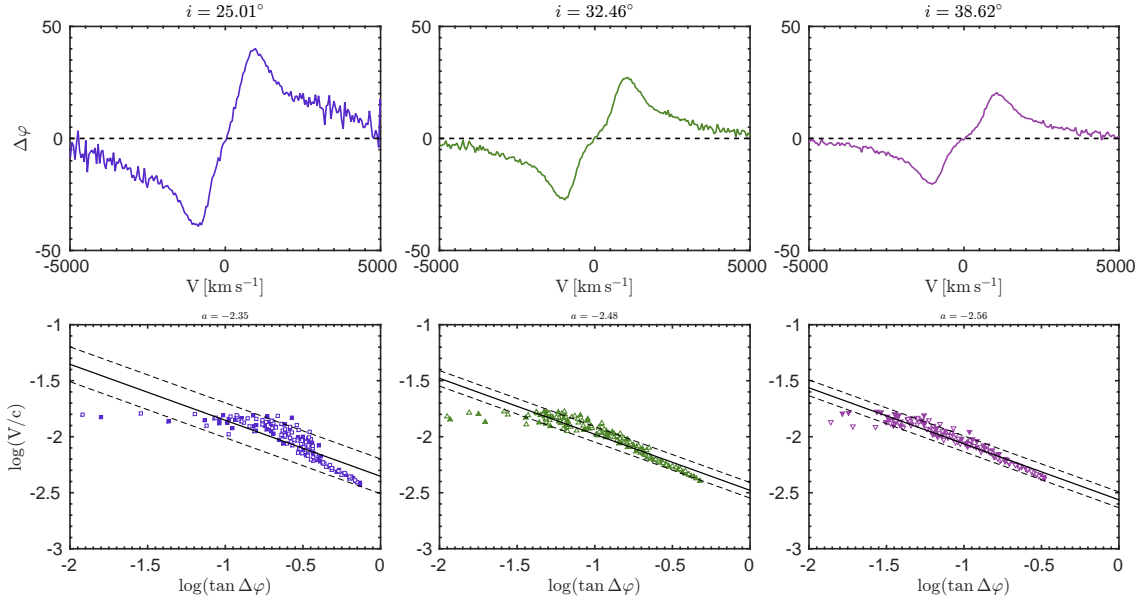
Figure 6: Modeled polarization angle φ (upper panels) and velocities (lower panels) across Hα profiles for the model with central mass of $10^6\,M_\odot$. Filled symbols are for the blue part of the line and open symbols are for the red part of the line. Solid line represents the best fit. Credits: adapted from Savić et al. (2018).
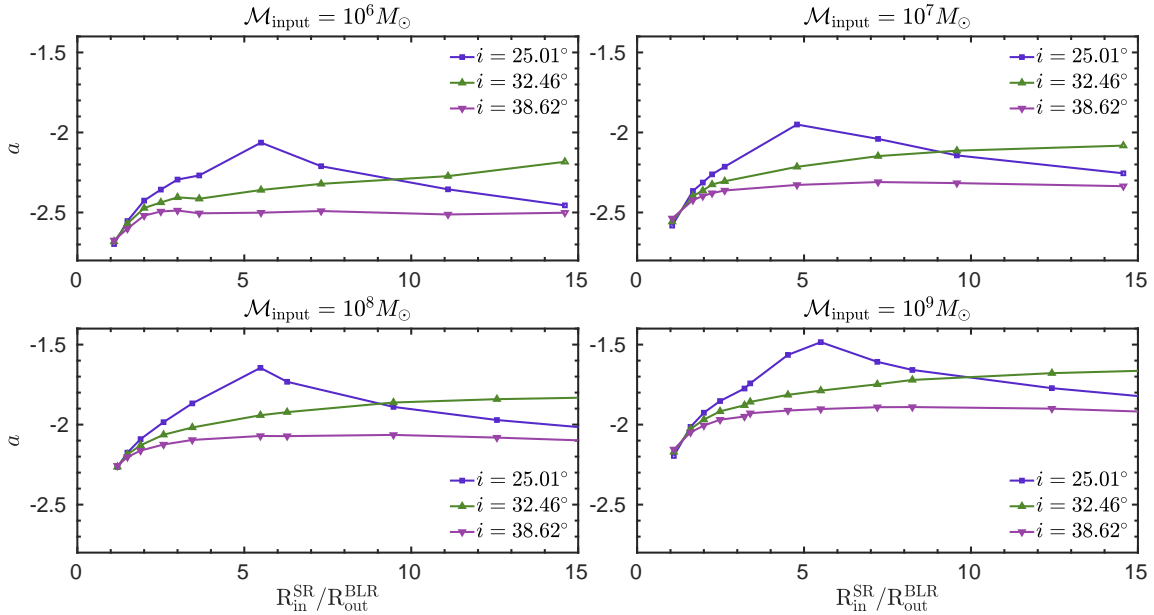
Figure 7: Dependance of the parameter a on the ratio between the inner radius of the SR ($R_{\mathrm{in}}^{\mathrm{SR}}$) and the outer radius of the BLR ($R_{\mathrm{out}}^{\mathrm{BLR}}$) for three given inclinations. Credits: adapted from Savić et al. (2018).
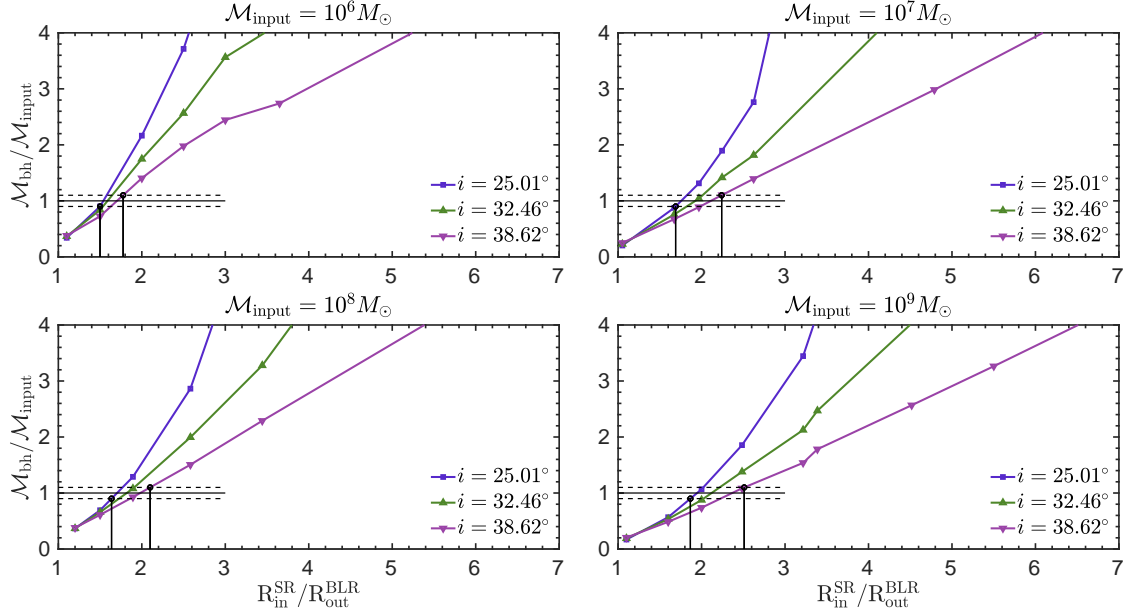
Figure 8: Black hole mass estimation as a function of the ratio between the inner radius of the SR ($R_{\mathrm{in}}^{\mathrm{SR}}$) and the outer radius of the BLR ($R_{\mathrm{out}}^{\mathrm{BLR}}$) for three given inclinations. Horizontal dashed lines represent the interval of 10% deviation from the input mass (solid line). Credits: adapted from Savić et al. (2018).

The φ-profiles are symmetric with respect to the line center which is not the case for a single case scenario where the swing occurs. The polarization position angle φ is showing double-peaked or even more complex profiles most of the time. p shows double-peak profiles with a minimum in the line core, which is common for the single SMBH scenario, but there are opposite profiles with minima in the line wings and maxima in the line core, which may be used as an indicator of the presence of a SMBBHs. The TF shows most of the time double-, or multi-peaked profiles which can be well explained with the disk profiles (Chen & Halpern 1989). There is a clear difference in the φ-profiles between the binary and the single SMBH model, namely in the symmetry of the φ-profiles. Profiles for SMBBHs are axis-symmetric with respect to the zero velocity line, which yields double-peaked profiles. On the contrary, φ-profiles for one SMBH is point symmetric even for complex motions including inflows and outflows (Savić 2019).

For all modeled objects, we were able to produce very similar profiles of φ as the observed ones. SMBH masses estimated from fits of the model data are higher than those obtained by fitting the observational data, but are still in agreement with those found in literature. Observational data are much more scattered from the predicted
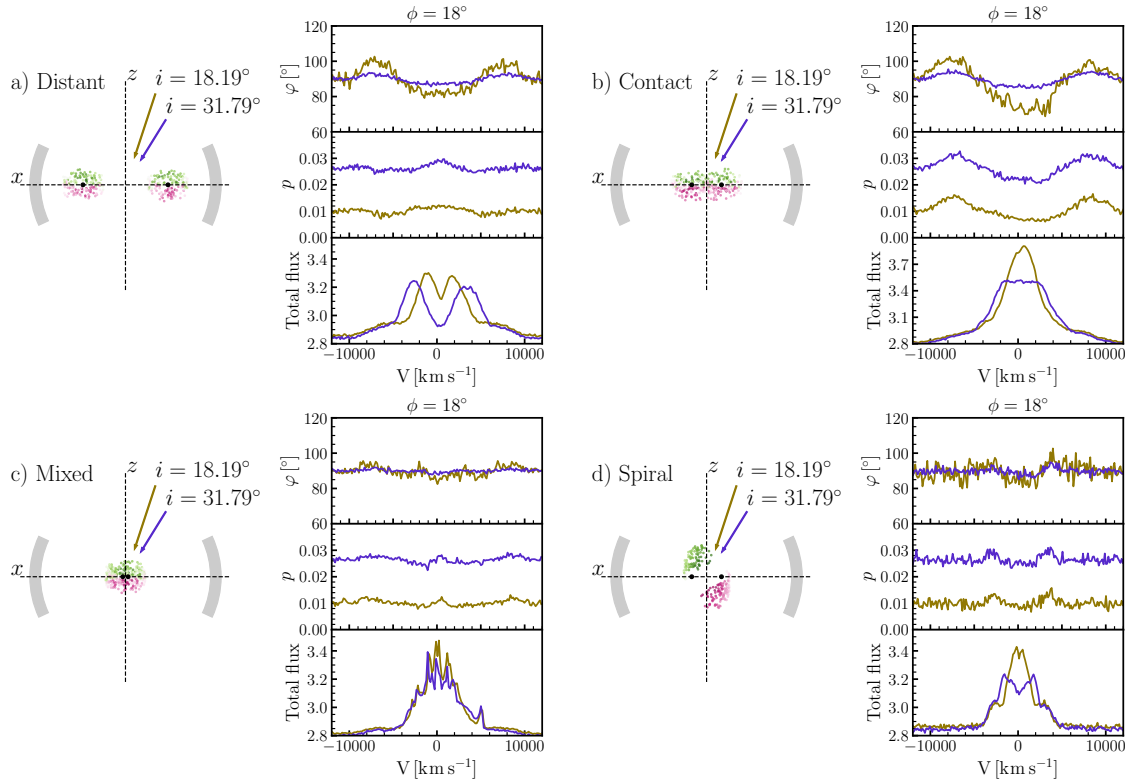
Figure 9: On the left panels the illustration of each model with SMBBH in the center: Distant (a), Contact (b), Mixed (c), Spiral (d). On the right panels, from top to bottom are φ, p and TF for two viewing inclination $i = 18°$ (brown line) and $i = 32°$ (blue line). Azimuthal viewing angle is $\phi = 18°$ for all plots. Credits: Savić et al. (2019).

straight line, which in general, yields an error in SMBH mass estimates a few times larger than wat is obtained using reverberation mapping.

Conclusions

From the work presented here, we draw the following conclusions (Savić et al. 2018; Savić 2019; Savić et al. 2019):

1. If Keplerian motion can be traced through the polarized line profile, then direct estimates of the SMBH mass can be performed for obtaining values in agreement with other methods.

2. The effects of possible inflow/outflow configurations of the BLR take its toll only in extreme cases where the velocity of inflowing/outflowing emitters is comparable to or higher than the Keplerian velocity, which in that case cannot be correctly used.

3. The polarization degree and the total flux exhibit profiles that are similar for single SMBHs and for SMBBHs and alone may prove inconclusive whether a SMBH or SMBBH drives the central engine of AGNs. On the other hand, the polarization position angle φ shows quite unique profiles that differ from those observed in the single SMBH scenario, and could be used for identifying SMBBH candidates.

4. The φ-profiles for a single SMBH model show point-symmetric profiles even when additional motions in the BLR are present.

5. The φ-profiles for SMBBH models produce axis-symmetric profiles which are often double or multi-peaked.

6. The application of the AP15 method is not feasible for the case of SMBBHs.

7. The AP15 method provides a new independent way of SMBH mass estimation. Estimated SMBH masses are in a good agreement with the values obtained by other methods such as reverberation mapping. The relative error of mass estimates between these two methods is around $30\,\%$.

Сажетак

Увод

Супермасивне црне рупе (СМЦР-е) се налазе у центру готово сваке масивне галаксије у свемиру. Њихова маса се обично креће између 10^6–$10^{9.5}$ Сунчевих маса $M_\odot$ (Kormendy & Richstone 1995). Већина су неактивне, али када у околини има доста гаса, започеће процес акреције услед кога се формира диск. Како се температура гаса који у процесу акреције повећава, огромна количина енергије се израчи и започиње активна фаза позната као активно галактичко језгро (АГЈ, Salpeter 1964; Zel'dovich & Novikov 1964; Lynden-Bell 1969). Без обзира да ли су у стању мировања или су активне, СМЦР-е не емитују никакву светлост, али гас и звезде које их окружују су осетљиве на њихово гравитационо присуство, што нам омогућава да измеримо њихову масу.

Стандардна парадигма, или тзв. обједињени модел АГЈ-а (Antonucci 1993; Netzer 2015) претпоставља да је СМЦР-а окружена акреционим диском који се даље од центра на већим растојањима фрагментише у у оптички густ торус прашине. Торус прашине колимише зрачење у поларном смеру и заклања средишњу област дуж екваторијалног правца посматрања. Област где се формирају широке емисионе линије (широколинијски регион, ШЛР) налази се у близини СМЦР-е на растојањима од неколико до више стотина светлосних дана. У њима се гас фотојонизује зрачењем акреционог диска, а широке линије већином настају услед радијативне рекомбинације (Netzer 2013). Ширина линија је неколико хиљада $\mathrm{km\,s^{-1}}$ услед кеплеровског кретања око СМЦР-е. У поларном смеру се појављују високо јонизовани и благо релативистчки поларни ветрови на скалама растојања које су мање од $1\,\mathrm{pc}$ (Tombesi et al. 2012). Подстакнути поларним ветровима, на већим растојањима се формирају одливи гаса биконичне структуре и ниске густине, који емитују забрањене уске линији – тзв. усколинијски регион (УЛР). Овај регион може достићи димензија реда kpc (Bennert et al. 2002). Понекад се формирају релативистички млазеви у правцу поларне осе стварајући јако радио-зрачење. Посматрана дихотомија између АГЈ-а типа 1 где су широке емисионе линије видљиве и типа 2 само са уским емисионим линијама у оптичким спектрима је у великој мери последица ефеката оријентације где АГЈ-а типа 1 посматрамо под инклинацијама блиским поларним, док се АГЈ-а типа 2 посматрају под много
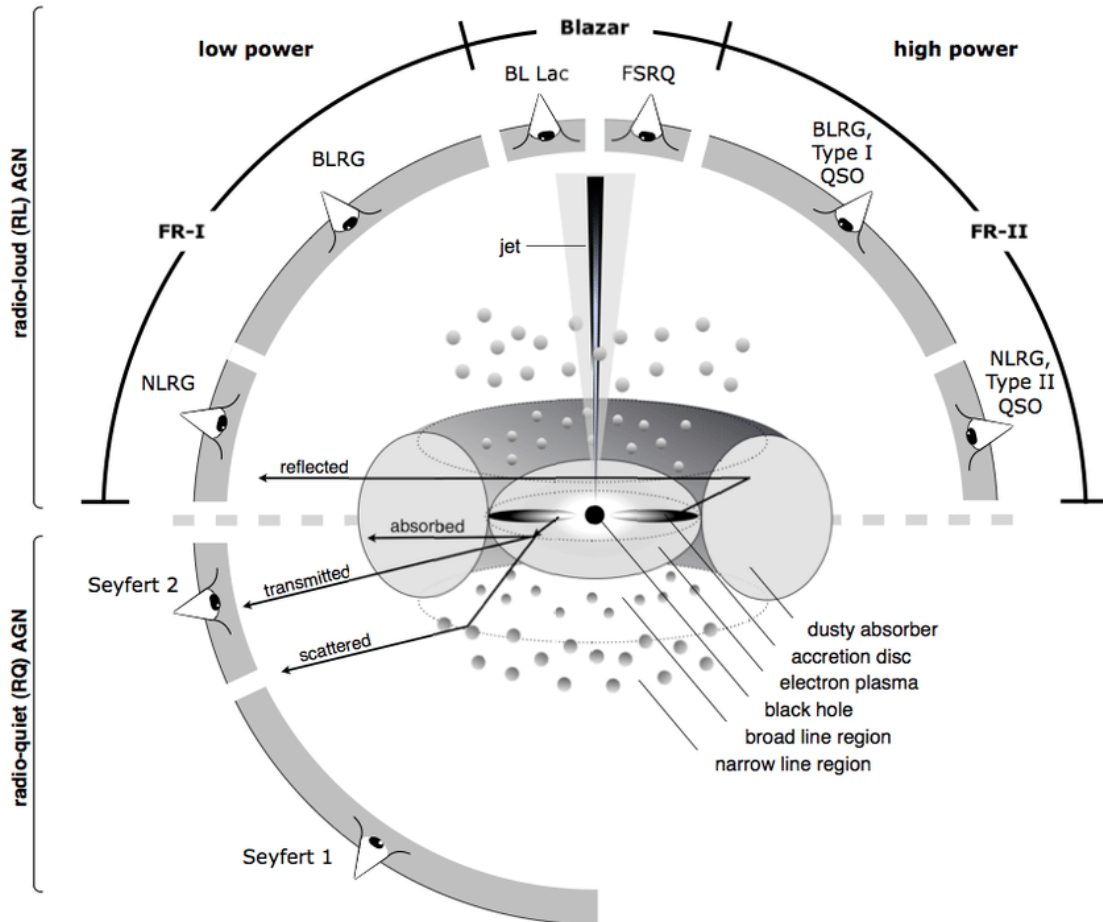
Слика 1: Обједињени модел АГЈ-а. Црна рупа се налази у средини окружена акреционим диском. На растојањима већим од сублимационог радијуса простире се торус прашине. На много већим растојањима реда kpc, изнад и испод диска налази се УЛР. Релативистички млаз се налази унутар уског конуса дуж поларне осе. У зависности од инклинације (угла) под којим их посматрамо, уочавамо различите типове АГЈ-а. Инклинација се мери од поларне осе ка екваторијалној равни у којој се налази акрециони диск. Преузето из књиге Бекмана и Шрејдера (Beckmann & Shrader 2012).

већим инклинацијама ближим екваторијалној равни. Илустрација структуре АГЈ-а приказана је на слици 1.

Велика већина АГЈ-а показује слабу линеарну поларизацију у континууму оптичког зрачења $p < 3\,\%$, док је кружна поларизација неколико редова величине нижа. Мањи део АГЈ-а са поларизацијом у континууму оптичког зрачења, који достиже чак и $p \sim 20\,\%$, су претежно блазари (Angel & Stockman 1980; Moore & Stockman 1981). Стокман са сарадницима (Stockman et al. 1979) и

Антонући (Antonucci 1982) је показао да АГЈ-а типа 1 показују јаку тенденцију да је вектор електричног поља у оптичком опсегу уско усклађен са поларном радио-осом. Супротно томе, код АГЈ-а типа 2, поларизациони позициони угао је нормалан на радио-осу – особина која се назива нормална (или ортогонална) поларизација (Antonucci 1982, 1983, 1984). У зависности од таласног опсега, различити физички процеси су одговорни за поларизацију. У Х-опсегу Комптоново и инверзно Комптоново расејање су доминатни механизми поларизације. Од УВ- (ултраљубичасто) до блиског ИЦ- (инфрацрвено) зрачења, то је Томсоново (на слободним електронима) и Миево (на честицама сферног облика) расејање. У средњем и даљем ИЦ-у, поравњањем прашине глобалним магнетним пољима (Lopez-Rodriguez et al. 2015) настаје паралелна поларизација. У радио-домену, расејање синхротронског зрачења на електронима је доминантан механизам поларизације. Оптичка спектрополаритметрија АГЈ-а типа 1 је показала да је поларизација у широким емисионим линијама изазвана екваторијалним расејањем (Smith et al. 2002). Посматрана поларизациона својства се могу објаснити по претпоставком да је ШЛР дисколиког облика са доминантним кеплеровским кретањем и да је окружен копланарним расејавајућим регионом (Smith et al. 2005). Дуж профила линије, позициони угао поларизационе равни (φ-профил) има тзв. „S" облик: далеко од центра спектралне линије, φ прати вредност позиционог угла континуума. При брзинама које одговарају плавом крилу, φ достиже максимум, након чега следи пад кроз језгро линије док се у црвеном крилу не постигне минимална вредност. Екваторијално расејање у АГЈ-има је главна претпоставка коју користимо у овом раду.

Мерење маса СМЦР-а

Када су у активној фази, СМЦР-е играју важну улогу у обликовању свог окружења у процесу који се назива повратни утицај АГЈ-а (Fabian 2012, и референце у њему). Као последица повратног утицаја АГЈ-а пронађене су бројне корелације између СМЦР-а и особина галаксије домаћина, од којих је најистакнутија $\mathcal{M}_{\mathrm{bh}} - \sigma_*$ релација (Ferrarese & Ford 2005; Kormendy & Ho 2013), што имплицира да СМЦР и галаксија домаћин коеволуирају заједно (Heckman & Kauffmann 2011). Стога је поуздано мерење маса СМЦР-а важан задатак савремене астрономије. У ту сврху развијене су различите технике, директне и индиректне (Peterson 2014), при чему се већина метода управо ослања на АГЈ-а због њихове изузетно високе

луминозности (чак и до $L_{\mathrm{bol}} \approx 10^{48}\,\mathrm{erg\,s^{-1}}$, Padovani 2017a), која се због тога могу посматрати на различитим космолошким растојањима.

Током протеклих година, масе СМЦР-а су највише мерене методом реверберационог мапирања (Bentz & Katz 2015). Мерењем временског кашњења између промена у јонизујћем континууму и промена у широким емисионим линијама, можемо добити фотометријски радијус ШЛР-а. Са познатим фотометријским радијусом и брзином измереном директно из широке емисионе линије, можемо добити масу СМЦР-е (Bahcall et al. 1972; Blandford & McKee 1982; Peterson 1993). Трајање експеримента реверберационог мапирања може бити прилично дуго. Појединачну галаксију треба посматрати изнова и изнова неколико месеци, док удаљена АГЈ-а захтевају чак и по неколико година успешног посматрања (Shen et al. 2016; Grier et al. 2017, 2019). Водоникове Балмерове линије се најчешће користе, али и вишеструко јонизоване широке емисионе линије попут Mg II, C III] и C IV се такође могу користити и за АГЈ-а на већим црвеним помацима (Mejía-Restrepo et al. 2016).

Друга метода која је недавно предложена користи ротацију позиционог угла поларизационе равни дуж профила широке емисионе линије како би се пратило кеплеровско кретање и одредила маса СМЦР-е (Afanasiev & Popović 2015, надаље метода AP15). Претпоставља се да је ШЛР спљоштен и да се зрачење доминантно расејава са унутрашње стране торуса прашине (екваторијално расејање Smith et al. 2005). Зависност између ротационе брзине система и позиционог угла поларизационе равни φ је (Afanasiev & Popović 2015):

$$\log \frac{V}{c} = a - 0.5 \log\left(\tan\left(\varphi\right)\right), \tag{4}$$

где је c брзина светлости. Константа a повезана је са масом црне рупе као:

$$a = 0.5 \log \frac{G\mathcal{M}_{\mathrm{bh}} \cos^2\theta}{c^2 R_{\mathrm{sc}}}, \tag{5}$$

где је G гравитациона константа, $\mathcal{M}_{\mathrm{bh}}$ је маса црне рупе, R_{sc} је унутрашњи радијус торуса прашине, и θ је угао између диска и равни расејања. Очекивана веза између брзине и φ приказана је на слици 1 (десно). У случају танког РР-а (расејавајћег региона), добра апроксимација је узети $\theta \sim 0$. У том случају, зависност брзине од φ не зависи од инклинације јер ШЛР емитује зрачење скоро потпуно бочно, у екваторијалној равни, у односу на РР. Ова метода се добро слаже са $\mathcal{M}_{\mathrm{bh}} -$
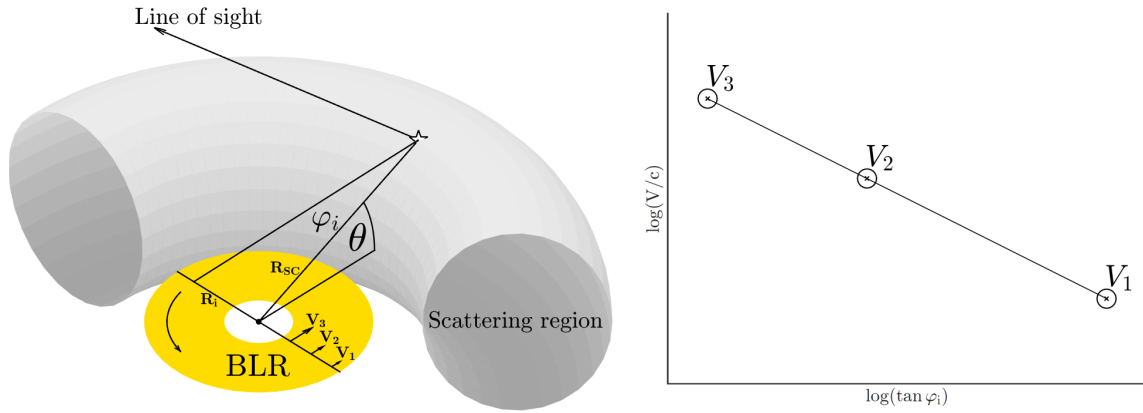
Слика 2: Шематски приказ светлости која се расејава на унутрашњој страни торуса прашине (лево). Наранџасти регион означава ШЛР. Расејавајући регион (торус прашине) означен је сивом бојом. Очекивана веза између φ и интензитета брзине (десно). Преузето из рада Савића са сарадницима (Savić et al. 2018).

σ_* релацијом и реверберационим мапирањем, а до сада је примењена на десетак ближњих АГЈ-а (Afanasiev et al. 2019).

Ова метода има неколико предности у односу на реверберационо мапирање. Потребна је само једно посматрање и не захтева пуно телескопског времена у поређењу са реверберационим мапирањем. Може се применити на линијама у различитим спектралним опсезима, од близу ИЦ- и оптичког опсега (Балмерове линије), до УВ опсега (Lyα, C III], C IV и Mg II), омогућавајући тако мерење маса црних рупа код АГЈ-а на различитим космолошким растојањима (AP15). Виријализација ШЛР није *a priori* претпостављена, већ се огледа у профилу φ. Међутим, овај метод захтева познавање унутрашњег радијуса торуса прашине R_{sc}, који се врло често налази управо реверберационим мапирањем зрачења прашине или из неких других закона скалирања (AP15). Поред тога, ова метода се може користити само за ротирајући дисколики ШЛР, док се у случају када су у ШЛР-у радијална кретања доминантна не може користити.

Такође истичемо да је у њој разматрано само једно расејање широколинијских фотона, док допринос вишеструких расејања није узет у обзир. Пошто је поларизација веома осетљива на кинематику и геометрију система (Goosmann & Gaskell 2007), за њено тестирање потребно је потпуно разматрање 3Д преноса зрачења са поларизацијом.

Методе

Главни задатак ове дисертације је испитивање могућности и граница AP15 методе као и испитати под којим се све околностима ова мотеда може користити. То је урађено извршавањем бројних симулација преноса зрачења са поларизацијом за скуп генеричких модела, узимајући у обзир најважније физичке процесе у централном делу АГЈ-а. Највише се ослањамо на 3Д Монте Карло (Монте Царло) програм за пренос зрачења STOKES за моделирање поларизације индуковане расејањем, покривајући широки спектрални опсег око Hα линије. Уз генеричке моделе, помоћу података пронађеним у литератури, направили смо моделе за четири АГЈ-а: NGC 4051, NGC 4151, 3C 273 и PG0844+349.Улазна маса за сваки објекат појединачно добијена је применом AP15 на посматрачке податке. Сва наша астрономска посматрања изведена су на 6-метарском алт-азимуталном телескопу Специјалне астрофизичке опсерваторије руске академије наука (САО РАН) коришћењем SCORPIO спектрографа (Afanasiev & Moiseev 2005). Рад представљен у овој тези је додатно унапређење модела екваторијалног расејања (Smith et al. 2005). Док су Смит са сарадницима (Smith et al. 2005) и Афанасиев и Поповић (Afanasiev & Popović 2015) претпоставили апроксимацију једноструког расејања, ми смо у потпуности базирали наше нумеричке симулације претпостављајући вишеструка расејања како бисмо добили опште и потпуније резултате.

Примењујемо потпун 3Д пренос зрачења са поларизацијом користећи јавно доступан програм STOKES (Goosmann & Gaskell 2007; Marin et al. 2012, 2015; Marin 2018b; Rojas Lobos et al. 2018). Програм је погодан за разматрање сложене геометрије и кинематике модела и укључује вишеструке процесе као што су расејање на електронима или честицама прашине и апсорпцију зрачења коју она врши. Луминозност извора је подељена на велики број фотонских пакета (обично више од 10^7 по подеоку таласне дужине) и има задату спектралну енергетску расподелу (СЕР-у) која је дата степеним законом за изворе непрекидног зрачења или је Лоренцов (Lorentz) профил за извор емисионих линија. Програм прати путању сваког емитованог фотона и израчунава Стоксове (Stokes) параметре I (укупан интензитет), Q (линеарна хоризонтална или линеарна вертикална поларизација), U (линеарна поларизација под углом $+45°$ или $-45°$) и V (лева или десна кружна поларизација) након сваког расејања. Стоксови параметри описују поларизационо стање електромагнетног зрачења и представљају реалне и мерљиве величине. Када се на трајекторији фотона више не налази ни један расејавајући
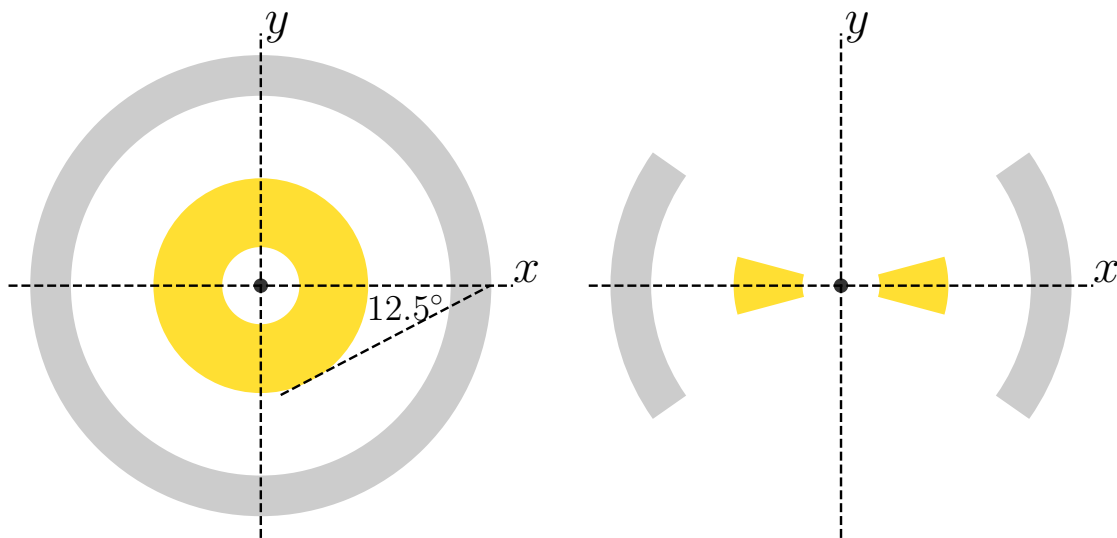
Слика 3: Илустрација геометрије модела ШЛР-а (жута) и РР-а (сива) у приказана у наличју (лево) и из екваторијалне равни (десно). Угао полуотвора ШЛР-а и РР-а је 15° и 35°. Преузето из рада Савића са сарадницима (Savić et al. 2018).

регион, тада, један од виртуелних детектора на небу који се налази у том смеру, региструје поларизационо стање фотона. Укупан неполаризовани флукс (НФ), степен поларизације p и φ рачунају се за сваки спектрални подеок сумирањем Стоксових параметара регистрованих фотона. Програм STOKES је првобитно развијен за моделирање УВ- и оптичке поларизације индуковане расејањем за радио-тиха АГЈ-а, али се може применити за проучавање поларизације разних астрофизичких појава (Marin & Goosmann 2014). Уобичајена излазна вредност програма $\varphi = 90°$ одговара поларизационом стању где вектор електричног поља $\vec{\mathbf{E}}$ осцилује у правцу паралелном оси симетрије система (z-оса, што је супротно конвенцији коју је увео Смит са сарадницима (Smith et al. 2005).

Наш модел се састоји од тачкастог извора смештеног у центру који емитује непрекидно изотропно неполаризовано зрачење задато степеним законом облика $F_c \propto \nu^{-\alpha}$, где је $\alpha = 2$. Ова вредност α одговара спектру константног интензитета када се пређе из фреквенционог домена у таласни домен. Извор континуума окружен ШЛР-ом, а даље затим и РР-ом. Попречни пресеци ШЛР-а и РР-а су облика клина са типичним углом полуотвора 15° за ШЛР и 35° за РР (Afanasiev & Popović 2015). Илустрација геометрије модела датаје на слици 3.

Генерисали смо четири пробна модела код којих СМЦР у центру може имати масу 10^6, 10^7, 10^8 и $10^9\,M_\odot$. Димензије ШЛР-а и РР-а добијене су скалирањем у
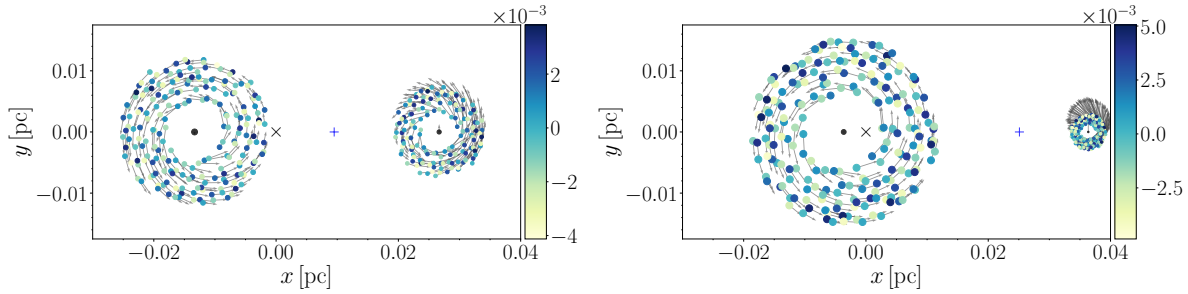
Figure 4: Геометрија и кинематика ШЛР-а за **раздвојен случај** код кога је однос маса $q = 0.5$ (леви панел) и $q = 0.1$ (десни панел). Црни $\times$ симбол означава центар масе. Плави крстић означава Лагранжову тачку L_1. Сиве стрелице означавају поље брзина сваког од облака ШЛР-а. Боја означава вертикално растојање од xy-равни. Преузето из рада Савића са сарадницима Savić et al. (2019).

форми степеног закона код ког је степени индекс одређен прикупљањем познатих вредности ШЛР-а и РР-а из литературе. Прво смо извршили симулације за различите масе црних рупа уз претпоставку чистог кеплеровског кретања, а након тога смо разматрали доприносе могућих радијалних прилива и вертикалних отицања као додатних компоненти брзина при кеплеровском кретању. Симулирали смо оба случаја где је смер кеплеровског кретања у смеру супротном од смера казаљке на сату (позитиван смер) и у смеру казаљке на сату (негативан смер).

Такође, комплексна кинематика ШЛР-а може бити услед присуства двојних супермасивних црних рупа (ДСМЦР-а) које покрећу АГЈ. Разматрали смо модел ДСМЦР-а које су на суб-pc растојањима и где свака црна рупа има свој акрециони диск и ШЛР (слика 4). За овако комплексан систем, поново смо разматрали екваторијално расејање са унутрашње стране торуса прашине. Систем ДМСЦР-а моделовали смо као две црне рупе које се крећу око заједничког центра масе под дејством гравитације. Ово је добро познат проблем за који је показано да је еквивалентан проблему једног тела редуковане масе μ које се креће у спољашњем гравитационом пољу (Landau & Lifshitz 1969; Postnov & Yungelson 2014). Редукована маса зависи од маса обе компоненте и дата је изразом: $\mu = \mathcal{M}_1 \mathcal{M}_2 / (\mathcal{M}_1 + \mathcal{M}_2)$. У нашем моделу полазимо од две претпоставке: прва је да обе СМЦР-е имају своје акреционе дискове и одговарајуће ШЛР-е, а друга је да су и акрециони дискови и расејавајући регион копланарни. У зависности од орбиталног растојања између црних рупа, разматрали смо четири различита случаја ДСМЦР-а: **раздвојен случај**, **контактни случај**, **мешовити случај** и **спирални случај**. Расејавајући регион је исти за сва четири модела.

Такође изабрали смо четири АГЈ-а са израженим S-профилима φ: NGC 4051, NGC 4151, 3C 273 и PG0844+349. Зрачење ових објеката, како поларизовано, тако и неполаризовано, проучавано је у последњих неколико деценија. Сви они показују доминантно екваторијално расејање у поларизованим спектрима. Током 2014. године спровели смо спектрополариметријска посматрања сва четири АГЈ-а користећи 6 m телескоп који припада САО РАН са монтираним фокалним редуктором SCORPIO. За сваки од објеката направили смо геометријски модел користећи податке добијене посматрањима и који су доступни у литератури и резултате нашег моделирања директно смо поредили са посматрачким подацима.

Резултати

На слици 5 приказани су симулирани профили φ, поларизованог флукса ПФ, степена поларизације p и укупног неполаризованог флукса НФ дуж профила линије за масу СМЦР-е једнаку $10^6\,M_\odot$. Из наших модела (слика 5, доњи десни панел) можемо видети да је степен поларизације осетљив на инклинацију под којом посматрамо систем. Профил p достиже максимум у крилима линије и минимуму језгру линије како је показао Смит са сарадницима (Smith et al. 2005). Поларизована линија (слика 5, средњи десни панел) је шира од неполаризоване (слика 5, горњи десни панел), као што је предвиђено екваторијалним расејањем. На слици 5 (леви панели) приказани су симулирани профили φ за три инклинације под којом посматрамо систем. Профили φ су S облика. Смер ротације утиче само на φ док НФ, ПФ и p остају нетакнути. За позитиван смер ротације, φ достиже максималну вредност у плавом делу линије а минималну у црвеном делу линије. Промена од минимума ка максимуму дешава се у језгру линије где централна вредност има вредност континуума $\varphi_\mathrm{c} = 90°$. Важна карактеристика φ је да је антисиметрична у односу на ниво континуума φ_c тако да за задату инклинацију посматрања система важи следеће:

$$\varphi(180° - i) = 180° - \varphi(i). \tag{6}$$

Када примењујемо AP15 на моделираним подацима, потребно је узети у обзир само поларизацију у широкој линији и зато је неопходно одузети поларизацију у континууму. За све инклинације типа 1 (систем није заклоњен торусом прашине) под којим посматрамо систем важи $\Delta\varphi = \varphi - 90°$. На слици 6 (доњи
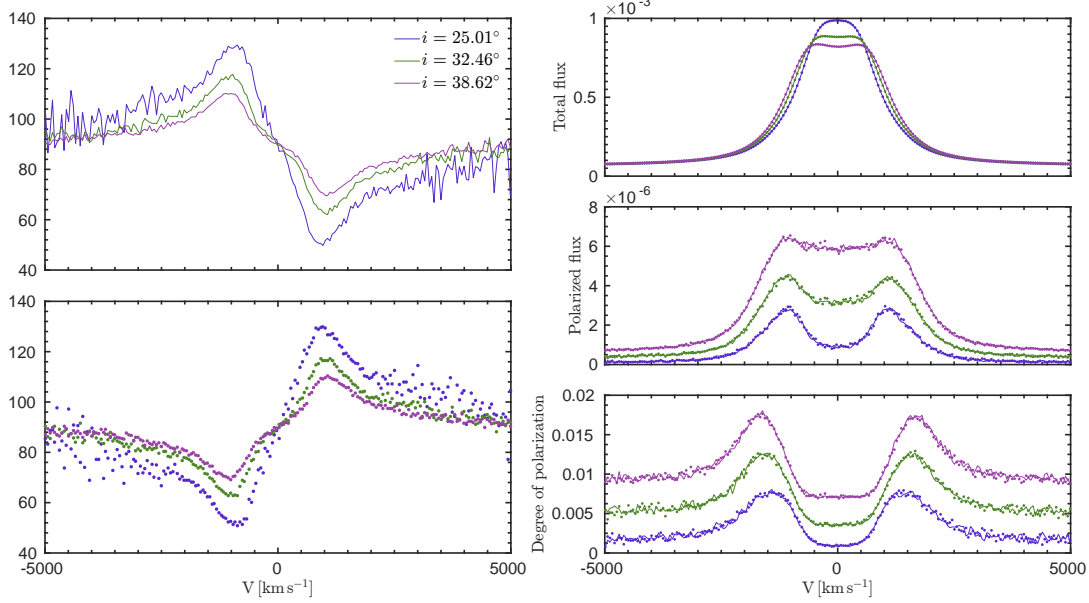
Слика 5: На левим панелима приказан је позициони угао поларизационе равни φ када систем ротира у позитивном смеру (горњи леви панел) или када ротира у негативном (доњи леви панел), укупни неполаризовани флукс НФ (горњи десни панел), поларизовани флукс ПФ (средњи десни панел), степен поларизације p (доњи десни панел). Резултати су приказани неиспрекиданим линијама за три инклинације под којим посматрамо систем $i = 25.01°$, $32.46°$ и $38.62°$ респективно. Ипрекиданом линијом приказани су резултати за супротан смер ротације. Наглашавамо да на φ утиче смер ротације. Ефекат смера ротације не утиче на НФ, ПФ и p. Преузето из рада Савића сарадницима Savić et al. (2018).

панели) приказан је линеарни фит описан AP15 методом. Видимо да се кеплеровско кретање може пратити дуж φ-профила за инклинације типа 1 под којим посматрамо систем. Област око 1σ несигурности линеарног фита постаје све ужа како посматрамо систем под све већим нагибом. За инклинације од $25°$ или мање, расипање од праве линије је много веће него за средње инклинације.

Међусобна удаљеност између ШЛР-а и РР-а у великој мери утиче на амплитуду φ. Да бисмо истражили овај ефекат, размотрили смо неколико случајева са различитим међусобним растојањима између ШЛР-а и РР-а, при чему смо задржали исту дебљину и оптичку дубину РР-а. На сликама 7 и 8 приказан је утицај међусобног растојања између ШЛР-а и РР-а на параметар a и на процене маса СЦМР-а. Наши резултати показују да међусобна удаљеност између ШЛР-а и
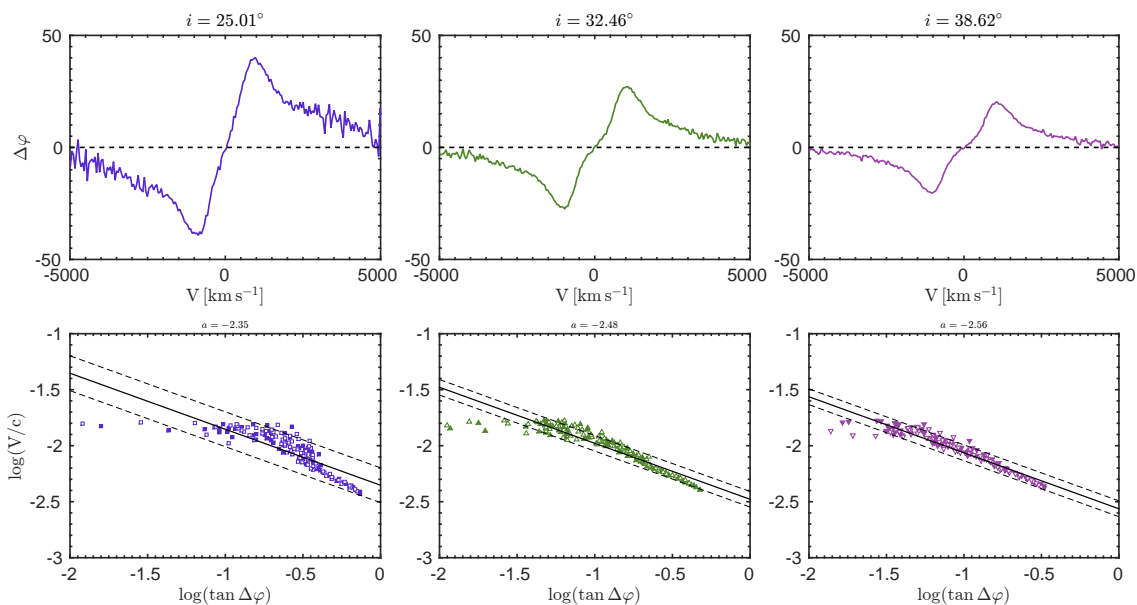
Слика 6: Моделирани φ-профили (горњи панели) и зависност брзине од угла (доњи панели) за модел код кога централна СМЦР-а има масу $10^6\, M_\odot$. Пуни симболи представљају плави део линије, а отворени симболи представљају црвени део линије. Пуна неиспрекидана линија представља најбољи фит. Преузето из рада Савића сарадницима Savić et al. (2018).

РР-а има велики утицај на параметар a што за последицу има велики утицај на процену маса СМЦР-а. Видимо да параметар a показује исти облик профила и исту зависност за све симулиране случајеве и за све инклинације. Једино када је РР поред ШЛР-а, добијамо да процена масе СМЦР-е не зависи од инклинације. Процена масе СМЦР-е расте када се међусобна удаљеност повећава. За задату тачност од $10\,\%$ налазимо да су најбоље процене СМЦР-а за сва четири случаја када је однос унутрашњег радијуса РР-а и спољашњег радијуса ШЛР-а између 1.5 и 2.5 (слика 8). За нагибе $25°$ или мање, допринос екваторијалног расејања је и низак и кеплеровско кретање се не може видети у φ-профилу. За додатне компоненте брзина као што су радијални приливи и вертикални одливи, закључујемо да се ови ефекти могу занемарити уколико њихов допринос није значајни део кеплеровске компоненте.

На слици 9 приказани су резултати симулираних φ, p и НФ за две инклинације под којим посматрамо систем и за исти азимутални угао ϕ. Профили φ су сложени и драстично се разликују од оних за случај једне СМЦР-е. За различите
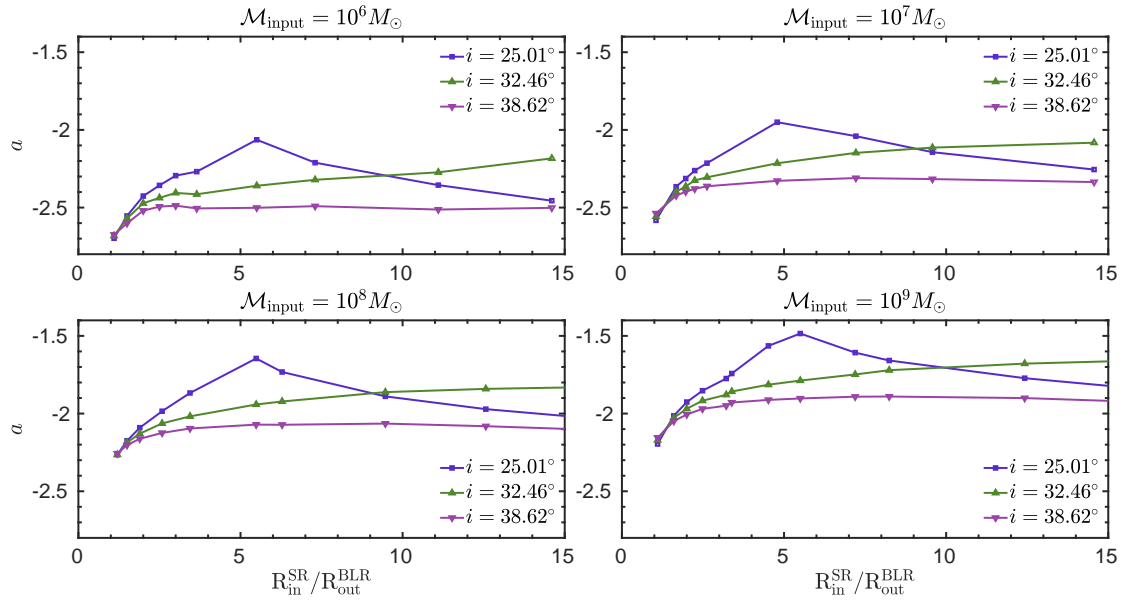
Слика 7: Зависност параметра a од односа између унутрашњег радијуса PP ($R_{\text{in}}^{\text{SR}}$) и спољашњег радијуса ШЛР ($R_{\text{out}}^{\text{BLR}}$) за три инклинације под којом посматрамо систем. Преузето из рада Савића сарадницима Savić et al. (2018).
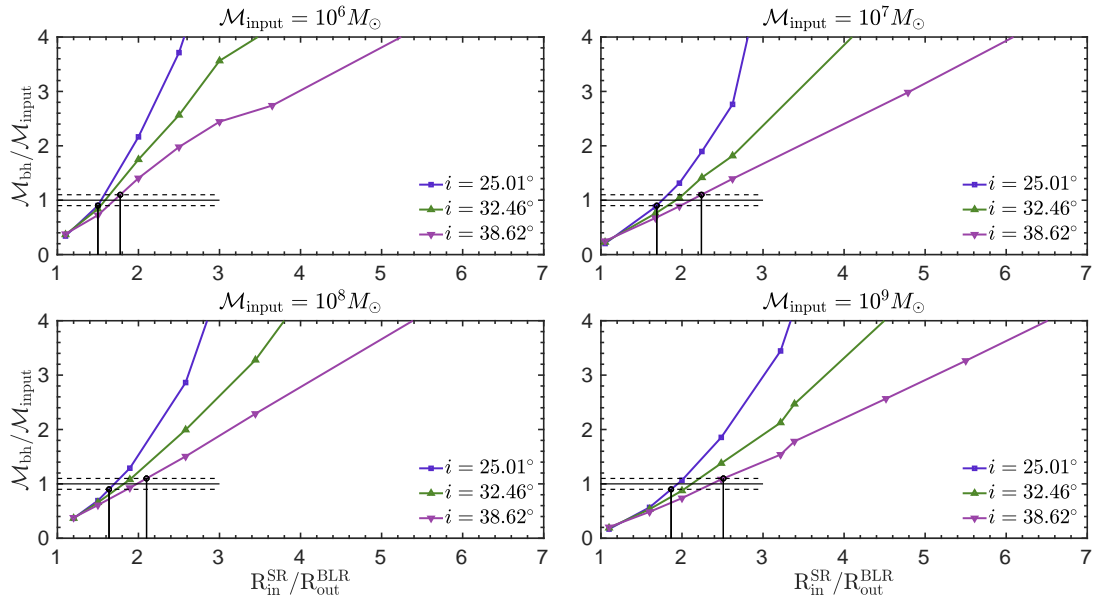
Слика 8: Процена масе црне рупе као функција односа између унутрашњег радијуса PP ($R_{\text{in}}^{\text{SR}}$) и спољашњег радијуса ШЛР ($R_{\text{out}}^{\text{BLR}}$) за три инклинације под којом посматрамо систем. Хоризонталне испрекидане линије представљају интервал одступања од $10\,\%$ од улазне масе (пуна линија). Преузето из рада Савића сарадницима Savić et al. (2018).
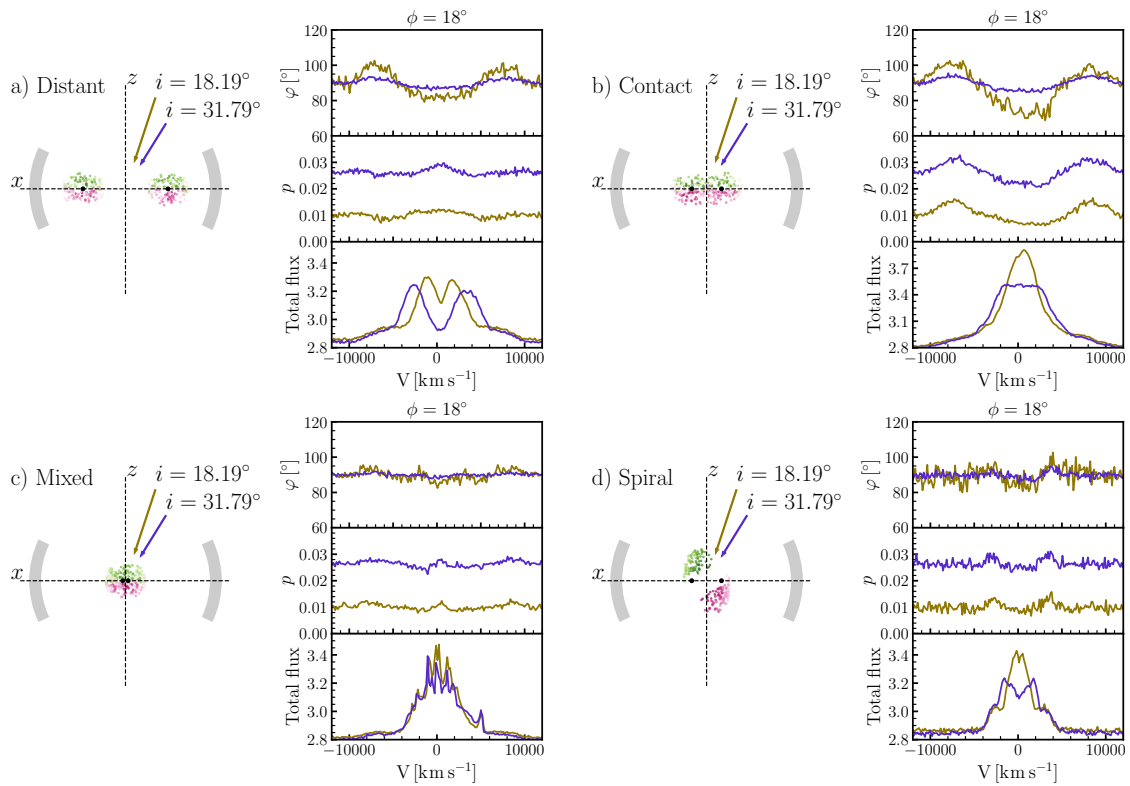
Слика 9: На левој страни приказаних панела илустрована је геометрија модела са ДСМЦР-ма у центру: раздвојен случај (a), контактни случај (b), мешовити случај (c) и спирални случај (d). На десним странама панела, од врха ка дну приказани су профили за φ, p и НФ за две инклинације $i = 18°$ (браон линија) и $i = 32°$ (плава линија). Азимутални угао посматрања је $\phi = 18°$ за све графике. Преузето из рада Савића са сарадницима Savić et al. (2019).

азимуталне углове посматрања, φ-профили су доста различити. Ова разноликост је резултат различитих пројекција брзина ка посматрачу јер модел није азимутално симетричан. Профили φ су симетрични у односу на средиште линије, што није случај код једне црне рупе у којем долази до промене φ од минималне до максималне вредности дуж језгра линије (или обрнуто у зависности од ротације). Угао φ углавном има сложене профиле са два или више минимума или максимума. Степен поларизације p има профиле са минимумом у језгру и максимумима у плавом и црвеном крилу, што је уобичајено за појединачне СМЦР-е, али се појављују и профили супротног облика са максимумом у језгру и минимумима у крилима што може бити показатељ ДМСЦР-а. Профили неполаризованог флукса углавном показују два максимума који се могу интерпретирати као профили услед дисколике геометрије емитера зрачења (Chen & Halpern 1989). Разлика између

φ-профила код модела ДСМЦР-а и само једне СМЦР-е је очигледна и највише се огледа у симетрији. За ДСМЦР-е φ-профили суососиметрични у односу на осу нулте брзине, услед чега имамо профиле са двоструким максимумима. Са друге стране, φ-профили за моделе са једном СМЦР-ом су централно-симетрични, чак и када је присутно комплексно кретање у форми прилива и отицања (Savić 2019).

За све моделиране објекте успели смо да репродукујемо веома сличне φ-профиле оним који су добијени из посматрања. Маса СМЦР-е нађена фитовањем моделираних података је нешто већа од оне добијене фитовањем посматрачких података, али се и даље добро слаже са резултатима из литературе. Посматрачки подаци су много више разбацани око предвиђене праве линије што уопштено доводи до грешке у проценама маса СМЦР-а неколико пута веће у поређењу са грешком добијеном користећи методу реверберационог мапирања.

Закључак

Из овде представљеног рада закључујемо следеће (Savić et al. 2018; Savić 2019; Savić et al. 2019):

1. Ако се кеплеровско кретање може детектовати у поларизације широких емисионих линија, тада се директно могу мерити масе СМЦР-а чије су добијене вредности у складу са оним које су мерене другим методама.

2. Ефекти могућих доприноса прилива или одлива у ШЛР-у узимају свој данак само за екстремне случајеве када је њихова брзина приближна или већа од кеплеровске брзина и у том случају не можемо примењивати AP15 методу.

3. Степен поларизације и неполаризовани флукс показују јединствене профиле карактеристичне само за ДСМЦР-е, али такође показују профиле који су присутни код појединачних СМЦР, и као такви не могу се користити за једнозначно разлучивање централног мотора АГЈ-а. Са друге стране, поларизациони угао поларизационе равни φ показује јединствене профиле у поређењу са онима код појединачне СМЦР-е, и може се користити за идентификовање ДСМЦР-ма.

4. φ-профили су централно-симетрични у случају једне СМЦР-е, чак и када су додатне компоненте кретања у ШЛР-у присутне.

5. φ-профили суососиметрични, често са два или више максимума, у случају ДСМЦР-е.

6. Примена AP15 методе није применљива у случају ДСМЦР-е.

7. AP15 метода омогућава нов и независан начин за мерење маса СМЦР-а. Процењене масе добро се слажу са масама добијеним другим методама, пре свега са методом реверберационог мапирања. Релативна грешка у процени маса између ове две методе је око $30\,\%$.

Résumé

Les trous noirs supermassifs (SMBH) se trouvent au coeur de presque toutes les galaxies massives de l'Univers. Leur masse varie généralement entre 10^6–$10^{9.5}\,M_\odot$ (Kormendy & Richstone 1995). La plupart d'entre eux sont dormants, mais lorsque le gaz à proximité est abondant, le processus d'accrétion pourra démarrer et former un disque. Comme la température de la matière accrétée augmente, une grande quantité d'énergie est rayonnée, déclenchant une phase active et former ce qu'on appelle aujourd'hui un noyau actif de galaxie (AGN, Salpeter 1964; Zel'dovich & Novikov 1964; Lynden-Bell 1969). Qu'ils soient inactifs ou actifs, les SMBH n'émettent pas de rayonnement, mais le gaz et les étoiles qui les entourent sont sensibles à leur présence gravitationnelle, ce qui nous permet de mesurer leur masse.

Le paradigme standard, ou le modèle dit unifié des AGNs (Antonucci 1993; Netzer 2015), suppose que le SMBH est entourée d'un disque d'accrétion qui, à grande distance, est fragmenté et forme un tore poussiéreux optiquement épais. Le tore de poussières collimate le rayonnement dans la direction polaire et obscurcit la région centrale dans le plan équatorial. La région des raies larges (BLR) se trouve à proximité du SMBH, à des distances de quelques jours lumière à quelques centaines de jours-lumière, et le gaz y est photoionisé par le rayonnement émis par le disque d'accrétion. La plupart des raies larges sont émises par recombinaison radiative (Netzer 2013) et leur largeur de quelques milliers $\mathrm{km\,s^{-1}}$ est principalement due au mouvement képlérien autour du SMBH (Clavel et al. 1991). Dans la direction polaire, des vents polaires hautement ionisés et faiblement relativistes émergent à des échelles inférieures au pc (Tombesi et al. 2012). Plus loin, alimentés par le vent polaire, les écoulements sortants forment une structure bi-conique de gaz à faible densité qui émet des raies étroites interdites - la région dite des raies étroites (NLR). Cette région peut avoir des dimensions de l'ordre du kpc (Bennert et al. 2002). Parfois, des jets relativistes se forment dans la direction de l'axe polaire et produisent ainsi une forte émission radio. La dichotomie observée entre les AGN de type 1 où les raies larges d'émission sont visibles et les AGN de type 2 dont les spectres optiques ne comportent que des raies d'émission étroites est largement due à un effet d'orientation où les AGN de type 1 sont observés le long de l'axe polaire alors que les AGN de type 2 sont observés à des inclinaisons beaucoup plus élevées. Une illustration de la structure de l'AGN est présentée à la figure 1.

La grande majorité des AGN présentent une faible polarisation linéaire du continuum optique $p < 3\,\%$, tandis que la polarisation circulaire est inférieure par quelques
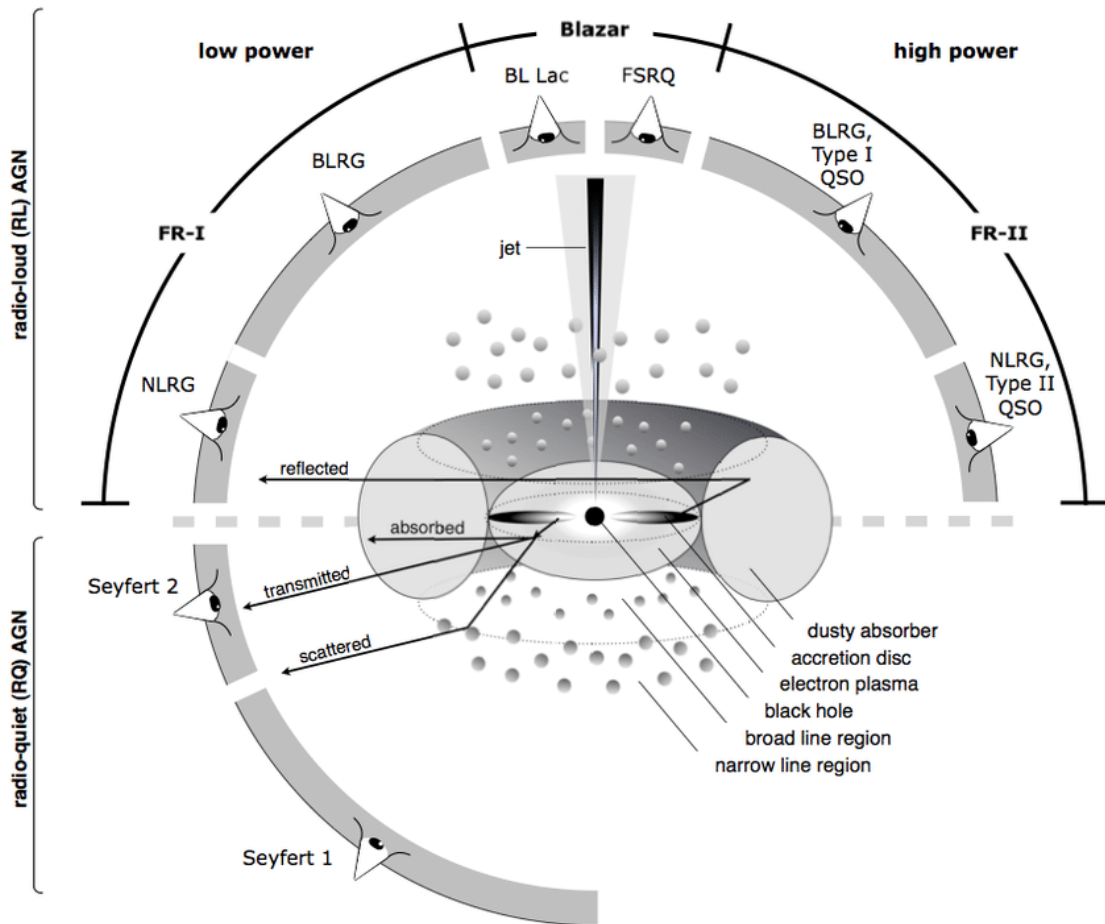
Figure 1: Le modèle unifié des AGN. Le trou noir se trouve au centre et est entouré d'un disque d'accrétion. Plus loin, au-delà du rayon de sublimation de la poussière, le disque d'accrétion forme un tore de poussières. La région des raies larges se trouve à proximité du disque et est obscurcie par le tore. Beaucoup plus loin, à des échelles du kpc au-dessus et au-dessous du disque, se trouve la région des raies étroites. Le jet relativiste se trouve à l'intérieur du cône étroit le long de l'axe polaire. Différents types d'AGN sont observés en fonction de l'inclinaison. L'inclinaison est mesurée à partir de l'axe des pôles vers le plan équatorial où se trouve le disque d'accrétion. Crédits Beckmann & Shrader (2012).

ordres de grandeur. Les AGN ayant une polarisation optique aussi élevée que $20\,\%$, sont principalement des blazars (Angel & Stockman 1980; Moore & Stockman 1981). Stockman et al. (1979) et Antonucci (1982) ont montré que les AGN de type 1 présentent une forte tendance à ce que le champ électrique de l'onde soit bien aligné avec l'axe de la structure radio étendue – une caractéristique appelée polarisation parallèle. Au contraire, dans les AGN de type 2, le champ électique est perpendiculaire à l'axes radio – polarisation perpendiculaire (orthogonale) (Antonucci 1982, 1983, 1984). Selon la gamme de fréquence, différents processus physiques sont responsables de la polarisation. En rayons X, la diffusion Compton et Compton inverse sont les mécanismes de polarisation dominants. De l'UV (ultraviolet) au proche IR (infrarouge), c'est la diffusion Thomson (électron) et Mie (particule sphérique). Dans l'infrarouge moyen et lointain, l'alignement de la poussière par des champs magnétiques à grande échelle (Lopez-Rodriguez et al. 2015) produit une polarisation parallèle. Dans le domaine radio, l'émission synchrotron diffusée par les électrons est le mécanisme dominant de polarisation.

La spectropolarimétrie optique des AGN de type 1 a montré que la polarisation des raies larges d'émission est causée par la diffusion équatoriale (Smith et al. 2002). Les propriétés de polarisation observées peuvent être expliquées en supposant une BLR en forme de disque képlérien entouré d'une région de diffusion coplanaire (SR, Smith et al. 2005). Dans la raie, l'angle de polarisation φ mesurée en fonction de la longueur d'onde présente un profil en forme de S: loin du centre de la raie, φ suit la valeur du continuum. Aux vitesses correspondant à l'aile bleue, φ atteint un maximum, suivi d'une chute dans le noyau jusqu'à ce que la valeur minimale soit atteinte dans l'aile rouge. La diffusion équatoriale dans les AGN est la principale hypothèse que nous utilisons dans ce travail.

Mesure des masses des SMBH

Lorsqu'ils sont en phase active, les SMBHs jouent un rôle important sur leur environnement, dans un processus appelé rétroaction de l'AGN (Fabian 2012, et références). En conséquence de la rétroaction de l'AGN, de nombreuses corrélations entre la masse du SMBH et les propriétés de la galaxie hôte ont été trouvées, dont la plus notable est la relation $\mathcal{M}_{\rm bh} - \sigma_*$ (Ferrarese & Ford 2005; Kormendy & Ho 2013), impliquant que le SMBH et la galaxie hôte évoluent ensemble (Heckman & Kauffmann 2011). Par conséquent, la mesure fiable de la masse du SMBH est une tâche importante en astronomie

moderne. Pour ce faire, différentes techniques ont été mises au point, à la fois directes et indirectes, (Peterson 2014), la plupart des méthodes ciblant les AGN en raison de leur forte luminosité (allant jusqu'à $L_{\text{bol}} \approx 10^{48}\,\text{erg}\,\text{s}^{-1}$, Padovani 2017a) qui peuvent être facilement observées à distances cosmologiques.

Au cours des dernières années, les mesures de masse des SMBH sont provenus le plus souvent de la cartographie par réverbération des AGNs (Bentz & Katz 2015). En mesurant le délai entre la variabilité du continuum ionisant et la variabilité des raies d'émission larges, on peut obtenir un rayon photométrique de la BLR. Avec un rayon photométrique connu et une vitesse mesurée directement à partir de la largeur de la raie, on peut obtenir la masse du SMBH (Bahcall et al. 1972; Blandford & McKee 1982; Peterson 1993). La durée d'une campagne de cartographie par réverbération peut être assez longue. Une galaxie individuelle doit être observée à maintes reprises pendant plusieurs mois, et les AGN distants nécessitent même plusieurs années de surveillance (Shen et al. 2016; Grier et al. 2017, 2019). Les raies de Balmer de l'hydrogène sont les plus couramment utilisées, cependant, les raies d'émission hautement ionisées comme Mg II, C III] et C IV peuvent également être utilisées pour les AGNs à des décalages spectraux plus élevés (Mejía-Restrepo et al. 2016).

Une autre méthode récemment proposée utilise la rotation de l'angle de polarisation le long du profil de la raie d'émission large afin de tracer le mouvement képlérien et déterminer la masse SMBH (Afanasiev & Popović 2015, herafter AP15). Elle suppose que la BLR est aplatie et que la lumière est principalement diffusée sur les parties internes du tore de poussière (diffusion équatoriale Smith et al. 2005), ce qui entraîne la polarisation de la raie large. La relation entre la vitesse V du gaz diffusant le long du profil de la raie et l'angle de polarisation φ est citep2015ApJ...800L..35A:

$$\log \frac{V}{c} = a - 0.5 \log \left(\tan \left(\varphi \right) \right), \tag{7}$$

où c est la vitesse de la lumière. La constante a est liée à la masse du trou noir par

$$a = 0.5 \log \frac{G\mathcal{M}_{\text{bh}} \cos^2 \theta}{c^2 R_{\text{sc}}}, \tag{8}$$

où G est la constante de la gravitation, $\mathcal{M}_{\text{bh}}$ est la masse du trou noir, R_{sc} est le rayon interne du tore, et θ est l'angle entre le disque et le plan de diffusion. La relation attendue entre la vitesse et φ est montrée à la figure 2 (à droite). Dans le cas d'un SR (région de diffusion) mince, une bonne approximation serait de prendre $\theta \sim 0$. Dans ce
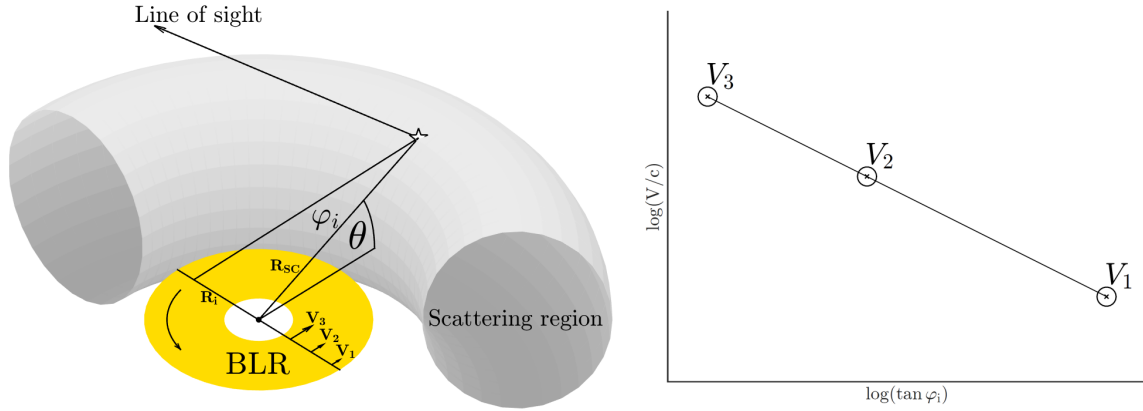
Figure 2: Vue schématique de la lumière diffusée depuis l'intérieur du tore (à gauche). Relation attendue entre φ et la vitesse (à droite). Crédits: Savić et al. (2018).

cas, la relation entre les vitesses et φ ne dépend pas de l'inclinaison puisque l'émission de la BLR vers la SR est presque latérale. Cette méthode est en accord avec la relation $\mathcal{M}_{\mathrm{bh}} - \sigma_*$ et avec la cartographie par réverbération, et elle a été appliquée jusqu'à présent à une douzaine d'AGNs proches (Afanasiev et al. 2019).

Cette méthode offre un certain nombre d'avantages par rapport à la méthode de cartographie par réverbération. Elle ne nécessite qu'une seule période d'observations et peu de temps de télescope par rapport à la méthode de cartographie par réverbération. Elle peut être appliquée à des raies dans différentes gammes spectrales allant du proche infrarouge et de l'optique (raies de Balmer) aux UV (Lyα, C III], C IV et Mg II), permettant ainsi des mesures de la masse de trou noir pour des AGNs à des décalages spectraux très divers (AP15). La virialisation de la BLR n'est pas a priori supposée, mais elle se mesure dans le profil en φ observé. Cependant, cette méthode nécessite de connaître le rayon intérieur du tore; R_{sc} est souvent trouvée en utilisant la réverbération par la poussière ou d'autres relations de mise à l'échelle (AP15). De plus, cette méthode ne peut être utilisée que pour une BLR en forme de disque en rotation ; dans le cas où la BLR est dominée par un mouvement radial, elle ne peut être utilisée. Nous soulignons également que dans cette méthode, nous ne considérons qu'une seule diffusion par photon de la raie et que la contribution de diffusions multiples n'est pas prise en compte. Comme la polarisation est très sensible à la cinématique et à la configuration géométrique (Goosmann & Gaskell 2007), le traitement complet du transfert radiatif 3D avec polarisation est nécessaire pour tester cette méthode.

Méthodes

La tâche principale de cette thèse est d'explorer les possibilités et les limites de cette méthode et de trouver dans quelles conditions elle peut être utilisée. Pour ce faire, de nombreuses simulations de transfert radiatif avec polarisation ont été réalisées pour un ensemble de modèles génériques, en tenant compte des processus physiques importants dans la partie centrale des AGN. Nous avons beaucoup utilisé le code de transfert radiatif de Monte Carlo en 3D STOKES pour modéliser la polarisation induite par la diffusion dans les AGNs, en couvrant une large gamme spectrale autour de la raie Hα. Outre ces modèles génériques, nous avons réalisé des modèles pour quatre AGN à partir de paramètres disponibles dans la littérature: NGC 4051, NGC 4151, 3C 273 et PG0844+349. La masse d'entrée de chaque objet a été obtenue en appliquant la méthode AP15 à nos observations. Enfin, nous avons comparé les résultats des modèles avec des données d'observation. Toutes nos observations ont été réalisées avec le télescope alt-azimutal SAO RAS (Observatoire spécial d'astrophysique de l'Académie des sciences de Russie) 6 m en utilisant le spectrographe SCORPIO (Afanasiev & Moiseev 2005). Le travail présenté dans cette thèse est une nouvelle amélioration du modèle de diffusion équatoriale Smith et al. (2005). Alors que Smith et al. (2005); Afanasiev & Popović (2015) ont fait l'approximation d'une seule diffusion, nous avons pris en compte dans nos simulations des diffusions multiples pour des résultats plus généraux.

Nous effectuons un calcul de transfert radiatif 3D complet avec polarisation en utilisant le code public STOKES (Goosmann & Gaskell 2007; Marin et al. 2012, 2015; Marin 2018b; Rojas Lobos et al. 2018). Le programme est adapté à la géométrie et à la cinématique complexes du modèle et traite des événements multiplesde diffusionsur les électrons ou la poussières ainsi que l'absorption par la poussières. Le rayonnement émis par la source est divisée en un grand nombre de paquets de photons (typiquement plus de 10^7 par bin de longueur d'onde) qui suivent une SED (distribution spectrale d'énergie) qui est une loi de puissance pour le continuum ou un profil de Lorentz pour la raie large en émission. Pour chaque photon émis, le code suit son chemin et calcule les paramètres de Stokes I (intensité lumineuse totale), Q (polarisation linéaire horizontale ou linéaire verticale), U (polarisation linéaire $+45°$ ou $-45°$) et V (polarisation circulaire gauche ou droite) après chaque diffusion. Ces paramètres décrivent l'état de polarisation des ondes électromagnétiques et sont des quantités mesurables. Lorsqu'il n'y a plus de région de diffusion sur sa trajectoire, le photon avec son état de polarisation est enregistré par un des détecteurs virtuels dans le ciel. Le flux total (non polarisé, TF), le degré de
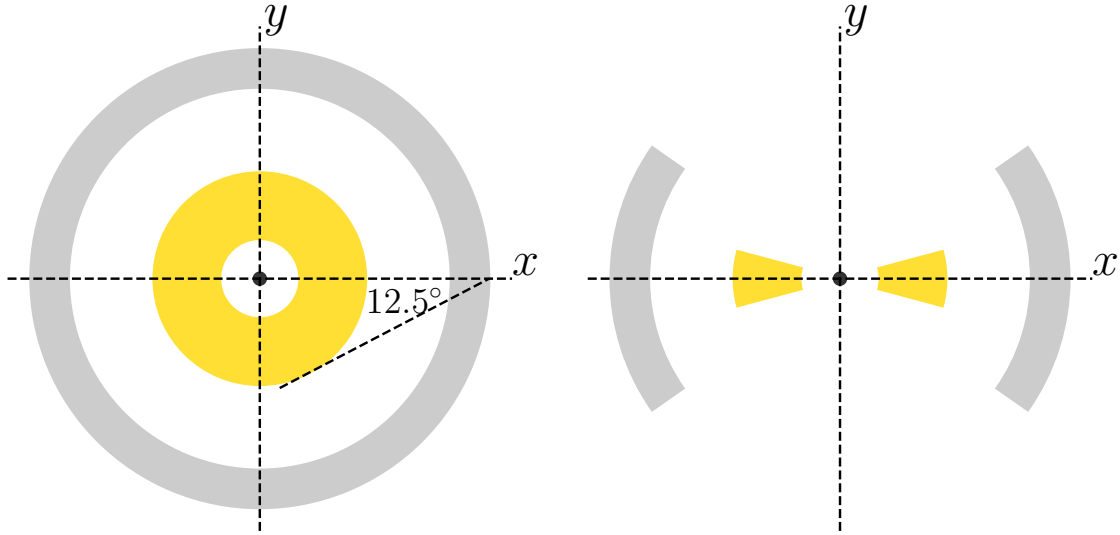
Figure 3: Schéma de la géométrie du modèle, avec la BLR (jaune) et le disque de diffusion (gris) vue de face (à gauche) et de profil (à droite). Les angles d'ouverture de la BLR et de la SR sont respectivement de 15° et 35°. Crédits: Savić et al. (2018).

polarisation p et φ sont calculés en additionnant les paramètres de Stokes de tous les photons détectés pour chaque bin spectral. Le code a été développé à l'origine pour modéliser la polarisation optique et UV induite par la diffusion du continu dans les AGNs, mais il peut être appliqué pour étudier la polarisation de nombreux objets astrophysiques (Marin & Goosmann 2014). Dans le code $\varphi = 90°$ correspond à un état de polarisation où le vecteur de champ électrique E oscille dans une direction parallèle à l'axe de symétrie du système (z-axis). C'est l'opposé de la convention utilisée par Smith et al. (2005).

Dans notre modèle, une source ponctuelle est située au centre et émet un rayonnement dans le continu isotrope non polarisé dont le flux est donné par un spectre de puissance $F_C \propto \nu^{-\alpha}$ avec $\alpha = 2$. Cette valeur correspond à spectre plat lorsque la fréquence est remplacée par la longueur d'onde. La source du continuum est entourée d'une BLR et, plus loin, d'une SR. La BLR et la SR sont modélisées par une géométrie de disque évasé avec un angle typique de demi-ouverture par rapport au plan équatorial de 15° pour la BLR et 35° pour la SR (Marin et al. 2012). Une illustration de la géométrie du modèle est donnée dans la figure 3.

Nous avons réalisé quatre modèles tests dans lesquels le SMBH central a une masse de 10^6, 10^7, 10^8 et $10^9\,M_\odot$. La taille de la BLR et de la SR dépendent la masse en une loi de puissance, pour laquelle l'exposant a été obtenu en recherchant dans la

littérature les rayons déjà connus de la BLR et de la SR. Nous avons tout d'abord effectué la simulation pour différentes masses des trous noirs avec l'hypothèse d'un mouvement képlérien pur, puis nous avons considéré des écoulements radiaux et des éjections verticales comme des composantes supplémentaires du mouvement du gaz par rapport au mouvement képlérien causé par la masse du trou noir. Nous avons simulé les deux cas où le mouvement képlérien est dans le sens antihoraire (positif) et dans le sens horaire (négatif).

De plus, la cinématique complexe de la BLR pourrait être due au fait que l'AGN contient un trou noir binaire binaire supermassif (SMBBBH). Nous considérons un modèle de SMBBBH séparés par moins d'un parsec, où chaque trou noir a son propre disque d'accrétion et sa propre BLR (figure 4). Nous considérons également la diffusion équatoriale sur la partie interne du tore. Les deux trous noirs orbitent autour du centre de masse commun sous l'effet de la gravité. Il s'agit d'un problème bien connu pour lequel il a été démontré qu'il est équivalent au problème d'un seul corps dont la masse réduite μ se déplace dans un champ gravitationnel externe (Landau & Lifshitz 1969; Postnov & Yungelson 2014) déterminé par la masse de chaque composante selon $\mu = \mathcal{M}_1\mathcal{M}_2/(\mathcal{M}_1 + \mathcal{M}_2)$. Nous avons fait deux hypothèses dans notre modèle: la première est que les deux SMBH ont des disques d'accrétion et des BLR correspondants, et la seconde que les disques d'accrétion et la région de diffusion sont coplanaires. En fonction de la distance entre les trous noirs, nous avons traité quatre cas de SMBBH différents: **distant**, **contact**, **mixte** et **spiralé**. La région de diffusion est la même pour les quatre modèles binaires. Nous présentons ici pour la première fois les profils des paramètres de polarisation des raies larges dans le cas d'une émission par un système SMBBH à l'échelle sub-pc.

Nous avons également sélectionné quatre AGNs présentant des variations importante de φ le long du profil de la raie: NGC 4051, NGC 4151, 3C273 et PG0844+349. Ces objets ont été très bien observés au cours des dernières décennies, tant en lumière polarisée que non polarisée. Ils présentent tous une diffusion équatoriale dominante dans leurs spectres. En 2014 et 2015, nous avons réalisé des observations spétropolarimétriques de ces quatre AGNs avec le télescope de 6 m BTA du SAO RAS avec le réducteur focal SCORPIO. Nous avons modélisé chacun de ces objets à l'aide des données d'observation disponibles dans la littérature et nous comparons les résultats de nos modèles avec nos propres observations.
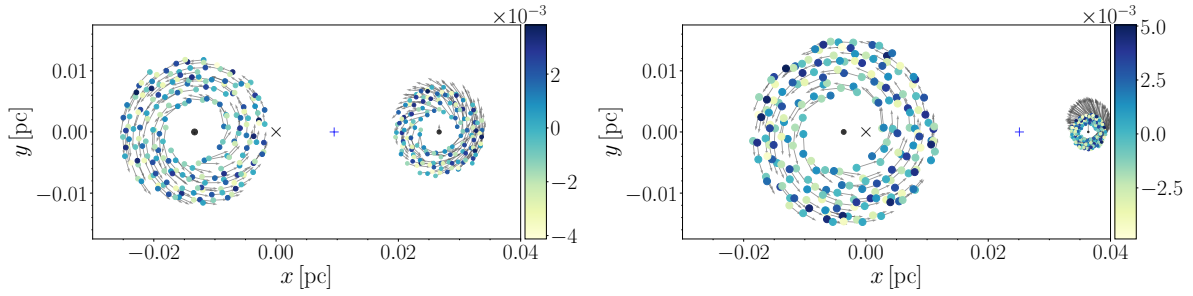
Figure 4: Géométrie et cinématique de la BLR pour le modèle **distant** avec un rapport de masse $q = 0.5$ (gauche) et avec $q = 0.1$ (droite). La croix noire ($\times$) indique le centre de masse, tandis que le symbole bleu $+$ marque le point de Lagrange L_1. Les flèches grises indiquent la vitesse de chaque élément de la BLR. Le code couleur indique la hauteur par rapport au plan xy. Crédits: Savić et al. (2019).

Résultats

Dans la figure 5, nous montrons les profils simulés de φ, du flux polarisé PF, du degré de polarisation p et du flux total TF le long du profil de la raie large lorsque la masse SMBH est de $10^6\,M_\odot$. Nos modèles (figure 5, en bas à droite), montrent que le degré de polarisation est sensible à l'inclinaison. Le profil en p atteint son maximum dans les ailes de la raie et son minimum se situe dans le coeur de la raie comme l'a montré Smith et al. (2005). La raie polarisée (figure 5, panneau central droit) est plus large que la raie non polarisée (figure 5, panneau supérieur droit), comme prévu par la diffusion équatoriale. Dans la figure 5 (panneaux de gauche), nous montrons les profils simulés de φ pour trois inclinaisons. Les profils φ sont en forme de S. Le sens de rotation n'affecte que φ, alors que TF, PF et p ne sont pas affectés. Pour une rotation dans le sens inverse des aiguilles d'une montre, φ atteint son maximale dans l'aile bleue de la raie et son minimum dans l'aile rouge. Les variations de φ se produisent autour du niveau du continuum $\varphi_c = 90°$. Une caractéristique importante de φ est ma symétrie par rapport à la polarisation du continuum : pour une inclinaison donnée i, φ satisfait l'équation :

$$\varphi(180° - i) = 180° - \varphi(i). \tag{9}$$

Lors de la mise en oeuvre de la méthode AP15 sur les données modélisées, il faut considérer la polarisation seulement dans la raie large et pour cela, il était nécessaire de soustraire la polarisation du continuum pour toutes les inclinaisons correspondant aux AGN de type 1: $\Delta\varphi = \varphi - 90°$. Dans la figure 6 (panneaux inférieurs), nous montrons l'ajustement décrit par la méthode AP15. Nous trouvons que le mouvement képlérien
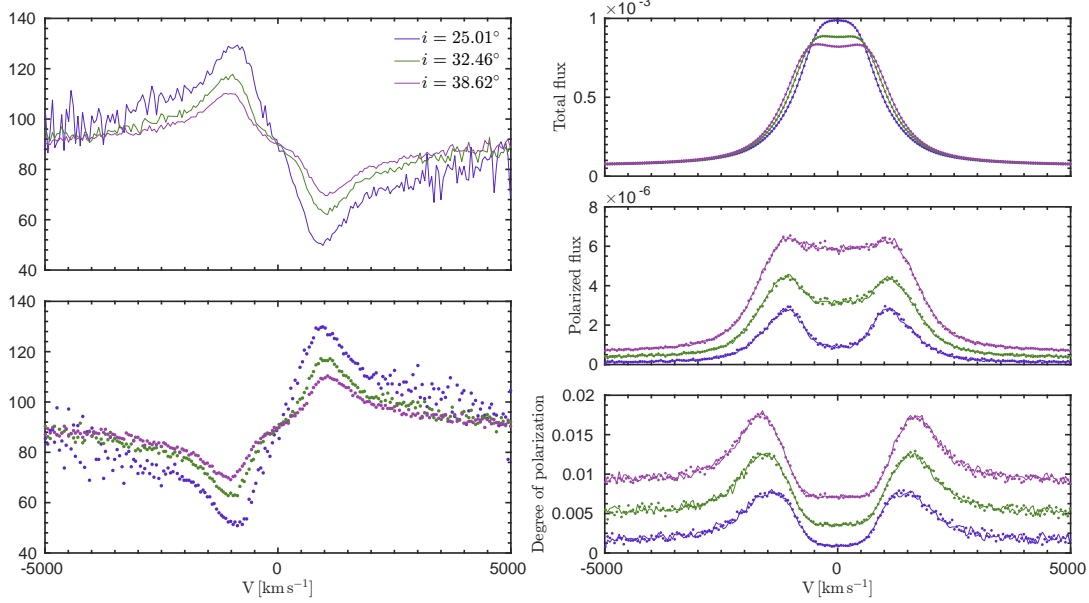
Figure 5: A gauche, l'angle de polarisation modélisé φ lorsque le système tourne dans le sens antihoraire (en haut) ou dans le sens horaire (en bas), le flux total non polarisé (TF, en haut à droite), le flux polarisé (PF, au milieu à droite), le degré de polarisation p, en bas à droite. SMBH a une masse de $10^6\,M_\odot$. Nous traçons les résultats en traits pleins pour trois inclinaisons : $i = 25.01°$, $32.46°$, et $38.62°$, tandis que les traits pointillés représentent les résultats pour un sens de rotation opposé. Noter la symétrie de φ par rapport au sens de rotation. Le sens de rotation n'affecte pas TF, PF et p. Les flux totaux et polarisés sont donnés en unités arbitraires. Crédits: adapté de Savić et al. (2018).

peut être déterminé via le profil φ pour les inclinaisons des AGN de type 1. La région située à $\pm 1\sigma$ autour de l'ajustement linéaire devient de plus en plus petite au fur et à mesure que l'on passe des inclinaisons de face à des inclinaisons de profil. Pour des inclinaisons de 25° ou moins, les données simulées montrent une dispersion beaucoup plus élevée autour de l'ajustement linéaire en comparaison aux cas avec une inclinaison intermédiaire.

La distance entre la BLR et la SR affecte énormément l'amplitude φ. Afin de tester cet effet, nous avons étudié différents cas avec différentes distances entre la BLR et la SR tout en conservant la même épaisseur et la même profondeur optique de la SR. Dans les figures 7 et 8, nous montrons l'influence de cette distance, et comment elle affecte le paramètre a et la masse du SMBH. Nos modèles montrent que la distance entre la BLR et la SR a une grande influence sur le paramètre a, ce qui affecte grandement
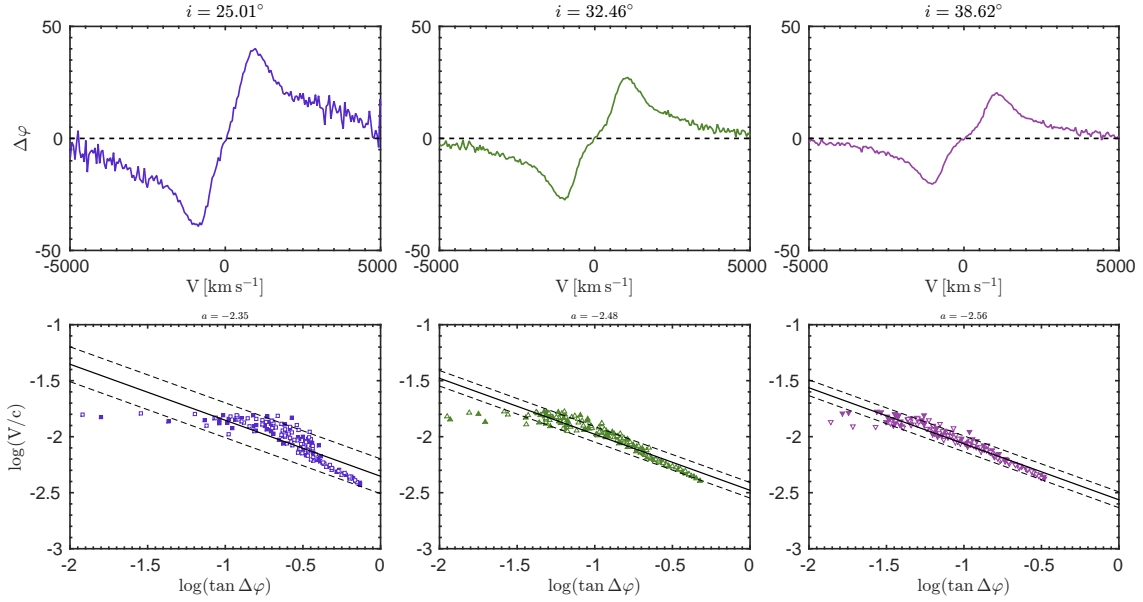
Figure 6: Angle de polarisation φ (panneaux supérieurs) et vitesses (panneaux inférieurs) calculés le long du profils Hα pour un modèle avec une masse centrale de $10^6 \, M_\odot$. Les symboles pleins correspondent à la partie bleue de la raie et les symboles ouverts à la partie rouge. Le trait plein représente le meilleur ajustement. Crédits: adapté de Savić et al. (2018).

nos estimations de la masse du trou noir. On peut voir que le paramètre a montre le même profil et la même dépendance en inclinaison pour tous les cas simulés. Ce n'est que lorsque la SR est adjacent à la BLR que l'estimations de masse du SMBH devient indépendante de l'inclinaison. Les estimations de masse du SMBH augmentent lorsque la distance augmente. Dans les quatre cas, et pour une précision demandée de 10 %, nous constatons que les estimations correctes de la masse du SMBH sont obtenues lorsque le rapport du rayon interne de la SR et du rayon externe de la BLR se situe entre 1,5 et 2,5 (figure 8). Pour des inclinaisons de 25° ou moins (vue de face), la contribution de la diffusion équatoriale est faible et nous trouvons que le mouvement képlérien ne peut être déduit du profil en φ. En ce qui concerne d'autres composantes de vitesse dans la BLR telles que des écoulements radiaux ou des éjections verticales, nous constatons que ces effets peuvent être négligés si les composantes supplémentaires de la vitesse ne représentent pas une fraction significative de la vitesse képlérienne.

Dans la figure 9 nous montrons les résultats pour φ, p et TF obtenus pour deux inclinaisons i et pour un angle de visualisation azimutal ϕ. Les variations de φ sont
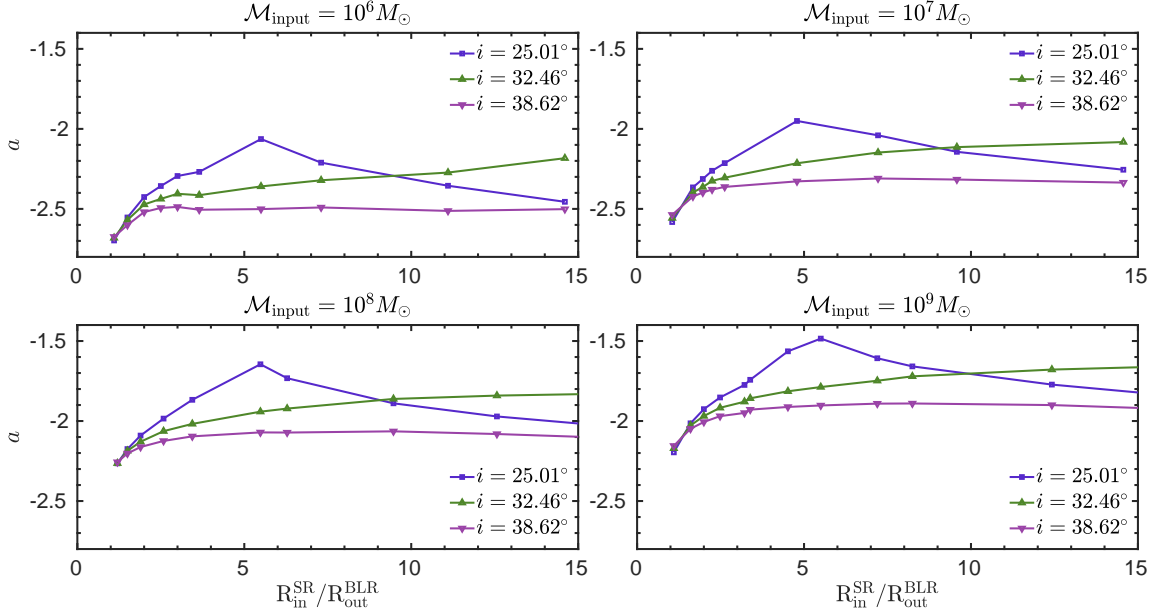
Figure 7: Dépendance du paramètre a sur le rapport entre le rayon interne de la SR (R_{in}^{SR}) et le rayon externe de la BLR (R_{out}^{BLR}) pour trois inclinaisons. Crédits: adapté de Savić et al. (2018).
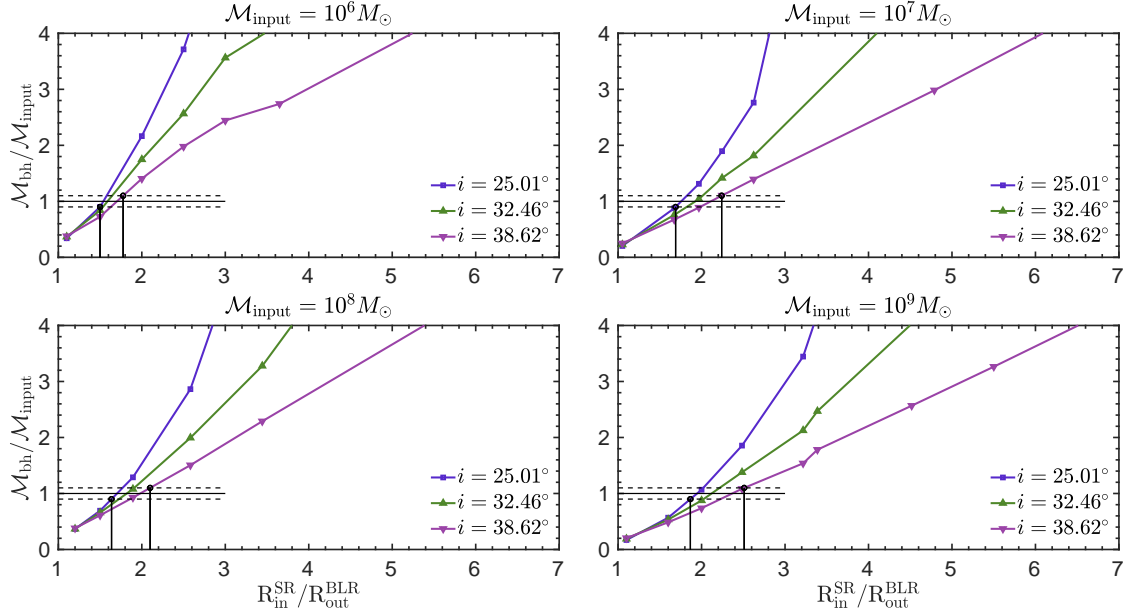
Figure 8: Estimation de la masse du trou noir en fonction du rapport entre le rayon interne de la SR (R_{in}^{SR}) et le rayon externe de la BLR (R_{out}^{BLR}) pour trois inclinaisons. Les pointillés horizontaux correspondent à un intervalle de 10% d'écart par rapport à la masse d'entrée (trait continu). Crédits: adapté de Savić et al. (2018).
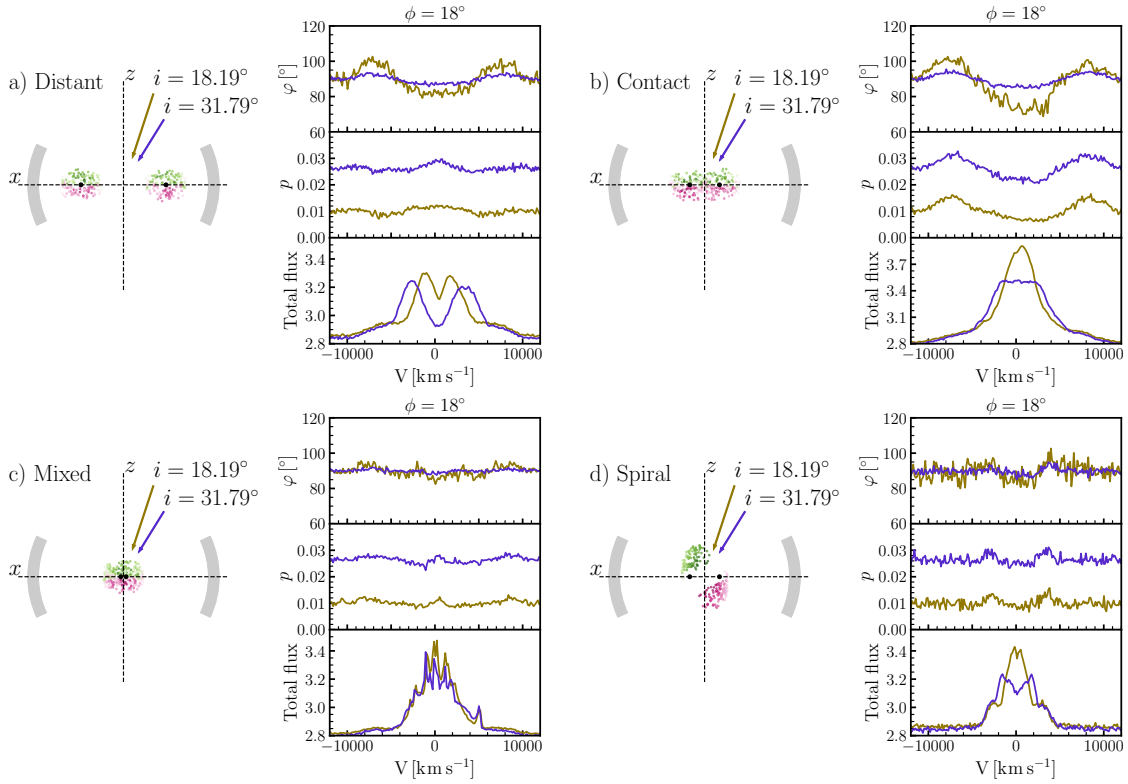
Figure 9: Modèles correspondant aux cas Distance (a, en haut à gauche), Contact (b, en haut à droite), Mixte (c; en bas à gauche), Spirale (d, en bas à droite). Pour chaque cas, la partie gauche donne un schéma de la géométrie. La partie droite, donne de haut en bas, φ, p et TF pour deux inclinaisons $i = 18°$ (en brun) et $i = 32°$ (en bleu). L'angle azimutal est $\phi = 18°$ dans tous les cas. Crédits: Savić et al. (2019).

complexes et très différentes des profils obtenus pour un trou noir isolé. Les profils en φ sont en outre très dépendants de l'angle de vue azimutal. Cette variabilité résulte des différences des projections de la vitesse vers l'observateur puisque le modèle n'est pas symétrique en azimut. Les profils φ sont maintenant symétriques par rapport au centre de la raie, ce qui n'est pas le cas pour un scénario unique où un swing se produit. L'angle de polarisation φ montre la plupart du temps des profils à deux pics ou même plus complexes. p montre des profils à deux pics avec un minimum dans le coeur de la raie, ce qui est habituel pour le scénario à SMBH unique, mais il y existe des profils opposés avec des minima de p dans les ailes de raies et des maxima dans le noyau de ligne qui peuvent être un indicateur de la présence de SMBBHs. TF montre la plupart du temps des profils doubles ou multi-pics qui sont souvent associés aux profils du disque (Chen & Halpern 1989). Il y a une différence claire dans les profils φ entre le modèle binaire et le modèle SMBH simple, en ce qui concerne la symétrie des profils φ.

Les profils des SMBBH sont symétriques par rapport à l'axe par rapport à la vitesse zéro, ce qui donne des profils à double pic. Au contraire, les profils φ pour une SMBH sont symétriques même pour les mouvements complexes incluant des accrétions et des éections (Savić 2019).

Pour tous les objets modélisés, nous avons pu produire des profils de φ très similaires à ceux observés. Les masses des SMBH estimées à partir de l'ajustement des données du modèle sont supérieures à celles obtenues en ajustant les données d'observation, mais toujours en accord avec celles de la littérature. Les données d'observation sont beaucoup plus dispersées par rapport à la ligne droite prédite, ce qui, en général, produit une erreur dans les estimations de masse SMBH un peu plus grande que celle obtenue par la cartographie de réverbérantion.

Conclusions

A partir des travaux présentés ici, nous tirons les conclusions suivantes (Savić et al. 2018; Savić 2019; Savić et al. 2019):

1. Si le mouvement képlérien peut être déduit du profil de la raie polarisée, alors des estimations directes de la masse du SMBH peuvent être effectuées et donnent des valeurs en accord avec d'autres méthodes.

2. Les effets des configurations possibles des écoulements entrants/sortants du TLB ne se font sentir que dans les cas extrêmes où la vitesse de ces écoulements est comparable ou supérieure à la vitesse képlérienne, qui dans ce cas ne peut être utilisée correctement.

3. Le degré de polarisation et le flux total présentent des profils similaires pour les SMBH simples et pour les SMBBH simples et pour les SMBBH; ces deux quantités à elles seules peuvent ne pas permettre de savoir si un SMBH ou une SMBBH est le moteur central de l'AGN. D'autre part, l'angle de position de polarisation φ montre des profils assez uniques qui diffèrent de ceux observés dans le scénario SMBH unique, et pourraient être utilisés pour identifier les candidats SMBBH.

4. Les profils φ pour le modèle SMBH montrent des profils symétriques par rapport à l'origine même lorsque des mouvements supplémentaires dans le BLR sont présents.

5. Les profils φ-profiles pour les modèles SMBBH produisent les profils symétriques par rapport à l'axe axes qui sont souvent doubles ou multi-pics.

6. L'application de la méthode AP15 n'est pas possible dans le cas des SMBBH.

7. L'application réussie de la méthode AP15 donne des estimations de masse qui sont en bon accord avec celles de la littérature.

8. La méthode AP15 fournit une nouvelle méthode indépendante d'estimation de la masse des SMBH. Les masses estimées sont en bon accord avec les valeurs obtenues par d'autres méthodes telles que la cartographie par réverbération. L'erreur relative des estimations de masse entre ces deux méthodes est d'environ 30 %.

Chapter 1

Introduction

A few percent of galaxies show an extraordinary huge activity in their nucleus with the core brightness several times surpassing the brightness of the rest of the galaxy. The tremendous amount of energy in these objects is coming from the galaxy nucleus and therefore the terms *active galaxies* (AG) and *active galactic nuclei* (AGNs) are coined in order to distinguish these objects from the regular (inactive) galaxies which represent the dominant majority. The spectra of AGNs cover a broad frequency range from γ- and X-rays in the high energy domain to radio waves in low energy domain. Presently, it is widely accepted that a large amount of energy is emitted from the accretion disk which is formed around the supermassive black hole (SMBH) by the infalling matter (Salpeter 1964; Lynden-Bell 1969). The strong radiation of the central source is ionizing the surrounding matter, which is capable of producing strong emission lines due to radiative recombination. These emission lines are superimposed on the underlying continuum. Absorption lines could also be present in the AGN spectra, either from the AGN itself, the host galaxy or from intergalactic matter. Optical variations of the AGN light curves (Fitch et al. 1967), with time scales of the order of few days, have indicated that the emitting region is compact with the size ranging from a few light days to a few light months. Historically, this was perceived as a major problem since the luminosity of the nucleus comparable in size with the Solar system is often thousands of times greater than the luminosity of regular galaxies. Until recently, and for very few cases, such compact regions could not be spatially resolved with the current observing facilities. We therefore rely on studying AGN radiation using spectroscopic and spectropolarimetric methods. By analysing AGN spectra, namely emission lines, we can obtain invaluable information on the physical and kinematic parameters. Since

we are dealing with the most luminous long-lived objects ($L_{\mathrm{bol}} \approx 10^{48}\,\mathrm{erg\,s^{-1}}$, Padovani 2017a), AGNs were observed at high redshifts, it makes them important for cosmology and the studies of the early Universe.

AGNs are triggered when there is enough gas to be accreted onto the SMBHs. The radiation produced by accretion strongly interact with the surrounding environment by heating or ejecting the gas - a process called AGN feedback. It can have a profound effect on the host galaxy by prematurely terminating star formation in the galaxy bulge, or in the most extreme cases to completely expel the gas out of the host galaxy. SMBHs in their active phase play a major role in the coevolution with the host galaxy (Heckman & Best 2014), which is well supported by the correlation of the SMBH mass with many properties of the host galaxy (Kormendy & Ho 2013). The properties of massive galaxies cannot be successfully reproduced by semi-analytic models nor numerical simulations without the inclusion of AGN feedback (Fabian 2012). Measuring SMBH masses reliably is therefore a crucial task in order to better understand how are they linked with the evolution of galaxies and AGNs.

The work in this thesis was inspired by the discovery of a new independent method for measuring the masses of SMBHs using the polarization of broad emission lines (Afanasiev et al. 2014; Afanasiev & Popović 2015) in AGNs. The method was first introduced in 2014 with the active galaxy Mrk 6 using the observations carried out with the 6 m telescope of the Special Astrophysical Observatory of the Russian Academy of Science[1] (SAO RAS). The method was discussed in details by Afanasiev et al. (2019) and it was successfully applied to thirty nearby AGNs.

The goal of the thesis is to theoretically explore the possibilities and limits of this method. This was done by performing numerous radiative transfer simulations with polarization for a set of generic models, taking into account important physical processes in the central part of AGNs. We heavily rely on the 3D Monte Carlo radiative transfer code STOKES[2] for modeling scattering induced polarization in AGNs, covering broad spectral range around Hα line. In addition to generic models, with the data found in literature, we made models for four AGNs: NGC 4051, NGC 4151, 3C 273 and PG0844+780 and compared them to observational data. All of our observations were carried out with the SAO RAS 6 m alt-azimuthal telescope using the SCORPIO spectrograph (Afanasiev & Moiseev 2005). The work presented in this thesis is a further

---

[1]The Special Astrophysical Observatory of the Russian Academy of Sciences, $43°38'49''$N, $41°26'26''$E.

[2]http://www.stokes-program.info/

improvement of the Smith et al. (2005) equatorial scattering model. While Smith et al. (2005); Afanasiev & Popović (2015) have assumed a single scattering approximation, we have entirely based our simulations allowing multiple scattering events for more general results.

The second part of this work deals with the broad line polarization in the case where the AGN central engine is driven by a supermassive binary black hole (SMBBH). We aim to predict what should be the observational signature we expect from those yet-to-be-confirmed sources. We consider a model of sub-pc SMBBHs, where each of the BH components has its own accretion disk and BLR. We also consider equatorial scattering of such complex system on the inner part of the torus. We predict here for the first time the polarization parameters across the broad lines for different azimuthal and inclination viewing angles in the case of an AGN with a SMBBH.

The thesis is organized as follows: in chapter 1, we outline the unification scheme and the main components of AGNs with their properties. In chapter 2, we summarize AGNs characteristics when viewed in polarized light. In chapter 3, we review the most commonly used methods for measuring the SMBH masses. In chapter 4, we introduce the polarization formalism necessary for dealing with observations and radiative transfer. In chapter 5, we describe in detail the radiative transfer code STOKES. In chapter 6, we describe the geometry and kinematics of our models. We also present the observations of the selected type-1 AGNs: NGC 4051, NGC 4151, 3C 273 and PG 0844+780. In chapter 7, we perfomed radiative transfer simulations for a large grid of models, with a particular accent on scattering induced polarization. We take into account additional complex motions such as inflows/outflows and how it affects polarization in lines. Further, we investigate the polarization effects of AGN broad emission lines in the case of SMBBHs. Detailed results of the models involving SMBBHs are given in the appendix A. We also produce models for NGC 4051, NGC 4151, 3C 273 and PG 0844+780 and we compare our results to observational data. in the last part of the chapter 7, we discuss our results. Finally, in chapter 8, we summarize our conclusions and we give prospects for future work.

1.1 Active galactic nuclei

1.1.1 Historical discovery

The beginning of the 20th century marked the development of extragalactic astronomy. The first discovery of emission lines in a spiral nebula (today NGC 1068) were carried out at Lick observatory[3] by Fath (1909a,b). A decade later, the activity of a giant elliptical galaxy M87 in the form of a thin jet connected with its nucleus was observed by Curtis (1918). Around the same time, Hubble (1922) detected emission lines in several galaxies. Seyfert (1943) observed and carefully studied several spiral galaxies (most notably NGC 1068 and NGC 4151) with bright nucleus and remarkable emission lines – a feature that is not common for regular galaxies dominated by stellar spectra with absorption lines. Until a few decades later, his work had remained with little interest. The development of radio astronomy in the 1950s and 1960s was followed by identifying some of the quasars (quasi stellar radio sources) with their optical counterparts. The first stellar-like optical source was identified with the quasar 3C 48 (Matthews et al. 1961). Soon after, few more quasars were identified in the same way, namely 3C 196; 3C 286 (Matthews & Sandage 1963) and 3C 147 (Schmidt & Matthews 1964). However, the optical spectra of these quasars were quite dissimilar and no emission line could be identified at the time. The optical spectra of the famous quasar 3C 273 was showing that hydrogen Balmer emission lines are exhibiting large redshifts $z = \Delta\lambda/\lambda_0 = 0.158$ (Schmidt 1963). Few scenarios explaining such large redshifts in the case of 3C 273 and 3C 48 were extensively discussed by Greenstein & Schmidt (1964). In a first attempt, redshifts were interpreted as gravitational redshifts; the object was considered as collapsed. Using the emissivity of Hβ line, they showed that the spectrum of 3C 273 and 3C 48 could not be explained by the gravitational redshift of a collapsed star with a mass of about $1\,M_\odot$, as this would lead to electron densities 10 order of magnitudes higher than the upper limit estimated from the spectral analysis of the forbidden emission lines. In order to interpret observed redshift as gravitational redshift, and to match the observational data, Greenstein & Schmidt (1964) discussed the possibility of a supermassive object with a lower mass boundary of $10^{11}\,M_\odot$ within a fraction of parsec. The compactness and stability of these objects proved to be problematic and the hypothesis of gravitational redshift was dismissed. Another interpretation was that objects 3C 273 and 3C 48 were of extragalactic origin and the observed redshifts could be considered

---

[3]The Lick Observatory, 37°20′29″N, 121°38′34″W.

as cosmological redshifts. In that case, assuming abundances typically found in H II regions, Greenstein & Schmidt (1964) found that the mass of the central source is of the order of $5 \times 10^6 \, M_\odot$ and the electron densities of the order of $3 \times 10^4 \, \text{cm}^{-3}$ or less. Assuming that the age of these objects is of the order of 10^6 years, a mass of $10^9 \, M_\odot$ inside a H II region is required to stabilize high internal motions. The first model explaining the observations consisted of a massive object in the center surrounded by shells of increasing radius where the optical continuum, the emission lines and the radio continuum emerge. Nevertheless, despite the large discrepancy of the estimated mass, two things became clear: a supermassive object is residing in the center of these objects; the second is that the emitting region is compact.

Hoyle & Fowler (1963) proposed the model of quasars as supermassive stars in which the angular momentum of the star is transferred to the surrounding disk of stars. Lynden-Bell (1969) showed that powering AGNs by nuclear reactions was insufficient and the model by Hoyle & Fowler (1963) proved to be short-lived due to dynamical instability (Lynden-Bell 1978). Alternative scenario was an accretion of gas around a supermassive object (Salpeter 1964; Zel'dovich & Novikov 1964). Accretion can effectively convert gravitational potential energy into radiation when enough material is being accreted. The time-scales in this case are much larger due to the effects of the radiation pressure. A $10^9 \, M_\odot$ SMBH has a Schwarzschild radius (the radius of the event horizon for a neutral and non-rotating black hole, equation 1.1) of around 10^{-4} pc. Accretion onto a SMBH, studied by Lynden-Bell (1969), became the widely accepted scenario of the AGN nature, capable of explaining many observational properties.

The work of Karl Seyfert came to interest again as the number of similarities such as color, spectra and variability between quasars and Seyfert galaxies was observed (Burbidge et al. 1963; Pacholczyk & Weymann 1968; O'Connell 1971). This lead to the hypothesis that quasars are being hosted by galaxies, and it was later confirmed by Kristian (1973) who found diffuse galaxy signatures by analysing the photographic plates of 26 AGNs. The advancement of technology encouraged the observations of AGNs in different wavelength domains. As the number of observed AGNs was growing, many different types of AGNs were introduced based on spectral characteristics, radio morphology and variability. Several criteria were introduced for classifying any extragalactic object as an AGN, of which at least one condition needs to be satisfied. These are the following:

a The total luminosity is dominated by radiation from the nucleus
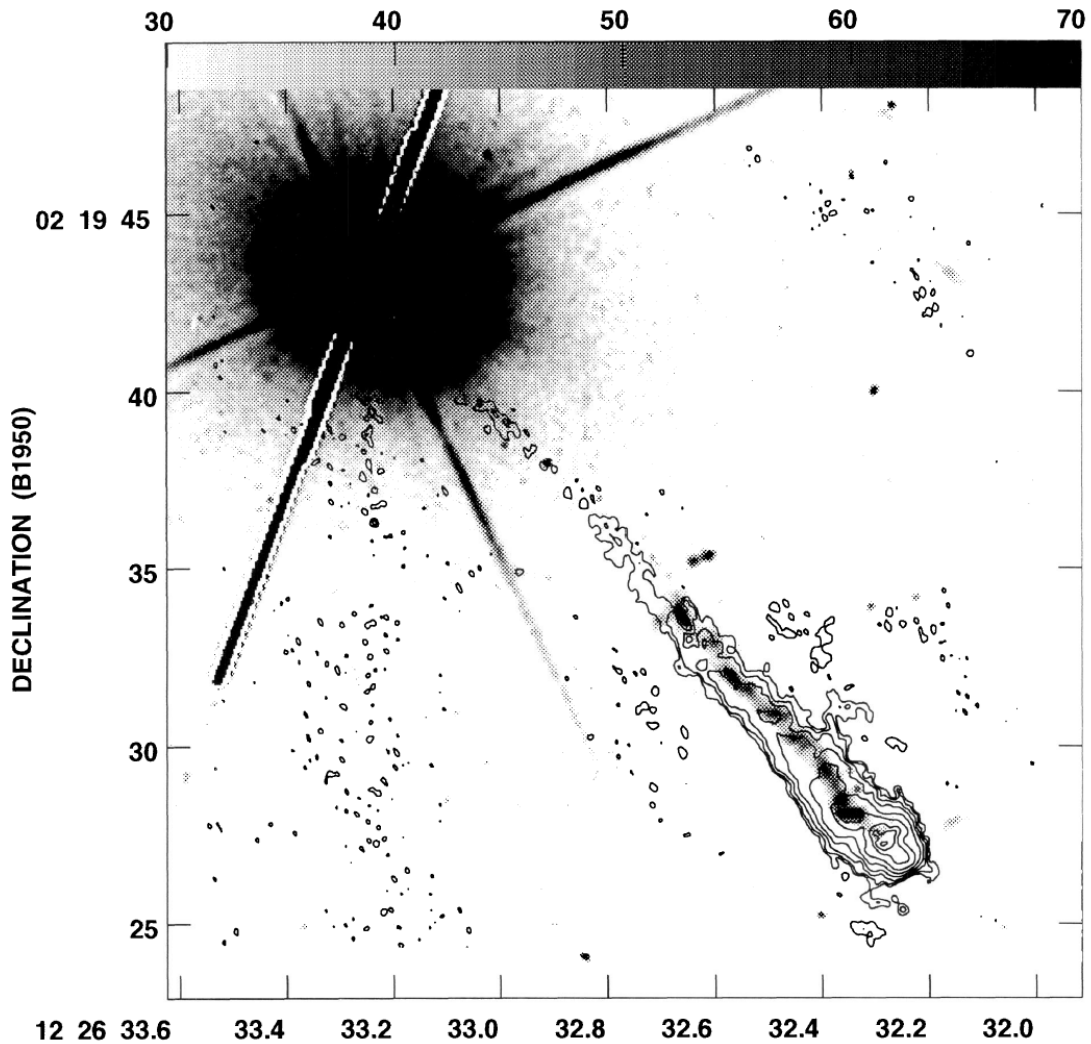
Figure 1.1: The combined image of optical (black) and radio emission (contours) for 3C 273 (Bahcall et al. 1995). Optical emisison is dominated by a bright central source, but a small fraction of the jet emission is also visible. Radio emission comes from an extended radio jet. Optical observations were taken by the Hubble Space Telescope (HST) at a wavelength of 5935 Å. Radio observations were carried out at MERLIN array at 1658 MHz (wavelength 18 cm).

b The nucleus emits broadband continuum radiation with prominent emission lines excited by radiation of non-stellar origin

c Continuum and line radiation are highly variable

d The presence of radio jets or radio lobes indicates gas ejection

Due to the powerful broadband spectrum of AGNs, their identification is possible in every frequency-wavelength domain. It is worth to mention here different catalogs and surveys as well as methods for their differentiation from other objects. For detailed review of methods for AGN discovery and sky surveys, we refer to Netzer (2013); Popović & Ilić (2017) and for the history on the AGN discovery we refer to Shields (1999).

Discovery in the UV-optical domain

Spectroscopic analysis of AGN optical spectra has been present since their discovery. It allows us to identify AGNs with strong broad emission lines, but it is not efficient when lines are weak. The First Byurakan Survey (FBS) started by Markarian (1967) took an important part in AGN discovery. Each FBS plate contains low-dispersion spectra of 15 000–20 000 objects. The objects selection and classification were made by their color, broad emission or absorption lines and SED. The FBS contained around ~ 1500 galaxies with enhanced UV radiation – the so called Markarian galaxies.

The typical AGNs spectral energy distribution (SED) is different from stellar SED. It does not resemble a single temperature black body and covers a broader frequency range (see Sect. 1.2). This difference provides an efficient way of discovering AGNs using broadband multicolor photometry. Earlier methods were based on using UBV photometry for large samples of observed objects. This method is useful for low redshift AGNs and less efficient for high redshift AGNs due to the AGN colors resembling those of stars. The more innovative five-band photometry provides an efficient way of detecting AGNs up to a redshift $z \simeq 6$ (Richards et al. 2009). Additional color bands help to separate AGNs from white dwarfs. The SDSS (Sloan Digital Sky Survey) up to now produced a catalog of more than 500 000 AGNs, with an estimation of total $\sim 700\,000$ AGNs in the next data release (Pâris et al. 2018). In the UV band, the Galaxy Evolution Explorer (GALEX) played an important role in AGN discovery. The survey consisted with imaging in the far-UV (FUV, around $\sim$1528 Å) and near-UV (NUV, around $\sim$2310 Å). The GALEX database provides $\sim 500\,000$ source measurements and

over 100 000 low-resolution UV spectra (Bianchi et al. 2017), of which a significant fraction are AGN sources.

Another method for discovering AGNs in the optical domain is by exploiting their variability. The variability of AGNs is reflected in a different way in a color-color diagram when compared to variable stars (Sesar et al. 2007). This method requires at least two visits per field of view and will be extensively used when the Large Synoptic Survey Telescope (LSST) becomes operational in 2022. Detailed simulations have shown that the LSST quasar sample will contain up to 10 000 000 AGNs (Ivezić 2017, and references therein).

Discovery in the radio domain

Most of the early AGNs were discovered in the radio domain. The First Cambridge Catalogue of Radio Sources (1C, Ryle et al. 1950) pioneered the northern sky radio survey at 178 MHz. Improved results were listed in the third edition (3C, Edge et al. 1959) with a total of 471 resolved radio sources. Strong point radio sources are most likely to be jet dominated AGNs since stars are extremely weak radio sources. The positional precision of radio and optical telescopes is of the order of one arcsec or better and the identification is confirmed by correlating radio and optical positions. Around 10 % of AGNs are jet dominated AGNs and mostly reside in elliptical galaxies (Malkan 1984).

Discovery in the IR domain

The search for AGNs in the infrared (IR) domain requires the use of at least two IR bands or a combination of one IR band with observations in the optical or X-rays. This technique is very useful for highly obscured AGNs at high redshifts for which the optical spectrum is dominated by the host galaxy. The mid-IR (MIR) is dominated by warm dust emission which is heated by the central source. The luminosity ratio $L\,(24\,\mathrm{\mu m})\,/L\,(658\,\mathrm{nm})$ is much larger for AGNs in comparison with regular galaxies. Additional spectroscopic follow-up is often required for confirmation. The SST (SPITZER Space Telescope) combined both photometry with a spectroscopic follow-up for a number of AGN candidates. This way a catalog of less than a thousand highly redshifted AGNs was produced (Lacy et al. 2013). The WISE (Wide-field Infrared Survey Explorer) produced one of the largest AGN catalog with $\sim 4\,500\,000$ AGN candidates with 90 % reliability (Assef et al. 2018).

Discovery in the X-ray domain

Almost all AGNs are powerful X-ray emitters and deep X-ray surveys are required for AGN identification. In soft X-rays, the ROSAT all-sky survey identified numerous bright AGN sources with strong 0.5–2.0 keV emission (Krumpe et al. 2010). CHANDRA and XMM-Newton can observe up to 10 keV, but those surveys cover a small fraction of the sky. CHANDRA provides extremely deep surveys with angular resolution of 1″. Sky surveys at hard X-rays with energies 15–150 keV include Swift Burst Alert Telescope (BAT) and INTEGRAL missions which contributed to the discovery of many obscured AGNs (Koss et al. 2017; Malizia et al. 2016). X-ray surveys are not very efficient in discovering high redshifted AGNs mostly due to the sensitivity of the instruments, and very often optical spectroscopic follow-up is required for confirmation.

1.1.2   AGN Classification

The AGN continuum radiation has been observed through the whole electromagnetic spectrum which greatly differs from the continuum SED of regular galaxies (Fig. 1.2). In optical and UV many emission lines (sometimes absorption lines) are prominent with the intensity largely surpassing the host galaxy stellar absorption lines. Although nuclear activity is common for all AGNs, they can be largely diverse in the sense of the SED shape and spectral lines characteristics. The classifications of AGNs has its roots in the history of research and in which frequency domain in which they were initially discovered. The early AGN classification was based on spectral characteristics and implied that the nature of these objects is intrinsically different; and some of the early AGN types are still widely used today (Antonucci 2012). The current AGN classification is based on larger sample of observations, better understanding of the accretion process and of the fact that many observed properties depend on the luminosity, accretion rate and viewing inclination towards the central source (Sect. 1.2). These include Seyfert galaxies; quasars; radio galaxies; low luminosity AGNs and blazars, which accounts for the majority of AGNs. A detailed and up to date list of AGN types abbreviations can be found in the work of Padovani (2017a).

Seyfert galaxies

Seyfert galaxies were first discovered by Seyfert (1943). He noticed strong emission lines coming from the bright nucleus. Seyfert galaxies are usually spiral, mostly Sb or
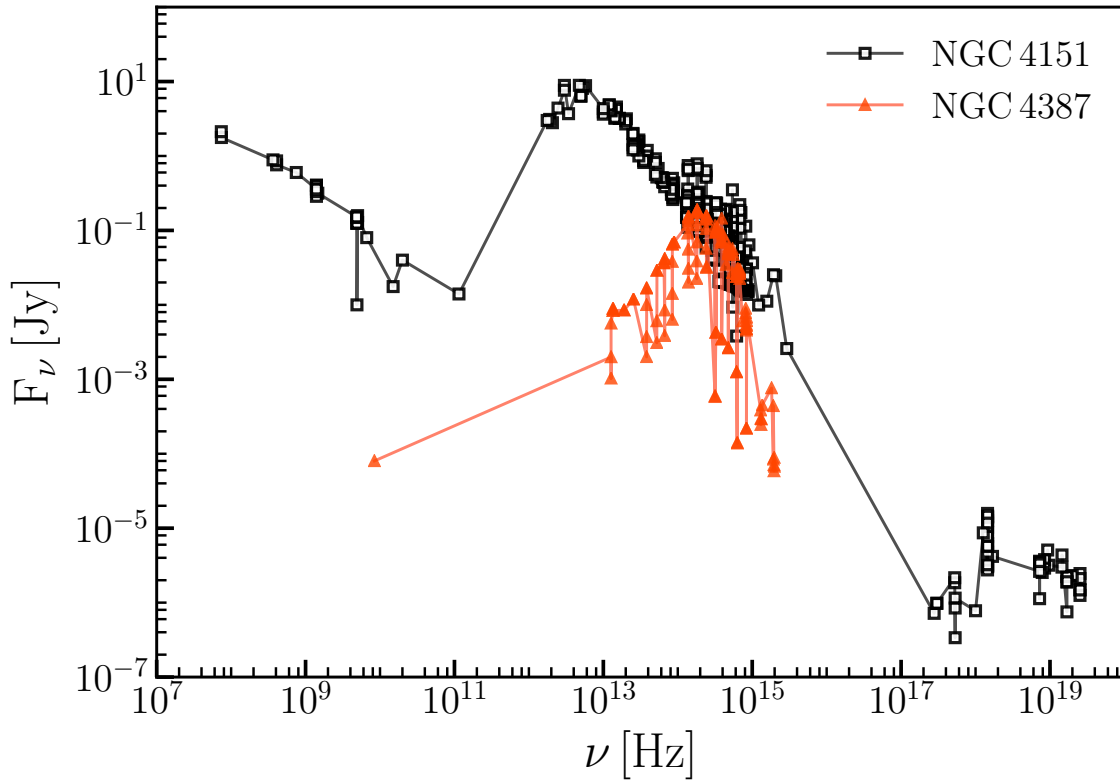
Figure 1.2: An example of a SED for an AGN NGC 4151 (empty squares) and for a regular elliptical galaxy NGC 4387 (filled triangles). The SED of NGC 4151 covers broad frequency range while the SED of NGC 4387 covers much narrower frequency range. Data was obtained from NED (NASA/IPAC extragalactic database) https://ned.ipac.caltech.edu/.

SBb[4] with a very bright nucleus. There are two types: Seyfert 1 (Sy 1) and Seyfert 2 (Sy 2) galaxies.

Seyfert 1 galaxies are showing both broad and narrow emission lines in their spectra. Broad emission lines, such as Balmer lines; Ly α; Mg II λ2798 Å; C IV λ1549 Å etc. are due to the allowed transitions, while narrow lines such as [O III] $\lambda\lambda$4659,5007 Å; [S II] $\lambda\lambda$6716,6731 Å etc., are due to the forbidden transitions. The absolute magnitude of Sy 1 galaxies is $M_{bol} \leqslant 21$. They show strong continuum features with UV and optical Fe lines. In X-rays, broad Fe Kα line at 6.4 keV that is coming from the accretion disk can also be observed. Depending on the ratios between the broad and narrow lines intensity, several intermediate classes were introduced e.g. Sy 1.5, 1.8 and

---

[4]de Vaucouleurs (1959) extended the Hubble sequence (Hubble 1926) for galaxy classification based on morphology.
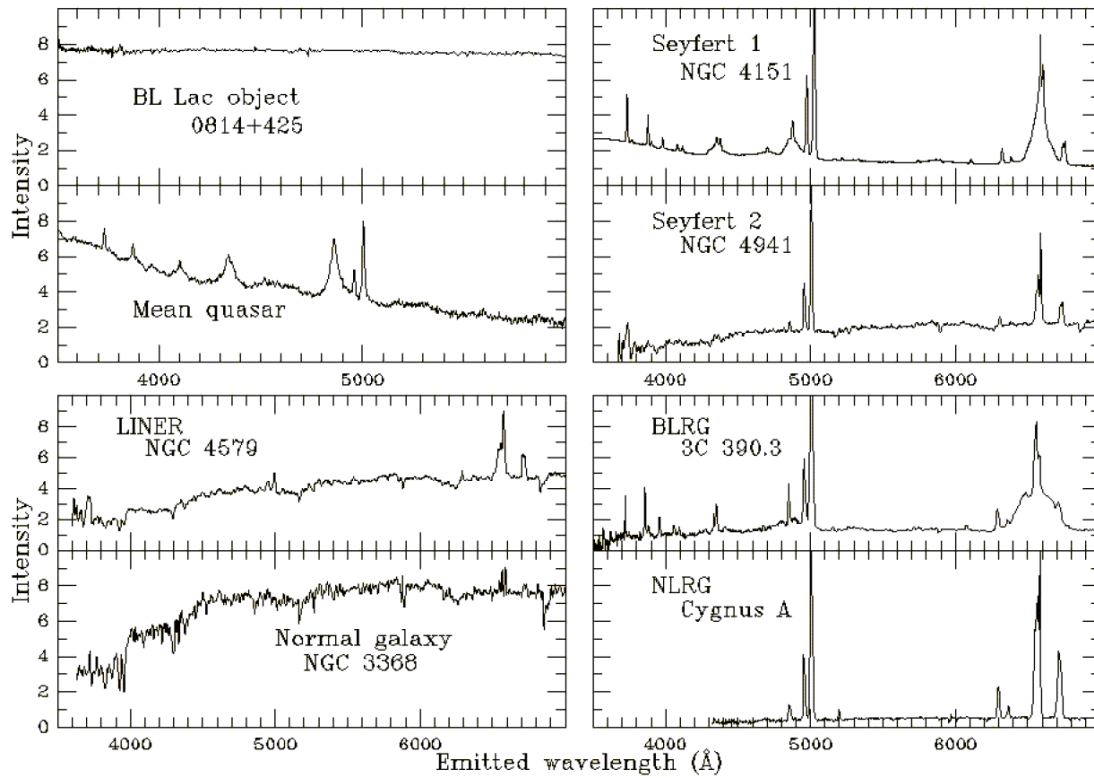
Figure 1.3: Optical spectra for different AGN types. AGN type is written on each panel. Credits http://pages.astronomy.ua.edu/keel/agn/spectra.html.

1.9 (Osterbrock 1989; Osterbrock & Ferland 2006). An example of optical spectrum for Sy 1 NGC 4151 is shown in Fig. 1.3 (top right panel).

Seyfert 2 galaxies only show narrow emission lines due to both allowed and forbidden transitions in their optical spectra. They are fainter than Sy 1s ($M_{\mathrm{bol}} \leqslant 20$) and accounts for approximately one third of Seyfert Galaxies. The continuum in Sy 2s is usually weaker than in Sy 1s. The optical spectrum of Sy 2 NGC 4941 is shown in Fig. 1.3 (top second, right panel). Both Sy 1s and Sy 2s are weak radio sources.

Quasars

When the first quasar (quasi-stellar radio source) was first discovered in the radio domain (Schmidt 1963), its nature was not well understood. As the number of observed quasars increased, it was noted that they are similar as Seyfert galaxies, but with higher luminosities. Despite the early discovery in radio domain, it was later shown that around 10 % of quasars are strong radio emitters (historically 'radio-loud'), while the rest are weak radio sources ('radio-quiet', Padovani 2011). The term QSO (quasi-stellar object)

11

was referring to types of objects and nowadays it is used interchangeably with the term 'quasar'.

Similarly with Seyfert galaxies, we divide quasars into two types: type-1 quasars with both broad and narrow emission lines and type-2 quasars with narrow emission lines only. Quasars can be observed at very high redshifts ($z \geqslant 7$, Mortlock et al. 2011; Bañados et al. 2018) since their absolute bolometric magnitude is $M_{\rm bol} \leqslant 23$. Finding and identifying type-1 quasars is straightforward due to the presence of broad emission lines. This is not the case for type-2 quasars and their identification is much more difficult. There are many type-2 quasars candidates (Alexandroff et al. 2013; Yuan et al. 2016, and references therein), but much less confirmed cases (Urrutia et al. 2012). Type-2 quasars are faint in optical, ultraviolet and soft X-rays, but luminous ones may be identified through hard X-ray (Brusa et al. 2010), infrared (Lacy et al. 2013, 2015) and radio (Martínez-Sansigre et al. 2006) surveys. An example of quasar optical spectrum is shown in Fig. 1.3 (top second, left panel).

Radio galaxies

Radio galaxies are type of AGNs with strong radio emission. The radio emission is coming from highly collimated outflowing matter - jets that are perpendicular to the accretion disk. Very often, extended symmetric structures called radio lobes are visible with sizes of tens to hundreds of kpc. Two types of radio galaxies based on the radio lobes brightness were introduced: FR I (edge-darkened), for which the distance between the brightest spots is smaller than the half of the total size of the radio lobes and FR II (edge-brightened) where this distance is greater than one half of the total size of the radio lobes (Fanaroff & Riley 1974). The radio emission is produced by relativistic electrons spiraling in the magnetic field. Radio galaxies are mostly elliptical (Véron-Cetty & Véron 2001) unlike Seyfert galaxies that are spiral.

The optical spectra of radio galaxies are similar to quasars and Seyfert galaxies and they are divided into two groups: broad line radio galaxies (BLRG) with both broad and narrow emission lines visible and narrow line radio galaxies (NLRG) with only narrow emission lines in their spectra. An example of one BLRG 3C 390.3 and one NLRG Cygnus A optical spectrum is shown in Fig. 1.3 (top third, right panel and bottom right panel respectively.)

Low luminosity AGNs

Low luminosity AGNs, more commonly called LINERs (Low-ionization nuclear emission-line regions) are the least luminous AGNs with the nucleus luminosity being up to ~ 5 orders of magnitude lower than the ones typically found in bright AGNs. In the nearby Universe, they account for around one third of all AGNs (Ho et al. 1997). Their spectra include lines from weakly ionized ions and sometimes weak lines from highly ionized ions due to low accretion rate and central luminosity. The strongest optical emission lines in the LINERs spectra include [O III] $\lambda5007$ Å doublet; [O II] $\lambda3727$ Å; [O I] $\lambda6300$ Å; [N II] $\lambda6583$ Å doublet. Hydrogen Balmer lines are sometimes present, but they are usually very weak. LINERs are also classified into type-1 with broad emission lines and type-1 with only narrow emission lines. Broad lines are observed mostly in Hα and rarely in Hβ. LINERs show weak point-source emission in X-rays and radio domain. The spectrum of one LINER NGC 4579 is shown in Fig. 1.3 (top third, left panel).

Blazars

Blazars are characterized by strong, highly polarized non-thermal optical and radio continuum. They are divided into BL Lacertae (BL-Lac) objects and optically violently variable QSOs (Angel & Stockman 1980, OVVs). The spectrum of BL-Lac blazars is completely dominated by continuum radiation with no sign of emission or absorption lines. Their variability typically occurs on a daily basis and some objects reveal variability in both polarized and unpolarized optical flux on a time-scale of 1–1.5 h (Shablovinskaya & Afanasiev 2019). OVVs or sometimes FSRS (flat spectrum radio sources), due to their flat radio spectrum, are similar to BL-Lac objects with the only difference of showing broad emission lines in their spectra. Many blazars are also powerful X-ray and γ-ray emitters. The FERMI-LAT (large area telescope) shows that large amplitude variations in γ-rays are very common in most blazars. The optical spectrum of a blazar 0814+425 is shown in Fig. 1.3 (top left panel).

Classification based on physical processes

The most fundamental AGN classification is into thermal AGNs and non-thermal AGNs. The former are what we are dealing with in this work, AGNs where, as proposed by Lynden-Bell (1969), most of the energy is thermal emission from the accretion disk.

Non-thermal AGNs have low Eddington ratio L/L_{Edd} and the mechanical energy in jet dominates (Antonucci 2012). As Padovani (2017b) pointed out, the historical 50 years old division into 'radio-loud' and 'radio-quiet' AGNs should be substituted with 'jetted' and 'non-jetted' AGNs based on the direct evidence of the presence or lack of strong relativistic jets. It's important to stress out that the thermal/non-thermal division is not the same as a jetted/non-jetted division since there are many jetted thermal AGNs.

A considerable amount of gas rich regular galaxies have an exceptionally high rate of star formation in their nucleus (starburst galaxies) show emission lines that could be confused for AGNs, most notably with LINERs (Beckmann & Shrader 2012). Due to different photoionization mechanisms (thermal radiation from the accretion disk in AGNs or thermal emission from young O and B stars in starburst galaxies), a powerful line diagnostic method was introduced by Baldwin, Phillips, & Terlevich (1981) for separating AGNs from starburst galaxies – the so called BPT diagram. This method uses the line ratio of [O III] $\lambda 5007\,\text{Å}/\text{H}\beta$ as a function of line ratio [N II] $\lambda 6583\,\text{Å}/\text{H}\alpha$. This method is efficient for galaxies with redshifts up to 0.5, for which the spectral line [N II] $\lambda 6583\,\text{Å}$ lies in the optical window. Two other BPT diagrams are often used: [O III] $\lambda 5007\,\text{Å}/\text{H}\beta$ as a function of [S II] $\lambda 6716\,\text{Å}/\text{H}\alpha$ or [O III] $\lambda 5007\,\text{Å}/\text{H}\beta$ as a function of [O I] $\lambda 6300\,\text{Å}/\text{H}\alpha$. A significant improvement for separating AGNs from starburst galaxies was introduced by Trouille, Barger, & Tremonti (2011) – the TBT diagram. This diagnostic uses the rest-frame $g - z$ color and the line ratio [Ne III] $\lambda 3869\,\text{Å}/$[O II] $\lambda 3726\,\text{Å}$. This method can be used for galaxies with redshift up to 1.4. The TBT diagram is also very efficient for identifying CHANDRA X-ray selected AGNs.

1.2 The unified model

The observed similarities between type-1 and type-2 AGNs lead to an idea that these objects are intrinsically the same. Osterbrock (1978) suggested the existence of an optically thick dusty torus surrounding and obscuring the accretion disk, resulting in different optical spectra. Keel (1980) discovered that there is a deficiency of nearly edge-on Sy 1s in a sample of 91 observed galaxies, which was indicating that their orientation was not random. Optical spectropolarimetry played a pivotal role when broad emission lines were discovered in the polarized spectra of Sy 2 galaxy NGC 1068 (Antonucci & Miller 1985). These results led to the unification scheme (Antonucci 1993;

Urry & Padovani 1995) - the same physics, but explaining the difference between Sy 1s and Sy 2s by a different viewing inclination. According to this model, the AGN central engine consists of a SMBH situated in the center. The SMBH is surrounded by an accretion disk which is the source of strong X-ray to optical radiation (Jovanović 2012). In the vicinity of the disk, a broad line region (BLR) is composed of numerous clouds with velocities of a few thousands of $km\,s^{-1}$ (Gaskell 2009). Both the accretion disk and the BLR are surrounded by a geometrically and optically thick toroidal structure of dust and gas – the dusty torus (Elitzur 2006), which extends up to a few parsecs. Dust in the torus is responsible for the reprocessing of radiation at higher energies and re-emitting in the IR. In the polar direction, highly ionized and modestly relativistic polar winds are emerging on scales smaller than 1 pc (Tombesi et al. 2012). Farther away, fueled by the polar wind, the outflows form a bi-conical structure of low density gas which emits forbidden narrow lines – the so called narrow line region (NLR). This region can have dimensions of the order of kpc (Bennert et al. 2002). Sometimes relativistic jets are formed in the direction of the polar axis, and thus producing strong radio emission. Due to the low density of the interstellar medium (ISM) and intergalactic medium (IGM), jet can be of sizes even ten times the size of the host galaxy. A cartoon illustrating the unification scheme is shown in Fig. 1.4. Radiation from the accretion disk and the BLR can only be viewed from intermediate viewing angles, when they are both unobscured, and such object would appear as a type-1 AGN. For high viewing inclinations (close to edge-on), the central engine is obscured by the dusty torus and the object appears as a type-2 AGN with hard X-rays detectable if the equatorial column density is not too high. When the system is viewed along the jet, the AGN would be classified as a blazar due to the highly polarized and rapidly variable continuum. In Fig. 1.5, an example of AGN SED is shown, highlighting the contribution of each component.

The simple scheme of the unified model depicts the accretion disk, the BLR and the dusty torus as isolated regions, but in reality, they are closely connected. The BLR extends outwards to the inner boundary of the torus (Suganuma et al. 2006), that is set by dust sublimation (Netzer & Laor 1993). Therefore the AGN bolometric luminosity plays an important role in the unification scheme. As luminosity drops below a certain treshold, the BLR cannot be sustained anymore and starts to dissapear (Ho 2008; Elitzur & Ho 2009).

This was confirmed by simultaneous high signal to noise observations in X-rays and optical domain (Bianchi et al. 2008). Although the line of sight towards the central engine in this case is unobscured, the observed AGN would be classified as a 'true'
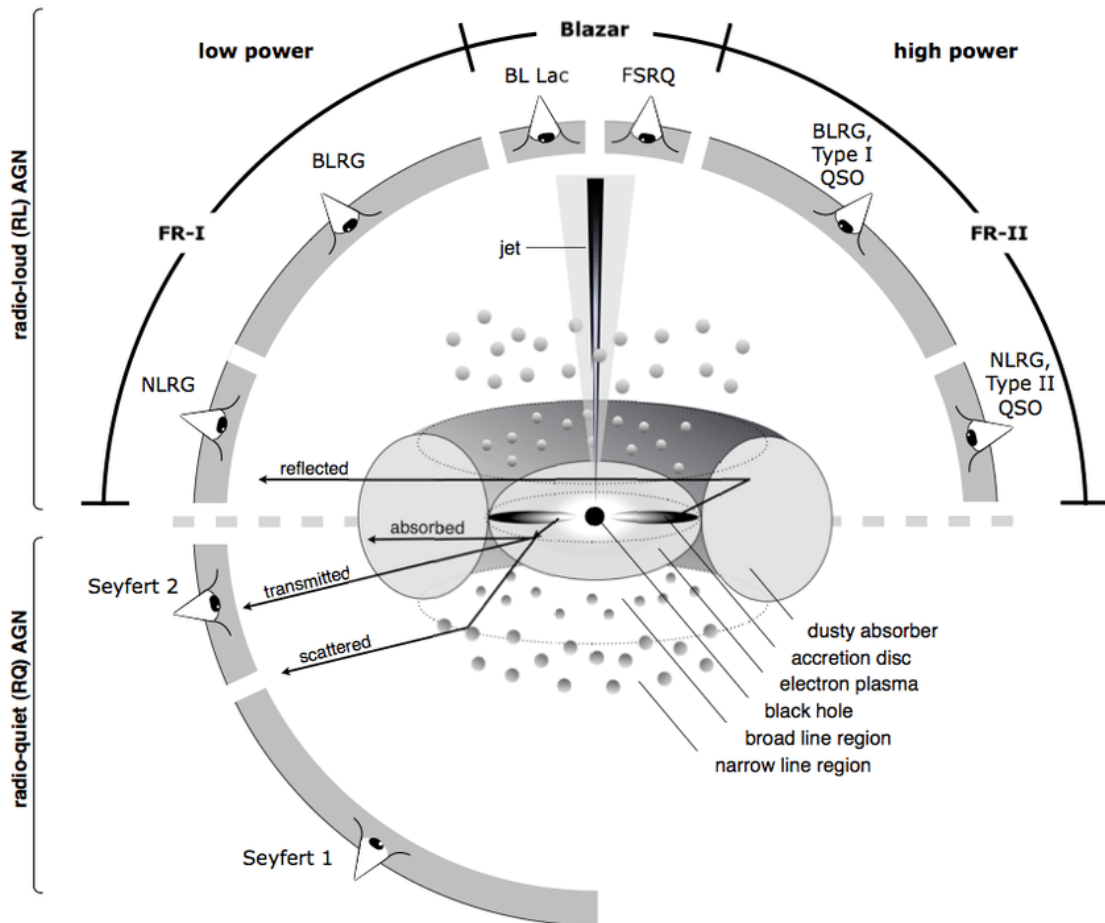
Figure 1.4: The unified model of AGNs. The black hole is residing in the center surrounded by an accretion disk. Farther away, past the sublimation radius, the accretion disk extends into the dusty torus. The broad line region is in the vicinity of the disk and is being obscured by the torus. Much farther away, on the kpc scales above and below the disk, lies the narrow line region. Relativistic jet is inside the narrow cone along the polar axis. Different AGN types are observed depending on the viewing inclination. Credits Beckmann & Shrader (2012).
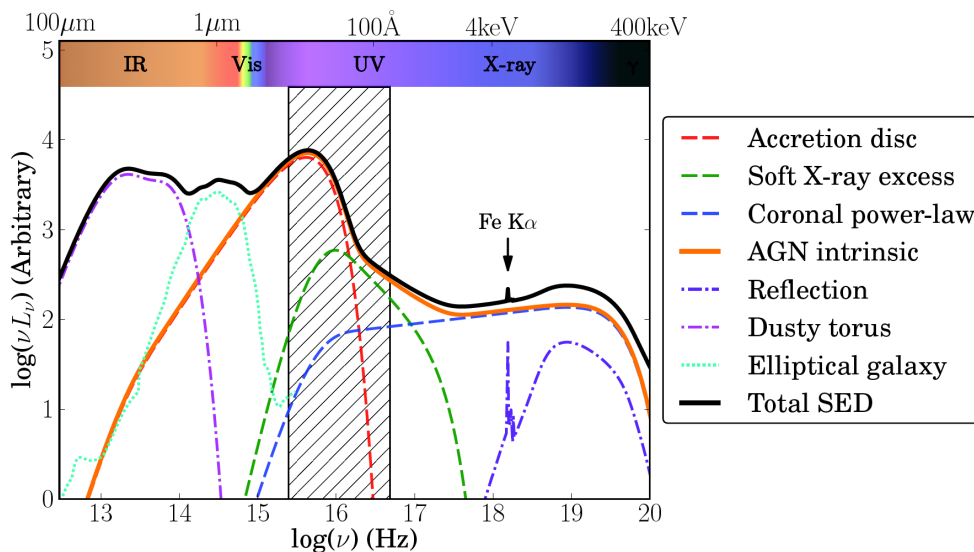
Figure 1.5: A simplified diagram of an AGN SED, showing the approximate shape and contribution of the various AGN components. Dashed lines denote AGN intrinsic emission. Dash-dot lines show emission reprocessed by the surrounding material and the dotted line shows the spectrum of the host elliptical. The hatched region marks the spectral range that is heavily obscured by absorption of the interstellar medium. Credits: Collinson et al. (2017).

type-2 AGN. For the more detailed development and challenges of the unified model, we refer to Netzer (2015).

In the following, we outline the main features of the mentioned AGN components highlighting radiative processes, gas composition, geometry and dynamics, updated with the latest theoretical and observational studies. The treatment of polarization in AGNs is discussed separately.

The supermassive black hole

Black holes are among the most extreme objects that can be found in the Universe and an ideal laboratory for testing fundamental physics. A black hole is a region of the spacetime where the gravity is so strong that nothing, not even light, can escape. Such a region is surrounded by an event horizon, beyond which events cannot affect an outside observer. Einstein (1916), in his general relativity, introduced a set of field equations which describe the fundamental interaction of gravitation as a result of spacetime being curved by mass and energy. The simplest solution was immediately found by Schwarzschild (1916) for a neutral, non-rotating mass. This solution had an

event horizon given by

$$R_{\text{Sch}} = \frac{2G\mathcal{M}_{\text{bh}}}{c^2}, \tag{1.1}$$

G is the gravitational constant, $\mathcal{M}_{\text{bh}}$ is the black hole mass and c is the speed of light. Black holes are relatively simple objects, in the sense they are completely characterized by a small number of parameters: mass, angular momentum and charge. The stationary solution for non-rotating charged black hole were found soon after (Reissner 1916; Nordström 1918) – Reissner-Nordström black hole. The solutions involving rotation and charge were found much later: Kerr black hole (Kerr 1963), an uncharged rotating black hole, and Kerr-Newman black hole (Newman et al. 1965) a charged rotating black hole. For astrophysical black holes, mass and angular momentum J are the two dominant parameters. For this purpose, it is convenient to introduce the dimensionless spin parameter

$$a_\bullet = \frac{cJ}{G\mathcal{M}_{\text{bh}}^2}. \tag{1.2}$$

The radial coordinate of the event horizon for a Kerr black hole is

$$r_{\text{H}} = r_{\text{g}} \left(1 + \sqrt{1 - a_\bullet^2}\right), \tag{1.3}$$

where $r_{\text{g}} = R_{\text{Sch}}/2$ is the gravitational radius. r_{H} ranges from $2r_{\text{g}}$ for Schwarzschild black hole to r_{g} for a maximally rotating black hole ($a_\bullet = \pm 1$). Equation 1.3 gives the constraint $|a| \leq 1$ (Kerr bound). For $|a| > 1$, the Kerr solution has no bound and we would have a naked singularity instead of a black hole, which poses a challenge to the general relativity since one could not predict the evolution of any region in space containing a singularity (Shapiro & Teukolsky 1991). In Newtonian gravity, circular orbits of a test particle around a massive object are always stable and the spin plays no role. Circular orbits of a test particle orbiting a Kerr black hole will not always be stable and there exists an innermost stable circular orbit (ISCO). For a Schwarzschild black hole the ISCO radius is $6r_{\text{g}}$ and can go to r_{g} if the test particle is orbiting in prograde direction; or it can go up to $9r_{\text{g}}$ if the test particle is orbiting in retrograde direction for a maximally rotating black hole.

Black holes can have an arbitrary mass as long as there exists a mechanism strong enough to compress such mass inside its own event horizon. Depending on the mass, they can be divided into stellar-mass black holes with a mass range 3–$100\,M_\odot$, intermediate-mass black holes with a mass range 10^2–$10^5\,M_\odot$ and supermassive black holes (SMBHs) with a mass range 10^5–$10^9\,M_\odot$ (see Bambi 2018, for a pedagogical

review). Some cosmological scenarios predict the existence of the so-called primordial black holes of any mass (Khlopov 2010), however, at present, the existence of such black holes has not yet been confirmed (see Sasaki et al. 2018, for the possible detection).

During stellar evolution, when a star has spent all its nuclear fuel, it starts collapsing. For relatively low-mass stars, the gravity is balanced by the electron degeneracy pressure for white dwarfs (Chandrasekhar 1931) and neutron degeneracy pressure for neutron stars (Oppenheimer & Volkoff 1939). For high-mass stars, no force is able to balance the gravity and the collapse to a black hole is unavoidable. Therefore, stellar-mass black holes represent the final stage of stellar evolution of high-mass stars. The initial mass of a stellar-mass BH depends only on the mass of the progenitor star, its evolution and the supernova explosion (Belczynski et al. 2010). However, finding isolated stellar-mass black holes is a challenging task (Beskin & Karpov 2005; Chmyreva et al. 2017).

Intermediate-mass black holes are black holes with a mass range 10^2–$10^5 \, M_\odot$, that is between the stellar-mass and the supermassive ones. Some intermediate-mass black hole candidates are associated with ultra luminous X-ray sources which have an X-ray luminosity exceeding Eddington luminosity for a stellar-mass object (Colbert & Mushotzky 1999). Intermediate-mass black holes could be expected to reside at the center of dense globular clusters as a result of mergers (Gebhardt et al. 2002, 2005). Due to its presence, the velocity dispersion in the cluster should be increased, however there are still no dynamical mass measurements of the intermediate-mass black holes.

The standard paradigm assumes that every massive galaxy is hosting a SMBH in its center (Kormendy & Richstone 1995), with the typical SMBH mass range between 10^6–$10^9 \, M_\odot$, although few examples of $10^{10} \, M_\odot$ cases exist (Shemmer et al. 2004; Walker et al. 2014; Zuo et al. 2015). The mass of the SMBH slowly evolves with time (Vika et al. 2009) and is tightly correlated with the properties of the host galaxy it resides in (e.g., bulge mass, velocity dispersion, see Kormendy & Ho 2013). It is then crucial to better understand the evolution of SMBHs in order to constrain galaxy formation models. The accretion of matter from the surrounding environment is a natural way to increase the mass of the SMBH. It is a slow process that has difficulties to explain the most massive cases (Mayer et al. 2010). In addition, the accreted mass is effectively transferred into the potential well, while up to $40\,\%$ of the gravitational potential energy is converted into high energy radiation (Frank et al. 2002). Another hypothesis for the evolution of SMBHs is via mergers with other SMBHs (Volonteri et al. 2003a,b). On large scales, dynamical friction is the main process that brings the SMBHs closer (Begelman et al. 1980) but once the merging of the two host galaxies has been achieved, the final parsec

problem onsets (Milosavljević & Merritt 2003). Dynamical friction becomes inefficient when the two SMBHs form a bound binary. The system has no efficient way to release energy and transfer angular momentum. One possible solution is that the spinning black holes lose energy by emitting gravitational waves (GW) until they finally merge (Begelman et al. 1980). Nevertheless, SMBHs play an important role in the host galaxy evolution.

The accretion disk

Accretion disks are common for many astrophysical systems such as proto-stars, young stars (T Tauri), disks in various types of close binary systems as cataclysmic variables, classical novae, β-Lyrae, X-ray binaries, etc., and AGNs. The gas infall onto the compact object releases part of the gravitational potential energy due to the viscosity present in the accretion flow. The amount of energy released this way is huge and it powers AGNs (Salpeter 1964; Zel'dovich & Novikov 1964). The simplest accretion disk model assumes optically thick and geometrically thin disks (Shakura & Sunyaev 1973) - the standard accretion disk model or the α-disk model[5], which was immediately generalized for relativistic effects (Novikov & Thorne 1973). In this model, the scenario is the following: the inner (faster) disk layer loses angular momentum due to viscosity and infalls slightly, while the outer (slower) disk layer gains angular momentum which is again transferred outwards in the same way, which results in the continuous mass flow towards the SMBH, while the angular momentum is transported to the outer region. At the same time, the friction between the layers heats up the accretion disk and the energy is radiated away. For this model, the effective temperature depends on radius as:

$$T_{\text{eff}}^4 = \frac{3G\mathcal{M}_{\text{bh}}\dot{M}}{8\pi\sigma r^3}\left(1 - \sqrt{\frac{r_{\text{isco}}}{r}}\right), \tag{1.4}$$

where r is the distance from the SMBH, $\dot{M}$ is the accretion rate, σ is the Stefan-Boltzmann constant. For regions far away from the center, where $r_{\text{isco}} \ll r$, the effective temperature scales as $T_{\text{eff}} \propto r^{-3/4}$. For a SMBH with $\mathcal{M}_{\text{bh}} = 10^8\,M_\odot$, the maximum temperature is roughly $\sim 10^5\,\text{K}$ (for a detailed derivation we refer to Netzer 2013). Such a disk is emitting mostly in the UV part of the spectrum. The accretion disks around SMBHs are much cooler than accretion disks around stellar-size BHs or neutron stars. The luminosity L_ν far away from the center scales with frequency as $L_\nu \propto$

---

[5]The viscosity parameter α introduced by Shakura & Sunyaev (1973) depends on the disk height scale and the sound of speed in the disk.
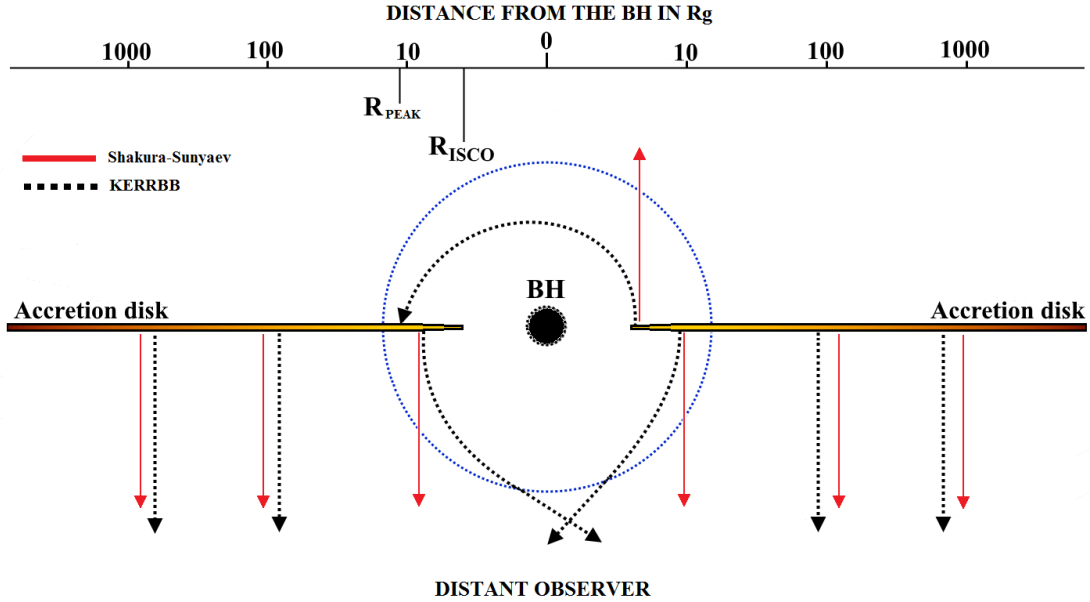
Figure 1.6: Schematic view of an accretion disk around a SMBH. A distant observer sees the disk face-on. The standard Shakura-Sunyaev disk does not take into account relativistic effects and photon paths are straight lines (red arrows). For more realistic scenario, the emission from a Kerr black body disk (KERRBB) takes into account the effects of general relativity (black arrows). The region with the strongest light bending is inside the blue circle. Relativistic effects are stronger for Kerr SMBHs than for Schwarzschild SMBHs. Photons emitted from the outer part of the disk are not under relativistic effects. The top axis denotes the logarithmic distance from the SMBH in R_{g}. At distance R_{PEAK}, the standard disk flux emission is maximized. Credits Campitiello et al. (2018).

$\mathcal{M}_{\mathrm{bh}}^{2/3} \dot{M}^{2/3} \nu^{1/3}$ for a limited frequency band. This part of the spectrum allows us to directly measure accretion rate and to constrain the SMBH mass from observations (Shields 1978; Campitiello et al. 2018, and references therein). The outer boundary of the disk is due to self-gravity effects, where the disk starts to fragment into smaller blobs. The minimal disk temperature is at the outer boundary and it corresponds to ν_{out} which is often in IR domain. Below this frequency, the spectrum resembles a single black body with luminosity dependence $L_\nu \propto \nu^2$. The maximal temperature is at the inner boundary associated with inner frequency ν_{in}. Beyond this frequency, L_ν drops exponentially. The normalized accretion rate is $L/L_{\mathrm{Edd}} \lesssim 0.3$ for standard accretion disks (Laor & Netzer 1989; McClintock et al. 2006). An illustration of the standard accretion disk is shown in Fig. 1.6.

We could expect that real AGN disks are quite different from the standard, geometrically thin, optically thick accretion disks. When the accretion rate is increased, the disk temperature is also increased (Eq. 1.4). The increase in temperature can drastically increase the local radiation pressure which can be much higher than the gas pressure for a large part of the disk, which results in disk thickening. Such disks are described as slim or thick accretion disks. Large accretion rates can result in large optical depths non-opaque to photons in the accretion flow. If the accretion flow is adiabatic, it retains its energy which is not radiated away, as it gets advected to the black hole. These are known as ADAFs (advection dominated accretion flows) that are predicted to have different spectrum shape and less luminous than standard disks (Madau 1988; Wang & Netzer 2003; Narayan & McClintock 2008). An illustration of the broadband AGN spectrum with the contribution from the accretion disk is shown in Fig. 1.5. The physics of accretion disks is much more complicated when the magnetic field and radiative transfer is taken into consideration.

The hot corona

The expected power-law emission does not extend into the X-ray domain. The presence of high X-ray radiation and the soft X-rays excess observed in AGNs (Walter & Courvoisier 1992) cannot be explained by the accretion disk emission only, but can be explained assuming the existence of a hot optically thin plasma (atmosphere) slightly above both sides of the disk - the hot corona. The emitted optical and UV photons from the disk undergo multiple inverse Compton scatterings in the hot corona resulting in the hardening of the observed spectrum (Sunyaev & Titarchuk 1980) and a much higher energy cut-off (Rybicki & Lightman 1979). Inverse Compton scattering is an efficient cooling mechanism and radiation originating from the disk is not strong enough to keep the corona hot above the disk. Magnetic field plays an important role in the heating of the hot corona. The magneto-rotational instability (MRI) can produce a strong vertical net magnetic flux (Balbus & Hawley 1998), allowing vertical outflows and the formation of the corona. Most of the magnetic energy is dissipated at a few height scales above the disk and strong shocks produced are continuously heating the corona to temperatures high enough for X-ray emission (Di Matteo et al. 1999; Miller & Stone 1999). The shape of the continuum spectrum depends on the energy distribution of the seed photons, corona temperature, optical depth and the viewing inclination. Variability in X-rays (Fabian et al. 2009; McHardy et al. 2005) and microlensing studies

(Popović et al. 2006; Chartas et al. 2009) show that the typical size of the hot corona is of the order 3–10 R_{g}. The X-ray spectrum can be very well described by a power law with photon index Γ ∼1.5–2.5 (Nandra & Pounds 1994; Page et al. 2005). Hard X-ray photons from the hot corona, if emitted in towards the accretion disk or the dusty torus may be reprocessed (secondary radiation due to reflection) resulting in a Compton hump peaking at around 30 keV (Ishibashi & Courvoisier 2010) and a strong iron Kα E6.4 keV line superimposed. The Compton hump can be produced only by Compton thick matter, while the iron Kα line can be produced both by Compton thick and Compton thin matter. The typical cutoff energy E_{c} is around ∼ 200 keV (Ricci et al. 2017a). The contribution of the hot corona to the broadband AGN SED is shown in Fig. 1.5.

The broad line region

It was named after the broad emission lines that emerge there, such as Ly α, the Balmer series, the C IV, C III], He II, He I, Fe II. The emission line Doppler width is in a range ∼1000–25 000 km s^{-1} (Peterson 2006) as a result of gas motion in the gravitational field. This is the region of ionized gas relatively close to the black hole, with dimensions of the order of only a few light days up to few hundreds of light days. The main source of the BLR heating is photoionization from the accretion disk. Recombination is followed by radiative de-excitation and cascade line emission (cooling). Estimated temperatures of the BLR using plasma diagnostic tools are of the order of ∼ 10^4 K (Popović 2003). The corresponding thermal line widths for such temperatures are of the order of ∼ 10 km s^{-1}, so it is clear that line broadening is due to dynamical motion. The lack of certain forbidden lines imply that the gas concentration is of the order of ∼10^8–10^{12} cm^{-3}. The BRL plasma conditions are thus more similar to stellar atmosphere rather than to photoionized nebulae such as H II regions or planetary nebulae (Osterbrock 1989). Electron temperature and optical depth can be estimated for some low luminosity AGNs with prominent exponential line wings (Laor 2006). For some type-1 AGNs, assuming partial local thermodynamical equilibrium (PLTE), the electron temperature of the BLR can be estimated using Boltzmann plot (Popović 2003; Popovic 2006; Ilić et al. 2006, 2007, 2012). Plasma conditions for pure recombination predicts a line ratio Lyα/Hβ $\geq$ 30 (Osterbrock 1989; Netzer et al. 1995), which is not often observed. For studying BLR emission lines, a more detailed approach is required taking into account photoionization, recombination, collisional excitation and
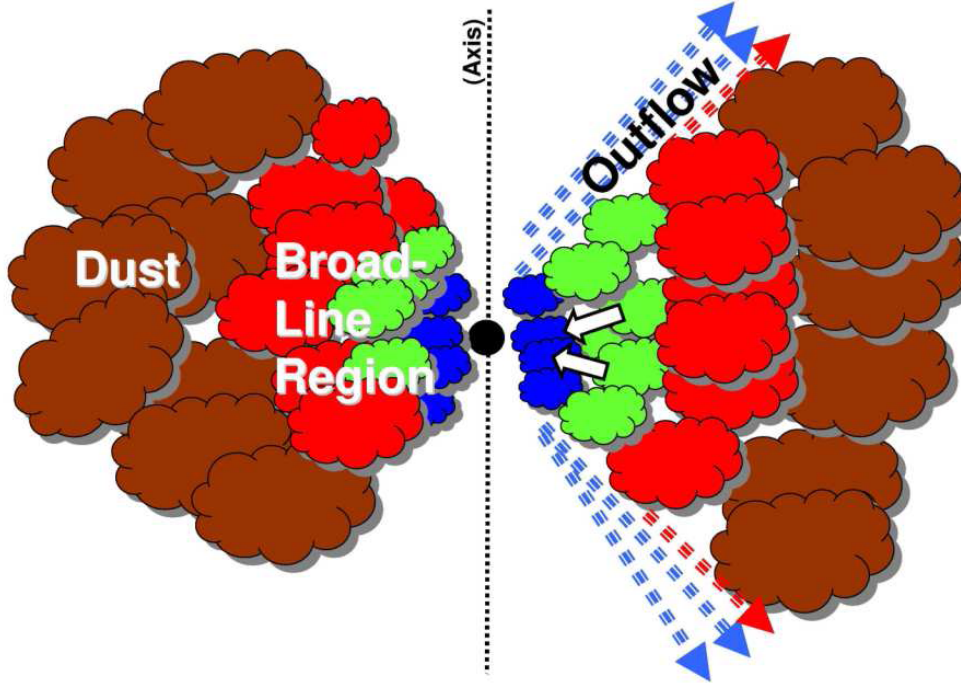
Figure 1.7: A schematic view of the BLR stratification. Highly ionization lines are coming from the region that is the closest to the black hole (blue region), followed by regions corresponding to low ionization lines (green and red). The dusty torus is embedding the BLR. Credits: Gaskell (2009).

de-excitation as well as extinction (Osterbrock & Ferland 2006, and references therein).

The side of each individual BLR cloud facing the central source will be highly ionized by the continuum radiation from the accretion disk, while the back side will be mostly neutral (if the column density is high enough) due to the continuum radiation from the accretion disk. We can thus expect that the BLR is stratified (the shape of a bird's nest, Gaskell 2009) in a way that the the high-ionization lines were coming from the inner region than the low-ionization lines (Fig. 1.7), which was confirmed by the earliest reverberation mapping (treated in detail in Sect. 3) of multiple lines (Gaskell & Sparke 1986). High-ionization lines are also wider (Shuder 1982; Mathews & Wampler 1985). Many reverberation mapping analyses have revealed that the BLR size is tightly correlated with the monochromatic luminosity at $5100\,\text{Å}$ (Kaspi et al. 2000; Peterson et al. 2004; Kaspi et al. 2005; Bentz et al. 2013; Du et al. 2018). The scaling relation is

24

given by (see Bentz et al. 2013):

$$\log\left(\frac{R_{\text{BLR}}}{1\,\text{light days}}\right) = 1.527^{+0.031}_{-0.031} + 0.533^{+0.035}_{-0.033}\log\left(\frac{\lambda L_\lambda\left(5100\,\text{Å}\right)}{10^{44}\,L_\odot}\right) \qquad (1.5)$$

where R_{BLR} is the BLR size with units in light days and $\lambda L_\lambda\left(5100\,\text{Å}\right)$ is the monochromatic luminosity given in $10^{44}\,L_\odot$. This relation is consistent with the expectations from simple photoionization arguments that predict a relation in a form $R_{\text{BLR}} \propto L^{0.5}$. The BLR extends to the dust sublimation radius (Barvainis 1987), and its outer radius depends on the bolometric luminosity as $R_{\text{out}}^{\text{BLR}} = 0.2L_{\text{bol},46}^{0.5}$ (Netzer & Laor 1993). A recent spectropolarimetric study of 30 type-1 AGNs by Afanasiev et al. (2019) has shown that the BLR outer radius is roughly three times larger than the one estimated from reverberation mapping.

The exact geometry of the BLR is still not well understood. The absence of Lyman continuum absorption by the BLR (MacAlpine 2003) suggests that the BLR is flattened. Various models have been proposed in order to explain the observed broad line profiles found in type-1 AGNs. These models include: a spherical distribution of a large number of clouds around the SMBH (Baldwin et al. 1995; Goad & Wanders 1996); a stream of gas in a biconical shape (Zheng et al. 1990; Marziani et al. 1996; Corbett et al. 2000); a relativistic Keplerian disk (Chen & Halpern 1989; Chen et al. 1989; Eracleous & Halpern 1994, 2003; Strateva et al. 2003); two components model (Popovic et al. 1995; Brotherton 1995; Sulentic et al. 2000; Popović 2003; Popović et al. 2004; Ilić et al. 2006; Bon et al. 2006, 2009a,b); a supermassive binary black hole (Gaskell 1983, 1988, 1996; Popovic et al. 2000; Popović 2012; Bon et al. 2012). Each of these models is able to explain the observed line profiles and each of them face a number of problems and challenges (see Popović & Ilić 2017). Recently, the GRAVITY collaboration team was able to spatially resolve the rotation of the broad-line region at sub-parsec scale of the quasar 3C 273 (Gravity Collaboration et al. 2018), which is in favor of the BLR located near the illuminated surface of the dusty torus and having a disk-like geometry (Baskin & Laor 2018).

The study of broad emission lines remains the central topic in understanding the central engine of AGNs. This will be largely improved with the sensitivity of the new generation of extremely large telescopes in the next decade.

The dusty torus

According to the unification scheme, the central engine of AGNs is surrounded by a thick toroidal structure of gas - the so called dusty torus. The optical depth of the dusty torus at all wavelengths is large, and hence the accretion disk and the BLR would be obscured in optical and UV when viewed from certain viewing inclinations. The dusty torus absorbs the high energy radiation from the accretion disk and re-emits it in the IR. X-ray observations allow us to infer the obscuring column densities which are of the order of $n_{\rm H} \sim 10^{22}$–$10^{24}\,{\rm cm}^{-2}$ for hydrogen (Netzer 2013). The torus is within the gravitational influence of the SMBH and beyond the dust sublimation radius where molecules and dust grains can form. Dust is typically made of carbonaceous grains and amorphous silicate grains (Draine 2003). Dust reverberation mapping in the near- and mid-IR of about twenty AGNs has revealed that the inner region of the dusty torus is compact (Suganuma et al. 2006; Koshida et al. 2014; Vazquez et al. 2015). The torus inner radius is tightly correlated with the optical V-band luminosity $R_{\rm in}^{\rm tor} \propto L_{\rm V}^{0.5}$ (Koshida et al. 2014) which is consistent with the sublimation radius for graphite (Barvainis 1987; Burtscher et al. 2013). On the other hand, the torus radius measured using interferometry (Kishimoto et al. 2011) is systematically larger roughly three times than the one obtained by dust reverberation mapping. This is related with the different definition of the two radii since the radius measured using interferometry is flux weighted while the radius measured by dust reverberation mapping is response weighted.

Past the self-gravity radius, the accretion disk becomes fragmented into clouds which keep moving in the same way. Cloud-cloud collisions drive a net inflow and the position of the torus inner edge is determined by the balance between the inflow and the rate at which the clouds evaporate due to the exposure to the nuclear continuum radiation (Krolik & Begelman 1988). Large numbers of clouds with distances between them that are much smaller than the size of the torus can be approximated by a model of a continuous uniform density torus (Pier & Krolik 1992). This requires however that the cloud size is not too small; is the cluid size tends to zero (and the cloud density to infinity, the torus becomes transparent. A smooth dusty torus (Pier & Krolik 1992, 1993) predicts a strong silicate feature at 9.7 μm and 18 μm that appears in emission for type-1 AGNs or in absorption for type-2 AGNs due to the large optical depth in the equatorial plane (Fritz et al. 2006). For a clumpy torus model, the illuminated surfaces of the dense and optically thick clumps would produce mid-IR spectrum that is less
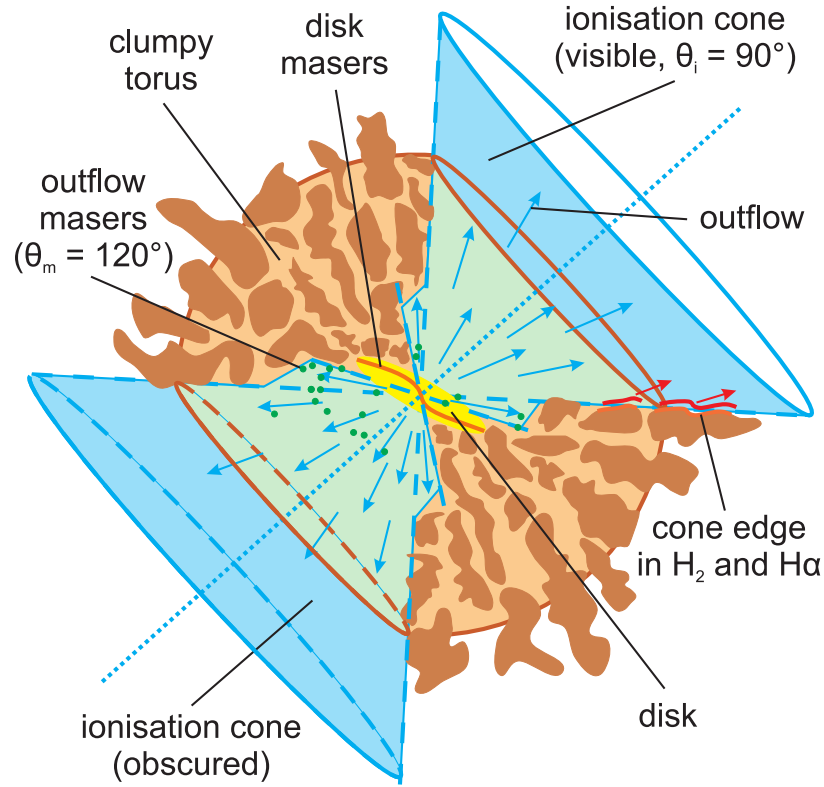
Figure 1.8: An illustration of the dusty torus derived from the mid-IR interferometric observations of the type-2 AGN Circinus. Credits: Tristram et al. (2007).

inclination dependent (Nenkova et al. 2008a,b; Hönig & Kishimoto 2010; Stalevski et al. 2012). X-ray variability studies have confirmed the clumpy structure by successfully detecting occultation events (Markowitz et al. 2014; Marinucci et al. 2016). The SED contribution of the dusty torus is shown in Fig. 1.5.

An important parameter of the dusty torus is the covering factor f_C i.e. the fraction of the sky covered by clumps when viewed from the center; and it is directly related to the half-opening angle of the torus. For individual objects, f_C can be estimated by direct modeling of the X-ray spectrum (Brightman & Nandra 2011) or by finding the ratio of the reprocessed IR emission to direct emission (Toba et al. 2014; Stalevski et al. 2016). Another way is to find the average f_C for a given luminosity as $f_C = $ N(type-2)/N(type-1). AGNs with high f_C are likely to be observed as obscured (Elitzur 2012). For nearby AGNs, Ricci et al. (2017b) found that $f_C \approx 0.8$ for $L/L_{\rm Edd} < 0.02$ and then drops drastically for higher Eddington ratio, independent of AGN luminosity. A strong dependence of Eddington ratio indicates that most of the obscuring material is inside the SMBH radius of influence suggesting that a compact torus-like structure is the dominant

source of obscuration (Hickox & Alexander 2018). In order for such thick torus to be long lived, various physical processes must be present including high velocity turbulent motion (Beckert & Duschl 2004), outflows due to UV, optical and IR radiation pressure (Hönig & Beckert 2007; Czerny & Hryniewicz 2011) or magnetic winds (Emmering et al. 1992; Elitzur & Shlosman 2006). The formation and evolution of the dusty torus were studied with R-HD (radiation-hydrodynamics) simulations taking into account AGN feedback and supernova feedback (Wada 2012; Schartmann et al. 2014; Wada et al. 2016). They found that AGN feedback drives a fountain-like outflows and the interaction between outflows and inflows results in the formation of a geometrically thick turbulent torus with density filaments and clumps. An illustration of the AGN dusty torus is given in Fig. 1.8. The most recent discoveries concerning the dusty torus are summarized in Netzer (2015); Ramos Almeida & Ricci (2017); Hickox & Alexander (2018)

Polar winds

Dusty torus efficiently collimates AGN radiation in polar directions resulting in biconical outflows that can be extended to scales comparable to or greater than the size of the host galaxy. Depending on the distance from the accretion disk, we could expect different physical, chemical and kinematic conditions of the outflowing gas. Polar winds can be roughly divided into three regions: ultra-fast outflows (UFOs), warm absorbers (WA) and the narrow line region (discussed separately).

Ultra-fast massive outflows were reported with high sensitivity X-ray observations with good spectral resolution over a wide energy band in the form of absorption lines from H-like and He-like iron, first for individual AGNs (Pounds et al. 2003; Reeves et al. 2003), and later confirmed to be common in nearby AGNs (Tombesi et al. 2010; Gofford et al. 2013). Inferred blueshifted velocities are mildly relativistic, in the range ~ 0.03–$0.3\,c$ (Tombesi et al. 2010). The UFOs are located in the vicinity of the SMBH with distances estimated to be in range 0.0003–$0.3\,pc$ (Tombesi et al. 2012). Column density estimated from photoionization modeling is around 10^{22}–$10^{24}\,cm^{-2}$ (Tombesi et al. 2011). The outflowing gas is highly ionized with ionization parameters[6] in the range $\log X_{ion} \sim 3$–6 and electron temperatures $T_e \sim 10^7\,K$ (Kraemer et al. 2018). Further away in the polar direction, Tombesi et al. (2012) identified non-UFOs – a

---

[6]The ionization parameter $X_{ion} = L_{ion}/n_H r^2$, where L_{ion} is the AGN ionizing luminosity, n_H is the hydrogen number density, and r is the radial distance (Kraemer et al. 2018).

region of Fe K absorbers with velocity $<10\,000\,\mathrm{km\,s^{-1}}$ located at a distance of 0.03–0.3 pc from the SMBH. The ionization parameter, column density and the electron temperature of the non-UFOs are typically an order of magnitude lower than the ones estimated for the UFOs (Kraemer et al. 2018). Mass loss rate for both UFOs and non-UFOs can reach values as high as $\sim 1\,M_\odot\,\mathrm{yr^{-1}}$, which is at least 5–10 % of the accretion rate (Tombesi et al. 2012). Compton scattering is the dominant heating process for UFOs, while cooling is via inverse Compton scattering or via free-free processes. For non-UFOs, ionization is the dominant heating process, while Compton scattering is less prominent. The cooling of non-UFOs can be dominated by line emission if the ionization is low enough. The UFOs are capable of providing a significant contribution to the AGN cosmological feedback (King & Pounds 2015). The origin and the acceleration mechanism of UFOs have been a subject of intense studies in the last decade. Radiative acceleration due to UV absorption of the gas in the low state of ionization can launch the high-velocity disk winds (Nomura & Ohsuga 2017). Wind regions far from the disk surface are highly ionized by the X-ray radiation from the hot corona producing Fe blueshifted absorption lines. This mechanism predicts fast winds even for AGNs at sub-Eddington regime. Another plausible explanation is that winds are magnetically driven (Fukumura et al. 2015). The presence of magnetic fields can explain the large velocity of the outflowing matter, but this model is prone to degeneracy requiring an a priori knowledge of the ionization state of the wind in order to explain the absorption lines.

Warm absorbers consist of clouds moving at moderate radial velocities 100–1000 km s^{-1} at typical distances of 0.1–10 pc showing complex ionization structures and having moderate to large column densities 10^{21}–$10^{23}\,\mathrm{cm^{-2}}$ and ionization parameters $\log X_{\mathrm{ion}} \sim 1$–3 (Netzer 2013; Reeves et al. 2013). The gas velocity shows a positive correlation with the ionization parameter (Pounds & King 2013). X-ray observations of type-I AGNs show a clear signature of the WA. The strongest spectral features involve numerous absorption lines of various chemical elements, prominent bound–free absorption edges mostly due to O VII and O VIII, and several emission lines (Netzer 2013). As an example, the X-ray spectrum of NGC 3783 by is shown in Fig. 1.9 X-ray absorption features appear to be common in AGNs. They are found to be present in more than 50 % of AGN spectra (Porquet et al. 2004; Laha et al. 2014). Deep inside WA, we could expect lower ionization and the presence of ions like C IV, N V, O V, O VI. These ions can absorb UV radiation producing strong absorption lines with typical widths similar to X-ray absorption lines. Comparison of absorption lines of the same
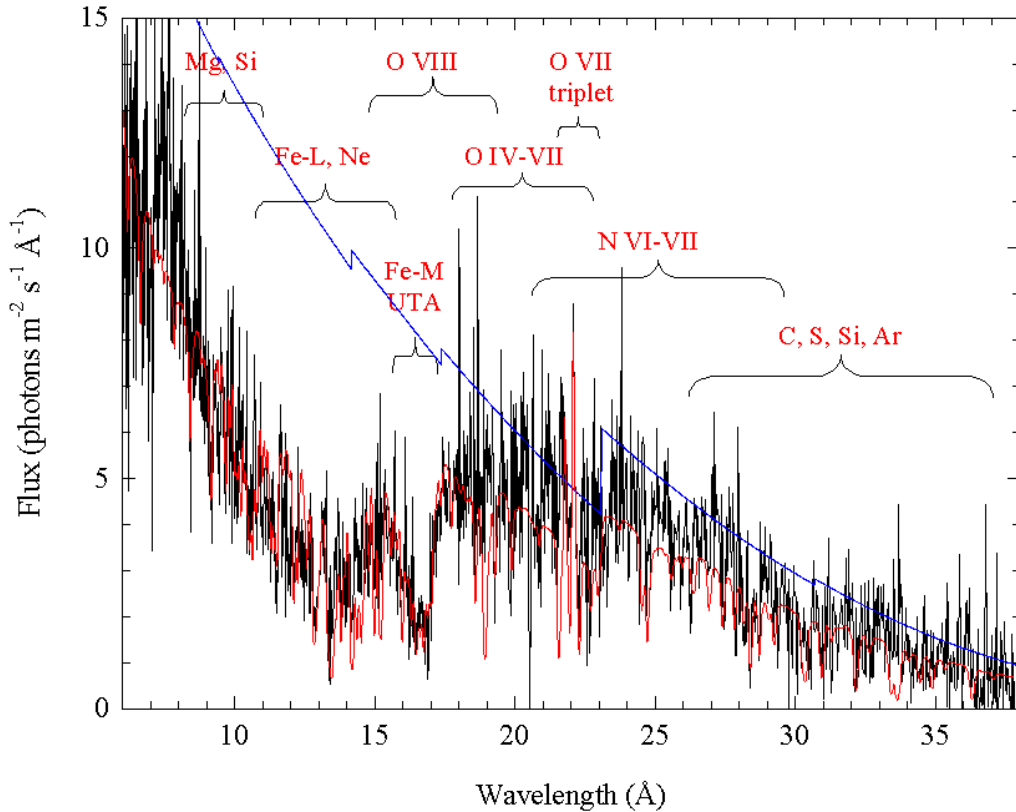
Figure 1.9: Reflection grating spectrometer (RGS) rest frame spectrum of NGC 3783 (black) observed with XMM-Newton on 28-29th December 2000. Power-law continuum is shown in blue and the power-law plus two-phase WA model fit is superimposed (Blustin et al. 2002). Observed spectral range is between 6–38 Å (0.326–2.066 keV). Spectral ranges of emission and absorption of different elements are indicated above. Credits Blustin et al. (2002).

element in the X-ray and the UV domains can be used to test whether the X-ray and UV absorbers are located in the same region. For some AGNs, the coinciding velocities of Lyβ and O VII (in the X-ray) have revealed a strong link between the UV and the X-ray absorption (Kaspi et al. 2002; Gabel et al. 2003). This is not always the case, and the UV absorbers cannot be solely identified with X-ray absorbers (Brotherton et al. 2002; Crenshaw et al. 2003).

More recently, a number of both theoretical and observational pieces of evidence suggest that the dust in the extended polar regions represents a significant (sometimes a major) fraction of the total IR emission (Hönig 2019). Using single-dish observations, Asmus et al. (2016) have identified 18 AGNs with clear detections of the extended mid-IR emission coming from the polar region on scales of 10–100 pc. Infrared interferometry

currently provides the only way to directly resolve and constrain the shape of the parsec-scale of nearby AGNs. Additional interferometric observations by López-Gonzaga et al. (2016) show that the mid-IR dust emission of some of AGNs in their sample is also elongated in the polar direction. These findings pose a challenge to the standard dusty torus models for interpreting the AGN IR emission and require the presence of a large scale dusty cone in addition to the dusty torus (Stalevski et al. 2017, 2019; Hönig 2019).

The narrow line region

This region is a natural continuation of the polar winds, extending up to few kpc for the most luminous AGNs (Netzer 2013). The narrow emission lines observed in AGNs are similar to the emission lines observed in H II regions and planetary nebulae, with the exception that the range of ionization parameters is considerably wider in AGNs (Osterbrock & Ferland 2006). Permitted hydrogen Balmer lines, as well as forbidden [He I] $\lambda 5876$ Å and [He II] $\lambda 5876$ Å are moderately strong. The most prominent forbidden optical emission lines are [O II] $\lambda 3727$ Å, [O III] $\lambda 5007$ Å doublet, [O I] $\lambda 6364$ Å doublet, [S II] $\lambda 6731$ Å doublet, [N I] $\lambda 5199$ Å, [N II] $\lambda 6583$ Å doublet, [Ne III] $\lambda 3967$ Å, [Ne V] $\lambda 3426$ Å and sometimes [Fe VII] $\lambda 5721$ Å and [Fe X] $\lambda 6375$ Å. Line widths are typically between 200–900 km s^{-1}. Gas in the NLR is dominantly ionized by the radiation from the central source on global scales; however, shocks due to the interaction of the outflows and the interstellar matter also have an important role in localized regions (Afanasiev et al. 2007; King & Pounds 2015). The presence of forbidden emission lines indicates that the NLR gas concentration is much lower than the gas in the BLR. Forbidden lines are formed exclusively due to collisional excitation of electrons to metastable states followed by radiative de-excitation for low density gas. Line diagnostic is a good method for determining physical conditions in the NLR. The [0 III] intensity ratio ($\lambda 4959$ Å $+ \lambda 5007$ Å$/\lambda 4363$ Å and the [N II] ratio ($\lambda 6548$ Å $+ \lambda 6583$ Å$/\lambda 5755$ Å correspond to temperatures of the order of $\sim 10^4$ K and electron concentrations $n_{\mathrm{e}} < 10^4$ cm^{-3} (Osterbrock & Ferland 2006).

Early imaging studies of the spatially resolved AGNs have shown that the NLR shape is bi-conical (Tadhunter & Tsvetanov 1989), supporting the unified model. In a more detailed study of a sample of nearby AGNs, it was found that the bi-conical morphology is more an exception than a rule (Schmitt et al. 2003a), and roughly one third of AGNs with extended narrow line structures have outflowing kinematics (Fischer et al. 2013). Integral field spectroscopy (IFS) is a powerful tool for mapping the gas
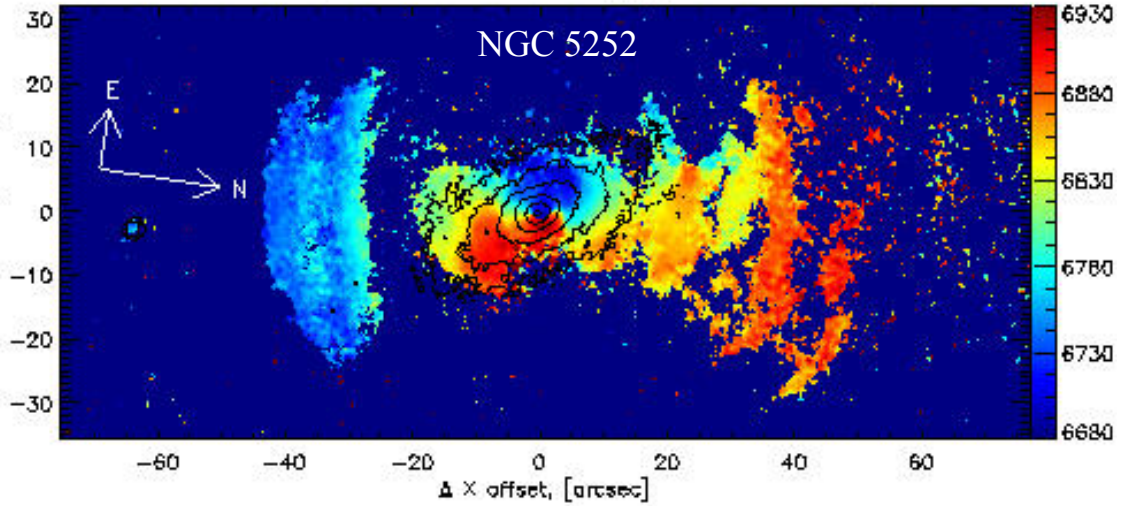
Figure 1.10: NGC 5252 observed in the [O III] λ5007 Å emission line. The colored areas show emission from the NLR: blue and red regions indicate emission from gas that is moving towards, or away from us respectively. The black contours show the isophotes of the host galaxy. Observations were carried out on 23 Feb. 1998 with the SAO RAS 6 m telescope. Credits: Viktor Afanasiev, https://www.sao.ru/hq/lsfvo/devices/scorpio/galleries/gal_ifp.html

kinematic (Storchi-Bergmann et al. 2018; Freitas et al. 2018, and references therein) in a form of two-dimensional (2D) velocity fields with high spatial resolution. An example of [O III] λ5007 Å emission is shown in Fig. 1.10. The inferred gas velocity projections are of the order of a few hundreds km s^{-1}. Very often, observations reveal kinematic signatures of rotation in addition to outflows in the NLR. The outflow rate is 2-3 orders of magnitude higher than the accretion rate, implying that the outflow is mass loaded by the surrounding interstellar medium (Müller-Sánchez et al. 2011). The NLR size is in good correlation with luminosity: $R_{\mathrm{maj}} \propto L([O\,III])^{0.33\pm0.04}$, where R_{maj} is the semimajor axis of the O III emission (Schmitt et al. 2003b). The NLR size increases with L([O III]) for a broad luminosity range in a more steeper way: $R_{\mathrm{maj}} \propto L([O\,III])^{0.51\pm0.03}$, implying that the NLR can extend to distances beyond the limit of the host galaxy (Storchi-Bergmann et al. 2018). The study of the NLR provides the most direct way for understanding the AGN feedback and how the SMBHs shape their surrounding.

Jets

Jets are collimated outflows of plasma and fields produced by accreting compact objects. The presence of non-thermal radio emission has been the primary signature of

relativistic jets, distinguishing jetted AGNs from non-jetted ones. Physical conditions in the jet plasma vary significantly along the jet propagation. The current paradigm assumes four distinct regions: launching, acceleration and collimation, kinetic flux dominated and dissipation (Boccardi et al. 2017). Magnetic field can extract energy and angular momentum from the accretion disk (Blandford & Payne 1982) or from the spinning black hole itself (Blandford & Znajek 1977), launching powerful outflows. In both cases, jets are launched at distances $\leq 10^2\,R_{\mathrm{Sch}}$ (Meier et al. 2001). The electromagnetic flow is then accelerated and collimated at distances 10^3–$10^5\,R_{\mathrm{Sch}}$ (Vlahakis & Königl 2004). The exact acceleration mechanism remains unknown and different scenarios have been proposed such as diffusive shock acceleration (DSA, Bell 1978); magnetic pressure gradients (Lyubarsky 2009); relativistic magnetic reconnection (Barniol Duran et al. 2017); and other (discussed by Blandford et al. 2018). The observed Lorentz factors of jets in AGN are ~10 (Lister et al. 2009). A jet can be collimated by the pressure of the surrounding medium or by the magnetic tension of the field lines. The kinetic flux dominated jet extends between 10^5–$10^9\,R_{\mathrm{Sch}}$. A large part of the magnetic energy has been converted to kinetic energy and the magnetic field is less dynamically important. The jet interacts with the surrounding medium and forms lobes at distances $\geq 10^9\,R_{\mathrm{Sch}}$. Since the jet velocity is much greater than the velocity of the medium, strong shocks form at the jet end. These shocks create compact hotspots of intense emission that are often observed. The jet inevitably loses its collimation and dissipates energy in the form of radiation. An illustration of the AGN jet is shown in Fig. 1.11.

The jet SED is strongly dominated by non-thermal radiation from radio up to γ-ray, extending in many cases up to GeV and TeV energies (Abdo et al. 2010). The overall SED shape shows a broad double bump distribution, where the first bump is due to synchrotron radiation and the second one due to inverse Compton emission. The jet radiation in X-rays coincides with optical and radio knots and hotspots (Clautice et al. 2016). Optical, UV and X-ray radiation from the jet that is the closest to the SMBH is highly variable (Rani et al. 2017, and references therein). The SED shape roughly matches the one predicted by the synchrotron self-Compton (SSC) radiation. In this scenario, relativistic electrons produce synchrotron radiation responsible for the low-energy bump. These photons will have some probability to undergo inverse Compton scattering, contributing to the high energy part of the SED. The SSC models allows to infer robust constraints of the physical parameters of the jet from the observed SED (Ghisellini 2013). Other models involve external low energy seed photons, namely from the accretion disk, that are upscattered to higher energies – external Compton radiation
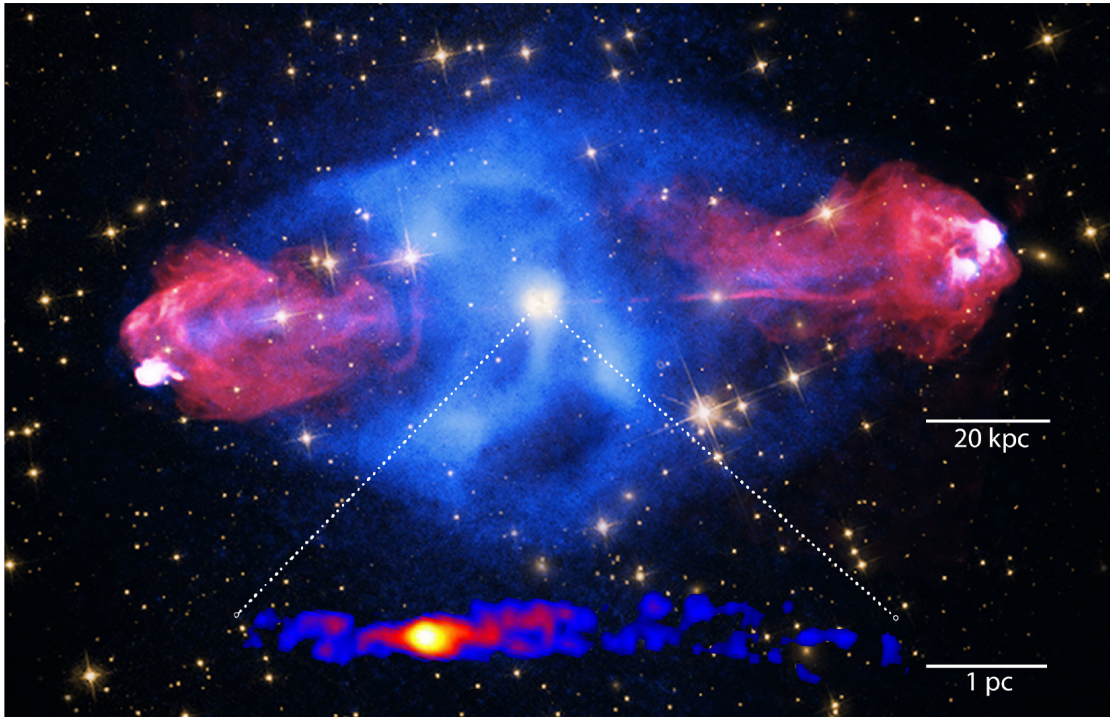
Figure 1.11: Radio (red), X-ray (blue) and optical images of the AGN Cygnus A, showing a complex jet morphology. The three primary hot spots are bright both in X-ray and radio bands and coincide with a synchrotron peak in the radio and a inverse Compton scattering peak in the X-ray. Bottom: the VLBI (very large baseline interferometry) observations at 3 mm in the black hole vicinity reveals a jet origin at scales 20 000 times smaller. Credits: Blandford et al. (2018); X-ray: NASA/CXC/SAO; Optical: NASA/STScI; Radio: NSF/NRAO/AUI/VLA; VLBI inset Boccardi et al. (2017).

(EC). Both SSC and EC are known in literature as *leptonic* models. Alternatively, if protons are accelerated to ultrarelativistic energies, they could significantly contribute to the jet SED. In addition to proton synchrotron radiation, the interaction of protons with photons may produce secondary particles: electron-positron pairs, neutral or charged pions and neutrinos, which contribute to high energy part of the SED. Models involving these processes are known as *hadronic* or *lepto-hadronic* models (Vila et al. 2012).

Despite decades of research, many fundamental aspects of the jets are still not well understood. Open questions still involve the acceleration and collimation of the jet; strength and topology of the magnetic field; dominant radiation mechanisms. High energy neutrinos TeV–PeV neutrinos have been confidently detected by IceCube (Aartsen et al. 2014) and would unambiguously confirm the presence of ultrarelativistic protons

in the jets if the neutrino sources could be identified with AGNs (Kadler et al. 2016). Deep images of M87 with spatial resolution of $7\,R_{\mathrm{Sch}}$, obtained with EHT (Event Horizon Telescope, Event Horizon Telescope Collaboration et al. 2019a) at 86 GHz, show that the jet core is magnetically energy dominated and that the jet originates from the inner accretion disk (Kim et al. 2018). CTA (Cherenkov telescope array), that is under construction, will have an improved energy coverage $\sim$30–100 TeV with angular resolution up to $\sim$3″ and it would greatly extend the current understanding of the jets. For a broad discussion regarding the jet phenomena, we refer to extensive reviews by Boccardi et al. (2017); Romero et al. (2017); Blandford et al. (2018).

Chapter 2

Polarization of AGNs

2.1 Astronomical polarimetry

Polarization is a fundamental property of electromagnetic radiation. It provides two more independent observables: the degree of polarization p and, in the case of linear polarization, the on-sky position angle φ. For astronomical sources of radiation, polarization can be induced in the source itself whenever geometrical asymmetries or magnetic fields are present, or both. Polarimetry yields information that is complementary to imaging and spectroscopy and is therefore an important tool in modern astrophysical research. It is a photon-hungry method requiring efficient optics and large apertures for observations and usually requires a different instrumentational setup than the one used for imaging or spectroscopy. A typical layout of an astrophysical spectrometer consists of: telescope, polarization calibration package (removed when the source is observed), polarization modulator, spectrometer and detector (Keller 2002). Nevertheless, polarimetry is widely applied for studying our Solar system; interstellar and intergalactic medium; up to the high-redshift Universe.

Astronomical objects generally show weak polarization that is usually just a few percent of the total radiation, however, both higher and (much) lower values have been observed (Hough 2006). The polarization pattern can be used to determine the location of an obscured source by locating the region where the lines perpendicular to each polarization vector intersect. The wavelength dependence of polarization can be used for determining the nature of the scatterers. The polarized radiation is particularly sensitive on the physical conditions and geometry, both of the source as well as of the intervening matter in the line of sight. Whenever scattering events occur, we can

expect that the observed radiation is partially polarized. In case of AGNs, where the central engine is surrounded by an optically and geometrically thick dusty torus, the polarized spectrum of some type-2 AGNs shows broad emission lines López-Gonzaga et al. (2016), proving that the obscured BLR exists in type-2 AGNs. Polar scattering in this case provides a periscope view of the AGN central engine. These findings led to the unification scheme of AGNs (Antonucci 1993). Different emission and reprocessing mechanisms have a deep impact on the polarization state over the broad frequency range, allowing us to better understand the physics in the innermost part of AGNs.

In this chapter, we focus on the observational traits of polarization found in AGNs for the broad frequency range. The formalism and necessary mathematical apparatus is introduced in Chapter 4. For the wide application of astronomical polarimetry, we refer to textbooks by Tinbergen (1996); Trujillo-Bueno et al. (2002); Kolokolova et al. (2015).

2.2   Broadband polarization of AGNs

Polarimetric observations of AGNs began simultaneously with the discovery of quasars in the 1960s. Early reports have initially shown little or no optical polarization (Matthews & Sandage 1963; Schmidt 1965). Subsequent observations of a dozen of AGNs were carried out at the Crimean astrophysical observatory (Dibai & Shakhovskoi 1966) and McDonald observatory (Appenzeller & Hiltner 1967). The observed degree of polarization was of the order of a few percent and it became clear that such small intrinsic polarization is a common feature of AGNs. For nearly half of the observed sample, it was interpreted as due to synchrotron radiation from the compact region, while for the rest, due to dust scattering (Dombrovskii & Gagen-Torn 1968). Historically, attention for studying optical polarization of AGNs has been focussed on blazars and OVVs due to their rapid variability both in unpolarized and polarized flux as well as their unusually high degree of polarization $p = 3$–20% (Angel & Stockman 1980; Moore & Stockman 1981). Extended AGN polarimetric surveys (Burbidge et al. 1977) have shown that the large majority of the observed AGN, largely consisting of quasars, Seyferts and radio galaxies, have $p \leq 3\%$, while blazar and OVVs account for only 1% of the AGN sample (Stockman et al. 1984). Another important finding was the orientation of the polarization angle with respect to the orientation of the jet axis. Stockman et al. (1979) and Antonucci (1982) have shown that type-1 AGNs exhibit a

strong tendency for the optical electric vector position angle to be closely aligned with the axis of the extended radio structure – a feature called parallel polarization. On the contrary, in type-2 AGNs, the polarization position angle is perpendicular to the radio axes – perpendicular (orthogonal) polarization (Antonucci 1982, 1983, 1984).

Spectropolarimetric observations of AGNs have provided many valuable insights into our current understanding of these objects. Optical spectropolarimetry has revealed that the broad hydrogen permitted lines have nearly the same position angle and a similar degree of polarization as the neighbouring continuum, suggesting that dust scattering is responsible for polarization. Forbidden lines are weakly polarized with a position angle different from the continuum, indicating that they come from a different emitting region that is outside the nuclear scattering region (Angel et al. 1976). Using the high resolution (around 10 Å) spectropolarimetric observations of Seyfert 2 galaxies, it was found that numerous objects show a hidden type-1 nucleus with broad permitted lines and often with strong Fe emission, visible only in polarized light (Antonucci & Miller 1985; Miller & Goodrich 1990; Kay 1990; Tran et al. 1992). These observations have provided a strong foundation for the classic "observation/reflection" picture where the optical polarized flux can be explained as scattering by dust or free electrons in the polar region above the obscuring torus (Antonucci 1993).

Up to now, there have been very few AGNs with polarization properties observed in a broad frequency range. One of the most intensively studied AGN is the nearby Sy 2 galaxy NGC 1068. Recently, Marin (2018a) compiled more than fifty years of observations of the continuum polarization, with different instruments and apertures, covering the spectral range 0.1–$100\,\mu m$, together with two measurements in radio at $4.9\,$GHz and $15\,$GHz. In Fig. 2.1, the degree of polarization (top panel), polarized flux (middle panel) and polarization angle (bottom panel) are shown. The linear polarization is highest in the UV, around $15\,\%$, where the stellar emission is weak, and drops down to a minimum $p \sim 1\,\%$ at $1\,\mu m$, where the stellar contribution is high. Then, both the degree of polarization and polarized flux rise in the near IR where p has a secondary maximum at $2\,\mu m$. The polarization angle remains perpendicular to the radio axis from UV up to $\sim 3\,\mu m$, indicating that most of the polarization is due to electron and Mie scattering. At wavelengths $\lambda \geq 4\,\mu m$, dust grains concentrated in the equatorial plane dominate the emission. Dust alignment by large-scale magnetic fields (Lopez-Rodriguez et al. 2015) produce parallel polarization. Polarized dust emission increases between 10–$20\,\mu m$, peaking somewhere between 20–$40\,\mu m$ and finally decreases in the 50–$100\,\mu m$ waveband (Fig. 2.1, middle panel). The polarized SED of NGC 1068 largely

resembles the averaged total flux of type-1 AGN SED given by Prieto et al. (2010). In the radio domain, the polarization angle is perpendicular to the radio axis, as in the optical and UV band, and the polarization degree is low, for which the most plausible explanation is electron scattered synchrotron emission (Krips et al. 2006). While certain frequency bands have been extensively used, such as optical and near-IR, some have been completely ignored when it comes to polarimetric observations of AGNs. In the following, we summarize the mechanisms responsible for AGN polarization from high to low energies. In addition, a brief overview of the future new era instruments with polarimetric capabilities, that will significantly push the limits in exploring the geometry and physics of AGNs, is provided.

In X-rays, Compton and inverse Compton scattering are the dominant processes for producing polarization. Relativistic effects are also expected to have an influence on the polarization state of the X-ray continuum since it is produced in the vicinity of the black hole (Dovčiak et al. 2004). The NASA IXPE (imaging X-ray polarimetry explorer) mission will cover the 2–8 keV energy band (Weisskopf et al. 2016). The launch is planned for April 2021. The Chinese satellite eXTP (enhanced X-ray timing and polarimetry) with a similar energy band (2–10 keV) is planned for 2025 (Zhang et al. 2016). Both instruments will significantly contribute to the determination of the polarization state of AGNs.

The UV polarization spectrum of AGNs is poorly observed. Instruments on board the HST and WUPPE (the Wisconsin ultraviolet photo-polarimeter experiment) have been used to probe the polarization of nearby AGNs in the 1400–3300 Å waveband, but the far UV from 1200 Å to the Lyman limit at 912 Å remains completely uncharted (Marin et al. 2018). Some key signatures of the accretion disk could be revealed if observed in polarized light in the UV domain (Kishimoto et al. 2008). Promising results could be expected from the future mission LUVOIR (The large UV optical infrared surveyor), which is a NASA multi-wavelength space observatory (Bolcar et al. 2018). A possible European contribution to the LUVOIR mission is the high resolution spectropolarimeter POLLUX which operates at 900–4000 Å. The proposed launch date is in the mid 2030s.

Far IR polarimetry offers an excellent insight into dust emission that typically peaks just below 100 μm. It should be able to discriminate between the nonthermal emission of AGNs and thermal emission from starburst regions (Andreani et al. 2003). Magnetic phenomena can also be explored using far IR polarimetry due to the alignment of dust grains in the external magnetic fields (Trujillo-Bueno et al. 2002) or due to radiative
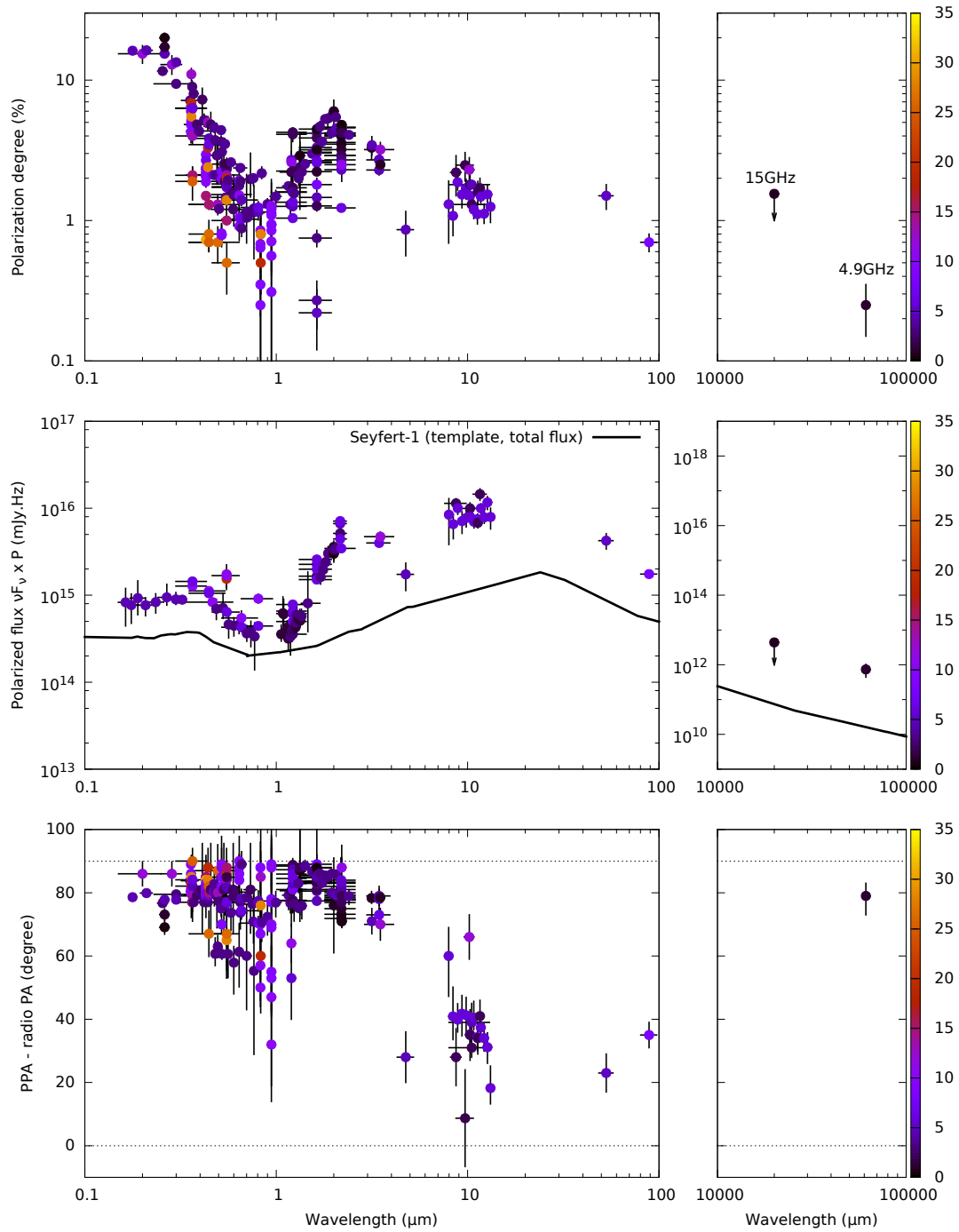
Figure 2.1: Broadband 0.1–100 µm, 4.9 GHz and 15 GHz continuum polarization of NGC 1068 measured at different ecpochs with various instruments. Top: degree of polarization p, middle: polarized fux $\nu F_\nu \times p$, bottom: polarization position angle φ for which the parsec-scale radio position angle is subtracted. The Seyfert 1 unpolarized flux (solid black line, middle panel) has been reduced roughly a hundred times for better comparison. Apertures are color-coded, in arcseconds. Credits: Marin (2018a).

torque alignment (Lazarian & Hoang 2019, and references therein). Observations in this waveband require altitudes above $\sim 14\,\mathrm{km}$ in order to overcome water vapor absorption. This is usually accomplished with airborne telescopes. The current US mission SOFIA (stratospheric observatory for infrared astronomy) operates in far IR with the ability to make polarimetric measurements of aligned dust grains (Harper et al. 2018).

In the radio domain, we expect to detect synchrotron emission since it is highly polarized (Rybicki & Lightman 1979). The MHz and GHz should be more exploited, particularly at locating the turnover frequencies between the dust polarized emission and synchrotron radiation (Marin 2018a). Submillimeter polarimetry offers the possibility of identifying magnetic fields, especially when it comes to accretion disks (Aitken et al. 2002). The POLAMI (Polarimetric Monitoring of AGN at Millimeter Wavelengths) program at IRAM has successfully detected circular polarization due to Faraday conversion when a magnetic field is present in the plasma (Thum et al. 2018). SKA (square kilometer array) will enable monitoring of the sky in unprecedented details. Wide-area wide-band polarimetric surveys with SKA will greatly improve our understanding of the relationship between supermassive black holes and their environments (Gaensler et al. 2015).

2.3   Optical polarization of type-1 AGNs

The polarization properties of type-1 AGNs in the optical domain have been a subject of numerous studies in the past few decades, both observationally as well as theoretically. According to the unified model, type-1 AGNs have an unobscured line of sight towards the central engine. If polar scattering were the main scattering mechanism for type-1 AGNs, we would expect perpendicular polarization. Optical polarization of type-1 AGNs is therefore not consistent with the simple polar scattering, since we observe parallel polarization (Antonucci 1984). High quality signal-to-noise ratio spectropolarimetric observations by Goodrich & Miller (1994) have revealed a diversity of characteristics in the polarization of Hα line. This includes a φ rotation across the line profiles and a new scattering paradigm was introduced – equatorial scattering. This scenario assumes that type-1 AGNs are polarized by scattering in an optically thin disk residing in the equatorial plane. Equatorial scattering can produce parallel polarization as well as the degree of polarization that is observed in type-1 AGNs.
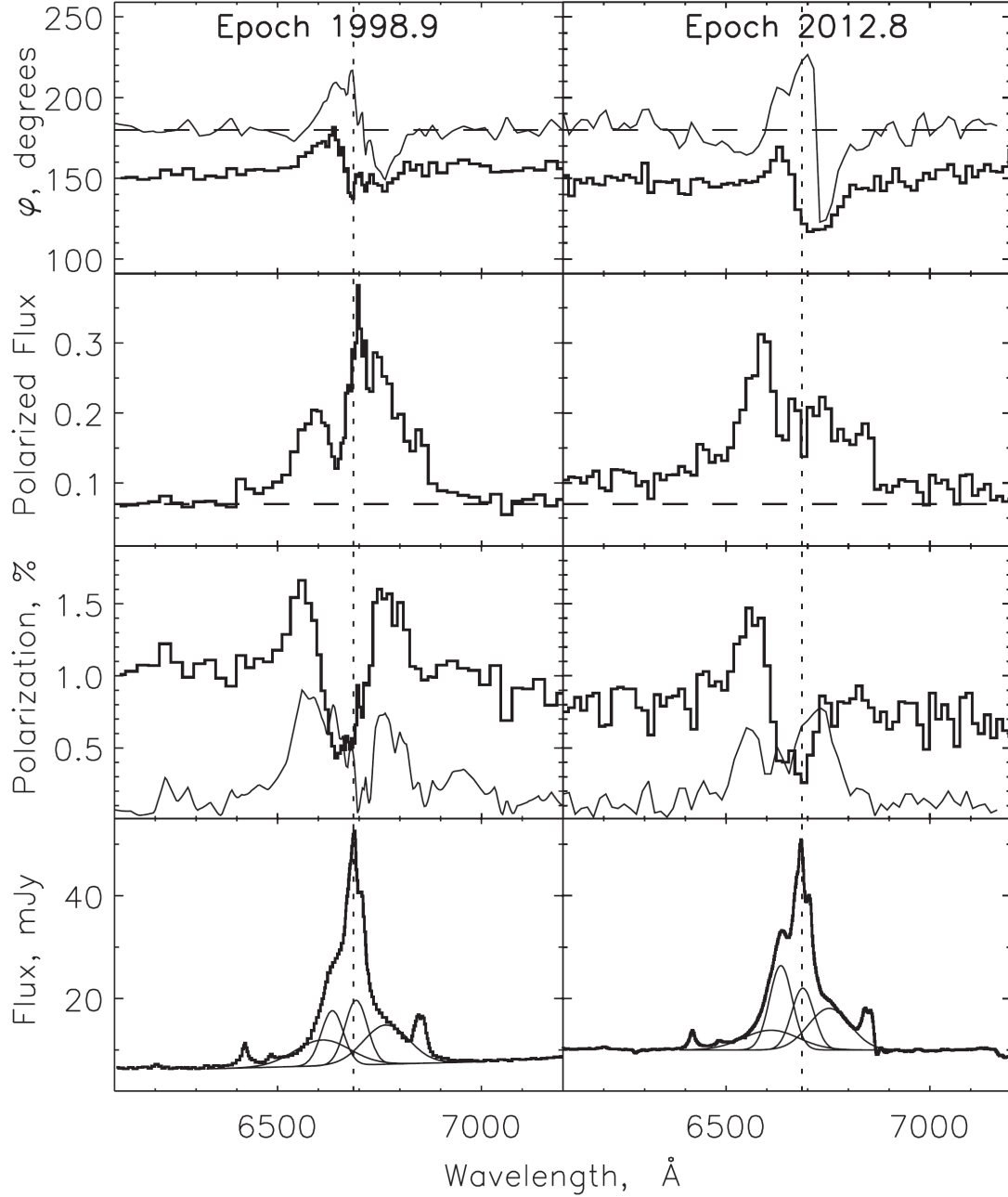
Figure 2.2: Spectropolarimetry of Mrk 6 for two epochs: 1998.9 (left half, Smith et al. 2002) and 2012.8 (right half, Afanasiev et al. 2014). From top to bottom: polarization position angle φ (top panel); polarized flux $p \times F_\lambda$ (top second); degree of polarization p (top third); unpolarized Hα line profile decomposed into Gaussian components (bottom panel). Thick lines show the observations corrected for interstellar polarization. Thin lines in the first and third panels are obtained when interstellar polarization is not accounted for. Credits: Afanasiev et al. (2014)

.
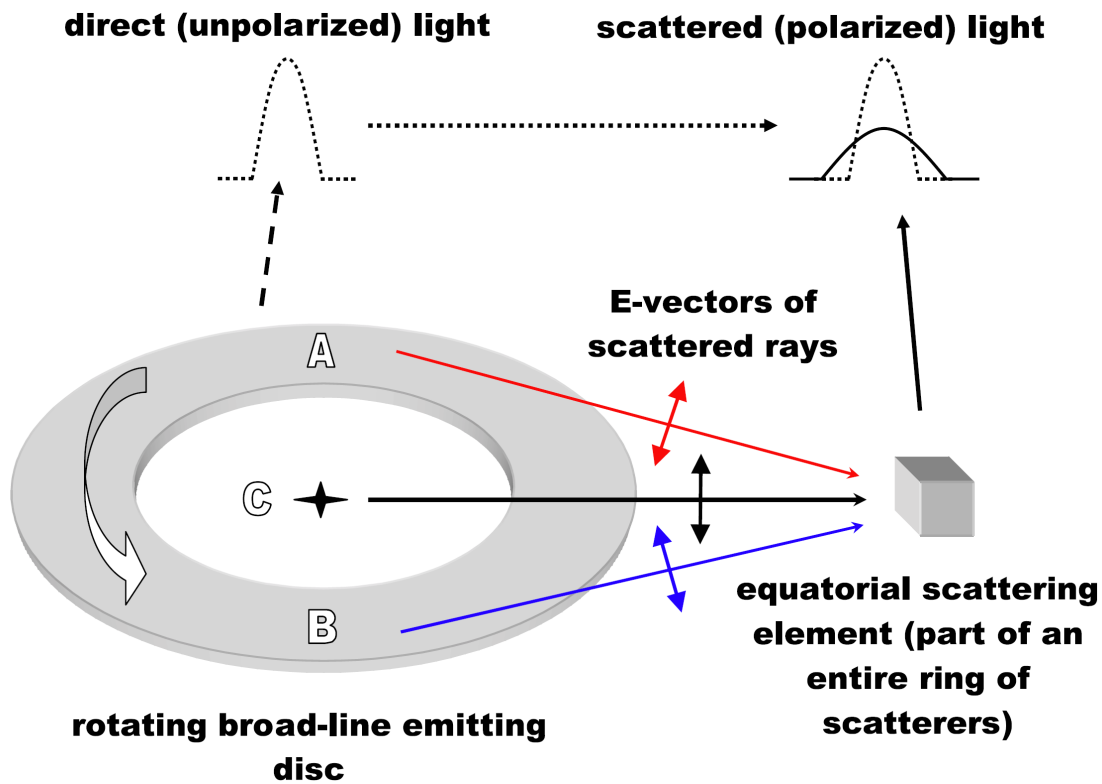
Figure 2.3: The central continuum source (C) and a flattened disk-like BLR are surrounded by a coplanar ring of scatterers (only a single element of the scattering region is shown). Emitting regions closer to the inner radius of the BLR produce φ closer to that of the central continuum source. Equatorial scattering produces characteristic variations in both φ and p across the broad-line profile. Credits: Smith et al. (2005).

A spectropolarimetric atlas of almost 40 nearby Seyfert 1 galaxies have shown new features common to type-1 AGNs (Smith et al. 2002). In Fig. 2.2, the polarized spectra of Mrk 6 is shown as an example. The characteristic φ profile is the following: far away from the spectral line φ follows the continuum value. At velocities corresponding to the blue wing, φ reaches a maximum, followed by a drop through the core until the minimum value is reached in the red wing – the so called S-shape profile[1] (Fig. 2.2, top panel). The polarized line is broader than the unpolarized one and for some objects it clearly shows double-peaked profiles (Fig. 2.2, top second panel). The degree of polarization for equatorial scattering shows a well known double-peaked profile. Polarization is the highest in the line wings, while at the line core, it has values lower than the local

---

[1]This effect depends on the direction of rotation. For the opposite direction, we observe the resulting profile: minimum in the blue wing and maximum in the red wing.

continuum (Fig. 2.2, top third panel). The observed polarization properties can be explained assuming a Keplerian disk-like BLR surrounded by a coplanar scattering region (Smith et al. 2005). A single scattering element can fully resolve the BLR velocity field, therefore the produced polarized line will be additionally broadened than the unpolarized line that is coming directly to the observer (Fig. 2.3). The line flux coming closer to the inner radius has the greatest Doppler shift from the rest wavelength, as seen by the scatterers, and hence forms the wings of the polarized line. The largest variations in φ are observed closer to the line center due to the scattering of the line radiation originating closer to the outer radius. Smith et al. (2005) have also demonstrated that additional motions such as inflows and outflows significantly influence the broad line polarization profiles. A few percent of Sy 1 galaxies with perpendicular polarization due to polar scattering have also been observed (Smith et al. 2002, 2004). Both equatorial and polar scattering regions are present in all type-1 AGNs and the observed range of polarization properties can be broadly understood as an inclination effect. In this scenario, polar-scattered type-1 AGNs represent the transition between unobscured (the majority of type-1) and obscured (type-2) AGNs (Smith et al. 2004). It is worth mentioning that some type-1 AGNs (e.g. 3C 390.3) have unpolarized line much broader than the polarized line, supporting the biconical flow geometry of the BLR (Corbett et al. 1998, 2000). The cross-correlation (CCF) analysis for Hα and Hβ for 3C 390.3 shows that red and blue line wings vary almost simultaneously. This is also the case for the variation of line wings with respect to the line core, suggesting that the Keplerian motion is dominant in the BLR (Afanasiev et al. 2015).

Accretion disk radiation dominates the UV and optical spectral domain. Since the region of the disk in which emitted radiation is dominated by electron scattering opacity, some linear polarization could be expected (Chandrasekhar 1960; Coleman & Shields 1990). In the case of a pure scattering, plane-parallel accretion disk atmosphere, the polarization ranges from zero for a face-on view and rises to over 10 % for an edge-on view. The predicted polarization is perpendicular and thus equatorial scattering is a preferable mechanism for the observed optical continuum polarization. Type-1 AGNs usually have $0 \leq p \leq 5\,\%$ (Smith et al. 2002). The degree of polarization is usually wavelength dependent in the form of $p_\lambda \propto \lambda^n$, where n is the polarization index (Afanasiev et al. 2011). Both p and n show weak correlated with the SMBH mass.

For the recent summary on the equatorial scattering and the polarization signatures of the BLR in type-1 AGNs, see Savić et al. (2018); Lira et al. (2019).

Chapter 3

Methods for measuring the SMBH masses

The last few years have seen a rapid advancement in our understanding of the role that SMBHs play in the evolution of galaxies (Heckman & Best 2014). Part of this progress has come from an increased confidence in the techniques for measuring SMBH masses and part has arisen from the discovery of new correlations between SMBH masses and the properties of the host galaxies (Heckman & Kauffmann 2011; Kormendy & Ho 2013). We can distinguish between direct and indirect methods for measuring the masses of SMBHs (Peterson 2014). In the following, we briefly summarize them.

Direct methods are those for which the mass of the black hole is obtained from stellar dynamics by studying the motions of individual stars around the black hole. These include observations of stellar motions (Genzel et al. 2010; Meyer et al. 2012), or gas dynamics (Miyoshi et al. 1995); water MASER (microwave amplification by stimulated emission of radiation) emission (Greenhill et al. 1996; Herrnstein et al. 2005); optical/near-IR interferometry (Gravity Collaboration et al. 2018); direct imaging of the black hole shadow (Event Horizon Telescope Collaboration et al. 2019b,c); reverberation mapping (Blandford & McKee 1982); and using the polarization of the broad emission lines (Afanasiev & Popović 2015).

Indirect methods use observables that are tightly correlated with black hole mass. Such examples are the SMBH mass - bulge velocity dispersion relation $\mathcal{M}_{\mathrm{bh}} - \sigma_*$ (Gebhardt et al. 2000; Ferrarese et al. 2001; Ferrarese & Ford 2005); the SMBH mass - bulge luminosity relation $\mathcal{M}_{\mathrm{bh}} - L_{\mathrm{bulge}}$ (Kormendy & Richstone 1995); the BLR size -

luminosity (e.g. equation 1.5) relation $R_{\mathrm{BLR}} - L_{5100}$ (Kaspi et al. 2000; Bentz et al. 2013; Du et al. 2016, 2018; GRAVITY Collaboration et al. 2019).

We can also distinguish among "primary", "secondary", and even "tertiary" methods, based on the number of assumptions used, and on model dependence. For example, the reverberation mapping method is a direct method since it is based on observations of the gas that is moving around the SMBH, but it is a secondary method since it requires a previous calibration from some other method (Peterson 2014). The reverberation mapping method and the method using the polarization of broad emission lines are treated separately and more extensively in the next two sections. For a review of the methods for SMBH mass measurements, see Peterson (2014).

3.1   Reverberation mapping

AGNs are highly variable sources, typically on daily timescales. Reverberation mapping measures the time lag between the continuum flux and the emission lines of AGNs, knowing that line and continuum variations are strongly correlated. The time lag between the continuum and line variations provides an estimate of the photometric BLR radius. The formalism for this method was introduced by Blandford & McKee (1982). Reverberation mapping requires few assumptions (Peterson 2014):

1 The emission lines respond rapidly to continuum changes. The response time scales of individual clouds to changes in the ionizing flux are the recombination and ionization times. These are much shorter than the typical time scale for continuum variations.

2 The continuum emitting region is much smaller than the BLR, and can be considered as a point source.

3 The dynamical timescale of the BLR is much longer than the reverberation timescale, so the BLR structure and kinematics are constant over the duration of the reverberation monitoring program.

4 There is a known relationship between the variations of the ionizing continuum and of the observed UV or optical continuum.

A successful RM experiment provides two observables: a continuum light curve and an emission-line light curve (Fig. 3.1). Line flux and continuum flux are related via the

transfer function Ψ through a convolution:

$$F_l(v,t) = \int_{-\infty}^{\infty} \Psi(v,\tau) F_c(t-\tau)\,d\tau, \qquad (3.1)$$

where F_l is the flux integrated over the spectral boundaries of a given line, F_c is the continuum flux, typically at $5100\,\text{Å}$, and $\Psi(v,\tau)$ is the 2D transfer function depending on the BLR geometry, kinematics and the physics of the gas reprocessing the continuum radiation. Transfer function in general depends on velocity v since different BLR geometry will have different line response for a given v. Obtaining transfer functions is difficult since it requires a high-quality and well sampled spectra of AGNs, which are faint sources. A handful of objects have their 2D transfer function established (Netzer 2013), which makes it more convenient to use 1D transfer function $\Psi(\tau)$ assuming that Ψ does not depend on velocity. Time lag, that is a measure of the photometric radius, can be obtained by cross-correlating the line and the continuum flux. Assuming that the BLR dynamic is dominated by the SMBH, i.e. the BLR is virialized, we can obtain the SMBH mass as

$$\mathcal{M}_{\text{bh}} = f\left(\frac{\Delta V^2 c\tau}{G}\right), \qquad (3.2)$$

where ΔV is the line width and f is a dimensionless quantity called *virial factor* that accounts for everything that is unknown – the BLR geometry, kinematics and inclination, that is in principle different for different AGNs and it is expected to be of the order of unity. Virial factors can be obtained if there is another way of determining the SMBH mass, and commonly the $\mathcal{M}_{\text{bh}} - \sigma_*$ relation is being used. The standard value that is used in literature is $f = 5.5 \pm 1.9$ (Onken et al. 2004) or $f = 4.3 \pm 1.0$ (Grier et al. 2013) or $\log f = 0.05 \pm 0.12$ (Woo et al. 2015).

Much effort has been invested in the successful application of this method resulting in a vast literature (e.g. Netzer 2013; Peterson 2014, and references therein). The most reliable SMBH mass measurements using reverberation mapping has been performed for around sixty AGNs (Bentz & Katz 2015, online database[1]). However, an individual galaxy needs to be observed over and over for months, while distant AGNs require even several years of successful monitoring (Shen et al. 2016; Grier et al. 2017, 2019). Hydrogen Balmer lines are the most commonly used (Du & Wang 2019, and references therein), however, highly ionized broad emission lines like Mg II, C III] and C IV can also be used for AGNs at higher redshifts (Mejía-Restrepo et al. 2016). We use the
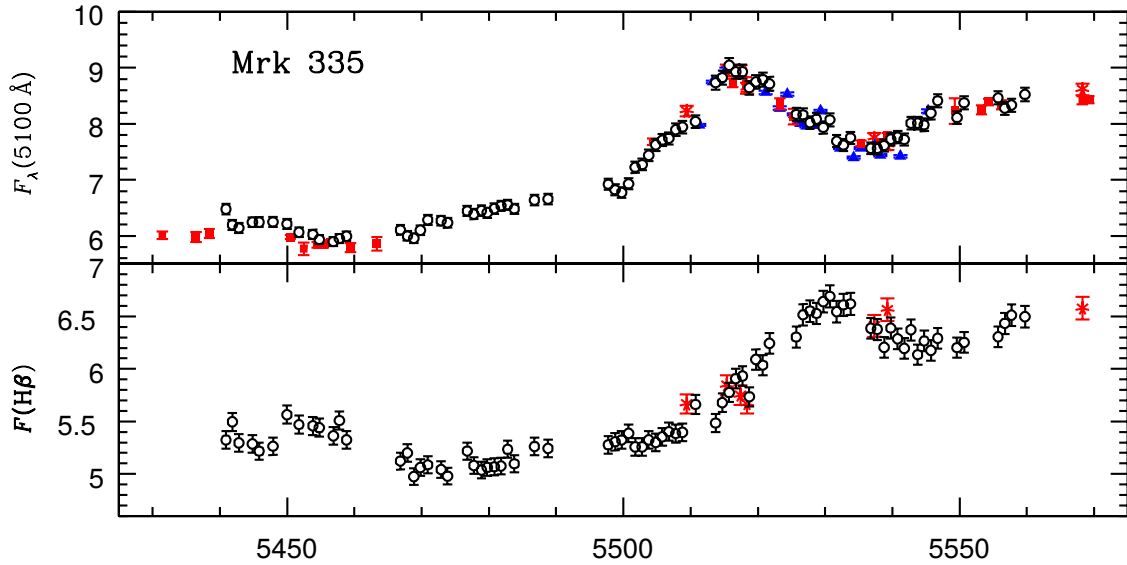
---

[1] http://www.astro.gsu.edu/AGNmass/

Figure 3.1: A 150 d light curves of the continuum flux at 5100 Å (top panel) and of the integrated Hβ flux (bottom panels) of the Sy 1 galaxy Mrk 335. The variations of Hβ are lagging by 13.9 ± 0.9 days the continuum flux. The continuum flux is in units of $10^{-15}\,\mathrm{erg\,s^{-1}\,cm^{-2}\,\text{Å}^{-1}}$; the line flux is in units of $10^{-13}\,\mathrm{erg\,s^{-1}\,cm^{-2}}$. Open black circles: observations from MDM Observatory; red asterisks represent spectra taken at CrAO; closed red squares: photometric observations from CrAO; closed blue triangles: photometric observations from the WISE Observatory. Credits: Grier et al. (2012).

SMBH mass values obtained this way as a reference for comparing results throughout this thesis.

Polarization reverberation mapping is another way to explore the size and geometry of the AGN central engine (Gaskell et al. 2012; Afanasiev et al. 2014). The time lag between the polarized and unpolarized flux is highly sensitive to the geometry of the scattering regions involved and may provide new way of resolving the innermost parts of AGNs (Rojas Lobos et al. 2018). Also, Songsheng & Wang (2018) have found the polarization virial factor $\log f_{\mathrm{pol}} \in [-0.65, -0.62]$, and found that it is more stable and less inclination dependent than the standard f.

3.2 SMBH mass measuring using the polarization of broad emission lines

This method assumes that equatorial scattering is the main mechanism for the polarization of the broad emission lines (Afanasiev & Popović 2015, hereafter AP15). We can

expect near-Keplerian motion of the emitting gas in the BLR (Gaskell 2009). Farther away, the central region is surrounded by a geometrically thick dusty torus with large radial optical depth (Krolik & Begelman 1988). The inner side of the torus is directly illuminated and we expect a large number of free electrons here. The inner wall of the torus thus acts as the scattering region (SR) for the equatorial scattering. The BLR is situated inside the SR which produces polarized broad lines and a characteristic change of polarization plane position angle φ across the line profile is expected (Smith et al. 2005). According to AP15, φ in the broad emission line is affected by the velocity field in the BLR and there is a specific linear relationship between $\log V$ and $\log(\tan\varphi)$ (Fig. 3.2, right panel). If the motion in the BLR is Keplerian, for the projected velocity in the plane of the scattering region, we can write (see Afanasiev et al. 2014, AP15):

$$V_{\text{i}} = V_{\text{i}}^{\text{rot}} \cos\theta = \sqrt{\frac{G\mathcal{M}_{\text{bh}}}{R_{\text{i}}}} \cos\theta \qquad (3.3)$$

where V_{i} is the rotational velocity of emitting gas, $\mathcal{M}_{\text{bh}}$ is the BH mass and R_{i} is the distance from the center of the disk, and θ is the angle between the disc and the plane of scattering (AP15). Superscript i denote the position of the i-th ring constituting the BLR. R_{i} can be connected with the corresponding polarization angle φ_{i} as $R_{\text{i}} = R_{\text{sc}} \tan\varphi_{\text{i}}$, where R_{sc} is the distance from the center to the SR (Fig. 3.2). When we substitute this into Eq. (3.3) and integrating over the disk, the velocity-angle dependence can be written as:

$$\log\frac{V_{\text{i}}}{c} = a - 0.5\log(\tan(\varphi_{\text{i}})), \qquad (3.4)$$

where c is the speed of light. The expected relation between velocity and φ is shown in Fig. 3.2 (right). The constant a is related to the black hole mass as

$$a = 0.5\log\frac{G\mathcal{M}_{\text{bh}}\cos^2\theta}{c^2 R_{\text{sc}}}. \qquad (3.5)$$

In the case of a thin SR (equatorial scattering region), a good approximation would be to take $\theta \sim 0$. In this case, the relation between velocities and φ does not depend on the inclination since the BLR is emitting nearly edge-on oriented line light to the SR. From the previous equation, the mass of the black hole can be calculated as

$$\mathcal{M}_{\text{bh}} = 1.78 \times 10^{2a+10}\frac{R_{\text{sc}}}{\cos^2\theta}M_{\odot} \approx 1.78 \times 10^{2a+10}R_{\text{sc}} \, [M_{\odot}], \qquad (3.6)$$
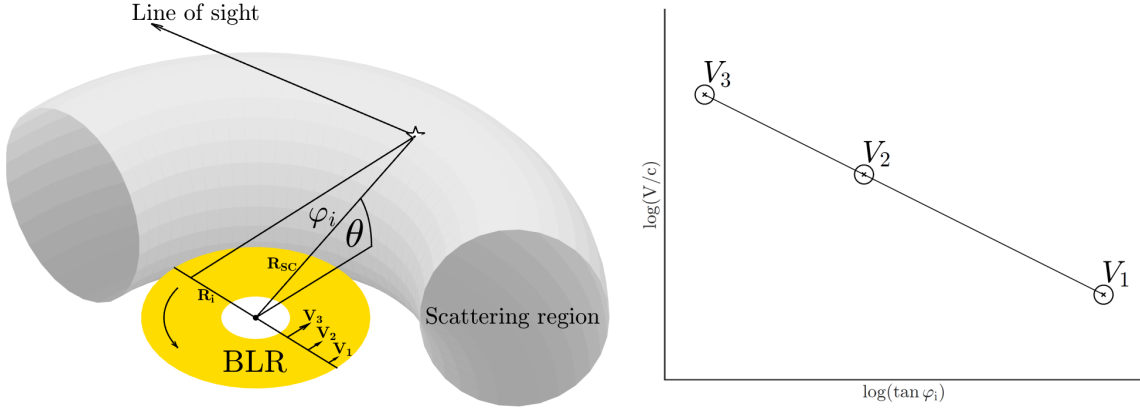
49

Figure 3.2: Schematic view of light scattered from the inner part of the torus (left). Expected relation between φ and velocity intensity (right). Credits: Savić et al. (2018)

or

$$\log \frac{\mathcal{M}_{\mathrm{bh}}}{M_\odot} = (10 + 2a) \log\left(1.78 R_{\mathrm{sc}}\right), \tag{3.7}$$

where R_{sc} is in light days. How does this method work in practice? From the observed φ it is necessary to subtract the continuum polarization position angle $\Delta\varphi = \varphi - \varphi_{\mathrm{c}}$. The next step is to perform a linear fit using both the red and blue parts of the line and apply equation 3.4 in order to obtain a (the y-axis intercept of the fitted line). The final step is to substitute a and R_{sc} in equation 3.7, which yields the measured $\mathcal{M}_{\mathrm{bh}}$. An example is shown for 3C 273 and NGC 4051 in Fig. 3.3.

This method provides results in a good agreement with the reverberation mapping method and offers a number of advantages. It requires only one epoch of observations and it is not telescope time consuming when compared to the reverberation mapping method. It can be applied to lines in different spectral ranges from near IR and optical (Balmer lines) to UV (Lyα, C III], C IV and Mg II), thus allowing black hole mass measurements for AGNs at different cosmological epochs (AP15). The virialization of the BLR is not a priori assumed, but it is reflected in the observed φ profile. However, this method requires the inner radius of the torus to be known; R_{sc} is often found using dust reverberation or some other scaling relations (AP15). In addition, this method can only be used for a rotating disk-like BLR; in the case where the BLR is dominated by radial motion, it cannot be used.

We also stress out that in this method, we consider only one scattering event per line photon and the contribution of multiple scattering events are not taken into account.
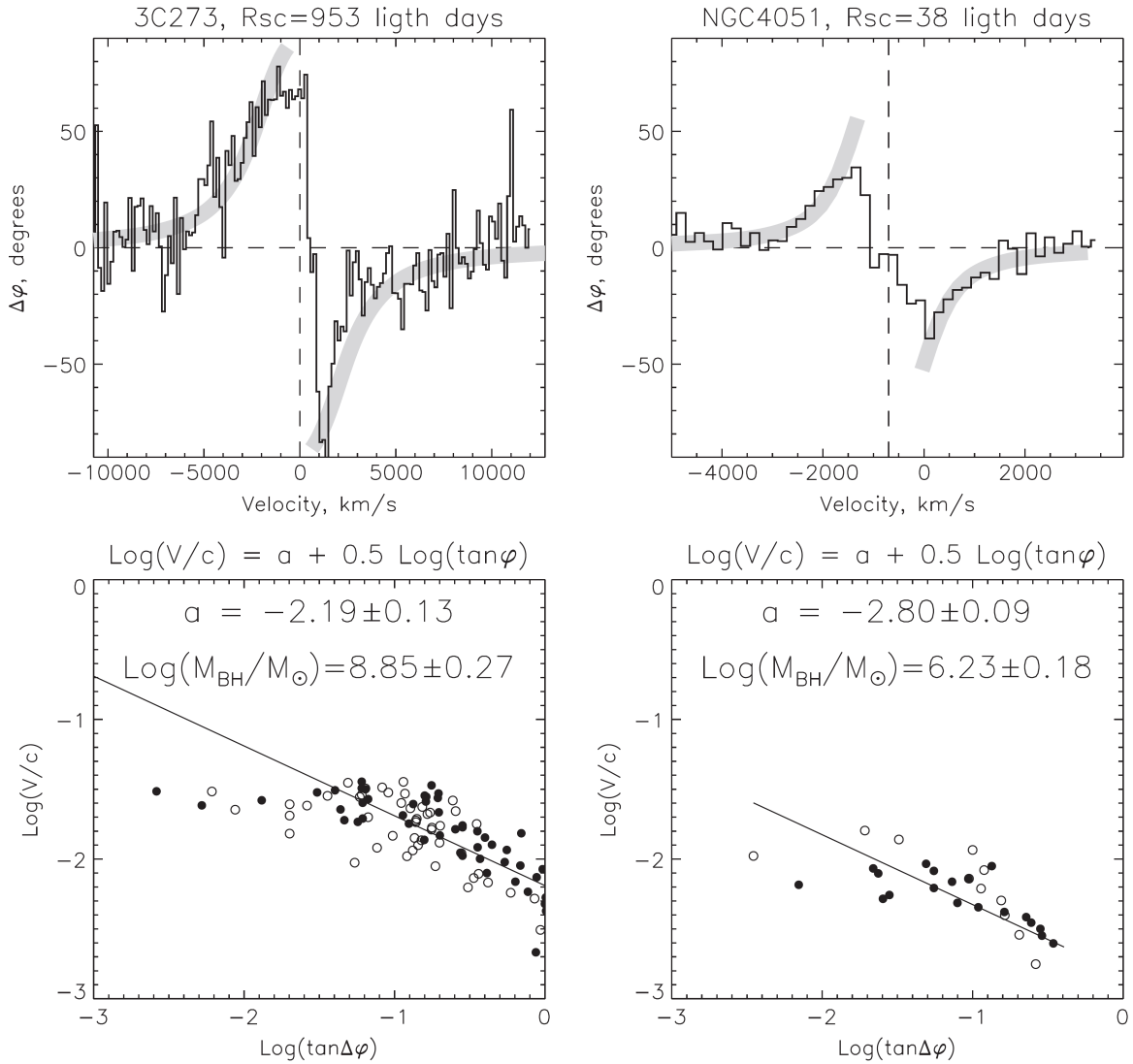
Figure 3.3: The observed continuum subtracted $\Delta\varphi = \varphi - \varphi_c$ (top panels) and $\log V$-$\log(\tan\varphi)$ relation (bottom panels) for 3C 273 (left panels) and NGC 4051 (right panels). The filled and open circles correspond to the blue and red part of the line respectively. Solid line represent the best fit. The gray curves in the upper panels trace the Keplerian motion. Credits: AP15.

Since polarization is very sensitive to kinematics and geometrical setup (Goosmann & Gaskell 2007), the full treatment of 3D radiative transfer with polarization is required to test this method. The major task of this work is to explore the possibilities and limitations of this method and to find in which conditions it can be used.

Chapter 4

Polarization formalism

4.1 Electromagnetic waves

The work by James Clerk Maxwell in the late 19th century have made it apparent that the light is electromagnetic in nature. In classical electrodynamics, light is described as a continuous transfer of energy in the form of electromagnetic waves, a conjecture directly verified in an experiment by Heinrich Hertz (1888). The presence of electric charges in space induces an electromagnetic field. It is represented by two vectors, $\vec{\mathbf{E}}$ and $\vec{\mathbf{B}}$, called the *electric vector* and *magnetic induction* respectively. The properties of $\vec{\mathbf{E}}$ and $\vec{\mathbf{B}}$ as well as how are they related is given by a set of partial differential equations (Maxwell's equation) that form the foundation of the classical electrodynamics. The equations in their differential form are:

$$\nabla \cdot \vec{\mathbf{E}} \quad = \quad \frac{\rho}{\epsilon_0}, \qquad\qquad \text{(Gauss's law)} \quad (4.1)$$

$$\nabla \cdot \vec{\mathbf{B}} \quad = \quad 0, \qquad\qquad \text{(Gauss's law)} \quad (4.2)$$

$$\nabla \times \vec{\mathbf{E}} \quad = \quad -\frac{\partial \vec{\mathbf{B}}}{\partial t}, \qquad\qquad \text{(Faraday's law)} \quad (4.3)$$

$$\nabla \times \vec{\mathbf{B}} \quad = \quad \mu_0 \left(\vec{\mathbf{j}} + \epsilon_0 \frac{\partial \vec{\mathbf{E}}}{\partial t} \right), \qquad \text{(Ampére's law)} \quad (4.4)$$

where ρ is the charge density, $\vec{\mathbf{j}}$ is current density, $\epsilon_0 \approx 8.854 \times 10^{-12}\,\mathrm{F\,m^{-1}}$ is the permittivity of free space and $\mu_0 \approx 1.257 \times 10^{-7}\,\mathrm{H\,m^{-1}}$ is the permeability of free

space[1]. The above equations are the "microscopic" version of Maxwell's equations or the so called Maxwell's equation in vacuum. The material medium is not built into the structure of the equations, but appears only in the charge and current terms. The so called Maxwell's equation in matter or Maxwell's "macroscopic" equation are similar and keep the same form. The equations above are coupled and very often they are difficult to solve. Certain analytical solutions exist for simplified cases e.g. far from the source in the absence of charges and currents. In this case Maxwell's equations take the form:

$$\nabla \cdot \vec{\mathbf{E}} = 0, \tag{4.5}$$

$$\nabla \cdot \vec{\mathbf{B}} = 0, \tag{4.6}$$

$$\nabla \times \vec{\mathbf{E}} = -\frac{\partial \vec{\mathbf{B}}}{\partial t}, \tag{4.7}$$

$$\nabla \times \vec{\mathbf{B}} = \mu_0 \epsilon_0 \frac{\partial \vec{\mathbf{E}}}{\partial t}. \tag{4.8}$$

By inspecting the previous equations, we can conclude that the time-varying electric field $\vec{\mathbf{E}}$ generates the magnetic field $\vec{\mathbf{B}}$ which is perpendicular everywhere to $\vec{\mathbf{E}}$-field, while in the same way, a time-varying field $\vec{\mathbf{B}}$ induces $\vec{\mathbf{E}}$-field which is perpendicular everywhere to the $\vec{\mathbf{B}}$-field. The fields $\vec{\mathbf{E}}$ and $\vec{\mathbf{B}}$ can be thus considered as a two aspects of a single phenomenon - *electromagnetic field*. The disturbance created by a moving charge continues to propagate in the form of electromagnetic waves. After a simple vector calculus procedure, which is described in almost every book in optics or classical electrodynamics (Goldstein 2003; Born & Wolf 2013; Hecht 2016), it can be shown that $\vec{\mathbf{E}}$ and $\vec{\mathbf{B}}$ each satisfy the wave equation:

$$\nabla^2 \vec{\mathbf{E}} = \mu_0 \epsilon_0 \frac{\partial^2 \vec{\mathbf{E}}}{\partial t^2}, \tag{4.9}$$

$$\nabla^2 \vec{\mathbf{B}} = \mu_0 \epsilon_0 \frac{\partial^2 \vec{\mathbf{B}}}{\partial t^2}, \tag{4.10}$$

which directly yields the phase velocity or the speed of light in vacuum:

$$c = \frac{1}{\sqrt{\mu_0 \epsilon_0}}, \tag{4.11}$$

---

[1]Recommended values of the fundamental physical constants from CODATA (Mohr et al. 2016)

One of the simplest solution to wave equation are plane waves. The electric field associated with plane wave is exclusively transverse. Any waveform can be expressed as an infinite sum of simple sine waves using Fourier series. Without any loss of generality, we limit our treatment only to harmonic waves. In general form, $\vec{\mathbf{E}}$-field for a monochromatic plane wave can be expressed in the form:

$$\vec{\mathbf{E}}\left(x,y,z,t\right) = \sum_{i=1}^{3} E_{0i} \cos\left(\omega t - \vec{k}\cdot\vec{r} + \alpha_i\right)\vec{e}_i, \tag{4.12}$$

where E_0 is the amplitude term, ω is the angular frequency, k is the wavenumber and $\vec{k}\cdot\vec{r} = k_x x + k_y y + k_z z$, α is the phase shift. The vector $\vec{e}_i$ is the unit vector in Cartesian coordinates which can take the values $\vec{e}_x$, $\vec{e}_y$, $\vec{e}_z$. The wavenumber can be expressed in term of wavelength as $k = 2\pi n/\lambda$, where λ is the wavelength in vacuum and n is the refractive index of the medium along the light propagation direction. From the wave equation, we can obtain the dispersion relation:

$$\frac{\omega^2}{c^2} = k_x^2 + k_y^2 + k_z^2, \tag{4.13}$$

which describes how ω and k are connected with the phase velocity. If we chose the preferred direction of propagation e.g. along the z-axis, and taking into account that $\vec{k}$ and $\vec{\mathbf{E}}$ are orthogonal in isotropic media, and substituting $k_x = k_y = 0$, we can obtain the simplified equations for the electric field components in the form:

$$E_x\left(z,t\right) = E_{0x} \cos\left(\omega t - kz + \alpha_x\right), \tag{4.14}$$

$$E_y\left(z,t\right) = E_{0y} \cos\left(\omega t - kz + \alpha_y\right), \tag{4.15}$$

$$E_z\left(z,t\right) = 0. \tag{4.16}$$

If we eliminate time dependence from the equations 4.15 and 4.16, we obtain the following equation:

$$\left(\frac{E_x}{E_{0x}}\right)^2 + \left(\frac{E_y}{E_{0y}}\right)^2 - 2\left(\frac{E_x}{E_{0x}}\right)\left(\frac{E_y}{E_{0y}}\right)\cos\alpha = \sin^2\alpha, \tag{4.17}$$

where $\alpha = \alpha_x - \alpha_y$ is the phase difference. The equation 4.17 is an equation of an ellipse rotated for an angle φ with the respect for the (E_x, E_y)-coordinate system (Fig.
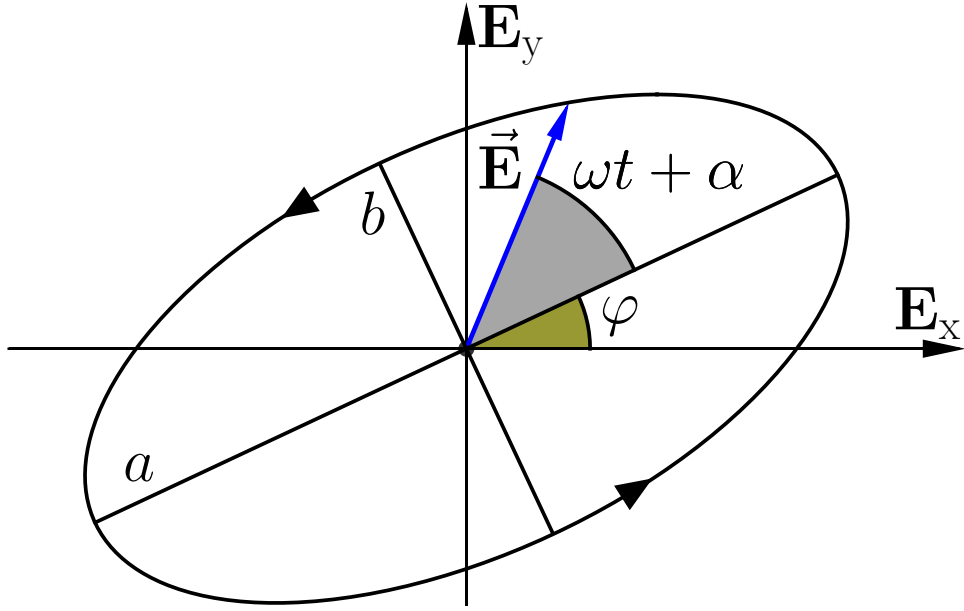
Figure 4.1: Elliptically polarized light. The tip of electric fields (blue arrow) sweeps an ellipse which is rotated by angle φ. Adapted from Hecht (2016).

4.1), where φ is given by:

$$\tan 2\varphi = \frac{2E_{0x}E_{0y}\cos\alpha}{E_{0x}^2 - E_{0y}^2}. \tag{4.18}$$

In other words, the tip of the electric field vector sweeps an ellipse in the direction depending on the sign of $\sin\alpha$. The most general representation of the plane electromagnetic wave is elliptically polarized light. The resultant electric-field vector $\vec{E}$ is rotating and changing magnitude in such way that the endpoint of $\vec{E}$ will trace out an ellipse in a fixed-space perpendicular to the direction of propagation. Both linear and circular light can be viewed as the special cases of elliptically polarized light. The period over which ellipse is traversing is inversely proportional to the wave frequency (i.e. roughly 10^{-15} s for optical domain) and is far too short to be detected since measurements made in practice are generally averages over comparatively long time intervals (Hecht 2016).

4.2 Jones calculus

The Jones formalism (Jones 1941, 1942) is a mathematical description of light in the form of phase and amplitude. Jones vectors are the two element vectors that describe the polarization state of light, and Jones 2×2 matrices describe optical elements. The

vectors are complex and describe the amplitude and phase of the light in the form:

$$\vec{\mathbf{J}}(t) = \begin{pmatrix} \vec{\mathbf{E}}_{\mathrm{x}}(t) \\ \vec{\mathbf{E}}_{\mathrm{y}}(t) \end{pmatrix}.$$ (4.19)

The two components of the Jones vector are orthogonal and represent the horizontal and vertical polarization states. Jones matrices are also complex and describe the action in both amplitude and phase of optical elements on a light beam. Jones matrices are in the form:

$$J = \begin{pmatrix} j_{xx} & j_{xy} \\ j_{yx} & j_{yy} \end{pmatrix},$$ (4.20)

where j_{ik}, $i, k = x, y$, are transforming elements. The four elements of the Jones matrix composes the transfer function from the input to the output Jones vector. If we denote $\vec{\mathbf{E}}$ as an incident and $\vec{\mathbf{E}}'$ as an emerging beam, we have:

$$\vec{\mathbf{J}}' = \begin{pmatrix} E'_{\mathrm{x}} \\ E'_{\mathrm{y}} \end{pmatrix} = \begin{pmatrix} j_{xx} & j_{xy} \\ j_{yx} & j_{yy} \end{pmatrix} \begin{pmatrix} E_{\mathrm{x}} \\ E_{\mathrm{y}} \end{pmatrix} = J\vec{\mathbf{J}}.$$ (4.21)

The effect of multiple optical components or the traversing medium can be described by the matrix product of Jones matrices for each of the components. The polarization state of the emerging light beam will be:

$$\vec{\mathbf{J}}' = J_n J_{n-1} \cdots J_2 J_1 \vec{\mathbf{J}},$$ (4.22)

where J_i is the Jones matrix for each optical component. The exact values of Jones matrices for ideal polarizer, retarder and rotator can be found in Goldstein (2003). Jones formalism is useful when knowledge of the phase is required e.g. for beam superposition in interferometers.

4.3 Stokes parameters

The polarization ellipse is applicable for describing the completely polarized light and it cannot be used to describe unpolarized or partially polarized light. The plane of polarization of unpolarized light fluctuates arbitrarily around the propagation direction, i.e., on average, there is no preferred direction of the polarization plane. Another limitation is the amplitude of the electric field varies with high frequency and cannot

be observed (except in the radio domain). These limitations require an alternative description of polarization in terms of observables, e.g. intensity. Stokes (1851) found that any polarization state can be completely described by four measurable quantities known as Stokes parameters. A time-average of the unobserved polarization ellipse leads to measurable observables. Time average of a given physical quantity is represented by the symbol $\langle \cdots \rangle$ and it is defined as:

$$\langle F(t) \rangle = \lim_{T \to \infty} \frac{1}{T} \int_0^T F(t) \, dt. \tag{4.23}$$

Since electric field is periodic, it is enough to take an average over one single period. If we perform time averaging of the equation 4.17, multiply it by four, add and subtract the quantity $E_{0x}^4 + E_{0y}^4$, and after a minor algebraic manipulation, we obtain the following equation:

$$\left(E_{0x}^2 + E_{0y}^2\right)^2 - \left(E_{0x}^2 - E_{0y}^2\right)^2 - \left(2E_{0x}E_{0y}\cos\alpha\right)^2 - \left(2E_{0x}E_{0y}\sin\alpha\right)^2 = 0. \tag{4.24}$$

Writing the quantities inside the parenthesis, we obtain Stokes parameters:

$$I \equiv S_0 = E_{0x}^2 + E_{0y}^2, \tag{4.25}$$

$$Q \equiv S_1 = E_{0x}^2 - E_{0y}^2, \tag{4.26}$$

$$U \equiv S_2 = 2E_{0x}E_{0y}\cos\alpha, \tag{4.27}$$

$$V \equiv S_3 = 2E_{0x}E_{0y}\sin\alpha. \tag{4.28}$$

These four equations represent Stokes polarization parameters for a plane wave. They are real and measurable quantities. Alternatively, Stokes parameters can be defined via complex notation in Cartesian and spherical coordinates as:

$$I = E_x E_x^* + E_y E_y^* \quad = E_\phi E_\phi^* + E_\vartheta E_\vartheta^*, \tag{4.29}$$

$$Q = E_x E_x^* - E_y E_y^* \quad = E_\phi E_\phi^* - E_\vartheta E_\vartheta^*, \tag{4.30}$$

$$U = E_x E_y^* + E_y E_x^* \quad = E_\phi E_\vartheta^* + E_\vartheta E_\phi^*, \tag{4.31}$$

$$V = i\left(E_x E_x^* - E_y E_y^*\right) = i\left(E_\phi E_\phi^* - E_\vartheta E_\vartheta^*\right), \tag{4.32}$$

where ϑ and ϕ are polar and azimuthal angles, and * denotes complex conjugation. The first Stokes parameter I is the total intensity of the light. The second parameter Q is
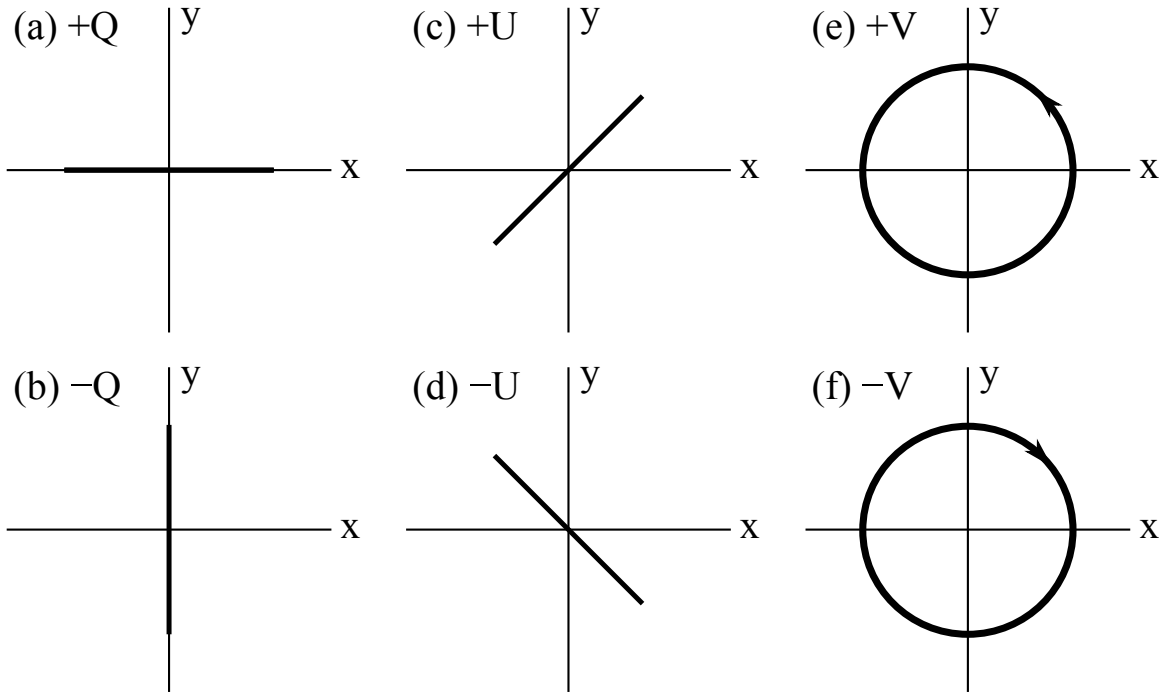
Figure 4.2: Polarization of light for different values of Stokes parameters. Horizontal linear polarization (a): $Q > 0$, $U = 0$, $V = 0$; vertical linear polarization (b): $Q < 0$, $U = 0$, $V = 0$; +45° linear polarization (c): $Q = 0$, $U > 0$, $V = 0$; −45° linear polarization (d): $Q = 0$, $U < 0$, $V = 0$; right circular polarization (e): $Q = 0$, $U = 0$, $V > 0$; left circular polarization (f): $Q = 0$, $U = 0$, $V < 0$. Credits: Kislat et al. (2015).

the amount of linear horizontal or linear vertical polarization. The third one describes the amount of linear +45° or −45° polarization. The fourth one describes left or right circular polarization. For a completely polarized light, the equation 4.24 becomes

$$I^2 = Q^2 + U^2 + V^2. \tag{4.33}$$

If we have partially polarized light, Stokes parameters become time-averaged quantities which for every state satisfy the following inequality:

$$I^2 \geq Q^2 + U^2 + V^2. \tag{4.34}$$

The degree of polarization is thus defined as:

$$p = \frac{\sqrt{Q^2 + U^2 + V^2}}{I}, \quad 0 \leq p \leq 1. \tag{4.35}$$

The polarization angle from the equation 4.18 becomes:

$$\tan 2\varphi = \frac{U}{Q}. \tag{4.36}$$

Similarly, the ellipticity angle χ is calculated as:

$$\tan 2\chi = \frac{V}{I}. \tag{4.37}$$

The four Stokes parameters can be represented as a column matrix in the form:

$$S = \begin{pmatrix} I \\ Q \\ U \\ V \end{pmatrix}. \tag{4.38}$$

The previous column matrix is called Stokes vector, however, mathematically, it is not a vector in a geometrical sense, but a column with four elements, which got accustomed to call it a vector. In Fig. 4.2, the polarization state for different values of the Stokes parameters is shown. The representation of polarization introduced by Stokes was perceived with little interest for nearly a century. Its importance was brought to the attention of the scientific community by Chandrasekhar in the late 1940s, who used the Stokes parameters to formulate the radiative transfer equations for different scattering mechanisms (Chandrasekhar 1960).

4.4 Mueller Calculus

Interaction of an optical beam with matter is almost always followed by a change of the beam polarization state. The polarization state can be changed by optical elements in the following ways:

1. Changing the amplitudes – polarizer

2. Changing the phase – retarder

3. Changing the direction of the orthogonal components – rotator

4. Transferring energy from polarized state to unpolarized state – depolarizer

These effects can be understood by analyzing the incident and the emerging Stokes parameters. For this purpose, an elegant procedure using matrix formalism was devised by Mueller and published by his student Parke III (1949). It deals with predicting the polarization state of an emergent wave after the interaction of the incident wave with the complex systems of polarizing elements. An incident beam S, after it interacts with the polarizing medium will emerge with a new set of Stokes parameters S'. Under the assumption that the S' can be expressed as a linear combination of the Stokes parameters of the incident beam, we obtain in matrix form:

$$\begin{pmatrix} I' \\ Q' \\ U' \\ V' \end{pmatrix} = \begin{pmatrix} m_{11} & m_{12} & m_{13} & m_{14} \\ m_{21} & m_{22} & m_{23} & m_{24} \\ m_{31} & m_{32} & m_{33} & m_{34} \\ m_{41} & m_{42} & m_{43} & m_{44} \end{pmatrix} \begin{pmatrix} I \\ Q \\ U \\ V \end{pmatrix}, \tag{4.39}$$

or simply

$$S' = MS, \tag{4.40}$$

where M is the Mueller matrix of size 4×4 and m_{ik}, $i, k = 1, 4$ are matrix elements. The values of matrix elements can be derived from the definition of Stokes parameters, but also from Jones matrix elements (Goldstein 2003). Similarly, for a train of optical elements, the Stokes parameters of the emerging beam can be calculated as:

$$S' = M_n M_{n-1} \cdots M_2 M_1 S, \tag{4.41}$$

where M_i is the Mueller matrix for the i-th optic element encountered. Measuring Stokes values can be performed in many ways: the quarter-wave retarder polarizer train, using circular polarizer (Goldstein 2003, for detailed derivation).

4.5 Polarization mechanisms

Polarization properties of AGNs can be understood by studying the basic physical processes causing it. The most important astrophysical processes concerning AGNs include light scattering and the presence of a magnetic field. For high energy photons,

inverse Compton and Compton scattering in the hot corona are the main polarization mechanisms. Additionally, the electric polarization vector will not stay parallel along the propagation direction in a curved spacetime. The general relativity effects lead to a rotation of the polarization vector when a beam passes through a strong gravitational field (Plebanski 1960) and this mechanism is important in considering the X-ray polarized radiation in the vicinity of a black hole (Dovčiak et al. 2004). The UV/optical continuum and line photons are prone to electron (Thomson or Rayleigh) scattering, both in polar and equatorial regions. Dust (Mie approximation) scattering can also significantly change the polarization state of incident radiation at all frequencies. Moreover dust alignment produces IR polarization seen as dichroic absorption or dichroic emission. The polarization angle exhibits a 90° shift between absorption and emission regime (Efstathiou et al. 1997). The wavelength at which the polarization angle flip occurs is very sensitive to the optical thickness of the torus. The study of dichroic emission and absorption can help in constraining the magnetic field for various torus geometries (Aitken et al. 2002). Finally, synchrotron emission from jets is highly variable and polarized (Rybicki & Lightman 1979) and provides insight in the magnetic field.

In this work, we focus on scattering mechanisms since our main assumption is that the origin of the optical broad line polarization in type-1 AGNs is due to equatorial scattering. For that purpose, we analyze the polarization properties of scattering mechanisms which are implemented in the radiative transfer code STOKES. These are Thomson, Rayleigh, Mie and Compton scattering. We start with the equations for the electric and magnetic field for accelerated charged particles. For velocities which are much lower than the speed of light, we have (Jackson 1962):

$$\vec{\mathbf{E}}\left(\vec{\mathbf{r}}, t\right) = \frac{q}{4\pi\epsilon_0 c^2} \left[\frac{\vec{\boldsymbol{n}}}{\kappa^3 R} \times \left\{ (\vec{\boldsymbol{n}} - \vec{\boldsymbol{v}}) \times \dot{\vec{\boldsymbol{v}}} \right\} \right], \tag{4.42}$$

where q is particle charge, $\vec{\boldsymbol{v}}$ is the charge velocity, $\kappa = 1 - \vec{\boldsymbol{n}} \cdot \vec{\boldsymbol{v}}$, n is the unit vector from the position of the charge towards the observed point, and R is the distance between the charge and the observing point. The geometry of the accelerated particle is shown in Fig. 4.3. Since the electric field is transversal, the application of spherical coordinates reduces the electric field into polar and azimuthal components. Many of the physical phenomena involving polarization are symmetric in ϕ, so for $\vec{\mathbf{E}}$ we have (Goldstein
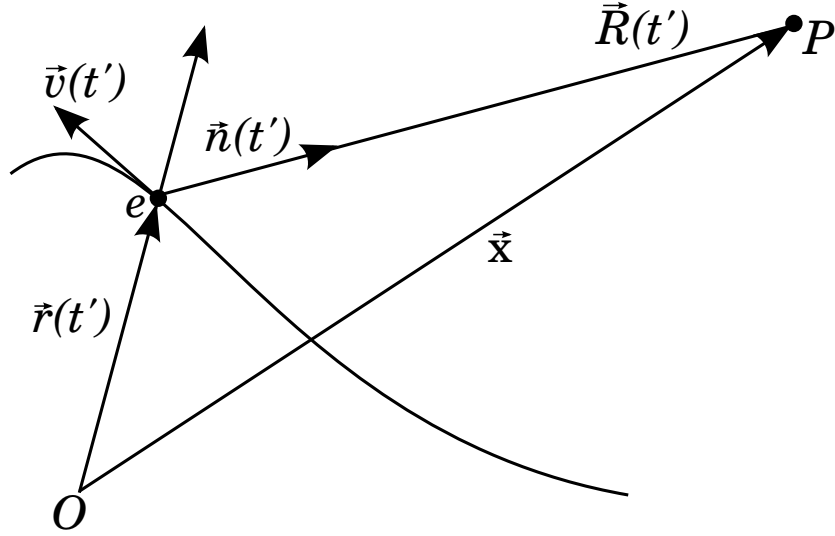
Figure 4.3: Radiation field from a moving charge at the observed point P. Adapted from Jackson (1962).

2003):

$$E_\vartheta = \frac{q}{4\pi\epsilon_0 c^2 R}\left(\ddot{x}\cos\vartheta - \ddot{z}\sin\vartheta\right), \tag{4.43}$$

$$E_\phi = \frac{q}{4\pi\epsilon_0 c^2 R}\,\ddot{y}. \tag{4.44}$$

The procedure for obtaining Stokes parameters and Mueller matrices is straightforward, but lengthy, so we skip the details. For polarization mechanisms involving the interaction of radiation with charged particle, it is required to obtain particle acceleration, and to apply equations 4.43–4.44. With known electric field, Stokes parameters can be obtained from the definition (equations 4.25–4.32). For detailed derivations, we refer to Rybicki & Lightman (1979).

4.5.1 Thomson scattering

Thomson scattering occurs when an incident field of radiation is being elastically scattered by free electron. The electron will be accelerated and will re-radiate the incident radiation. The re-radiation or scattering takes place in an extremely short time which is of the order of nanoseconds or less for optical waveband. If we consider an incident wave propagating in the z direction with known E_x and E_y field components (Fig. 4.4),

we have:

$$E_x(t) = E_{0x}e^{i(\omega t - kz + \alpha_x)}, \tag{4.45}$$

$$E_y(t) = E_{0y}e^{i(\omega t - kz + \alpha_y)}. \tag{4.46}$$

An electron acceleration is due to an electric field:

$$\ddot{x} = \frac{-e}{m_e}E_x(t), \tag{4.47}$$

$$\ddot{y} = \frac{-e}{m_e}E_y(t), \tag{4.48}$$

Where e is electron charge and m_e electron mass. With known acceleration, using equations 4.25–4.32, we obtain the electric field of the accelerated electron:

$$E_\vartheta(t) = \frac{-e^2}{4\pi\epsilon_0 m_e c^2 R}E_{0x}e^{i(\omega t - kz + \alpha_x)}\cos\vartheta, \tag{4.49}$$

$$E_\phi(t) = \frac{-e^2}{4\pi\epsilon_0 m_e c^2 R}E_{0y}e^{i(\omega t - kz + \alpha_y)}. \tag{4.50}$$

The Stokes parameters of the incident and the scattered radiation can be calculated from equations 4.25–4.32, and we obtain the following:

$$\begin{pmatrix} I' \\ Q' \\ U' \\ V' \end{pmatrix} = \frac{1}{2}\left(\frac{e^2}{4\pi\epsilon_0 m_e c^2 R}\right)^2 \begin{pmatrix} I(1 + \cos^2\vartheta) + Q\sin^2\vartheta \\ I\sin^2\vartheta + Q(1 + \cos^2\vartheta) \\ 2U\cos\vartheta \\ 2V\cos\vartheta. \end{pmatrix}, \tag{4.51}$$

from which we obtain Mueller matrix for Thomson scattering:

$$M_{\mathrm{T}} = \frac{1}{2}\left(\frac{e^2}{4\pi\epsilon_0 m_e c^2 R}\right)^2 \begin{pmatrix} 1 + \cos^2\vartheta & \sin^2\vartheta & 0 & 0 \\ \sin^2\vartheta & 1 + \cos^2\vartheta & 0 & 0 \\ 0 & 0 & 2\cos\vartheta & 0 \\ 0 & 0 & 0 & 2\cos\vartheta \end{pmatrix}. \tag{4.52}$$

The intensity of the scattered radiation is proportional to the intensity of the incident light, but it also depends on the contribution of the linear polarization Q of the incident beam 4.51. For unpolarized incident beam, the scattered radiation varies with the
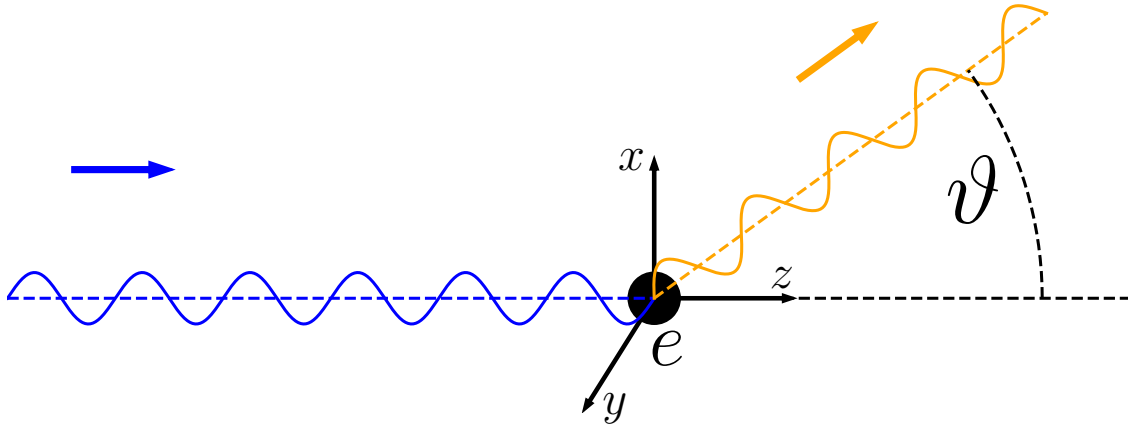
Figure 4.4: Schematic diagram for Thomson scattering. The incident photon (blue) is being scattered by a free electron at a deflection angle ϑ (orange). Wavelength of the incident and the scattered radiation is the same.

scattering angle as $I' \propto I(1+\cos^2\vartheta)$. The maximum intensity of the scattered radiation is along the axis of incident radiation and the minimum intensity is along the direction perpendicular to the incident beam direction. The degree of polarization depends on the polarization of the incident radiation and on the scattering angle. If the incident beam is completely linearly polarized, the scattered radiation is also completely polarized. For an unpolarized incident beam, the scattered radiation can be calculated as:

$$p = \frac{\sin^2\vartheta}{1 + \cos^2\vartheta}. \tag{4.53}$$

We see that for $\vartheta = 0$ (on-axis scattering), the degree of polarization is zero, whereas for $\vartheta = 90°$ (off-axis scattering) the degree of polarization is unity. This behavior of p is characteristic for all types of scattering. The ratio of the scattered to incident intensity can be used to derive the scattering differential cross-section:

$$\frac{d\sigma}{d\Omega} = \frac{1}{2}\left(\frac{e^2}{4\pi\epsilon_0 m_{\mathrm{e}}c^2}\right)^2 \frac{I\left(1+\cos^2\vartheta\right) + Q\sin^2\vartheta}{I}, \tag{4.54}$$

which for unpolarized radiation yields:

$$\frac{d\sigma}{d\Omega} = \frac{1}{2}\left(\frac{e^2}{4\pi\epsilon_0 m_{\mathrm{e}}c^2}\right)^2 \left(1+\cos^2\vartheta\right). \tag{4.55}$$

This equation is known as Thomson's formula for the scattering by free charges. The total cross section can be defined by integrating the previous equation of the whole 4π solid angle:

$$\sigma_{\mathrm{T}} = \int_{4\pi} \frac{d\sigma}{d\Omega} d\Omega = \frac{8\pi}{3} \left(\frac{e^2}{4\pi\epsilon_0 m_{\mathrm{e}}c^2} \right)^2 = 6.652 \times 10^{-29}\,\mathrm{m}^2. \tag{4.56}$$

An important result for Thomson scattering is that it does not depend on the frequency of the incident radiation. However, this is only valid at low frequencies (UV and optical). Relativistic effects become important when the the photon energy $h\nu$ is comparable with, or larger than the particle rest energy mc^2. Thomson scattering will be the dominant scattering mechanisms we use in the radiative transfer modeling of the equatorial scattering in AGNs.

4.5.2 Rayleigh scattering

Rayleigh scattering occurs when light is scattered by bound electrons within atoms and molecules. The incident radiation acts on electrons within a particle, causing them to oscillate with the same frequency. Electrons thus becomes small radiating dipoles which reprocess the incident radiation. The equation of motion for the bound electron is:

$$m_{\mathrm{e}}\ddot{\vec{\mathbf{r}}} + k\vec{\mathbf{r}} = -e\vec{\mathbf{E}}, \tag{4.57}$$

where k is positive constant related with angular frequency $\omega_0 = (k/m_{\mathrm{e}})^{1/2}$. If we consider again that the incident wave is propagating in the z direction, after solving the equation of motion and applying equations 4.25–4.32, we obtain the electric field of the scattered radiation as:

$$E_\vartheta(t) = \frac{-e^2\omega^2}{4\pi\epsilon_0 m_{\mathrm{e}}c^2 R\left(\omega^2 - \omega_0^2\right)} E_{0\mathrm{x}} e^{i(\omega t - kz + \alpha_{\mathrm{x}})} \cos\vartheta, \tag{4.58}$$

$$E_\phi(t) = \frac{-e^2\omega^2}{4\pi\epsilon_0 m_{\mathrm{e}}c^2 R\left(\omega^2 - \omega_0^2\right)} E_{0\mathrm{x}} e^{i(\omega t - kz + \alpha_{\mathrm{y}})}. \tag{4.59}$$

We find the Stokes parameter to be:

$$\begin{pmatrix} I' \\ Q' \\ U' \\ V' \end{pmatrix} = \frac{1}{2} \left(\frac{e^2}{4\pi\epsilon_0 m_e c^2 R \left(\omega^2 - \omega_0^2 \right)} \right)^2 \omega^4 \begin{pmatrix} I \left(1 + \cos^2 \vartheta \right) + Q \sin^2 \vartheta \\ I \sin^2 \vartheta + Q \left(1 + \cos^2 \vartheta \right) \\ 2U \cos \vartheta \\ 2V \cos \vartheta. \end{pmatrix}. \qquad (4.60)$$

This is very similar to Thomson scattering, except that for a bound electron $(\omega \ll \omega_0)$, the scattering intensity is proportional to ω^4 or λ^{-4}. As the wavelength decreases from red to blue, the intensity of scattered light increases. Rayleigh scattering accounts for the blue sky. The polarization behavior is similar to the Thomson scattering case. The total scattering cross section is wavelength dependent:

$$\sigma_{\mathrm{R}} = \int_{4\pi} \frac{d\sigma_{\mathrm{R}}}{d\Omega} d\Omega = \frac{8\pi}{3} \left(\frac{e^2}{4\pi\epsilon_0 m_e c^2} \right)^2 \left(\frac{\omega}{\omega_0} \right)^4 = \sigma_{\mathrm{T}} \left(\frac{\omega}{\omega_0} \right)^4. \qquad (4.61)$$

Rayleigh scattering holds for non-relativistic particles with sizes much smaller than the wavelength.

4.5.3   Mie scattering

Very often, the size of the scattering particle is similar or larger than the wavelength of the incident radiation, e.g. dust scattering. In this case, another approach is required for calculating the polarization properties of the scattered radiation. Naturally, the simplest case is when the scattering particle is a homogeneous sphere with a constant index of refraction – Mie scattering. The formal solution of this problem requires solving Maxwell's equation, and is rather lengthy and cumbersome. Here we present Mueller matrix without derivation, and focus on a qualitative analysis of results which have been well known in the literature. For a full and detailed derivation, we refer to Bohren & Huffman (1983). The relation between the scattered and the incident Stokes parameters is:

$$\begin{pmatrix} I' \\ Q' \\ U' \\ V' \end{pmatrix} = \frac{k^2}{r^2} \begin{pmatrix} S_{11} & S_{12} & 0 & 0 \\ S_{12} & S_{11} & 0 & 0 \\ 0 & 0 & S_{33} & S_{34} \\ 0 & 0 & -S_{34} & S_{33} \end{pmatrix} \begin{pmatrix} I \\ Q \\ U \\ V \end{pmatrix}, \qquad (4.62)$$
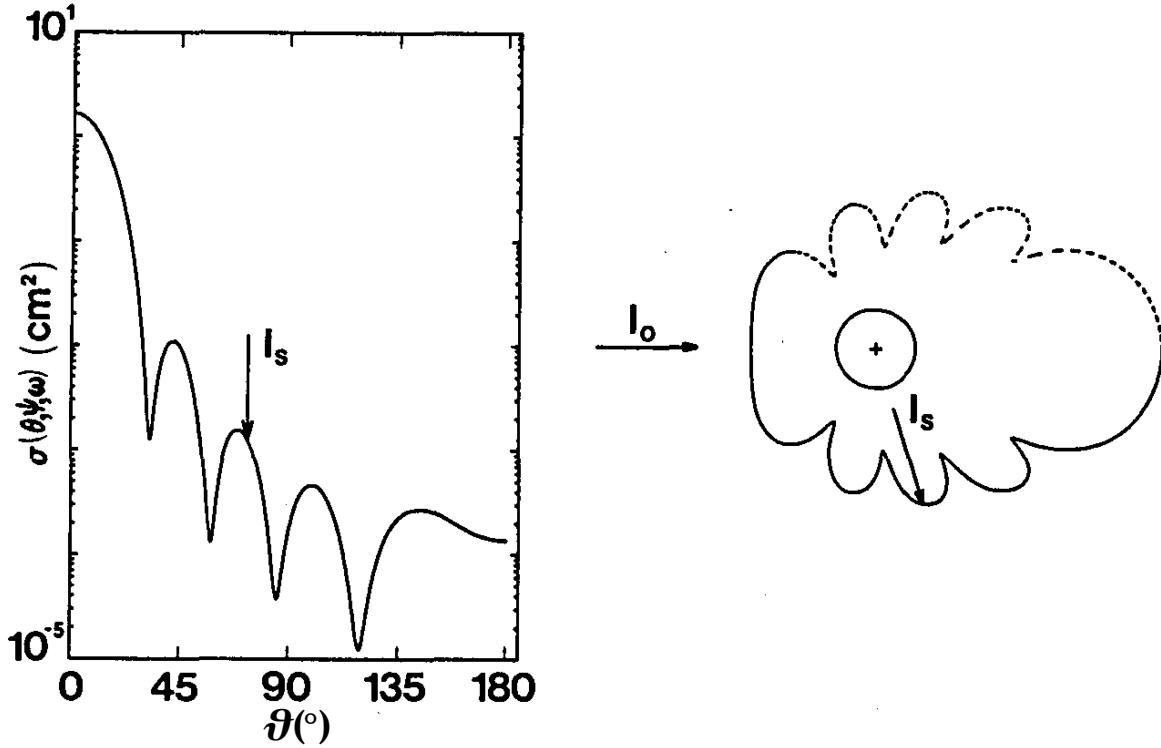
Figure 4.5: Scattering cross section σ_{Mie} as a function of polar scattering angle for a sphere of volume $1\,\mu m^3$, $\lambda = 0.5\,\mu m$, and refraction index $n = 1.05$ (Latimer et al. 1978). Cartesian plot (left) and semilog polar plot (right). Arrows indicate the incident beam and a scattered beam at $74°$. Credits: Latimer et al. (1978).

Only three of these matrix elements are independent: $S_{11}^2 = S_{12}^2 + S_{33}^2 + S_{34}^2$. If the incident wave is completely polarized and parallel to the scattering plane, the scattered wave will also be completely parallel to the scattering plane. This is the same for a completely polarized plane wave perpendicular to the scattering plane. For any other orientation of the completely polarized incident wave, the scattered radiation will be elliptically polarized. Mie scattering strongly depends on inclination and forward scattering is dominantly preferred (Latimer et al. 1978). For a high refractive index, scattering is enhanced in all direction. In Fig. 4.5, the differential cross section is shown as a function of scattering angle ϑ. Mie theory provides a first-order description of scattering due to non-spherical particles such as dust in the interstellar medium. Dust represents around $1\,\%$ of the total ISM mass (Zasov & Postnov 2006), and has a huge impact on observations, especially in UV and optical bands. Mie scattering on dust

absorbs a large fraction of the incident radiation, which heats dust grains. Dust grains reradiate energy in IR in a form of unpolarized emission.

4.5.4   Compton scattering

Compton scattering is inelastic scattering of high energy photon by an electron. Part of the photon energy and impulse is transfered to the electron depending on the scattering angle. The energy of the scattered photon E'_γ is depending only on the incident energy E_γ and the scattering angle as:

$$\frac{E'_\gamma}{E_\gamma} = \frac{1}{1 + \dfrac{E_\gamma}{m_\mathrm{e}c^2}(1 - \cos\vartheta)} = P(E_\gamma, \vartheta), \tag{4.63}$$

where $P(E_\gamma, \vartheta)$ is photon ratio before and after the collision. The explicit form of Mueller matrix for Compton scattering has been obtained by Wightman (1948) and Fano (1949). Full derivation requires the application of quantum electrodynamic. The relation between the incident and the scatter photon is:

$$\begin{pmatrix} I' \\ Q' \\ U' \\ V' \end{pmatrix} = \frac{1}{2}\left(\frac{e^2}{4\pi\epsilon_0 m_\mathrm{e}c^2}\right)^2 \times$$

$$\times \begin{pmatrix} 1+\cos^2\vartheta+(k-k')(1-\cos\vartheta) & \sin^2\vartheta & 0 & (1-\cos\vartheta)(\vec{\mathbf{k}}\cos\vartheta+\vec{\mathbf{k}'})\cdot\vec{\mathbf{S}} \\ \sin^2\vartheta & 1+\cos^2\vartheta & 0 & (1-\cos\vartheta)\vec{\mathbf{k}'}\times\vec{\mathbf{n}}\cdot\vec{\mathbf{k}}\times\vec{\mathbf{S}} \\ 0 & 0 & 2\cos\vartheta & (1-\cos\vartheta)\vec{\mathbf{k}}\times\vec{\mathbf{n}}\cdot\vec{\mathbf{S}} \\ (1-\cos\vartheta)(\vec{\mathbf{k}}\cos\vartheta+\vec{\mathbf{k}'})\cdot\vec{\mathbf{S}} & (1-\cos\vartheta)\vec{\mathbf{k}'}\times\vec{\mathbf{n}}\cdot\vec{\mathbf{k}}\times\vec{\mathbf{S}} & (1-\cos\vartheta)\vec{\mathbf{k}}\times\vec{\mathbf{n}}\cdot\vec{\mathbf{S}} & 2\cos\vartheta+(k-k')(1-\cos\vartheta)\cos\vartheta \end{pmatrix}\begin{pmatrix} I \\ Q \\ U \\ V \end{pmatrix}, \tag{4.64}$$

where $\vec{\mathbf{n}}$ and $\vec{\mathbf{n}}'$ are the directions of the incident and scattered photon, $\vec{\mathbf{k}}$ and $\vec{\mathbf{k}'}$ are momenta of the incident and scattered photon expressed in units of $m_\mathrm{e}c$, $\vec{\mathbf{S}}$ is the initial spin of the electron. The non-diagonal elements in the lower and right edge of the matrix represent the effects of elliptical or circular polarization. Those elements

average out when radiation is being scattered by electrons of different spin orientation. In that case, no elliptical polarization arises unless the incident radiation is elliptically polarized. The differential cross-section for unpolarized incident radiation is:

$$\frac{d\sigma_{\mathrm{C}}}{d\Omega} = \frac{1}{2} \left(\frac{e^2}{4\pi\epsilon_0 m_{\mathrm{e}} c^2} \right)^2 P\left(E_\gamma, \vartheta\right)^2 \left[P(E_\gamma, \vartheta) + P(E_\gamma, \vartheta)^{-1} + \cos^2\vartheta - 1 \right], \qquad (4.65)$$

which is known as the Klein & Nishina (1929) formula. The cross-section integrated over solid angle tends to the Thomson scattering cross-section for photon energies much smaller than the electron rest mass energy. For higher energies, when $E_\gamma / m_{\mathrm{e}} c^2 \gg 1$, we have:

$$\sigma_{\mathrm{C}} \propto \frac{3\sigma_{\mathrm{T}}}{x} \ll \sigma_{\mathrm{T}}, \qquad (4.66)$$

where $x = E_\gamma / m_{\mathrm{e}} c^2$. High energy photons may pass without interaction, and if scattered, on-axis direction is strongly preferred.

Chapter 5

Radiative transfer

Transport of radiation through the surrounding media is one of the most fundamental process in the universe. Before reaching the observer, photons coming from the radiation source interact with matter (atoms, ions, molecules and electrons). The observed spectral energy distribution is determined by the physical properties of the media and it can give us information on the source as well as insights on the physical processes that are present between the source and the observer. Properties of radiation depend on the propagating media, but simultaneously, the same media is affected by radiation. The observed spectrum is finally the product of interaction between the radiation and the media with the contribution of other physical phenomena e.g. presence of magnetic fields, rotation, turbulence.

The radiation field is in general case described by the specific intensity $I(\vec{\mathbf{r}}, \vec{\mathbf{n}}, \nu, t)$ defined as

$$I(\vec{\mathbf{r}}, \vec{\mathbf{n}}, \nu, t) = \frac{dE_\nu}{da \cos \vartheta \, d\nu \, d\Omega \, dt},$$ (5.1)

which describes the amount of energy dE_ν flowing through an area da located at $\vec{\mathbf{r}}$ per unit frequency $d\nu$ per unit time dt per unit solid angle $d\Omega$ around the direction $\vec{\mathbf{n}}$ that forms an angle ϑ with the normal surface (Mihalas 1978). The typical convention for indicating specific intensity per unit frequency or unit wavelength uses subscript I_ν or I_λ respectively. We adopt the per unit frequency convention. In its general form, the continuum radiation transfer equation (RTE) can be written as:

$$\left(\frac{1}{c} \frac{\partial}{\partial t} + \vec{\mathbf{n}} \cdot \nabla \right) I_\nu(\vec{\mathbf{r}}, \vec{\mathbf{n}}, t) = -\kappa_\nu(\vec{\mathbf{r}}, \vec{\mathbf{n}}, t) \rho(\vec{\mathbf{r}}) I_\nu(\vec{\mathbf{r}}, \vec{\mathbf{n}}, t) + j_\nu(\vec{\mathbf{r}}, \vec{\mathbf{n}}, t),$$ (5.2)

where $\kappa_\nu(\vec{r}, \vec{n}, t)$ is an absorption coefficient per unit mass, $\rho(\vec{r})$ is the mass density, and $j_\nu(\vec{r}, \vec{n}, t)$ is the mass emission coefficient. The left-hand side of this equation represents the change of intensity along the path determined by the position $\vec{r}$ and the propagation direction $\vec{n}$. The first term on the right-hand side represents the loss of energy due to radiation interaction with matter. The second term on the right-hand side represents the possible existence of an additional radiation source at $\vec{r}$ radiating in direction $\vec{n}$. In a stationary case, the time derivative vanishes, and if we use the path distance s along the direction defined by $\vec{n}$ and a position $\vec{r}$, we obtain:

$$\frac{dI_\nu(s)}{ds} = -\kappa_\nu(s)\rho(s)I_\nu(s) + j_\nu(s). \tag{5.3}$$

If the source term j does not depend on I, we have a simple first-order differential equation which can be solved by integrating along the line of sight, obtaining the formal solution (Steinacker et al. 2013):

$$I_{\mathrm{s}} = \int_{-\infty}^{s} j_\nu(s')e^{-\tau_\nu(s', s)}ds', \tag{5.4}$$

where the optical depth τ_ν between two points is defined as:

$$\tau_\nu(s_1, s_2) = \int_{s_1}^{s_2} \kappa_\nu(s)\rho(s)\, ds \tag{5.5}$$

The intensity at any position s along the path results from the contribution of all interior points s' along the path, but accounting for extinction from the encountered matter. The emission coefficient includes every process than can add up to the radiation field e.g. stellar emission, AGN radiation, Brehmsstrahlung, etc. Absorption is a process in which the incoming radiation is being converted into internal energy. When scattering is taken into account, the complexity of the RTE is increased. Scattering, together with absorption removes radiation from the beam and emits it in another direction. Scattering is characterized by the scattering phase function $\Phi_\nu(\vec{n}, \vec{n}', \vec{r})$, which describes the probability of the incident photon propagating in the direction $\vec{n}'$ will be scattered at the position $\vec{r}$ with a new direction $\vec{n}$. The phase function is normalized via solid angle in a way that

$$\int_{4\pi} \Phi_\nu(\vec{n}, \vec{n}', \vec{r})\, d\Omega' = \int_{4\pi} \Phi_\nu(\vec{n}, \vec{n}', \vec{r})\, d\Omega = 1. \tag{5.6}$$

This is true only in the case of elastic scattering; otherwise, as e.g. in the case of Compton scattering, there is a frequency shift that is not captured in equation 5.6. With scattering included, the RTE becomes:

$$\frac{dI_\nu(\vec{\mathbf{r}}, \vec{\mathbf{n}})}{ds} = - \kappa_{\nu,\text{ext}}(\vec{\mathbf{r}})\rho(\vec{\mathbf{r}})I_\nu(\vec{\mathbf{r}}, \vec{\mathbf{n}}) + j_\nu(\vec{\mathbf{r}}, \vec{\mathbf{n}})$$
$$+ \kappa_{\nu,\text{sca}}(\vec{\mathbf{r}})\rho(\vec{\mathbf{r}}) \int_{4\pi} \Phi_\nu(\vec{\mathbf{n}}, \vec{\mathbf{n}}', \vec{\mathbf{r}})I_\nu(\vec{\mathbf{r}}, \vec{\mathbf{n}}')d\Omega', \tag{5.7}$$

where the extinction coefficient is separated into absorption and scattering $\kappa_{\nu,\text{ext}} = \kappa_{\nu,\text{abs}} + \kappa_{\nu,\text{sca}}$. The RTE is an integro-differential equation in which radiation at different locations is coupled with radiation at all directions.

A complete description of the radiation field is obtained when polarization is also taken into account. Applying the same formalism for the Stokes column vector S, we obtain the polarized RTE

$$\frac{dS_\nu(\vec{\mathbf{r}}, \vec{\mathbf{n}})}{ds} = - \kappa_{\nu,\text{ext}}(\vec{\mathbf{r}})\rho(\vec{\mathbf{r}})S_\nu(\vec{\mathbf{r}}, \vec{\mathbf{n}}) + \boldsymbol{j}_\nu(\vec{\mathbf{r}}, \vec{\mathbf{n}})$$
$$+ \kappa_{\nu,\text{sca}}(\vec{\mathbf{r}})\rho(\vec{\mathbf{r}}) \int_{4\pi} M_\nu(\vec{\mathbf{n}}, \vec{\mathbf{n}}', \vec{\mathbf{r}})S_\nu(\vec{\mathbf{r}}, \vec{\mathbf{n}}')d\Omega', \tag{5.8}$$

which is a set of four coupled scalar equations. Intensity is substituted by the Stokes column vector and the phase function is substituted by the Mueller matrix M. The emission coefficient $\boldsymbol{j}_\nu$ now accounts for the contribution of polarized radiation.

The complexity of RTE is further increased when line transitions are included, which requires accounting for absorption, spontaneous and stimulated emission. When dust emission is taken into account, additional source term will be present, which often depends in a nonlinear way on the intensity of radiation itself. A widely used assumption is that the dust grains are in thermal equilibrium with the local interstellar radiation field.

In general, no analytic solution exists for stationary 3D polarized RTEs. A common approach is to apply numerical methods via discretization of the physical processes. This includes 3 spatial coordinates, 2 coordinates representing the direction and 1 wavelength coordinate, resulting in a 6D integro-differential equation. In a stationary case, the radiation field needs to be determined in all directions, at any spatial location, and for each wavelength. The radiative transfer problem is nonlocal in space, direction of propagation and wavelength. The thermal source term is nonlinearly coupled to a scattering integral, making it difficult to solve such high-dimensional nonlinear, nonlocal

problem. Therefore, a 3D line and dust radiative transfer is one of the major challenges in computational astrophysics requiring high computing power and memory at disposal.

Various methods with different approach for solving RTE have been widely studied. Some use purely discretization approach which transforms the RTE into a system of algebraic equations that can be solved numerically (Feautrier 1964); iterative procedures such as Λ-iteration (e.g. Atanacković-Vukmanović et al. 1997); ray tracing methods (e.g. Natale et al. 2014) and Monte Carlo (MC) methods (Steinacker et al. 2013, and references therein).

5.1 Monte Carlo radiative transfer

Monte Carlo method was invented in the 1940s by Stanislaw Ulam and John von Neumann for studying neutron transport (Whitney 2011). It is a probabilistic method which simulate the propagation of individual photon packets through a given medium. Photons interact with matter in a probabilistic way such that every interaction (e.g. scattering, absorption) is defined by its own cross section. The fundamental principle of Monte Carlo methods is sampling from probability density functions (PDFs). In order to sample a quantity x_0 from a given PDF f, it is necessary to invert the cumulative distribution function (CDF) F. In the one-dimensional case, we have:

$$F(x_0) = \frac{\displaystyle\int_{-\infty}^{x_0} f(x)\,dx}{\displaystyle\int_{-\infty}^{\infty} f(x)\,dx}, \tag{5.9}$$

where $F(x_0)$ ranges between 0 to 1 uniformly. In order to sample a random variable x_0, it is enough to uniformly sample random numbers from 0 to 1, and invert the previous equation in order to obtain x_0.

If we consider the interaction of an incident beam of light with a homogeneous distribution of scatterers and absorbers where no sources of radiation are present, and if we ignore scattering back to the beam, we obtain the simplified RTE:

$$\frac{dI_\nu}{ds} = -\kappa_\nu \rho I_\nu. \tag{5.10}$$

This can be solved analytically, obtaining a well known law of light attenuation for a given optical depth:

$$I_\nu = I_\nu(0)e^{-\kappa_\nu \rho s} = I_\nu(0)e^{-\tau}, \tag{5.11}$$

where $I_\nu(0)$ is the intensity of incident light before interaction. The fraction of photon scattered or absorbed per unit length is $\kappa_\nu \rho$, which is called volume absorption coefficient. It is related to concentration and cross section as $\kappa_\nu \rho = \sigma_\nu n$. The volume absorption coefficient is related to mean free path as $\bar{s}_\nu = 1/\kappa_\nu \rho$, which is the average photon travel distance between two interactions. The probability of a photon traveling a distance L with no interaction with matter is

$$P(L) = e^{-\tau}. \tag{5.12}$$

Large optical depths yield low photon mean free paths and many interactions. On the contrary, for low optical depths, radiation can pass through matter almost without interaction. After the photon has traveled some distance, it can be scattered or absorbed. The probability that the photon will be scattered is defined by the albedo:

$$a_\nu = \frac{n_s \sigma_{\nu,s}}{n_s \sigma_{\nu,s} + n_a \sigma_{\nu,a}}, \tag{5.13}$$

where n_s and n_a are the concentration of scatterers and absorbers respectively, and $\sigma_{\nu,s}$ and $\sigma_{\nu,a}$ are the cross-sections for scattering and absorption respectively. A photon can be absorbed in different ways (line or continuum absorption, resonant scattering, etc.) and re-emitted at another frequency and direction, or it can be thermalized. When a photon is scattered, its direction and frequency are determined by the scattering function Φ_ν for a given type of scattering.

For simulating photon interactions, we rely on random number generators for sampling optical depths and scattering angles. For high numbers of photons, e.g. 10^8 per wavelength bin, the generation of such long series may show periodicities. Algorithms that pass tests for randomness and with high periodicity such as Mersenne Twister are commonly invoked (Matsumoto & Nishimura 1998). The photon number in each direction bin obeys Poisson statistics. The standard deviation in Monte Carlo simulations is proportional to the square root of the number of samples (Gordon et al. 2001). The errors are minimized when PDFs are sampled exactly. Naive Monte Carlo methods are inefficient in general when dealing with optically thin or optically very thick regions. For that purpose, many accelerating methods have been developed such as e.g. biased

emission (biased sampling in the desired direction) and forced scattering (photon propagation length is sampled to guarantee scattering), and many others (Steinacker et al. 2013).

Monte Carlo methods for dealing with radiative transfer are commonly used. Mathematical details and practical implementations of Monte Carlo radiative transfer have been widely discussed in literature (Baes et al. 2011, and references therein). A list of published 3D radiative transfer codes with their main application can be found in Steinacker et al. (2013). The most widely used codes for studying AGNs are STOKES (Goosmann & Gaskell 2007) and SKIRT (Camps & Baes 2015; Baes & Camps 2015). The performance of various codes with their benchmarks is discussed in details by Camps et al. (2015); Gordon et al. (2017). The lack of agreement between the codes for the scattered radiation at high optical depths suggests that one should be cautious when interpreting those results. Overall conclusion is that scattering at high optical depth is still a challenging task in computational astrophysics.

5.2   STOKES code

STOKES is a C++ radiative transfer code originally developed by René W. Goosmann (2007) for studying scattering induced optical polarization in AGNs. The code uses the basic Monte Carlo method and follows the photon journey from the creation inside an emitting region, through multiple scattering events, until they are either absorbed or they reach a distant observer (Fig. 5.1).

Photons are generated inside the emitting regions of various geometries: point source, slab, cylinder, sphere and double-cone. The continuum radiation is defined by a power-law in the form $F_\nu \propto \nu^{-\alpha}$. Spectral lines have Lorentz profiles where intensity is normalized as a fraction of total continuum radiation and line width is user-defined. Stokes parameter of emitted photons are always set to represent completely unpolarized light. The code operates in the UV/optical 1400–10 000 Å waveband and in X-rays in the range 0.8–300 keV.

Scattering and absorption can occur in a finite pre-defined regions of different morphologies: toroidal, spherical and biconical. Scattering regions are filled either with dust or free electrons with a user-defined concentration. Dust is assumed to be of spherical shape with size distribution following a power-law such that it reproduces the extinction curves observed in our Galaxy (Mathis et al. 1977). Scattering and extinction

cross-sections are computed with the procedure given by Bohren & Huffman (1983) for Mie theory. The prescription for graphite and silicate dust grains were adopted from Draine & Lee (1984).

In the following, we describe the journey of one photon from its creation. For a given source region of constant density, a random position of a newly created photon is sampled. By inverting Eq. 5.9 for isotropic emission, the propagation direction is determined using random numbers ξ in the range $[0, 1]$. The sampling equations for polar angles ϑ and ϕ are:

$$\vartheta = \arccos(1 - 2\xi_1), \tag{5.14}$$

$$\phi = 2\pi\xi_2. \tag{5.15}$$

The photon wavelength is sampled over the interval $[\lambda_{min}, \lambda_{max}]$ from the power-law spectrum:

$$\lambda = \begin{cases} [\lambda_{min}^{\alpha} + \xi_3 (\lambda_{max}^{\alpha} - \lambda_{min}^{\alpha})]^{\frac{1}{\alpha}}, & \text{for } \alpha \neq 1, \\ \lambda_{min} \left(\frac{\lambda_{min}}{\lambda_{min}}\right)^{\xi_3}, & \text{for } \alpha = 1. \end{cases} \tag{5.16}$$

If there are no scattering regions on the photons trajectory, the photon is registered by a virtual detector in that direction. If there is a scattering region (SR) along the photon path, the photon is placed inside the SR at the point where the path of the photon intersects with the boundary surface of the SR. Inside the SR, a routine checks whether the photon is scattered or absorbed. This routine generates a random number from the interval $[0, 1]$. If this number is less than the calculated albedo (equation 5.13), the photon is scattered, otherwise, the photon is absorbed. If absorbed, a new photon is generated, and the procedure so far is repeated. If scattered, the photon path length inside a SR is sampled from the equation:

$$l = \frac{1}{n\sigma_s} \ln(1 - \xi_4). \tag{5.17}$$

If the photon path is larger than the size of the region in that direction, the photon leaves that SR and if there is no other SR along the way the photon is registered. The whole procedure is repeated until the photon is registered or is absorbed. The program ends when the desired number of photons have been registered. The polarization state of each photon is described by the Stokes column vector in the co-moving reference frame of the photon. In order to determine the Stokes parameters after a scattering,
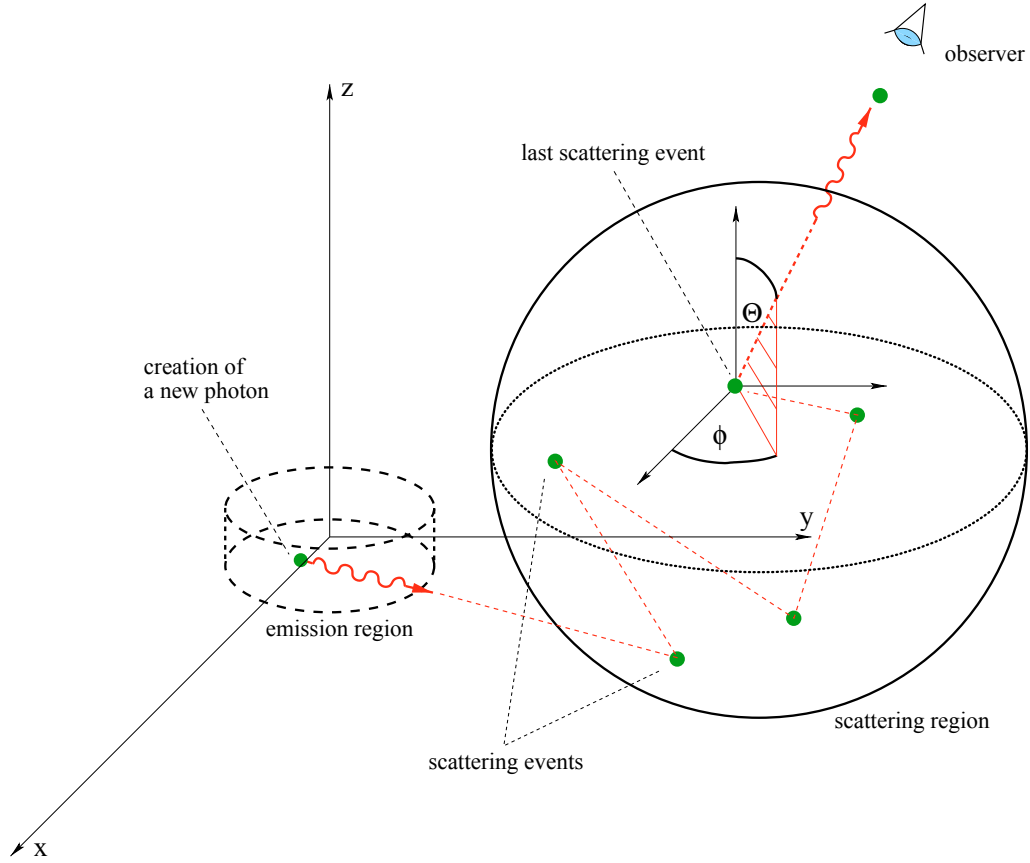
Figure 5.1: An emitted photon working its way through an arbitrary spherical scattering region. Credits: Goosmann & Gaskell (2007).

the co-moving coordinate system needs to be rotated by an azimuthal angle ϕ in order for the $\vec{\mathbf{E}}$-field to lie in the scattering plane. The second rotation is in the scattering plane for the scattering angle Θ. The change of the Stokes parameters is obtain applying the scattering Mueller matrix:

$$S' = M(\Theta)R(\phi)S, \tag{5.18}$$

where $R(\phi)$ is the Mueller matrix for rotation:

$$R(\phi) = \begin{pmatrix} 1 & 0 & 0 & 0 \\ 0 & \cos 2\phi & \sin 2\phi & 0 \\ 0 & -\sin 2\phi & \cos 2\phi & 0 \\ 0 & 0 & 0 & 1 \end{pmatrix}. \tag{5.19}$$

The wavelength shift due to the scatterer velocity is properly included, giving STOKES the edge over the other Monte Carlo codes. The 3D velocity components are defined in cylindrical or spherical coordinates in a user-defined way. STOKES follows the recommendation of the International Astronomical Union [1] (IAU 1974) for which φ increases counter-clockwise when looking at the source. A flowchart diagram of STOKES is shown in Fig.5.2.

Many upgraded features were included in the recent versions of the code. STOKES is also capable of running in imaging mode which allows for generating polarization maps (Marin et al. 2012, 2015). Photons have their spatial coordinates registered along with their polarization state, which allow us to produce the image of the system when projected onto the observer's plane of the sky. Another possibility with STOKES is to explore the time domain. The code computes the length of the photons path between each scattering event and those photons registered without interaction will have a zero time delay. This offers a unique way to model polarized reverberation mapping (Rojas Lobos et al. 2018). The most recent improvement of the code can account for the dilution by interstellar polarization and starlight emission of the host galaxy (Marin 2018b).

The fifteen years of the STOKES code have seen large improvements in our understanding of AGN polarization. Up to date, there have been around 55 publications[2] that have used STOKES code. In this work, we used a publicly available version STOKES 1.2 as well as an intermediate version STOKES 2.04.

---

[1]This convention has been enforced by the IAU with a Resolution by Commissions 25 and 40 at the IAU XVth General Assembly in Sydney in 1973. https://iau.org/static/archives/announcements/pdf/ann16004a.pdf

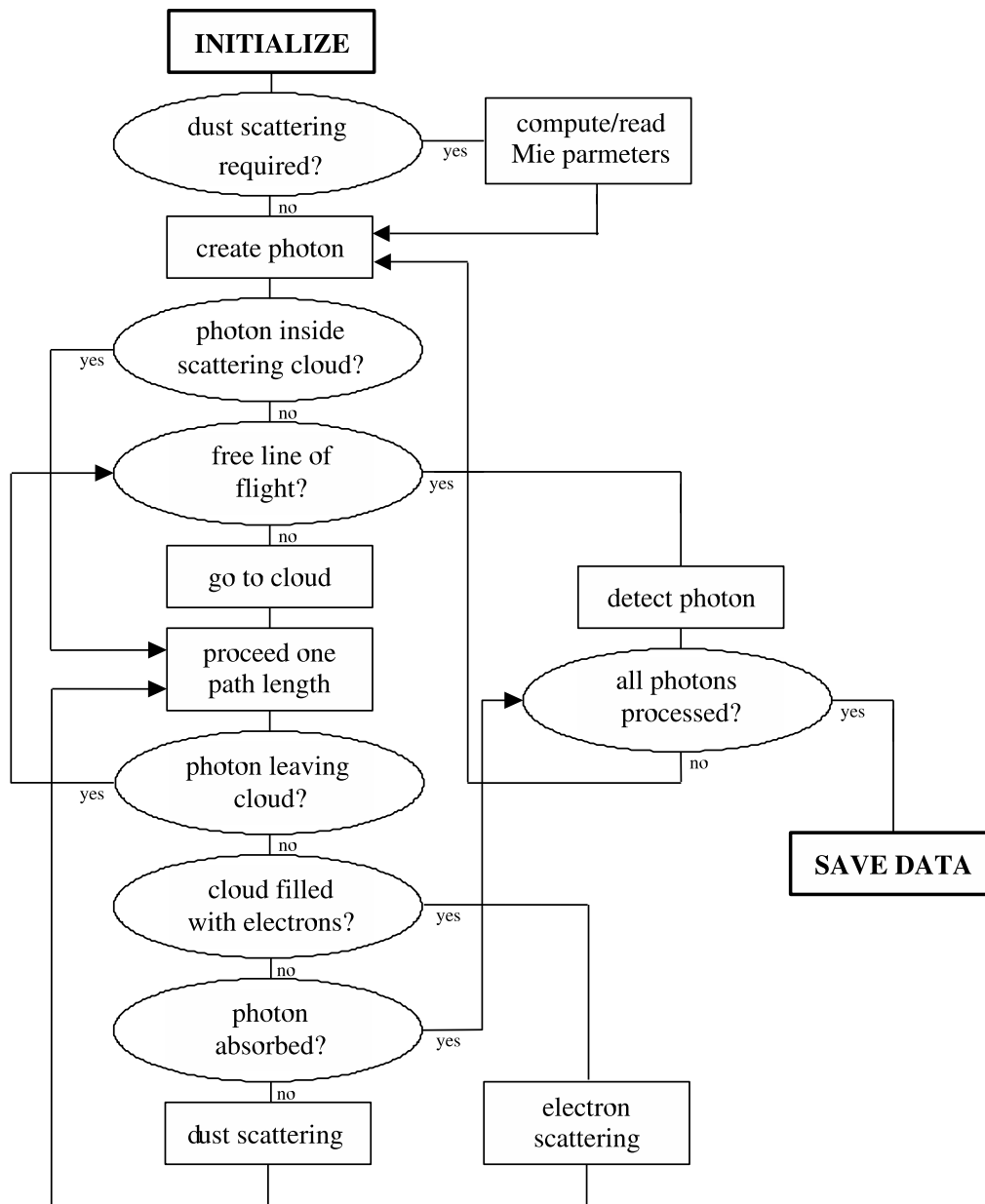[2]http://astro.u-strasbg.fr/~marin/STOKES_web/html/scientific_results.html

Figure 5.2: A flowchart of STOKES execution. Credits: www.stokes-program.info.

Chapter 6

Models and observations

6.1 Setup

So far, we have introduced the necessary apparatus for modeling equatorial scattering and to test the AP15 method theoretically using the 3D Monte-Carlo radiative transfer code STOKES. In our model, a point-like continuum source is situated in the center, emitting isotropic unpolarized radiation for which the flux is given by a power-law spectrum $F_C \propto \nu^{-\alpha}$ with $\alpha = 2$. This value correspond to the flat spectrum of constant intensity when frequency is substituted with wavelength in order to work with F_λ. The chosen value for the spectal index $\alpha = 2$ will not affect our research since we are investigating only a narrow spectral range around an Hα spectral line. Setting different value of α will result in a low change of the continuum between the left and the right wing of the line, which can be neglected.

The continuum source is surrounded by a BLR, and farther out by a SR. The BLR and the SR are modeled using flared-disk geometry with half-opening angle from the equatorial plane of 15° (covering factor ~ 0.25) for the BLR and 35° for the SR. High covering factor for the SR is necessary in order to obtain the observed profile of the φ. Low covering factor of the SR gives very small amplitude in the φ profile. For the BLR inner radius $R_{\rm in}^{\rm BLR}$, we adopted the value obtained by reverberation mapping (Kaspi et al. 2005; Bentz et al. 2006, 2013). The BLR outer radius was set by dust sublimation (predicted by Netzer & Laor 1993):

$$R_{\rm out}^{\rm BLR} = 0.2 L_{\rm bol,46}^{0.5}, \tag{6.1}$$

where $L_{\mathrm{bol,46}}$ is bolometric luminosity given in $10^{46}\,\mathrm{ergs\ s^{-1}}$. Bolometric luminosity is approximated from optical nuclear luminosity (Runnoe et al. 2012):

$$\log L_{\mathrm{iso}} = 4.89 + 0.91 \log L_{5100}, \tag{6.2}$$

where $\log L_{5100}$ is the optical nuclear luminosity. After correcting for average viewing angle ($\cos i = 0.75$), we obtain:

$$L_{\mathrm{bol}} = 0.75 L_{\mathrm{iso}}. \tag{6.3}$$

In our model, the BLR is transparent to photons i.e., photons can freely travel from the inner side to the outer side of the BLR. This is in a good agreement if one perceives BLR as a clumpy medium with small filling factor. For the flattened BLR (Gaskell 2009):

$$v_{\mathrm{Kepler}} > v_{\mathrm{turb}} \gtrsim v_{\mathrm{inflow}}, \tag{6.4}$$

where v_{Kepler} is Keplerian velocity, v_{turb} is the turbulence velocity and v_{inflow} is the inflow velocity.

In our model, SR is a radially (but not optically) thin region as we assume that the light is being scattered dominantly due to free electrons (Thomson scattering) in the innermost part of the torus. Assuming Thomson scattering only without dust scattering greatly simplifies the model setup. We assume that the electron density is decreasing radially outwards in the form of the power law $n_{\mathrm{e}} \propto r^{-1}$ (Smith et al. 2005). The SR inner radius $R_{\mathrm{in}}^{\mathrm{SR}}$ is found from the IR reverberation mapping (Kishimoto et al. 2011; Koshida et al. 2014). The SR outer radius $R_{\mathrm{out}}^{\mathrm{SR}}$ was chosen such that BLR angular diameter when viewed from the edge of the SR is 25°. This way the change in φ across the line profile will be significant. Investigation by Marin et al. (2012) for the SR with the flared-disk geometry have shown that optically thin SR ($\tau \leq 0.1$) cannot produce sufficient polarization for type-1 viewing angles. On the contrary, for optical depths $\tau > 3$, multiple scattering can occur, resulting in depolarization. For this reason, we chose to set the total optical depth in radial direction to be $\tau = 1$. An illustration of the model is shown in Fig. 6.1.

6.2 Generic models

We generated four probe models for which the central SMBH has mass of 10^6, 10^7, 10^8 and $10^9\,M_{\odot}$. We expect that the BLR distance from the center increases when the
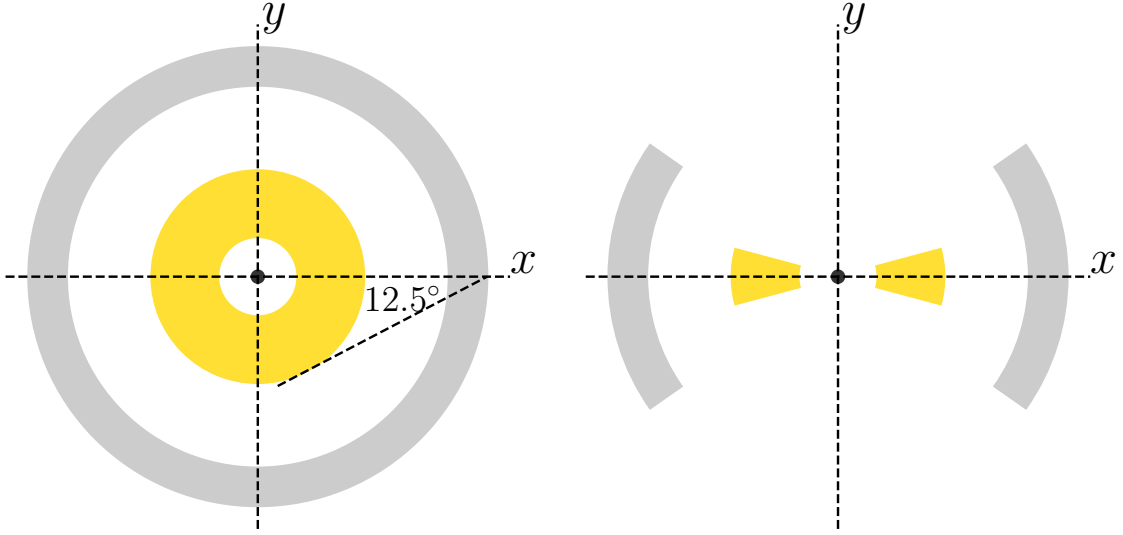
Figure 6.1: Cartoon showing the model geometry of the BLR (yellow) and the scattering disk (grey) in the face-on (left) and edge-on (right) view. The BLR and the SR half-opening angle is 15° and 35° respectively. Credits: Savić et al. (2018).

mass of the central SMBH increases, since the mass of the SMBH scales very well with the luminosity of the AGN (Laor 2000; Gu et al. 2001). In order to determine the size and the position of the BLR as well as the SR for our probe models, we compiled 14 AGNs for which BH masses and inner radii of the BLR and the SR are known from reverberation mapping (listed in Table 6.1). We fitted $\mathcal{M}_{\rm bh}$ – radius relation with a power law in the form:

$$\log \mathcal{M}_{\rm bh} = C_1 \log R + C_2, \tag{6.5}$$

where R takes the values for $R_{\rm in}^{\rm BLR}$, $R_{\rm out}^{\rm BLR}$ and $R_{\rm in}^{\rm SR}$. In Fig. 6.2, we show mass-radius relationship with 1σ uncertainty. Fit constants are listed in the Table 6.2. We represent the goodness of fit using the adjusted coefficient of determination $\bar{R}^2$ given by Devore (2011):

$$\bar{R}^2 = 1 - \left(1 - \frac{1 - \sum_i (y_i - f_i)^2}{1 - \sum_i (y_i - \bar{y})^2} \right) \frac{n-1}{n-k-1}, \tag{6.6}$$

where y_i are observed values, $\bar{y}$ is the mean observed value, f_i are predicted values, n is the number of observations and k is the number of independent variables in the equation of regression. This way we obtained a rough estimate of the BLR and the SR sizes for our model setup. The BLR and the SR size now depends only on the mass of the SMBH, which reduces the space of free parameters.

Table 6.1: List of objects with known $\log \mathcal{M}_{bh}$, L_{5100}, R_{in}^{BLR} and R_{in}^{SR} that we used for models. Mass was estimated from reverberation mapping using the Hβ line and for $< f > = 4.3$ (Grier et al. 2013). Radii are given in light days. Optical luminosities are taken from (1) Bentz et al. (2013), (2) Peterson et al. (2013). The estimates for R_{in}^{BLR} are taken from (3) Zu et al. (2011), (4) Grier et al. (2012), (5) Grier et al. (2013), (6) Kaspi et al. (2000), The estimates for R_{in}^{SR} are taken from (7) Koshida et al. (2014), (8) Kishimoto et al. (2011).

Object	z	$\log \mathcal{M}_{bh}$ $M_\odot$	$\log L_{5100}$ erg/s	Ref.	R_{in}^{BLR} ld	Ref.	R_{in}^{SR} ld	Ref.
Mrk335	0.025	7.23	43.71 ± 0.06	1	14.10 ± 1.20	3, 4	141.7	7
Mrk590	0.026	7.56	43.42 ± 0.07	1	25.50 ± 6.00	3	34.7	7
Ark120	0.032	8.06	43.78 ± 0.07	1	32.70 ± 3.00	3	428.8	7, 8
Mrk79	0.022	7.61	43.61 ± 0.04	1	29.30 ± 14.30	3	69.5	7
PG0844+349	0.064	7.85	44.24 ± 0.04	6	12.20 ± 5.20	3	104.3	7
Mrk110	0.035	7.29	43.60 ± 0.04	1	26.90 ± 7.00	3	104.3	7
NGC 3227	0.003	6.77	42.24 ± 0.11	1	4.40 ± 0.40	3	25.0	7, 8
NGC 3516	0.008	7.39	42.73 ± 0.21	1	14.60 ± 1.30	3	61.2	7
NGC 4051	0.002	6.12	41.96 ± 0.20	1	2.50 ± 0.20	3	38.0	7, 8
NGC 4151	0.003	7.55	42.09 ± 0.22	1	6.00 ± 0.40	3	44.0	7, 8
3C 273	0.158	8.83	45.90 ± 0.02	1	306.8 ± 90.9	3	963	8
NGC 4593	0.009	6.88	42.87 ± 0.18	1	4.50 ± 0.65	3	43.0	7
NGC 5548	0.017	7.71	43.23 ± 0.10	1, 2	17.60 ± 8.86	3, 5	60.0	7
Mrk817	0.031	7.58	43.68 ± 0.05	1	21.20 ± 14.70	3	180.0	7
PG1613+658	0.129	8.33	44.71 ± 0.03	1	35.00 ± 15.10	3, 6	595.0	7
PG1700+518	0.292	8.78	45.53 ± 0.01	1	251.80 ± 42.35	3, 6	687.0	7

Table 6.2: The constants C_1 and C_2 for the mass–radius relation (eq. 6.5, second and third column). Adjusted coefficient of determination $\bar{R}^2$ (the last column) for the performed fit.

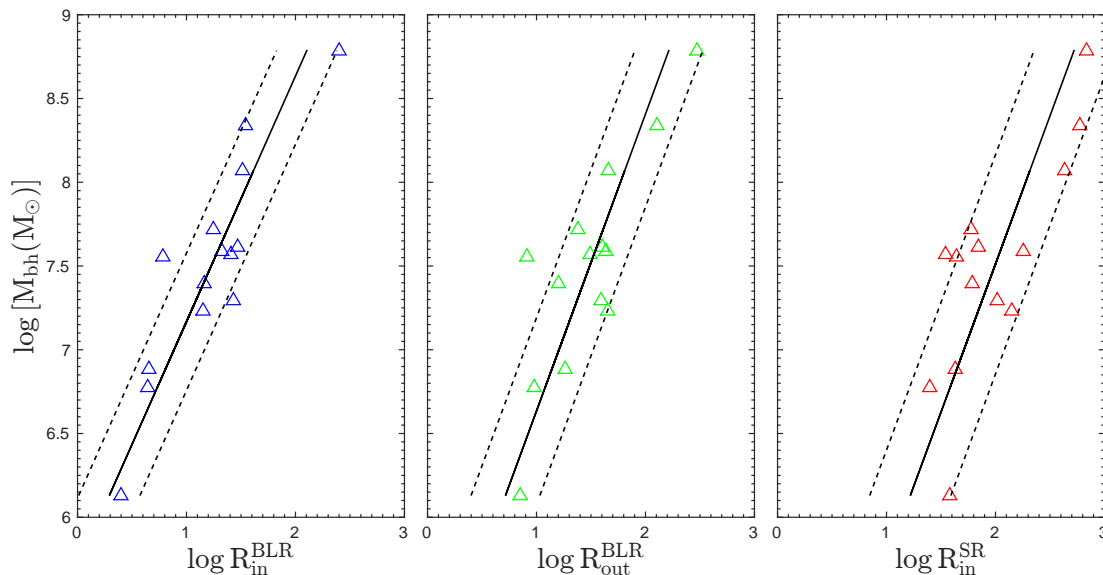| R	C_1	C_2	$\bar{R}^2$
R_{in}^{BLR}	0.682 ± 0.096	-3.890 ± 0.723	0.7915
R_{out}^{BLR}	0.564 ± 0.108	-2.743 ± 0.812	0.6690
R_{in}^{SR}	0.566 ± 0.127	-2.248 ± 0.958	0.5899

Figure 6.2: Mass – radius relation, for R_{in}^{BLR} (left panel), R_{out}^{BLR} (middle panel) and R_{in}^{SR} (right panel). Data taken from literature (see Table 6.1) are denoted as triangles, while solid lines represent the best fit. Dashed lines mark the 1σ uncertainty. Credits: Savić et al. (2018).

Table 6.3: Central SMBH masses, inner and outer radius of the BLR and inner radius of the SR that we used in our model. Radii are given in light days.

Mass	R_{in}^{BLR}	R_{out}^{BLR}	R_{in}^{SR}	R_{out}^{SR}
$M_\odot$	ld	ld	ld	ld
10^6	1.597	4.385	13.968	20.262
10^7	7.681	16.076	51.372	74.277
10^8	36.944	58.934	188.939	272.288
10^9	177.700	216.043	694.893	998.170

With known fit constants, we generated values for the R_{in}^{BLR}, R_{out}^{BLR}, R_{in}^{SR} and R_{out}^{SR} for the set of four different SMBHs (see Table 6.3). Our approach is the following. For each model with known input mass of the SMBH, we solve 3D radiative transfer using STOKES. We apply the AP15 method to the simulated results, and finally, we compare the value of the obtained SMBH mass with the value of input SMBH mass.

6.3 Equatorial scattering and SMBBHs

Finding observational evidences of binary SMBHs is a difficult task. First of all, it is hard to spatially resolve at pc-scale the central part of the nearest galaxies with existing telescopes, therefore one has to find other methods to search for sub-pc SMBBHs. The first discovery of GWs with frequency $\sim 10^2$ Hz coming from stellar-mass binary BHs (Abbott et al. 2016) is a major confirmation of general relativity. The GW frequency for SMBBHs with mass range from 10^6–$10^9 \, M_\odot$ falls in the range from nanohertz to milihertz band and so far, none have been detected. In this frequency regime, pulsar timing arrays (PTAs, Shannon et al. 2015) can be used for detecting GW by monitoring pulses from millisecond pulsars, however we are still waiting for the detection of such signatures that should be numerous. The occurrence of long-lived SMBBHs signals appears to be too rare. The emission of broad, double-peaked Balmer emission lines observed in the spectra of several active galactic nuclei (AGN) may (not) be associated with binary systems (Eracleous & Halpern 2003; Eracleous et al. 2009). During the merging effect of two galaxies, in a sub-pc phase of SMBBH system, there is enough gas which may produce an activity similar to the one observed in AGNs (Popović 2012). Since AGNs have some comparable and well-known spectroscopic characteristics, one of the promising methods of the SMBBH detection is broadband spectroscopy, i.e. observations in a wide wavelength band including the emission lines (see Popović 2012, for review) can give some indications for SMBBH presence in the center of some active galaxies (see e.g. Bon et al. 2012; Graham et al. 2015; Li et al. 2016; Du et al. 2018; Kovačević et al. 2018, 2019).

A significant fraction of AGNs show broad-line profiles that cannot be explained by this axisymmetric BLR model (see, e.g., Capriotti et al. 1979; Meyers & Peterson 1985; Netzer 1990; Gaskell & Klimek 2003; Shapovalova et al. 2016, etc.). They show strong asymmetric displaced BLR peaks with the broad peak redshifted or blueshifted by thousands of km s^{-1}. According to Boroson & Lauer (2009) those signatures could be due to a binary SMBH system, resembling a spectroscopic binary. As it was discussed by Popović (2012), the broad line profiles and their variability may indicate the SMBBH presence, however an additional evidence is needed to check it, as e.g. γ-ray and X-ray emission or polarization in the broad emission lines.

To test this hypothesis polarimetry is a natural tool since the geometry of the emitting and scattering system is expected to produce polarimetric features that are easily distinguishable from model to model (Goosmann & Gaskell 2007; Marin et al. 2012;

Goosmann et al. 2014; Marin et al. 2015). A single SMBH surrounded by coplanar cylindrically-shaped scattering regions produces very low amounts of polarization when seen from a close to pole-on inclination (Marin et al. 2012). The polarization in the line shares similar values as the continuum and shows characteristic, wavelength-dependent variations across the line profile (Smith et al. 2002; Afanasiev et al. 2014). The polarization angle across the line profile for a single SMBH can indicate Keplerian-like motion, and consequently can be used for the black hole mass measurements (AP15 Afanasiev & Popović 2015; Savić et al. 2018). The case of extremely asymmetric Balmer lines with large redshifted or blueshifted peaks could not be tested since the spectropolarimetric signal for binary SMBHs, each surrounded by its own BLR, is not known.

There is a number of publications which consider the broad line shapes of AGNs in the case of sub-pc SMBBHs (see e.g. Gaskell 1983; Popovic et al. 2000; Shen & Loeb 2010; Eracleous et al. 2012; Simić & Popović 2016; Nguyen & Bogdanović 2016, etc.), while the polarization effects in the line profiles was never considered in details. Exception is the observations (Robinson et al. 2010) and theoretical consideration (Piotrovich et al. 2017) of the shift of polarized broad lines for a kicked supermassive black hole. Robinson et al. (2010) gave an observational evidence that quasar E1821+643[1] may be an example of gravitational recoil, i.e. they found that broad Balmer lines indicate the kick off velocity of $2100 \, \mathrm{km \, s^{-1}}$ in polarized light. Piotrovich et al. (2017) also considered recoiling black hole, taking that the kick radius is similar to the BLR dimension and found that polarization data in this case can give an estimation of the kick off velocity.

We present here for the first time the polarization parameters across the broad lines in the case of an emission by a sub-pc scale SMBBH system. By doing so, we aim to predict what should be the observational signature from those yet-to-be-confirmed sources and whether the AP15 method can be applied in this case. We consider a model of sub-pc SMBBHs, where each of the BH components has its own accretion disk and BLR. Again, we consider equatorial scattering of such complex system on the inner part of the torus, and we model the Stokes parameters.

---

[1]The quasar has highly shifted Balmer lines around $1000 \, \mathrm{km \, s^{-1}}$ and a red asymmetry (Shapovalova et al. 2016)

6.3.1 SMBBH geometry and kinematics

We model SMBBH system as two black holes orbiting around the common center of mass due to gravity. This is a well known problem for which it was shown that it is equivalent to the problem of a single body with reduced mass μ moving in an external gravitational field (Landau & Lifshitz 1969; Postnov & Yungelson 2014) which is determined by the total mass of the system:

$$\mathcal{M} = \mathcal{M}_1 + \mathcal{M}_2, \tag{6.7}$$

where $\mathcal{M}$ is the total mass, and $\mathcal{M}_1$ and $\mathcal{M}_2$ are masses of each component. The reduced mass μ is

$$\mu = \frac{\mathcal{M}_1 \mathcal{M}_2}{\mathcal{M}}. \tag{6.8}$$

In general, the body μ moves in elliptical trajectory with semi-major axis a and eccentricity e. The relationship between the orbital period P, orbital frequency Ω, $\mathcal{M}$ and a is given by the Kepler's third law:

$$\Omega = \frac{2\pi}{P} = \sqrt{\frac{G\mathcal{M}}{a^3}}, \tag{6.9}$$

This relation is valid for any eccentricity e. Each component is moving around the center of mass in elliptical orbit with the same eccentricity e. Both ellipses lie in the same plane and have one common focus. The semi-major axes are inversely proportional to the masses:

$$\frac{a_1}{a_2} = \frac{\mathcal{M}_2}{\mathcal{M}_1}, \tag{6.10}$$

and they satisfy the equation:

$$a = a_1 + a_2. \tag{6.11}$$

Our goal is to create a simple, yet comprehensive model, without introducing hydrodynamic simulations or the numerical N-body problem. A second model, based on hydrodynamic simulations involving spiral arms is also investigated. In this work, we are considering the case with $e = 0$, i.e. orbits are circular. and with both black holes having the same mass $\mathcal{M}_1 = \mathcal{M}_2 = 5 \times 10^7 \, M_\odot$, i.e. the mass ratio $q = \mathcal{M}_2/\mathcal{M}_1 = 1$. We note that in that the usage of a is in the context of semi-major axis, and not the one used in the equation 3.4, which is related with the SMBH mass estimation using the AP15 method.

We have made two assumptions in our model: one is that both SMBHs have accretion disks and the corresponding BLRs and the second is that both the accretion disks and the scattering region are coplanar. We expect to have near coplanar accretion disks and scattering region (torus) because of following reason: In gas rich mergers, where the evolution of the SMBBHs is driven by interaction with the surrounding gas, the accretion onto the black holes leads to the alignment of black holes spin with the angular momentum of the binary (Bogdanović et al. 2007; Dotti et al. 2009) which effectively lowers the kick velocity (Dotti et al. 2010). The timescale of the angular momentum aligning with the individual spin of each component is few hundreds of times shorter than the timescale for which the angular momentum of the binary aligns with the angular momentum of the inspiraling circumbinary gas, unless the mass ratio is extreme (Miller & Krolik 2013). In case that the accretion occurs in the opposite direction of the binary rotation, there will be a misalignment of various axes on a timescale of the order of a fraction of the whole binary evolution time. As was mentioned above, each black hole has an accretion disc surrounding it, from which the isotropic continuum radiation is emitted. We used point source approximation for disc emission with emissivity given by a power law: $F_C \propto \nu^{-\alpha}$ where α is spectral index equal to 2. Both black holes are surrounded by the BLR. Depending on the distance between the black holes, we treated four different SMBBH cases: **distant**, **contact**, **mixed** and **spiral**. We modeled BLR with flared-disk geometry (Goosmann & Gaskell 2007) with half-opening angle of 25° and a volume filling factor 0.25, which yields an effective covering factor of the order of 0.1 (Netzer 2013). The size of the BLRs were set to few light days with BLR inner radius $R_{in}^{BLR} = 3$ and BLR outer radius $R_{out}^{BLR} = 12$ light days. These values for BLR inner and outer radius were chosen to reproduce typical BLR velocity values of few thousands km s^{-1} (Peterson et al. 2004; Kaspi et al. 2005). This was done for all cases except for the spiral one. Model geometry and kinematics is shown for each model in Fig. 6.3.

Distant

Both BLRs are distinctive and each black hole affects only the dynamics of the BLR it is surrounded with. Each BLR cloud has two velocity components: Keplerian motion around the black hole plus additional motion due to the binaries orbiting each other (see Fig. 6.3, top panel). Black holes are at the orbital distance $a = 47.6$ light days which corresponds to the orbital period of approximately 75 years. Additionally, we
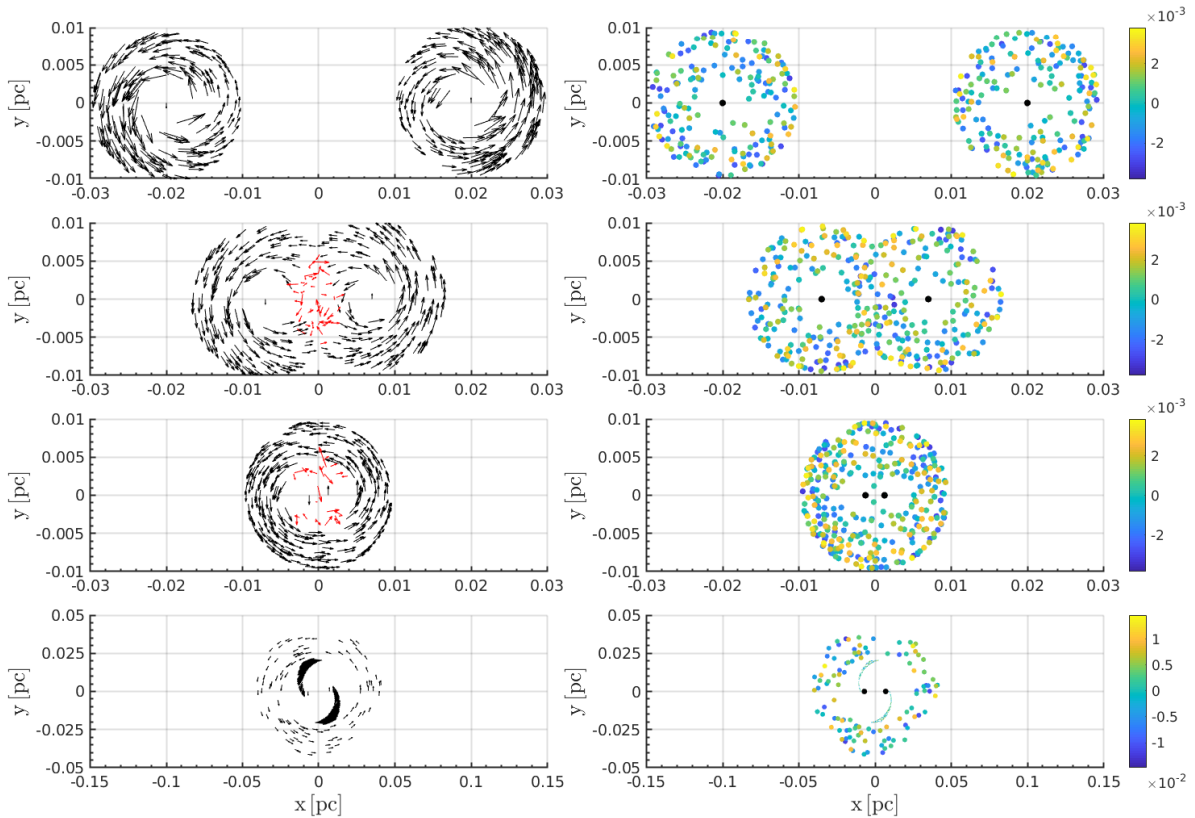
Figure 6.3: Geometry and kinematics of the SMBBH for each model. From top to bottom: Distant, Contact, Mixed and Spiral. Left panels denote velocity field. Black arrows show the non-perturbed velocity field, while red ones are for clumps with additional random component of the velocity. Right panels denote the position of each BLR cloud. Credits: Savić et al. (2019).

simulated two models with mass ratio $q = 0.5$ and $q = 0.1$ for this case. Assuming that photoionization and recombination following radiative de-excitation is the main mechanism for the emission of broad Balmer lines, the BLR size scales with luminosity in the form of $R_{\mathrm{BLR}} \propto L^{0.5}$ (Kaspi et al. 2005). We used mass luminosity relation $\mathcal{M}_{\mathrm{bh}} \propto L^{0.7}$ (Woo & Urry 2002) in order to obtain the BLR size depending solely on mass of each component. An illustration for these two cases is shown in Fig. 6.4.

Contact

Black holes are separated by $a = 16.7$ light days with orbital period of 15.5 years, which allows for certain parts of the BLRs to overlap (Fig. 6.3, middle panel). In this regime, the BLR kinematics is similar as in the previous model, except for the overlapping part
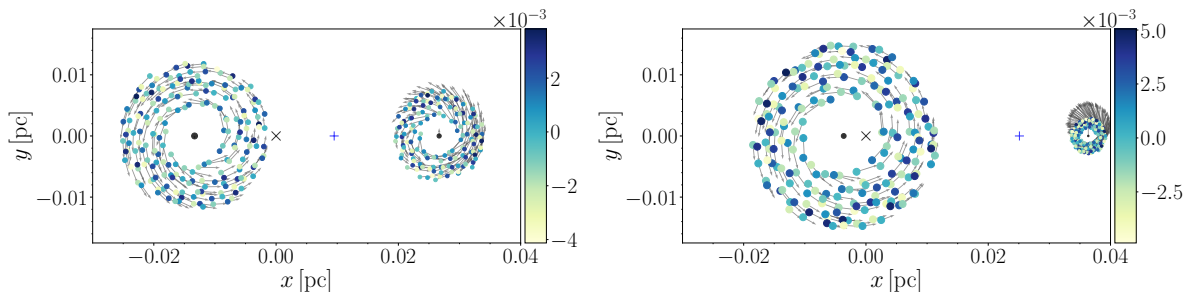
Figure 6.4: Distant model with mass ratio $q = 0.5$ (left panel) and with $q = 0.1$ (right panel). Black x shows the center of mass, while the blue + symbol marks the Lagrangian point L1. Grey arrows denote the velocity of each BLR clump. Color bar is denoting the vertical offset from the xy plane. Credits: Savić et al. (2019).

where we assigned chaotic component to the velocity for each clump due to chocks, stirring and inelastic collisions.

Mixed

For this model, black holes are much closer to each other, at the orbital separation of 3 light days and with orbital period of 1.2 years. On Fig. 6.3, third panel, clumps denoted in red are the ones with additional chaotic component, while for the rest we calculated velocity as if in the center was a single SMBH with mass equal to the sum of binary components.

Spiral

Hydrodynamic simulations involving subparsec SMBBHs have shown that black holes are surrounded by a common circumbinary (CB) disc. Accreting gas around the binaries forms a low density cavity inside the CB disc (MacFadyen & Milosavljević 2008; Cuadra et al. 2009). It was found that the accretion streams are in the form of spiral arms with higher density that is connecting mini accretion disk of each black hole with the surrounding CB disk (Noble et al. 2012; Shi & Krolik 2015). In this scenario, the cavity is of the order of a, and the CB disk extends from $1.5a$ to $3a$. Following the similar setup as Smailagić & Bon (2015), we built a SMBBH model with spiral arms and the surrounding CB disk in order to investigate the polarization signatures coming from the SMBBH. We keep the same mass of each component to be $5 \times 10^7 \, M_\odot$ with the orbital separation the same as in the case for contact model $a = 16.7$ light days. We approximated spiral arms with logarithmic spirals with boundaries in polar coordinates

given as:

$$R_1 = \frac{a}{2}e^{b\phi} < R(\phi) < R_2 = \frac{a}{2}e^{B\phi}, \tag{6.12}$$

where b and B are parameters describing the wrapping of the spirals. We chose wrapping parameters to be $B = 0.55$ and $b = 0.45$. This set of parameters for b and B were chosen in order to have two distinct spirals with single winding and to avoid mixture or interaction of the spirals. We chose the half-opening angle for the spirals and the CB disk to be $20°$. An illustration of the model is shown at Fig. 6.3 (bottom panel). For kinematics of the spirals, we used the rotation of absolute rigid body, i.e. the spirals are stationary in the rotating reference frame of the SMBBH. The CB is under the Keplerian motion around the common center of mass. The system is again surrounded by the same scattering region as in previous models, with the same radial optical depth in the equatorial plane. The BLR is represented by thousands of clumps. The volume filling factor of the BLR is 0.25, as constrained from simulations and observations (Marin et al. 2015). Total number of clumps per model as well as the other parameters used in the model are listed in Table 6.4

The scattering region

Similarly as in the case for a single SMBH, we model the SR with a flared-disk geometry with inner and outer radius of 0.1 and 0.5 parsec. These values are fixed for all BLR configurations. The half-opening angle is $30°$ with respect to the equatorial plane. Electron concentration is chosen in such a way that the total radial optical depth in the equatorial plane for Thomson scattering is 3, which is more than enough to produce the typical degree of polarization that is found in type-1 objects (Marin et al. 2012). We stress out that the values of the inner and the outer radius of the SR as well as the optical depth for SMBBH models were chosen by *trial and error* in order to maximize the polarization signal for better qualitative analysis. Radial optical depth higher than this value would cause depolarization due to multiple scattering. An illustration of the scattering region surrounding the central engine is illustrated on Fig. 6.5.

For solving the radiative transfer for SMBBH models, we used the intermediate 2.04 version of the code, which is not yet publicly available. This version of the code allows to define multiple emitting regions with arbitrary coordinates, unlike the version 1.2.
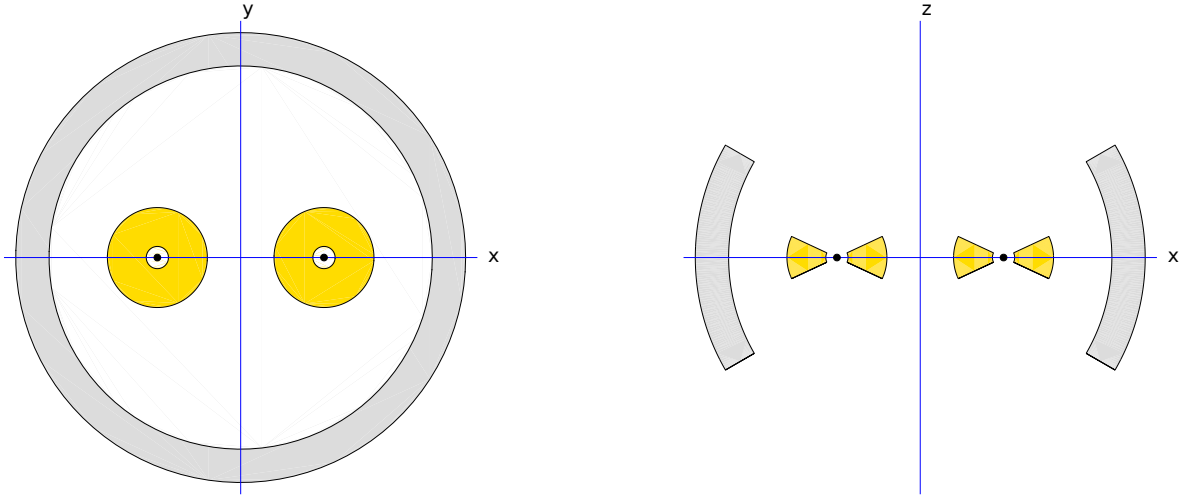
Figure 6.5: Cartoon illustrating equatorial scattering region. Left figure shows the face-on view, while on the right the same geometry is shown when viewed edge-on. An example is shown for the case with the two BLRs being separated. The BLRs are shown in yellow. Scattering region is denoted in grey. Credits: Savić et al. (2019).

Table 6.4: Description of the 3 SMBBH model. V_1 and V_2 are orbital velocities and q is the mass ratio.

Model	Orbital separation a light days	Period P years	Number of clouds	V_1 km s^{-1}	V_2 km s^{-1}	q
Distant	47.65	75.0	2000	1639	1639	1.0
Distant	47.65	75.0	2000	1093	2186	0.5
Distant	47.65	75.0	2000	298	2980	0.1
Contact	16.68	15.5	1600	2771	2771	1.0
Mixed	2.978	1.2	1000	6558	6558	1.0
Spiral	16.68	15.5	1600	2771	2771	1.0

Table 6.5: Central SMBH masses, inner and outer radius of the BLR and SR that we used in our model for the four AGNs. The BLR inner radius were taken from: (1) Kaspi et al. (2005) (2) Bentz et al. (2013), (3) Zu et al. (2011). The SR inner radius was taken from (4) Koshida et al. (2014), (5) Kishimoto et al. (2011). Radii are given in light days.

Object	$\log(\mathcal{M}_{\mathrm{POL}}/M_\odot)$	$R_{\mathrm{in}}^{\mathrm{BLR}}$	Ref.	$R_{\mathrm{out}}^{\mathrm{BLR}}$	$R_{\mathrm{in}}^{\mathrm{SR}}$	Ref.	$R_{\mathrm{out}}^{\mathrm{SR}}$
		ld		ld		ld	ld
NGC 4051	6.69 ± 0.21	4.3	1	11.6	38.1	4, 5	53.7
NGC 4151	7.21 ± 0.27	6.6	2	13.8	44.0	4, 5	63.8
3C 273	8.85 ± 0.27	306.8	3	440.6	963.7	5	2035.8
PG0844+349	7.70 ± 0.14	12.2	3	77.4	189.0	4	357.6

6.4 The four AGNs

We have selected four AGNs with prominent change of φ across the line profile: NGC 4051, NGC 4151, 3C 273 and PG0844+349. These objects have been very well observed in the last few decades, both in polarized and unpolarized light (Afanasiev et al. 2019). They all exhibit dominant equatorial scattering in their spectra. In order to test the AP15 method theoretically, we modeled each of these objects using observational data available from the literature. This is important since we can perform direct comparison of the results obtained from the model with the newest spectropolarimetric observations using the SAO RAS 6 m telescope. Input mass was obtained by applying the AP15 method to the observational data. Radii $R_{\mathrm{in}}^{\mathrm{BLR}}$ and $R_{\mathrm{in}}^{\mathrm{SR}}$ were taken from the literature, while $R_{\mathrm{out}}^{\mathrm{BLR}}$ and $R_{\mathrm{out}}^{\mathrm{SR}}$ were computed in the same way as for the generic models. Model parameters for these objects are given in Table 6.5.

6.5 Observations

In 2014 we carried out the spetropolarimetric observations of the AGNs NGC 4051, NGC 4151, 3C 273 and PG0844+349 with the 6 m telescope BTA of SAO RAS with the focal reducer SCORPIO (Afanasiev & Moiseev 2005). A schematic diagram and an actual footage of SCORPIO is given in Fig. 6.6. We used a 1″ slit and a volume phase holographic grating covering the 5800–9500 Å range with a maximum efficiency at 7350 Å to obtain the spectrum images. We used double Wollaston prism to divide the image of the entrance pupil according to the four polarization directions – 0° and

90°, 45° and 135°. Then the parameters of the linear polarization and intensity - the Stokes parameters Q, U and I are obtained simultaneously as:

$$Q(\lambda) = \frac{I_0(\lambda) - I_{90}(\lambda)K_Q(\lambda)}{I_0(\lambda) + I_{90}(\lambda)K_Q(\lambda)}, \tag{6.13}$$

$$U(\lambda) = \frac{I_{45}(\lambda) - I_{135}(\lambda)K_U(\lambda)}{I_{45}(\lambda) + I_{135}(\lambda)K_U(\lambda)}, \tag{6.14}$$

$$I(\lambda) = I_0(\lambda) + I_{90}(\lambda)K_U(\lambda) + I_{45}(\lambda) + I_{135}(\lambda)K_U(\lambda), \tag{6.15}$$

where K_Q and K_U are the coefficients of the channel transmission, $I_0, I_{90}, I_{45}, I_{135}$ correspond to the different polarization directions. Then the polarization degree p and polarization angle φ are obtained from the following relations:

$$P(\lambda) = \sqrt{Q^2(\lambda) + U^2(\lambda)}, \tag{6.16}$$

$$\varphi(\lambda) = \frac{1}{2}\arctan[U(\lambda)/Q(\lambda)] + \varphi_0, \tag{6.17}$$

where φ_0 is the zero point of polarization angle. To correct the device spectral sensitivity and to find φ_0 the non-polarized photometric and polarized standards were observed before the object. The polarimetric accuracy was up to variations of the atmospheric depolarization. The observations of the object were performed in a series of a dozen of frames with a few kilo-second exposure times in order to make robust statistical estimations. The correction for the interstellar matter (ISM) polarization was done by observing 10–15 bright stars in the field of the observed object. For those stars, the average value of Stokes parameters was calculated and then subtracted from the Q and U parameters of the observed object (Afanasiev et al. 2014). The observational technique, analysis method, data reduction and the method of calculating the polarization parameters was done in the same way as described by Afanasiev & Amirkhanyan (2012).

Details of the BTA observations are given in Table 6.6. In the following, we list the main properties of the four AGNs, and we show their polarization spectrum.

NGC 4051

It is a relatively nearby Seyfert 1 galaxy with the cosmological redshift equals to 0.0023, known for its highly variable X-ray flux (McHardy et al. 2004). NGC 4051 was extensively observed in the high energy band to see if the rapid continuum variations observed
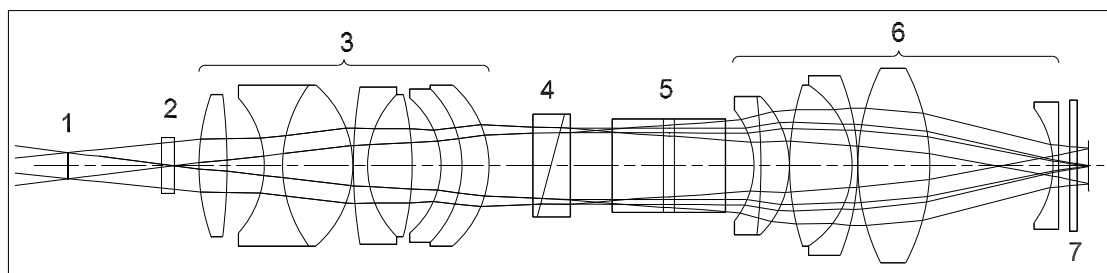
Figure 6.6: Upper panel: the optical scheme of the polarimetric mode of the focal reducer SCORPIO: 1–slit; 2–the phase plate; 3–the collimator, 4–the Wollaston prism; 5–the grism; 6–the spectrograph camera; 7–the entrance window of the CCD (charged coupled device) cryostat. Credits: Afanasiev & Amirkhanyan (2012). Bottom: a real picture of SCORPIO with all its optical elements marked in the figure. Credits: SAO RAS gallery https://www.sao.ru/hq/lsfvo/devices/scorpio/scorpio.html.

in the X-ray spectra are correlated to the optical band fluctuations. This is not the case, despite that the time-averaged X-ray and optical continuum fluxes are well correlated. Only the flux of the broad Hβ line is lagging behind the optical continuum variations by 4 days, allowing us to estimate the mass of the central supermassive black hole (Peterson et al. 2000). The optical continuum polarization of NGC 4051 was measured by Martin et al. (1983) and Smith et al. (2002), who found a polarization degree of $0.52 \pm 0.09\%$ and $0.55 \pm 0.04\%$, respectively. The polarization position angle was found to be parallel to the radio axis of the AGN, such as expected for most of type-1 objects. (Antonucci 1993). The polarized spectrum of NGC 4051 is shown in Fig. 6.7.

NGC 4151

It is a 1.5 Seyfert galaxy situated at $z = 0.0033$ (de Vaucouleurs et al. 1991), which is sometimes considered to be the archetypal Seyfert 1 galaxy (Shapovalova et al. 2008, 2010). It is one of the brightest type-1 AGN in the X-ray and ultraviolet band, and its bolometric luminosity is of the order of $5 \times 10^{43}\,\mathrm{erg\,s^{-1}}$ (Woo & Urry 2002). The mass of its central supermassive black hole was estimated by optical and ultraviolet reverberation techniques and is estimated at $4.5 \times 10^7\,M_\odot$ (Bentz et al. 2006). Since NGC 4151 stands out thanks to its high fluxes and proximity, its optical polarization was extensively observed (see Marin et al. 2016). The averaged 4000–8000 Å continuum polarization is below 1%, with a polarization position angle parallel to the radio axis of the system. In the optical range, NGC 4151 shows flux variations of the continuum and of the broad lines up to a factor of ten or greater (Shapovalova et al. 2008, 2010). The wings of broad lines also vary greatly from very intensive ones corresponding to type Sy1 in the maximum state of activity to almost complete absence in the minimum state of activity. In April 1984, the nucleus of NGC 4151 went through a very deep minimum and the broad wings of hydrogen lines almost completely vanished and the spectrum of the nucleus was identified as a Sy 2 (Penston & Perez 1984). In this phase, the intensity in the broad component of a spectral line is too weak that probably the AP15 method could not be used. Another technique must be used to explore the geometry of the object, such as proved by Hutsemékers et al. (2017) and Marin (2017). This object is a SMBBH candidate that shows periodic variations in the light and radial velocity curves with a 15.9 year period (Bon et al. 2012). The polarized spectrum of NGC 4151 is shown in Fig. 6.8.

3C 273

It is a well known flat-spectrum radio source AGN with broad emission lines. It is the brightest and one of nearest quasars known to us ($z = 0.158$, Courvoisier et al. 1987, 1990). It is a radio-loud object, i.e. its radio-to-millimeter energy output is dominated by synchrotron emission from a kilo-parsec, one-sided jet, whose emission extends up to the infrared and optical bands. 3C 273 is particularly bright in the optical and ultraviolet domains, which enabled the detection of the polarization of the optical emission. Its mean optical core polarization was measured by Appenzeller (1968) and is of the order of $0.2 \pm 0.2\%$, being consistent with galactic interstellar polarization (Whiteoak 1966). The optical polarization emerging from the jet structure is higher as resolved into a number of highly polarized knot structures by Thomson et al. (1993). Nevertheless, Balmer emission lines were first measured by Schmidt (1963) and allowed a determination of the central black hole mass from the average line profiles (Kaspi et al. 2000). The polarized spectrum of 3C 273 is shown in Fig. 6.9.

PG0844+349

It is a radio-quiet AGN at a cosmological redshift of $z = 0.064$ that, in comparison to most quasars, was not originally detected in the radio frequency: at radio wavelengths, its nucleus is unresolved (Kellermann et al. 1994). It was first discovered in the Palomar Green sample (Schmidt & Green 1983) and found to possess strong Fe II emission and weak forbidden narrow lines, a behavior that is expected from narrow-line Seyfert-1s (NLS1). On the other hand, the X-ray properties of PG 0844+349 are aligned with the NLS1 classification (a steep soft X-ray spectrum and strong variability, see Boller 2001), and the optical polarization measurements achieved by Afanasiev et al. (2011) also point towards a regular NLS1 object (optical continuum polarization of $0.85 \pm 0.10\%$). Hence, using type-1 AGN reverberation mapping techniques, Peterson et al. (2004) estimated the mass of the central black hole to be $(9.24 \pm 3.81) \times 10^8 \, M_\odot$. The polarized spectrum of PG0844+349 is shown in Fig. 6.10.

Table 6.6: Observation log: object name (Column 1), right ascension (Column 2), declination (Column 3), redshift (Column 4), date of observation (Column 5), total exposure time (Column 6), slit position angle (Column 7).

Object	α_{J2000} (hr min sec)	δ_{J2000} ($^\circ$ $'$ $''$)	z	Date of obs. (yyyy-mm-dd)	Total exp. (s)	φ_{SLIT} ($^\circ$)
NGC 4051	12 03 09.6	+44 31 53	0.002	2014-03-25	1800	1.6
NGC 4151	12 10 32.6	+39 24 21	0.003	2014-05-25	1200	30.0
3C 273	12 29 06.7	+02 03 09	0.158	2014-03-26	1320	-183.4
PG0844+349	08 47 42.4	+34 45 04	0.064	2014-11-22	2400	145.1
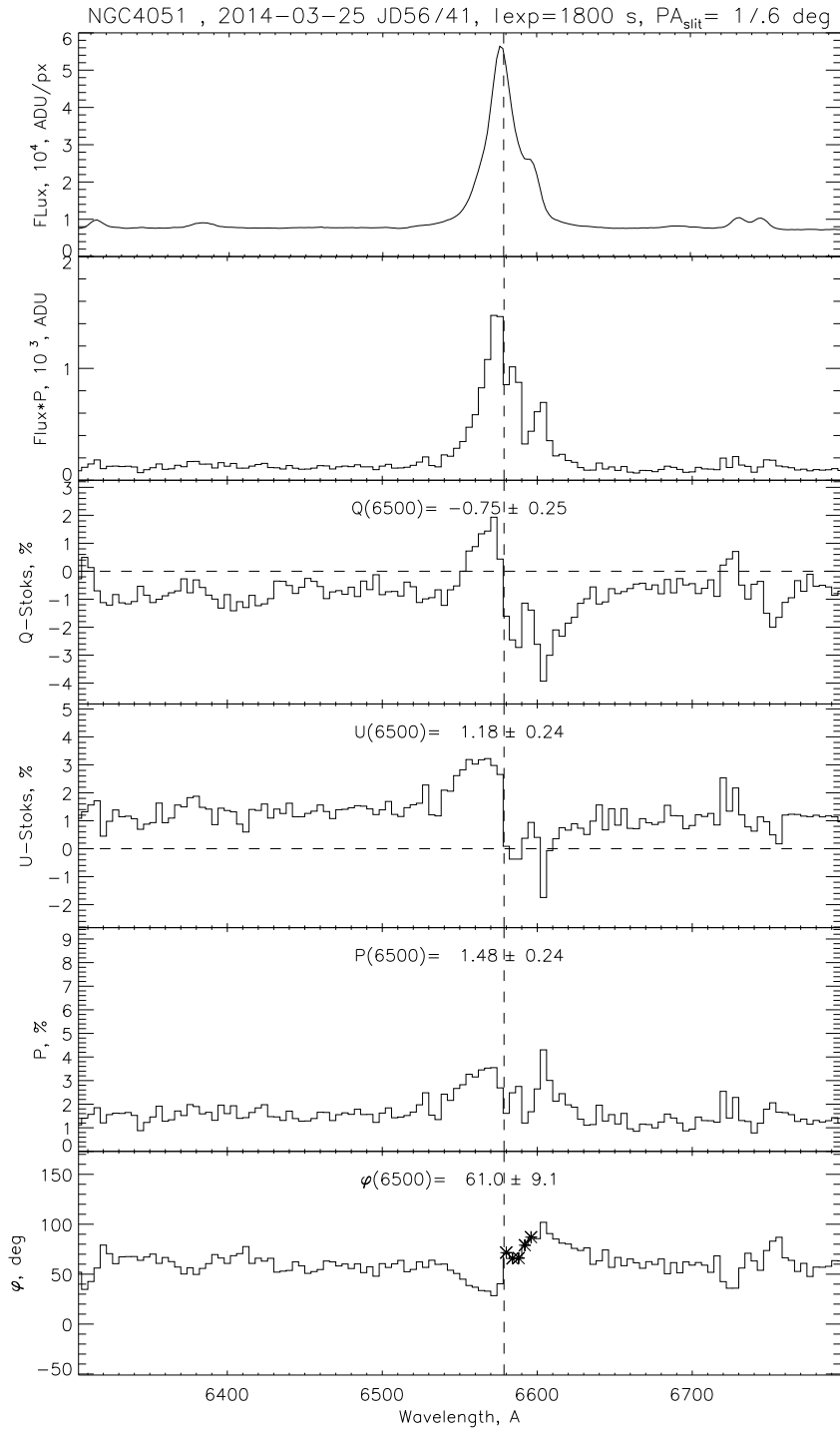
Figure 6.7: Polarized spectrum of NGC 4051. From top to bottom: Unpolarized flux; polarized flux; Q; U; p, φ. Values of the nearby continuum are denoted at each panel. At the top, the date of observations, exposure time and slit position is denoted. Credits: Viktor Afanasiev, private communications.
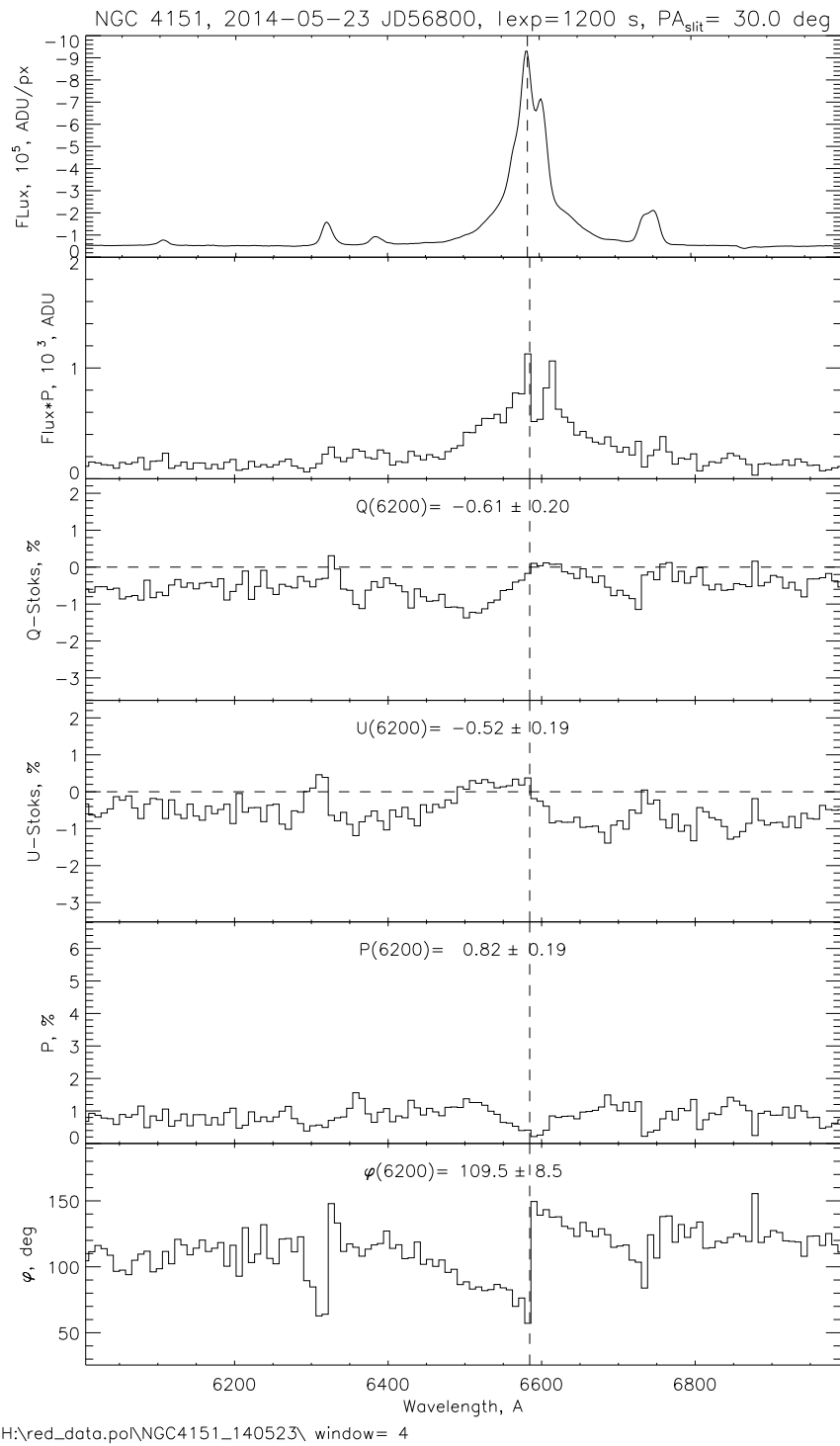
Figure 6.8: Same as in Fig. 6.7, but for NGC 4151. Credits: Viktor Afanasiev, private communications.
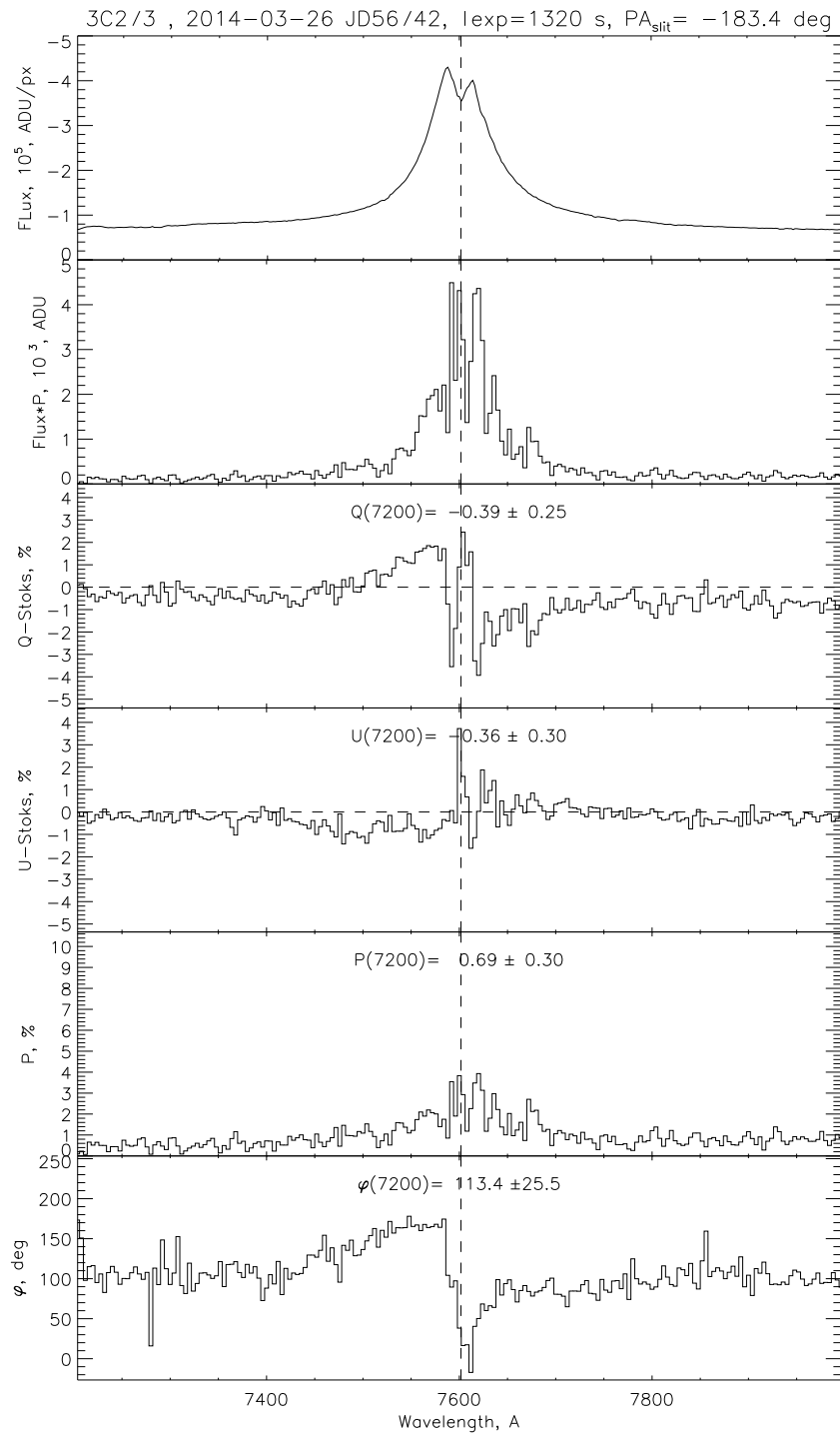
Figure 6.9: Same as in Fig. 6.7, but for 3C 273. Credits: Viktor Afanasiev, private communications.
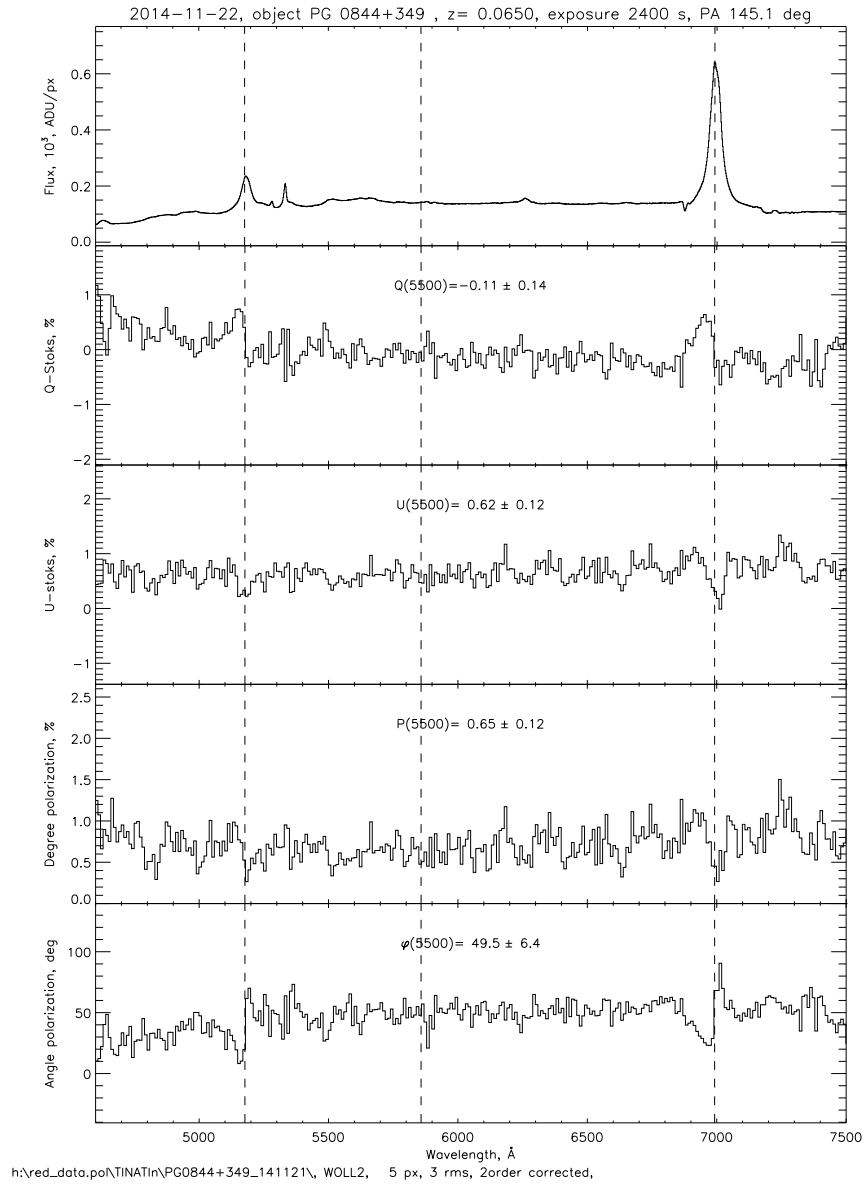
Figure 6.10: Same as in Fig. 6.7, but for PG0844+349. Credits: Viktor Afanasiev, private communications.

Chapter 7

Results and discussion

We present our results which can be divided into two parts, first, the results of modeling, and second we compare our models with observations. The same convention used by Goosmann & Gaskell (2007) was adopted in this work. Namely, φ is parallel to the symmetry axis of the model when $\varphi = 90°$, which was observed for type-1 objects, or φ is orthogonal to the symmetry axis when $\varphi = 0°$, that is again, observed for type-2 objects.

7.1 Generic modeling

We simulated different geometries of the BLR. First we performed the simulation for different masses of the black holes with assumption of a pure Keplerian motion, after that we consider the radial inflow and vertical outflow as additional components in gas motion to the Keplerian caused by the black hole mass. We simulated both cases where Keplerian motion is in anticlockwise (positive) and clockwise (negative) direction.

7.1.1 Pure Keplerian gas motion in the BLR

We consider the pure Keplerian motion of the BLR emitting gas, assuming that there are no other effects as e.g. outflows and inflows. We present the results of the four probe models. In Figs. 7.1 and 7.2, we show the simulated profiles of φ, polarized flux PF, degree of polarization p and total flux TF across the broad line profile.

Each scattering element can see the velocity resolved BLR emission which produces polarized lines that are broader than the unpolarized lines. Simulated degree of polarization is of the same order of magnitude as the one obtained from observations and is
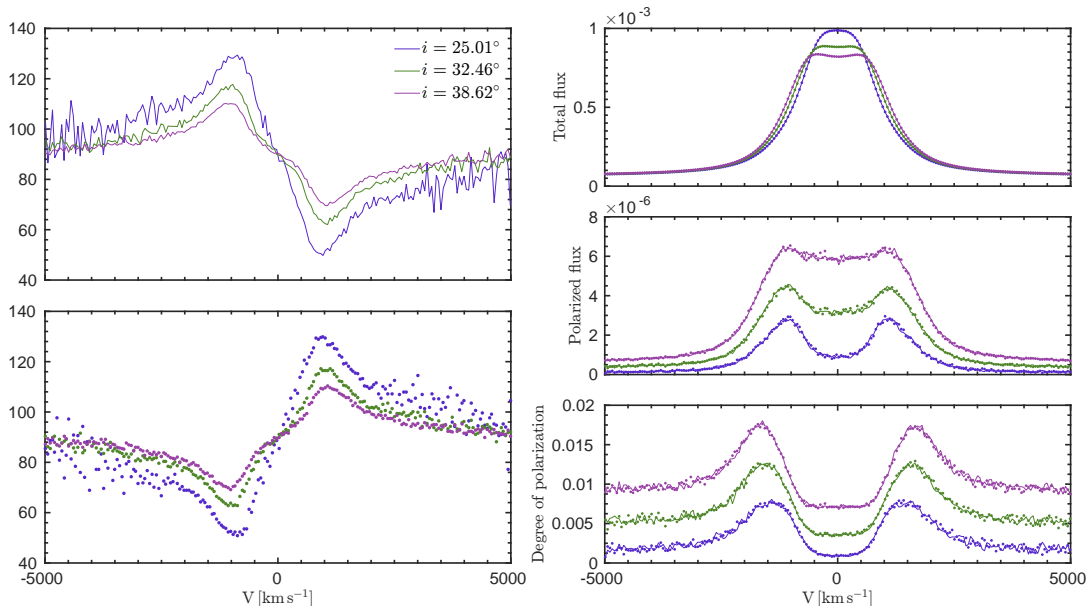
Figure 7.1: On the left panels, modeled polarization plane position angle φ is shown when the system is rotating anticlockwise (top) or when rotating in clockwise direction (bottom), total unpolarized flux (TF, top right), polarized flux (PF, middle right), degree of polarization p, bottom right. SMBH has mass of $10^6 \, M_\odot$. We plot the results in solid lines for three viewing inclinations: $i = 25.01°$, $32.46°$, and $38.62°$ respectively, while dotted lines represent the results for the opposite direction of rotation. Note the symmetry of φ with respect to the continuum level due to the opposite direction of rotation. Opposite direction of rotation does not affect TF, PF and p. Total and polarized fluxes are given in arbitrary units. Credits: adapted from Savić et al. (2018).

typically around 1% or less (Marin et al. 2016). From our models (Figs. 7.1 and 7.2, bottom right panels), we can see that the degree of polarization is sensitive to inclination. Extensive modeling with complex radiation reprocessing (see e.g. Marin et al. 2012, for more details) have shown that the total p is increasing as we start looking from the face-on viewing angle towards type-2 viewing angles. Although we included only equatorial scattering in our model, the dependence of p with inclination is following this trend. The p profile peaks in the line wings and reaches minimum in the line core just as it was shown by Smith et al. (2005). This feature was very well observed for the case of Mrk 6 (Smith et al. 2002; Afanasiev et al. 2014) and it is supporting the suggested scattering geometry.
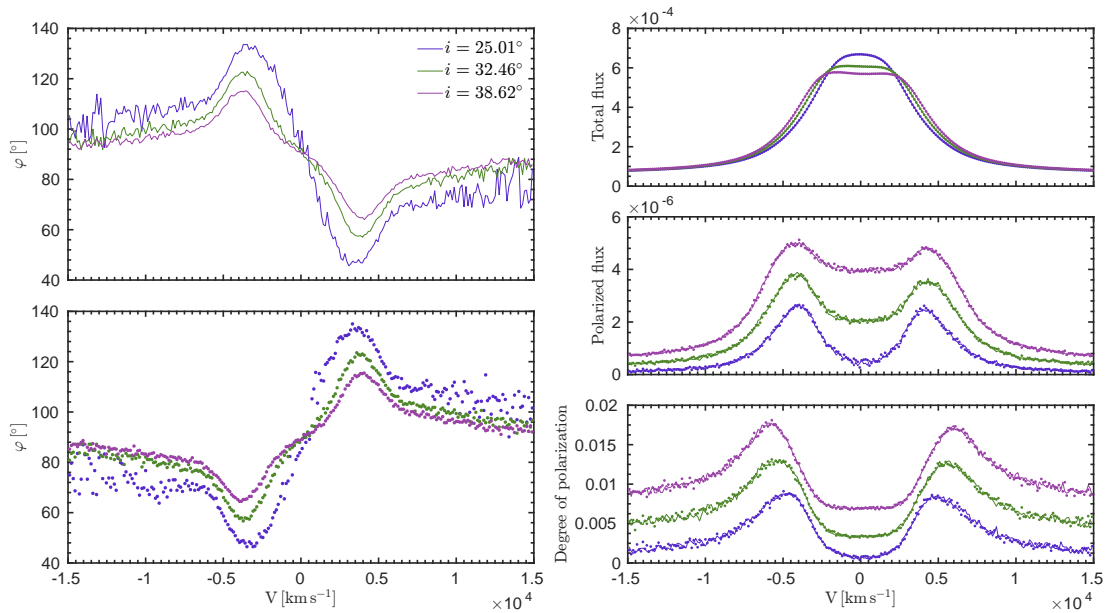
Figure 7.2: Same as Fig. 7.1, but for SMBH of $10^9 \, M_\odot$. Credits: adapted from Savić et al. (2018).

The polarization plane position angle is aligned with the disk rotation axis, hence also with the radio jet axis. In Figs. 7.1, 7.2 (left panels), we show the simulated profiles of φ for three viewing inclinations. The φ profiles show typical symmetric swing that was predicted for type-1 objects where the radiation from the Keplerian rotating disc-like BLR is being scattered by outer dusty torus (Smith et al. 2005, AP15). The direction of rotation only affect φ, while TF, PF and p remains unaffected. For anticlockwise rotation, φ reaches maximum value in the blue part of the line and minimum in the red part of the line. The φ swing occurs around the level of continuum $\varphi_c = 90°$. Due to the symmetry of the model (also for all other models performed in the paper), φ is symmetric with respect to the continuum polarization in such a way that for a given inclination i, it satisfies the following:

$$\varphi(180° - i) = 180° - \varphi(i). \tag{7.1}$$

In other words, for a given half-opening angle of the torus θ_0, and for type-1 inclinations where $0 \le i \le 90° - \theta_0$, observer can see one way of rotation, and the corresponding φ profile will be as shown in Figs. 7.1 and 7.2. If the system is viewed for type-1 viewing angle where $90° + \theta_0 \le i \le 180°$, opposite direction of rotation is observed

and the resulting φ satisfies Eq. 7.1. This symmetry can be seen in Figs. 7.1 and 7.2 (left panels). Thus spectropolarimetric observations of type-1 Seyferts can disentangle the rotation direction of the gas by observing the φ profile. The Eq. 7.1 is satisfied within the Monte Carlo uncertainty and it was used for improving photon statistics in our simulations by a factor of 2, by simply taking average value of the STOKES parameters for inclinations i and $180° - i$.

When performing AP15 method to the modeled data, one needs to consider polarization only in the broad line and for that, it was necessary to subtract the continuum polarization for all type-1 inclinations:

$$\Delta\varphi = \varphi - 90°. \tag{7.2}$$

Since all of our observed objects are rotating clockwise (see Sect. 7.2), we performed the AP15 method assuming opposite direction of rotation, without introducing new simulations. In Fig. 7.3 (lower panels), we show the fit described by AP15 method. We find that Keplerian motion can be traced across the φ profile for type-1 viewing inclinations. The region inside the 1σ error around the linear fit is becoming smaller as we go from face-on towards edge-on inclinations. For inclinations $25°$ or lower, the simulated data show much higher scatter around the straight line rather than for the cases with an intermediate inclination.

The effect of a wide SR (in our case $\theta_0 = 35°$) can lead to a mass estimates by a maximum of ~ 1.5 higher than the ones obtained for equatorial scattering, and only if the SR lies much farther away from the BLR (see Eq. 3.6). In this case, the influence of the viewing inclination must be taken into account.

It is important to note that in the Eq. 3.6, we used the inner radius of the SR in order to estimate the mass of the SMBH. However, the SR is not acting as a mirror from which the light is being scattered from the inner wall. Scattering events occur in the entire SR, and they all contribute to the total φ shape. Obtaining the value for parameter a is a straightforward procedure, but the final estimated SMBH value is largely depending on the actual value of R_{sc}. In the optically thick media, the largest fraction of photons is being scattered of the inner side of the SR.

One of the factors that have significant impact on the φ amplitude is the mutual distance between the BLR and the SR (Smith et al. 2005). The amplitude of φ is decreasing when mutual distance increases, which affects black hole mass estimation. Therefore, we investigated different cases with various mutual distances between the

Table 7.1: Input mass (Column 1), viewing inclinations (Column 2) and masses obtained for probe models (Column 3). Masses are given in $M_\odot$.

$\log(\mathcal{M}_{\text{input}}/M_\odot)$	$i(°)$	$\log(\mathcal{M}_{\text{mod}}/M_\odot)$
6.00	25.01	6.72 ± 0.10
	32.46	6.44 ± 0.06
	38.62	6.28 ± 0.05
7.00	25.01	7.59 ± 0.10
	32.46	7.30 ± 0.07
	38.62	7.17 ± 0.04
8.00	25.01	8.65 ± 0.11
	32.46	8.39 ± 0.07
	38.62	8.23 ± 0.06
9.00	25.01	9.67 ± 0.16
	32.46	9.43 ± 0.12
	38.62	9.27 ± 0.10
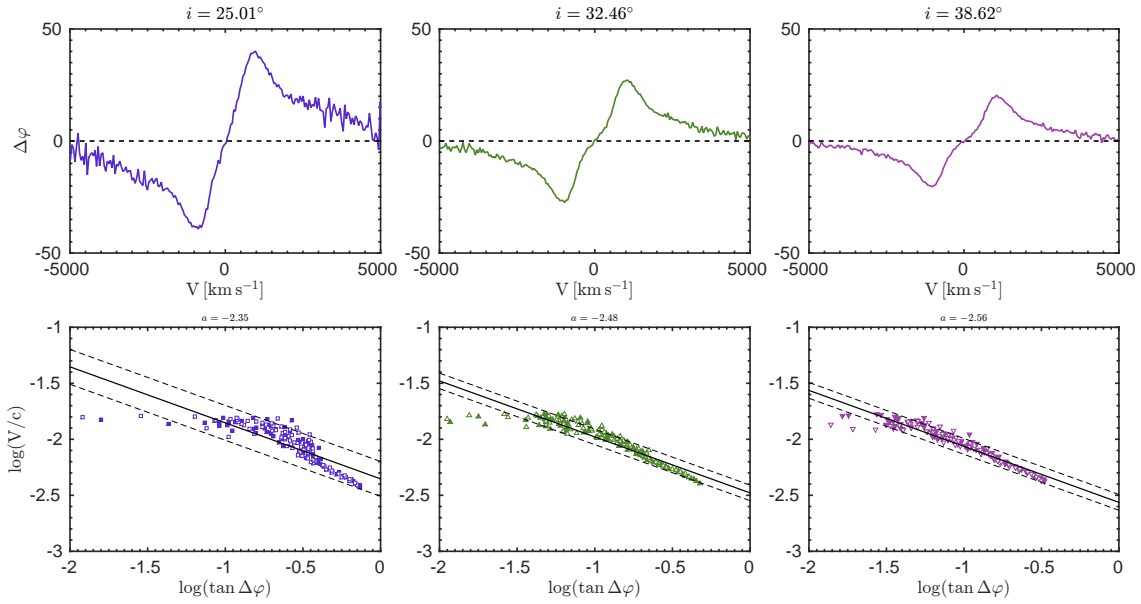
Figure 7.3: Modeled polarization φ (upper panels) and velocities (lower panels) across Hα profiles for the model with central mass of $10^6 \, M_\odot$. Filled symbols are for the blue part of the line and open symbols are for the red part of the line. Solid line represents the best fit of the straight line to the modeled data. Dashed lines denote 1σ uncertainty of the fit. Credits: adapted from Savić et al. (2018).
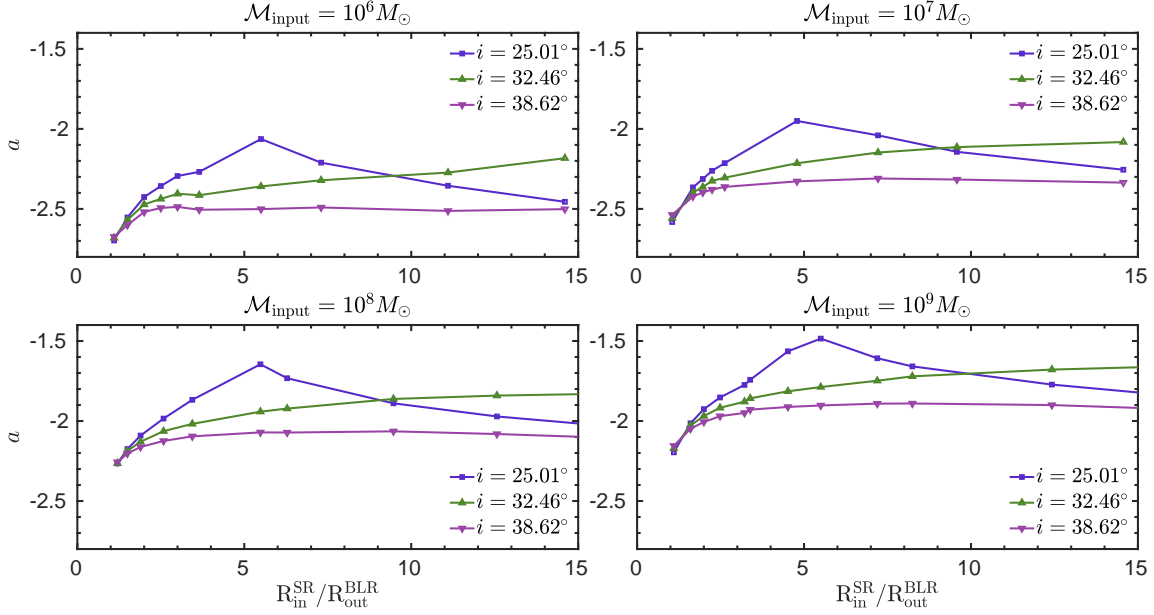
Figure 7.4: Dependence of the parameter a on the ratio between the inner radius of the SR ($R_{\mathrm{in}}^{\mathrm{SR}}$) and the outer radius of the BLR ($R_{\mathrm{out}}^{\mathrm{BLR}}$) for three given inclinations. Credits: adapted from Savić et al. (2018).
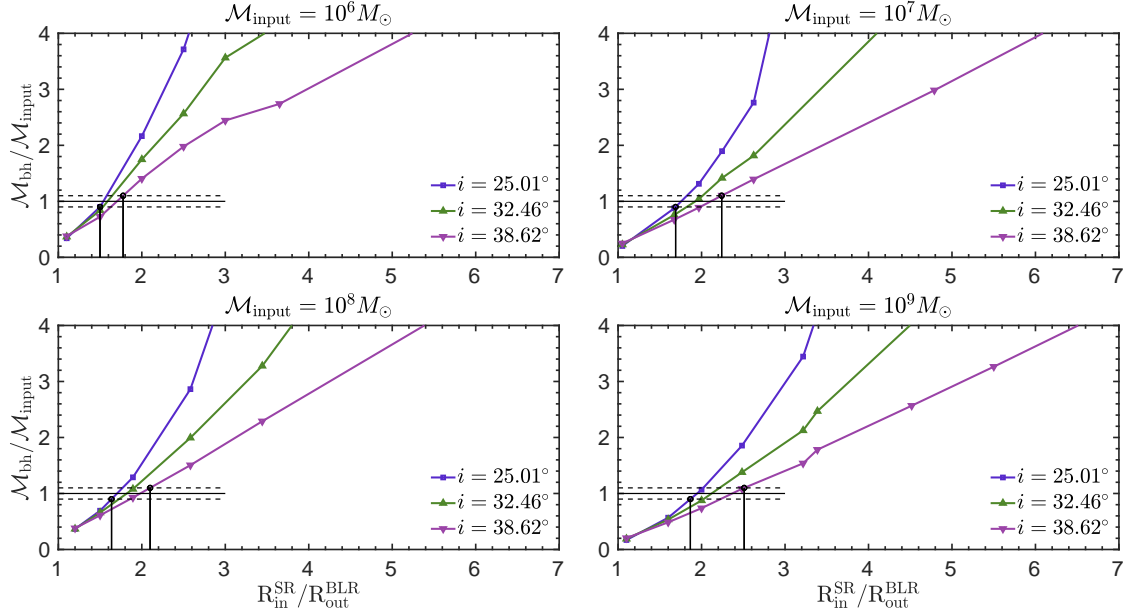
Figure 7.5: Black hole mass estimation as a function of the ratio between the inner radius of the SR ($R_{\mathrm{in}}^{\mathrm{SR}}$) and the outer radius of the BLR ($R_{\mathrm{out}}^{\mathrm{BLR}}$) for three given inclinations. Horizontal dashed lines represent the interval of 10% deviation from the input mass (solid line). Credits: adapted from Savić et al. (2018).

BLR and SR while keeping the same thickness and the optical depth of the SR. In Figs. 7.4 and 7.5, we show the influence of different mutual distance between the two regions, and how it affects the parameter a and SMBH estimates. Our models show that mutual distance between the BLR and SR has a great influence on the parameter a which consequently greatly affects our black hole mass estimates. One can see that parameter a shows the same profile and the same inclination dependence for all simulated cases. Only when the SR is adjacent to the BLR we obtain inclination independence of the SMBH mass estimates. Due to the nature of the Eq. 3.6, SMBH mass estimates are increasing when the mutual distance increase. For a given accuracy of 10%, we find that the best SMBH estimates for all four cases are when the ratio of the inner radius of SR and the outer radius of the BLR is between 1.5 and 2.5 (Fig. 7.5). For the inclinations of 25° or less (face-on view), contribution of equatorial scattering is low and we find that Keplerian motion cannot be recovered from the φ profile.

7.1.2 Keplerian motion and radial inflow

We investigated a particular case when the BLR is undergoing a constant radial inflow. We tested three cases with BLR radial inflow velocity equals to $500\,\mathrm{km\,s^{-1}}$, $1000\,\mathrm{km\,s^{-1}}$ and $2000\,\mathrm{km\,s^{-1}}$. Similarly as before, in Fig. 7.6, we show simulated profiles of φ, PF, p and TF. In this regime, the SR can see additional component of the BLR velocity, which as a net effect increases the absolute value of the radial velocity that a single scattering element can see. This leads to additional line broadening (Fig. 7.6, lower right panel) when compared with the case with pure gas Keplerian motion only. As a resulting effect, the distance between the positions of the maximum and the minimum of the φ is increased (Fig. 7.6, left panels). Therefore, for a low velocity radial inflow, mass estimates of the SMBHs are slightly higher than the ones obtained in the case with Keplerian motion only. This overestimation of the SMBH mass mostly affects the model for which the SMBH has mass of $10^6\,M_\odot$. For other models, Keplerian motion is even more dominant (except for the very extreme cases which are not expected) and the influence of the radial inflow can be neglected.

7.1.3 Keplerian motion and vertical outflow

Another contribution to velocity might be due to vertical outflows. We tested three cases for which the innermost one third of the BLR is undergoing a constant vertical
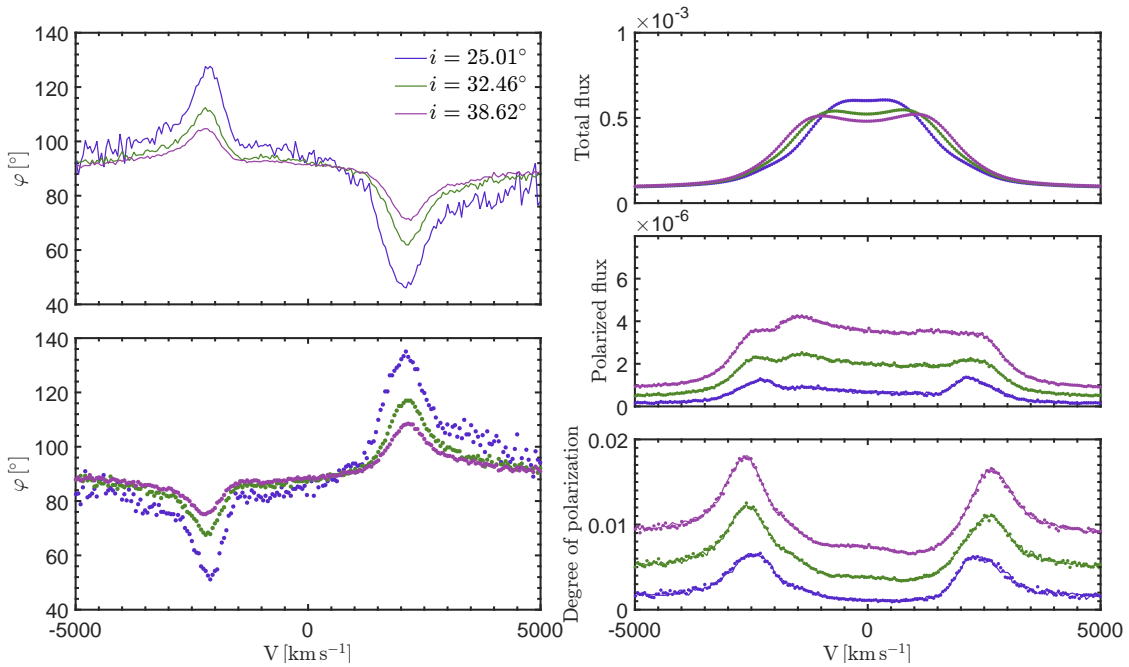
Figure 7.6: Same as Fig. 7.1, but beside Keplerian motion, by large inflow of $2000\,\mathrm{km\,s^{-1}}$ is included in the BLR kinematics. Credits: adapted from Savić et al. (2018).

outflow of $500\,\mathrm{km\,s^{-1}}$, $1000\,\mathrm{km\,s^{-1}}$ and $2000\,\mathrm{km\,s^{-1}}$. In this case, the equatorial scattering elements will not see this velocity component. Scattering elements above the equatorial plane will see this component multiplied by a factor of $\cos\alpha$, where α is latitude, to a maximum of $\cos 35°$. This can be neglected when the outflow velocity is much lower in comparison with Keplerian velocity. In Fig. 7.7, we show the results of simulated φ, PF, p and TF influenced by vertical outflows in the BLR of $2000\,\mathrm{km\,s^{-1}}$ for the case where SMBH has the mass of $10^6\,M_\odot$. Unpolarized line (bottom right panel) is additionally broadened in the wings. Polarized line (upper right panel) is almost the same as the one for the case with Keplerian motion only (Fig. 7.1, upper right panel) due to the reasons explained above. Contribution of outflow velocity is highest for nearly face-on view. In Fig. 7.8, left panels, the φ profile shows additional bump which prevents us from correctly using the AP15 method. It is important to point out that in our model, the BLR is transparent and that observer can see the radiation coming from both approaching and the receding part of the BLR outflows. We know from observations that this is not the case (e.g Mrk 6, Afanasiev et al. 2014), and we expect to observe radiation from the approaching side of the BLR outflows, while the radiation
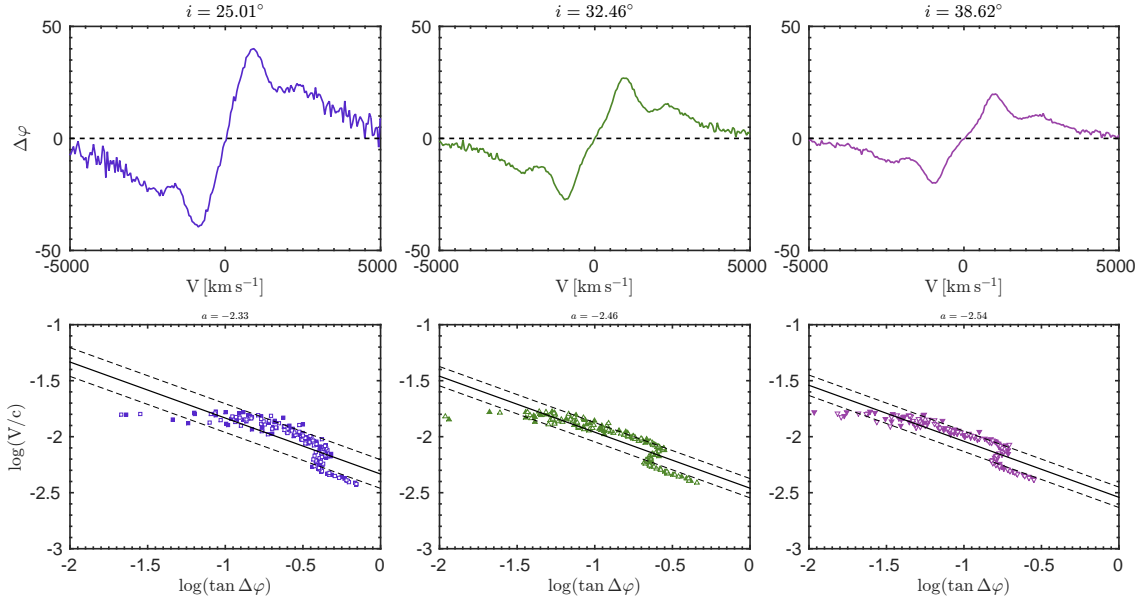
110
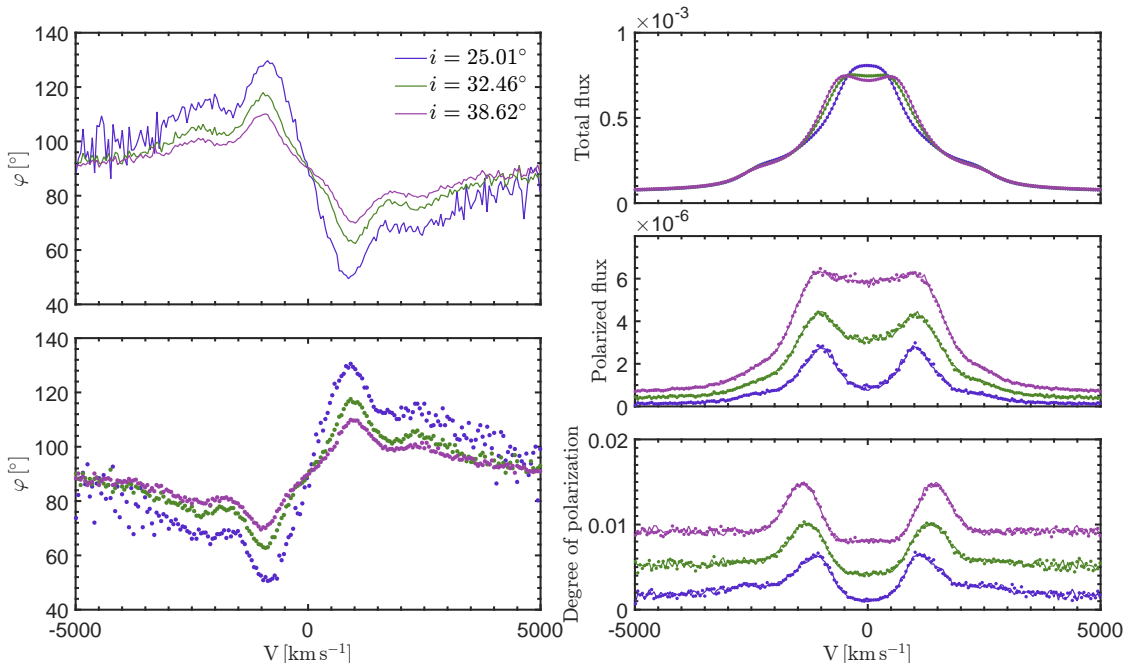
Figure 7.7: Same as Fig. 7.1, except that here the inner one third of the BLR undergoes a constant vertical outflow of $2000\,\mathrm{km\,s^{-1}}$. Credits: adapted from Savić et al. (2018).

from the receding side of the BLR outflows should be blocked, thus affecting only the blue part of the line which results in the asymmetric blue-shifted line.

7.1.4 The broad lines polarization due to the presence of SMBBHs

Distant

In Figs. 7.9 (panel a) and A.1 we show the simulated φ-profiles for two viewing inclinations i and for different azimuthal viewing angles ϕ. We can see that profiles of φ are complex and differ much from the profiles for the single black hole scenario. For a fixed viewing ϕ the φ-profiles show similar profiles with the peaks most prominent when viewed towards face-on inclinations. For different azimuthal viewing angles, φ-profiles are quite diverse. This diversity is the result of different velocity projections towards the observer since the model is not azimuthally symmetric. The φ-profiles are symmetric with respect to the line center which is not the case for a single case scenario where the swing occurs.

Figure 7.8: Same as Fig. 7.3, except that here the inner one third of the BLR undergoes a constant vertical outflow of $2000\,\mathrm{km\,s^{-1}}$. Credits: adapted from Savić et al. (2018).

Typical degree of polarization p found for type-1 objects is around $1\,\%$ or less. Our simulations show that p is in the range between 1–$4\,\%$ (Fig. A.2). This unusually high p is due to the high radial optical depth of the scattering region. It is inclination dependent and it is increasing when observing from face-on towards edge-on viewing inclinations as expected from Thomson law. For some ϕ (Fig. A.2, top left and bottom right panels), p profile peaks in the line wings and has a minimum value in the line core. This is the same as in the case for a single black hole scenario and it was confirmed by observations numerous times (e.g. Mrk 6 Smith et al. 2002; Afanasiev et al. 2014). However, this is not the case for all ϕ and we can see the opposite situation – p peaks in the line core and has minimum in the line wings.

The total flux shows variability in the line profiles A.3. Line profiles are sensitive both to viewing inclinations and viewing azimuthal angles. In general, double-peaked profiles are observed, with line width being broader when observing from face-on towards edge-on inclinations. Line widths are different with respect to ϕ with the broadest lines coming from the direction when $\phi = 90°$ or $\phi = 270°$ (Fig. A.3, middle upper and bottom panels). Some viewing angles are showing single-peak lines (Fig. A.3, top left and bottom right panels) and the corresponding p profiles are as in the case for a
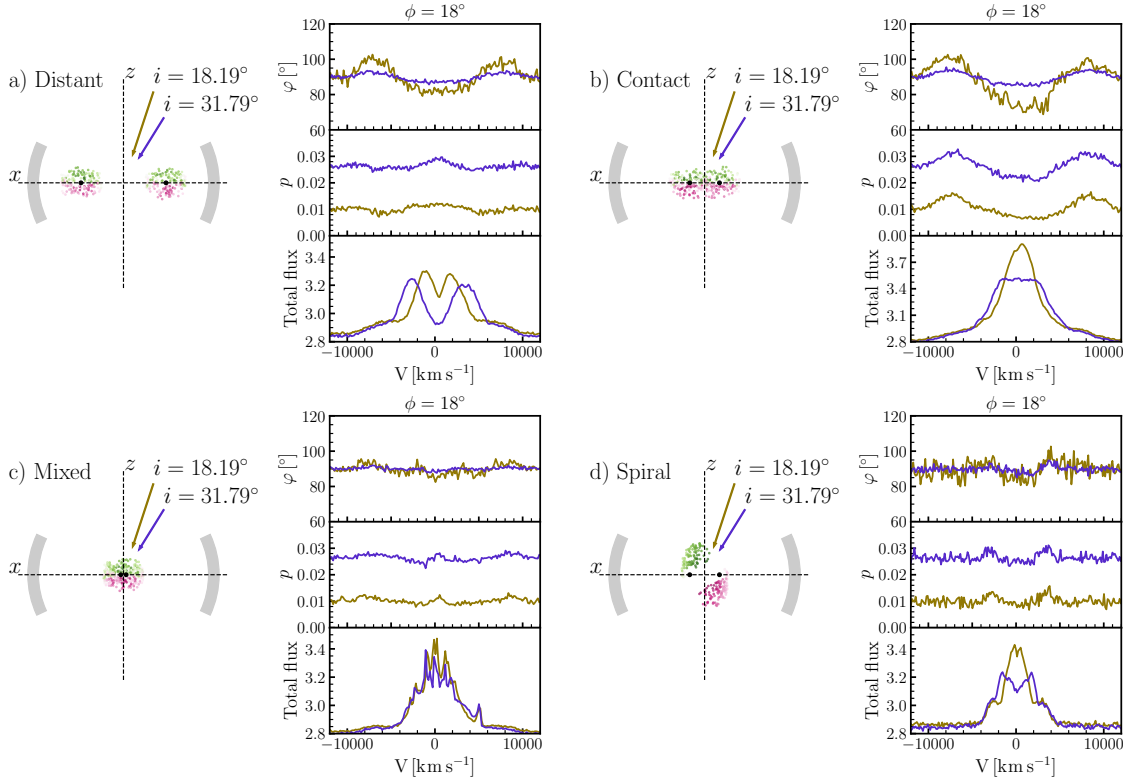
Figure 7.9: On the left panels the illustration of each model with SMBBH in the center: Distant (a), Contact (b), Mixed (c), Spiral (d). On the right panels, from top to bottom are φ, p and TF for two viewing inclination $i = 18°$ (brown line) and $i = 32°$ (blue line). Azimuthal viewing angle is $\phi = 18°$ for all plots. The projection of the Spiral model in the xz-plane is similar to the Contact model and for that purpose, spirals are slightly inclined for clarity. Credits: Savić et al. (2019).

single black hole scenario. This means that in the certain phase, we would not be able to observationally distinguish between the SMBBHs and SMBHs from the unpolarized optical spectra. However for this case, φ is showing different profile than expected, which could provide more insight if the SMBBHs is situated in the center.

For Distant model with mass ratio $q = 0.5$ we can expect asymmetric profiles for φ, p and TF (Figs. A.4, A.5, A.6). The φ is having similar profiles as for the case with mass ratio $q = 1$ except that peaks are not symmetric and they have different intensities. When compared with the previous case, the φ-profile is similar except for azimuthal viewing angles $\phi = 224°$ where the profile is flat in the core (Fig. A.4, lower left panel), or an additional swing can be noticed in the core for $\phi = 342°$ (Fig. A.4, upper right panel).

Degree of polarization is having profiles with the same shape as for the previous case except that they are asymmetric and it is the case for all viewing angles. We obtained the same order of polarization with the same inclination dependency (Fig. A.5).

The unpolarized line is showing a displaced single peak profiles when viewed almost face-on for most of the azimuthal viewing angles, except when $\phi = 224°$ and $270°$ where a clear double-peaked profile can be observed (Fig. A.6, bottom left and middle panels). For intermediate inclinations, line profiles are asymmetric with double peaks and with different line shifts depending on the azimuthal viewing angles (Fig. A.6).

For the same model with $q = 0.1$, we obtained similar profiles as before for φ, p and TF (Figs. A.7, A.8, A.9), however they are more asymmetric than for the case with $q = 0.5$. The φ is having similar profiles as for the cases with $q = 1$ and $q = 0.5$ with asymmetry highlighted (Fig. A.7).

The degree of polarization is showing profiles with the same shape in the same way as before for all viewing angles. Polarization is of the same order with the same inclination dependency (Fig. A.8).

The unpolarized flux is showing complex asymmetric profiles with line peaks having different positions as the system is viewed in different orbital phases (A.9). When $q = 0.1$, the more massive component is having smaller orbital velocity and it is much smaller compared to the Keplerian velocity of the BLR clouds surrounding it. For the less massive component, orbital velocity is of the same order in comparison with the Keplerian velocity of the BLR clouds surrounding it, which contributes to higher line shift. With these two effects combined, we observe highly asymmetric line profiles which significantly vary with the orbital phase.

Contact

This scenario is geometrically similar with the previous one with the SMBBHs being closer and allowing additional chaotic velocity component will affect the line profile mostly around its core. Simulated φ is shown on Figs. 7.9 (panel b); A.10. The φ profiles are also similar as in the case for separated BLRs. Figures A.10 (left panels; upper and middle right) clearly show two minima in the wings and a maximum in the line core; or minimum in the line core and maximum in the line wings. The observed φ profile is the most sensitive to random velocity when the system is viewed from $\phi = 90°$ and $\phi = 270°$ (Fig. A.10, middle up and bottom panels), for which we observe two minima and almost flat profile in the core. For $\phi = 342°$ (Fig. A.10, bottom right

panel) we see one peak in the red wing for the near face-on viewing i, while the profile is almost constant for the intermediate inclination. We expect that additional chaotic velocity component will affect the profile mostly the core, which is exactly what we get from the models.

In Fig. A.11 the resulting p is shown. The degree of polarization is in the same range as it was for the previous case. Again, p is increasing when viewing from face-on towards edge-on inclinations.

The total flux is largely affected by the additional random motion of the BLR clouds in the line core (Fig. A.12). We can clearly observe double-peaked lines for intermediate inclinations ($i = 38°$ and $i = 41°$, Fig. A.12, upper panels and bottom left and middle panels). For $\phi = 18°$, $198°$ and $342°$ (Fig. A.12), we observe single-peak profiles, and for intermediate inclinations, line cores are flattened. The highest line widths are for $\phi = 90°$ and $\phi = 270°$.

Mixed

With the two BLRs being mixed and surrounding both black holes, we can observe that the change of φ is small with the respect to the continuum level (Figs. 7.9 (panel c); A.13) and it is the highest for nearly face-on inclinations. For intermediate inclinations, the φ profiles could be considered as constant with additional noise. This is expected since the largest fraction of flux is coming from the clouds with additional random velocity components that are the close to the black holes.

Figure A.14 shows the resulting p for a set of viewing inclinations and azimuthal angles. We can see that the broad line profiles are almost flat with very low characteristic features. We obtain the same range for p as in the previous models.

The total flux is showing seemingly complex profiles (A.15) with multiple spikes. This is however due to the fact that we are very much limited to the number of BLR clouds when running the simulations. Running the STOKES code with more than 5000 individual clouds would be impractical and extremely time consuming. These results are in agreement as the ones obtained by Smith et al. (2005) i.e. we can see that an additional random velocity component besides the Keplerian applied to a large number of BLR clouds, have the tendency to smooth and flatten the resulting spectra. We obtain flat profiles for φ and PO, and we can expect a single peaked lines.

Spiral

In Figs. 7.9 (panel d); A.16 the results for φ for the spiral model are shown. The simulated φ is showing double peak profiles whether with minima or maxima occurring around $V \approx 3000 \, \text{km s}^{-1}$ for all i and ϕ. This velocity is close to the orbital velocity of each binary component for which $V \approx 2800 \, \text{km s}^{-1}$. This result is due to most of the emitted flux that is originating from the inner parts of the spiral arms closer to the black holes, and due to the velocity of the rigid body scaling with the distance. The intensity of the peaks is inclination dependent and is decreasing when the system is viewed from face-on towards edge-on inclinations.

In Fig. A.17 the results for the simulated p are shown. We can see that p is having similar profiles as φ – visible peaks in the line wings and minimum in the line core (Fig. A.17, left upper and middle panels; right bottom and middle panels) that is characteristic for a single black hole scenario, or the opposite profiles with maximum p in the line core and minimum in the wings.

The results for TF are shown in Fig. A.18. We can see various line profiles for different ϕ. For intermediate inclinations, we observe double-peaked line profiles. For near face-on viewing angles and some ϕ, profiles with strong single peak (Fig. A.18, bottom right panel), or two peaks very close to each other (Fig. A.18, middle left and right panels) are observed.

7.2   Comparison with observations

In table 7.2, we present the results of models for each observed AGN. First, we applied the AP15 method to observational data of each object – linear fit with a slope fixed to -0.5 and an offset a as the only free parameter (equation 3.4) in order to obtain $\mathcal{M}_{\text{pol}}$ (Table 7.2, Column 4). This value was then used as an input mass for running STOKES with model parameters given in Table 6.5 in order to obtain simulated (modeled) data for each observed AGN. Applying the AP15 method to modeled data, we obtain $\mathcal{M}_{\text{mod}}$ for three inclinations (Table 7.2, Column 3). Masses obtained by reverberation mapping are given for comparative purpose (Table 7.2, Column 5).

NGC 4051

We were able to obtain expected φ shape (Fig. 7.10, upper panels). The amplitude of the φ has very close value as the observed one for the lowest inclination in the model for

Table 7.2: Object name (Column 1), viewing angles (Column 2), SMBH masses estimated using AP15 method from the model (Column 3); from observations (Column 4) and from reverberation mapping (Column 5). $\mathcal{M}_{\mathrm{pol}}$ denotes masses obtained applying AP15 to the observational data, which were used as input mass. Masses obtained by reverberation mapping were taken from Bentz & Katz (2015) using virial factor $\langle f \rangle = 4.31 \pm 1.05$ (Grier et al. 2013).

Object	$i(°)$	$\log(\mathcal{M}_{\mathrm{mod}}/M_\odot)$	$\log(\mathcal{M}_{\mathrm{pol}}/M_\odot)$	$\log(\mathcal{M}_{\mathrm{rev}}/M_\odot)$
	25.01	7.2 ± 0.2		
NGC 4051	32.46	6.92 ± 0.09	6.69 ± 0.21	6.24 ± 0.13
	38.62	6.78 ± 0.06		
	25.01	7.56 ± 0.07		
NGC 4151	32.46	7.40 ± 0.03	7.21 ± 0.27	7.12 ± 0.05
	38.62	7.27 ± 0.04		
	25.01	8.94 ± 0.09		
3C 273	32.46	8.90 ± 0.09	8.85 ± 0.27	8.83 ± 0.11
	38.62	8.87 ± 0.08		
	25.01	8.00 ± 0.08		
PG0844+349	32.46	7.95 ± 0.06	7.70 ± 0.23	7.85 ± 0.21
	38.62	7.88 ± 0.06		

which $i = 25.01°$. For this inclination, the position of the maximum and the minimum of φ is displaced which yields the highest mass estimate. As we start viewing the system for larger inclinations, the φ amplitude is decreasing and we obtain better fits of the line wings (Fig. 7.10, lower panels), and the difference between the estimated values of the SMBH masses and the input mass is smaller. We can see that simulated data in the line wings for $i = 25°$ are deviating from the theoretically predicted straight line (Fig. 7.10, upper left panel). For intermediate inclinations the 1σ offset is smaller and the fit is better. Similarly, SMBH masses estimated from the fitting of the model data are higher than the input mass as it was in the previous case. For this object, $R_{\mathrm{in}}^{\mathrm{SR}}/R_{\mathrm{out}}^{\mathrm{BLR}} \approx 2.54$.

NGC 4151

Similar as in the previous case, we obtain the highest mass estimate for the lowest inclination. Keplerian motion is very well shown as a straight line (Fig. 7.11, lower panels), where 1σ error is small, especially in the case for which $i = 39°$. For this object, $R_{\mathrm{in}}^{\mathrm{SR}}/R_{\mathrm{out}}^{\mathrm{BLR}} \approx 2.51$. We can see that in the extreme wings of the line, the

modeled φ becomes very sensitive to spectral resolution and this sensitivity is smaller for higher inclinations.

3C 273

We obtained very low φ dependence on inclination, however, the φ amplitude is much smaller, around 19° for all inclinations (Fig. 7.12). Model data show deviation from the straight line in the line wings, however, the scatter is much smaller than it is for the observational data. The ratio $R_{in}^{SR}/R_{out}^{BLR} \approx 2.19$ is the lowest when compared with other observed objects. Mass estimates follow previous trend – the highest estimate for the lowest inclination.

PG 0844+349

We can see from observations that φ profile is asymmetric and that φ amplitude is greater for the red part of the line than for the blue part. Results are similar as for the first two objects (Fig. 7.13), $R_{in}^{SR}/R_{out}^{BLR} \approx 2.44$.

7.2.1   Overall results

For all modeled objects, we were able to produce very similar profiles of φ as the observed ones (Figs. 7.10, 7.11, 7.12, 7.13, upper panels). SMBH masses estimated from the fitting of the model data are higher than the ones obtained by fitting the observational data and the obtained values are decreasing as the viewing inclination increases (Table 7.2). This is due to the fact that the φ amplitude is very sensitive to inclination and is decreasing when viewing from face-on towards edge-on inclinations (from lower to greater). For all observed objects, modeled p ranges from 0.5% to 1.5% for inclinations from lowest to highest. As a measure of the strength of a linear association between the model data and the fit, we give the values of the Pearson correlation coefficient r. For all objects we find that the correlation coefficient r is greater than 0.9, except for NGC 4151 when viewed from inclination $i = 25.01°$ (Fig. 7.11, lower leftmost panel). The corresponding p values are very close to 0, indicating a strong linear connection between the modeled data and the fit. Observational data are much more scattered from the predicted straight line, which in general yields an error of the SMBH mass estimates a few times greater when compared with an error obtained by reverberation mapping Afanasiev & Popović (2015). In the case for NGC 4051 and NGC 4151, the
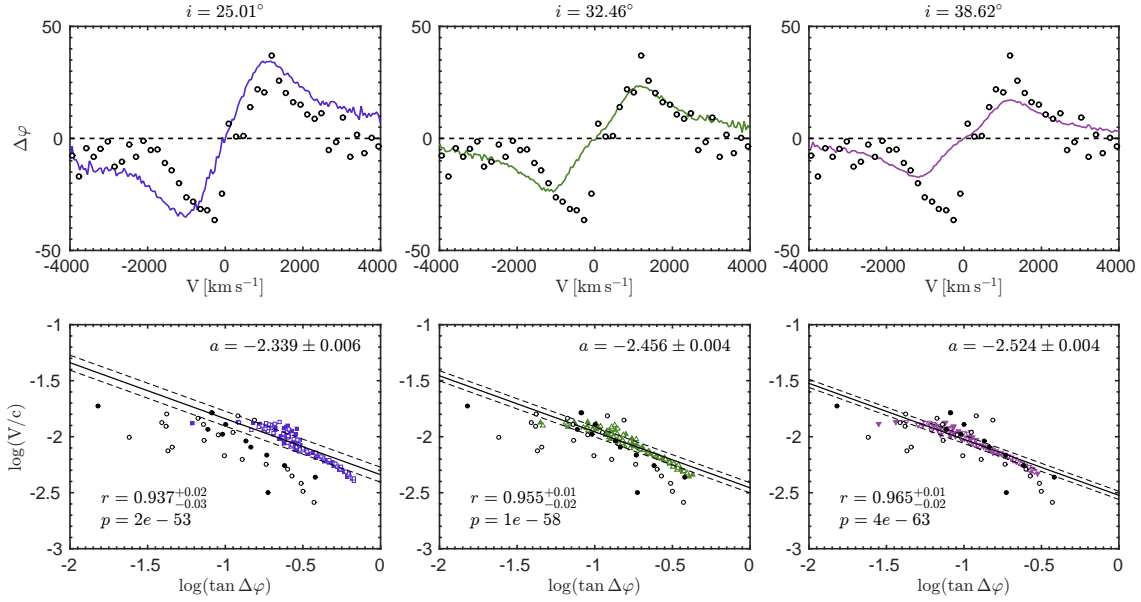
Figure 7.10: Modeled broad line polarization position angle φ (upper panels) and velocities (lower panels) across Hα profiles for the NGC 4051. On the upper panels, data obtained by models is depicted as line while observed data are depicted by empty circles. On the lower panels, filled symbols are for the blue part of the line and open symbols are for the red part of the line for model data. Black circles depict observed data. Solid black line represents the best fit of the straight line to the modeled data. Dashed lines denote 1σ uncertainty of the fit. Values of the parameter a, correlation coefficient r and the corresponding p values are shown. Credits Savić et al. (2018).

match between the modeled data and the observational data is the best for the highest inclination (Figs. 7.10, 7.11, rightmost bottom panels), while the offset is the largest when the system is viewed more towards pole on direction (Figs. 7.10, 7.11, bottom left and middle panels). The 1σ fit uncertainty of the modeled data is smaller for intermediate inclinations. The largest overestimate of the SMBH mass, by a factor of 3, is for NGC 4051 for $i = 25°$. For all models $R_{in}^{SR}/R_{out}^{BLR} > 2$. This falls in the regime where the SMBH mass estimates show dependence on inclination. We achieve the best SMBH mass estimates for inclinations $i \approx 39°$ which is close to the value of an average inclination ($i = 39°$ for type-1 objects (Lewis et al. 2010; Hryniewicz & Czerny 2012).
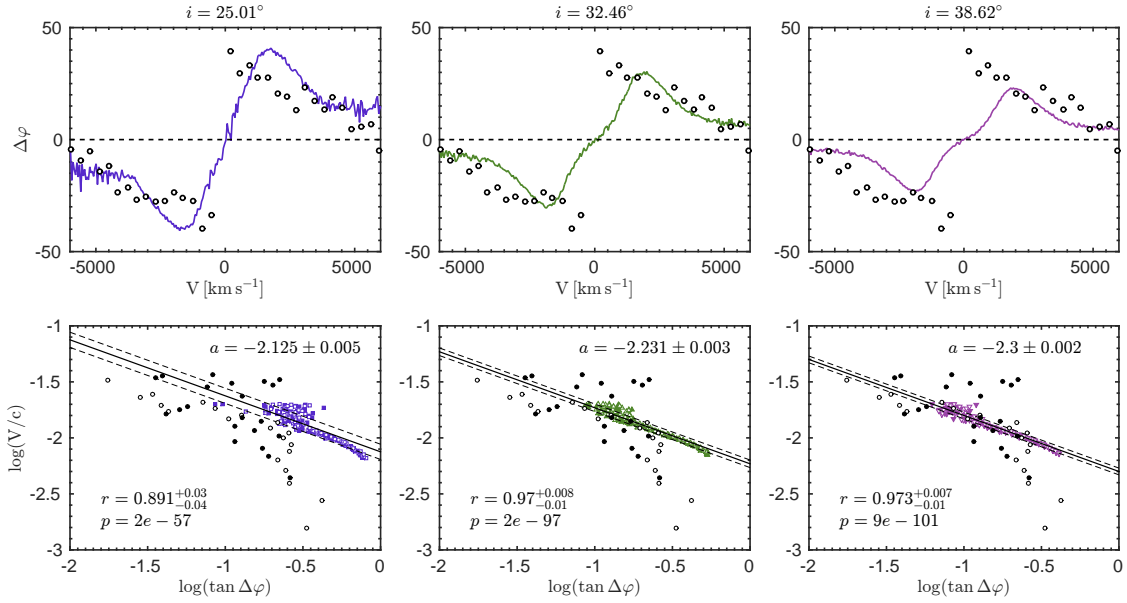
Figure 7.11: The same as in Fig 7.10, but for NGC 4151. Credits Savić et al. (2018).
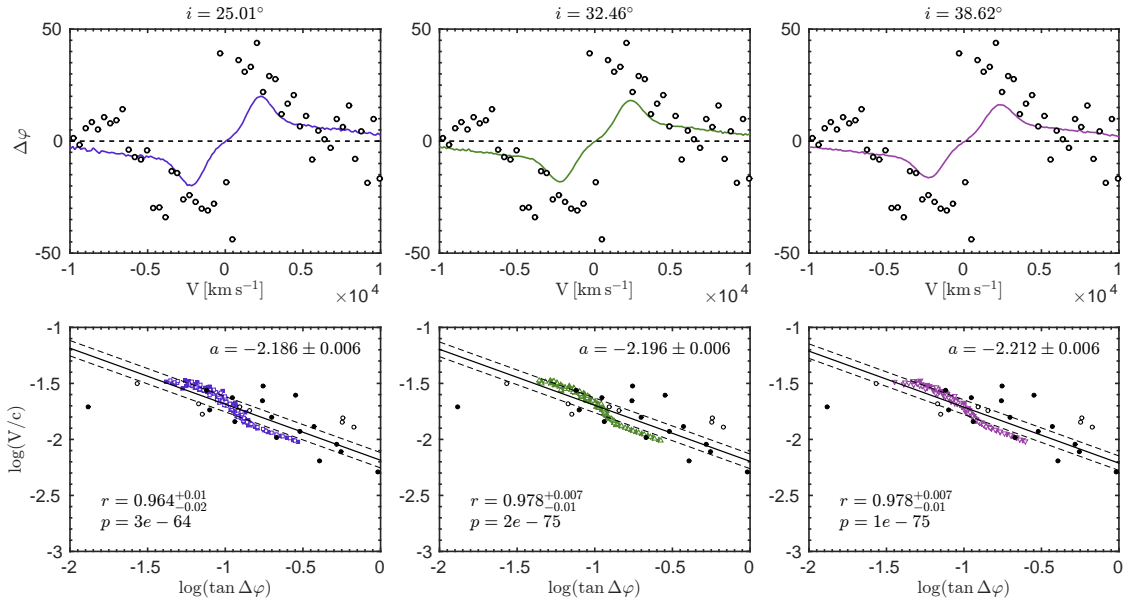
Figure 7.12: The same as in Fig 7.10, but for 3C 273. Credits Savić et al. (2018).
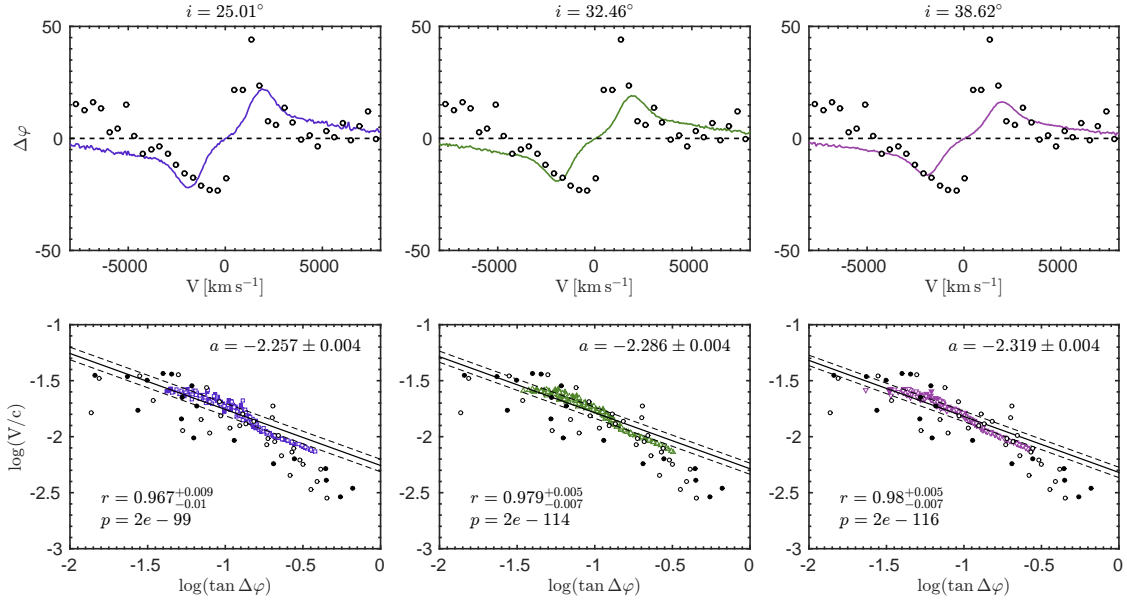
Figure 7.13: The same as in Fig 7.10, but for PG0844+349. Credits Savić et al. (2018).

7.3 Discussion

Previous spectropolarimetric studies of Type-1 Seyferts have shown that the polarization signature across the broad Hα is widely varying from object to object (Smith et al. 2002). At intermediate viewing inclinations, equatorial scattering is dominating the observed polarization and the wavelength averaged polarization angle φ is closely aligned with the projected radio source axis. In their original model, Smith et al. (2005), have used single scattering approximation i.e. photons emitted from the BLR are being scattered only once from the SR before finally reaching the observer. In their model, SR is optically thin and we find that optical depth of at least 1 along with the higher covering factor of the SR is required to in order to obtain φ and p comparable with observations.

In our Monte Carlo simulations, the treatment of multiple scattering events was fully performed and we find that the largest fraction of photons is being scattered only once, while the other, smaller fraction of photons is undergoing a backward scattering from one side of the SR to the other. This secures good circumstances for the application of the AP15 method. In our model, we approximated the emission of an accretion disk as a point source of isotropic continuum emission. We know that this is not the case and that anisotropy arises due to change in the projected surface area and due to limb darkening effects (Netzer 1987). The strongest emission is in the direction perpendicular

to the disk and is rapidly decreasing towards edge-on viewing angles. The inner radius of the SR thus cannot be constant, and should follow similar dependence on the polar angle as the disk emission (Stalevski et al. 2016). Silicate and graphite dust grains have different sublimation temperatures. Graphite grains can survive up to $\sim 1900\,\mathrm{K}$ and therefore reach closer than silicates which are destroyed when the temperature is $\sim 1200\,\mathrm{K}$. Furthermore, smaller dust grains are destroyed at the lower temperatures than the larger grains (Draine 1984; Draine & Lee 1984; Barvainis 1987). Therefore, we can expect an entire sublimation zone, from graphite to silicate and from larger to smaller dust grains (Kishimoto et al. 2007; Mor & Netzer 2012). This gives opportunity for dust particles to inhabit equatorial region in the close vicinity of the BLR. Equatorial scattering of broad lines from the adjacent SR gives very low inclination dependence on the parameter a rendering the AP15 method inclination independent.

For SMBH mass estimates using the AP15 method, the inner radius of the torus is needed. It can be obtained directly using dust reverberation in the infrared (Kishimoto et al. 2011). The number of objects for which dust reverberation has been performed is smaller than the number of objects for which the reverberation have been performed in optical. For most of the objects, $R_{\mathrm{in}}^{\mathrm{SR}}$ can be calculated only through scaling relations, which can additionally increases uncertainties in the SMBH estimates. Another way of calculating $R_{\mathrm{in}}^{\mathrm{SR}}$ is from the UV radiation (Barvainis 1987). For this we need to know a priori the physical and chemical composition of dust. Using the right value is important since estimated BH mass is directly proportional to the inner radius.

Seyfert 1 galaxies are often highly variable and when they are in a state of the minimum activity (up to the Type-2), the shape of the position angle of the polarization plane cannot be detected because of the weakness or absence of a flux from the broad line. In this case, the mass estimation using AP15 method is not applicable, even if the object is confidently assigned to the type of objects with equatorial scattering. Therefore, in future modeling, one must take into account the variability of an AGN.

Originally the AP15 method was proposed for systems with an inclination between $20°$ and $70°$. For high viewing inclinations, we have Type-2 objects for which polar scattering dominates the polarization signal and the methods is not longer valid. For almost pole-on AGN, the AP15 method faces two problems. First the amount of interstellar polarization can dominates over the amount of scattering-induced radiation from the innermost regions of AGN. The amount of interstellar polarization is wavelength-dependent and often maximum in the optical band (see Serkowski et al. 1975). Since the polarization signal of polar AGN in the optical band is usually much lower than 1%

in the optical (Smith et al. 2002; Marin 2014), the AP15 method is thus restricted to inclinations higher than 20 degrees. Second, the method overestimates SMBH mass by a factor of 1.5 in comparison with the value obtained for the lowest inclination when $R_{\text{in}}^{\text{SR}}/R_{\text{out}}^{\text{BLR}} \approx 2$. When the SR is closer, inclination effect is lower and the mass estimates are only depending on the SR inner radius.

7.3.1 The use of spectropolarimety for measuring SMBH masses

We point out at several recent works (Piotrovich et al. 2015; Baldi et al. 2016; Songsheng & Wang 2018) introduced new ideas to use the spectropolarimetry to estimate BH mass in AGNs. Basically, all above mentioned papers try to constraint the virial factor (Piotrovich et al. 2015; Songsheng & Wang 2018), or to use the broad polarized line (Baldi et al. 2016) to find the black hole mass. In the work by Songsheng & Wang (2018), the authors performed Monte Carlo simulations for a wide range of parameters assuming a static flared-disk geometry for the equatorial region. In comparison to the unpolarized spectra, the virial factor of the polarized spectra has a much narrower distribution. Besides, the half opening angle of the BLR and the nucleus inclinations appear to be the two parameters with the highest influence on the virial factor. The difference between the methods mentioned above and AP15 is that the AP15 method provide direct measuring of the BH mass from the polarization angle, and here we also used a similar geometry as Songsheng & Wang (2018), but focusing on a polarization plane position angle φ and the limits of the AP15 method. In comparison, our 3D polarized radiative transfer simulations have shown that the polarization plane position angle is largely affected by the distance between the BLR and SR. If the two share similar values, the mass estimated using AP15 method becomes inclination independent, which is a great advantage in comparison to traditional reverberation mapping techniques. AGNs with unpolarized double-peaked profiles with varying red and blue peak with respect to each other are probably the best candidates in the search for SMBBHs. Although a single SMBH in the center of AGNs is the most probable case, SMBBH in the central engine should have their distinctive signature in the polarized spectra due to the polarization sensitivity on geometry and kinematics. In the case of SMBBHs, we find that the AP15 method is not applicable due to the different φ-profiles

Chapter 8

Conclusions and future prospects

8.1 Conclusions

In this work we theoretically investigated the limits of applicability of a novel method for measuring masses of SMBHs in type-1 AGNs. This method (AP15) allows us to directly determine the SMBH mass from a single-epoch spectropolarimetric observation. This method assumes that the broad emission lines are formed in a disk-like region and that the line polarization is due to the light scattering of the inner side of the dusty torus (equatorial scattering). Unlike other methods, Keplerian motion is not *a priori* assumed, but is directly observed from the polarization angle profile. Although the optical polarization of type-1 AGNs is typically low, of the order of 1%, it is still measurable, and allows us to estimate the SMBH mass.

We modeled equatorial scattering using 3D Monte Carlo radiative transfer code STOKES that accounts for multiple scattering and includes kinematics for proper treatment of polarization. We considered a case where the BLR has a dominant Keplerian motion as well as complex BLR kinematics in the form of radial inflows, vertical outflows or due to the existence of SMBBHs. We investigated impact of these effects on the accuracy and the feasibility of the AP15 method. We employed the STOKES code for modeling spectropolarimetric data of NGC 4051, NGC 4151, 3C 273 and PG0844+780 that were observed with the 6 m BTA telescope of the SAO RAS. From the analysis presented here, we conclude the following (Savić et al. 2018; Savić 2019; Savić et al. 2019):

1. If Keplerian motion can be traced through the polarized line profile, then direct estimates of the SMBH mass can be performed for obtaining values in agreement with other methods.

2. The effects of possible inflow/outflow configurations of the BLR take its toll only in extreme cases where the velocity of inflowing/outflowing emitters is comparable to or higher than the Keplerian velocity, which in that case cannot be correctly used.

3. The polarization degree and the total flux exhibit profiles that are similar for single SMBHs and for SMBBHs and alone may prove inconclusive whether a SMBH or SMBBH drives the central engine of AGNs. On the other hand, the polarization position angle φ shows quite unique profiles that differ from those observed in the single SMBH scenario, and could be used for identifying SMBBH candidates.

4. The φ-profiles for a single SMBH model show point-symmetric profiles even when additional motions in the BLR are present.

5. The φ-profiles for SMBBH models produce axis-symmetric profiles which are often double or multi-peaked.

6. The application of the AP15 method is not feasible for the case of SMBBHs.

7. The AP15 method provides a new independent way of SMBH mass estimation. Estimated SMBH masses are in a good agreement with the values obtained by other methods such as reverberation mapping. The relative error of mass estimates between these two methods is around 30 %.

8.2 Future prospects

Afanasiev et al. (2019) have used the AP15 for a sample of 30 type-1 AGNs. The same authors have also found viewing inclinations, maximal extents of the BLR and the index of the power-law emissivity, demonstrating that the AP15 method is in a good agreement with the $\mathcal{M}_{\mathrm{bh}} - \sigma_*$ relation and that it can be used for calibrating the reverberation mapping method by constraining the virial factor as well as for calibrating any other secondary or tertiary method for SMBH mass measuring. However, the AP15 method has been applied so far only for nearby type-1 AGNs exploiting the polarization

of Hα spectral line, although it could also be applied to Hβ and also to highly ionized broad emission lines as Mg II, C III] and C IV. These lines are known for their slightly blueshifted peaks and very often asymmetric profiles with a larger excess in the blue part of line. Such line profiles are very often associated with the additional BLR complex motion as radial inflows and vertical outflows (Gaskell 1982; Baskin & Laor 2005). The Mg II line is no exemption, and recently, Popović et al. (2019) have shown that a significant inflow/outflow velocity component of a few thousand of $\mathrm{km\,s^{-1}}$ is present. Knowing that the polarization state is highly sensitive to geometry and kinematics, the presence of high inflowing/outflowing components in the BLR should have a strong influence on the polarization of the Mg II broad emission line. In order to test the AP15 for the Mg II line, in February 2019, we carried out the spetropolarimetric observations of the quasar SBS 1419+538 ($z = 1.862$) on the 6 m telescope BTA of SAO RAS with the focal reducer SCORPIO. We will compare these new observations with radiative transfer models, which will include calculations of Mg II line polarization (Savic et al. in preparation). We plan to observe a few more highly redshifted AGNs using the same equipment during the next observational cycle starting in January 2020. Future model extensions will include more complex kinematics of the scattering regions and clumpy or multi-phase dust medium.

This document contains 74 figures, 8 tables, and 455 references.

Appendix A

Detailed results of the SMBBHs polarization modeling

Simulations for all models are presented in the figures from A.1 to A.18. The simulated profiles for φ, p and TF are given for two inclinations: $i \approx 18°$ and $32°$. Azimuthal viewing angle takes eight values: $\phi = 18°$, $54°$, $90°$, $126°$, $198°$, $224°$, $270°$ and $342°$. The results are given as a function of velocity defined as $V = c(\lambda - \lambda_0)/\lambda_0$, where λ is wavelength and λ_0 is the central wavelength of a given spectral line. The broad line region for each model is shown in the center of every image. Arrows represent the velocity field of the BLR. For each model, we outline the main features for completeness.

Distant

This case is shown in Figs. A.1-A.3 for mass ratio $q = 1$. In Fig. A.1 the polarisation angle φ is shown. We can observe a double-peaked profiles of φ that drastically vary depending on the orbital phase of the system. For $\phi = 18°$ and $198°$, φ reaches maximum values in the line wings and minimum in the core, while for $\phi = 90°$ and $\phi = 270°$, it is the opposite way around. The p is shown in Figs. A.2 shows similar profiles as φ, but they are not correlated. Profiles with minimum in the core and maxima in the wings, which is common for the single SMBH scenario can be seen for $\phi = 126°$ and $342°$. The opposite profiles are for $\phi = 18°$, $54°$, $198°$ and $234°$. The TF is shown in Fig. A.3. Double-peaked profiles can be seen for $\phi = 18°$, $54°$, $198°$ and $234°$ and for all viewing inclinations. Single-peaked profiles are for $\phi = 342°$ and $\phi = 126°$.

 The results of the same model for mass ratio $q = 0.5$ are shown in Figs. A.4-A.6. The φ and p are shown in Figs. A.4 and A.5 respectively and both are following the same

trend as it was for the case with mass ratio $q = 1$ and both are showing mild asymmetry in profiles. The TF (Fig. A.6) is showing asymmetric double-peak or single-peak profiles with the positions of the peaks varying depending on the observed orbital phase of the system. For $q = 0.1$, simulated profiles for φ, p and TF are shown in Figs. A.7-A.9. The results are very similar as in the previous case with remarkable asymmetry in the profiles.

Contact

The results for this model are shown in Figs. A.10-A.12. The φ-profiles are shown in Fig. A.10 for different orbital phase of the system. Profiles are very similar as the ones obtained for **distant** model, but with greater amplitude of maxima/minima. The p profiles are shown in Fig. A.11. For $\phi = 18°$, $198°$ and $342°$, the profiles are the same as for the single SMBH scenario, while for all the other azimuthal viewing angles, the maximum p is in the line core. The TF is shown in Fig. A.12. Lines are the broadest when viewed for $\phi = 90°$ and $270°$. The random velocity component in this model that is present in the BLR flattens the line profiles, making it difficult to distinguish between sinle-peaked and double-peaked profiles.

Mixed

Simulations for this model are shown in Figs. A.13-A.15. Polarization angle is shown in Fig. A.13. The φ-profiles are double-peaked for $\phi = 18°$, $126°$ and $198°$. A swing in the φ-profile in the line core, common for single SMBH, can is when $\phi = 270°$. The p is overall flat with very mild features in the line core (Fig. A.14). As explained in the section 7.1.4, due to finite number of clouds in the simulations we obtain spiky profiles for TF (Fig. A.15).

Spiral

The results for this model are shown in Figs. A.16-A.18. The φ-profiles are shown in Fig. A.16. This model is unique for having double-peaked φ-profiles when viewed from all azimuthal angles, similar to those found for **distant** and **contact** models, but with lower amplitude. The p is shown in Fig. A.17. It shows profile common for single SMBH scenario for $\phi = 18°$, $126°$, $126°$ and $342°$, but also those with maximum p in the core when viewed for all the other azimuthal viewing angles. The TF is shown in Fig. A.18. For intermediate inclination, it shows clear double-peaked profiles, while for

nearly face-on viewing inclinations, a single-peaked profile or profiles with peaks very close to each other, can be seen when $\phi = 18°$, $198°$ and $342°$.
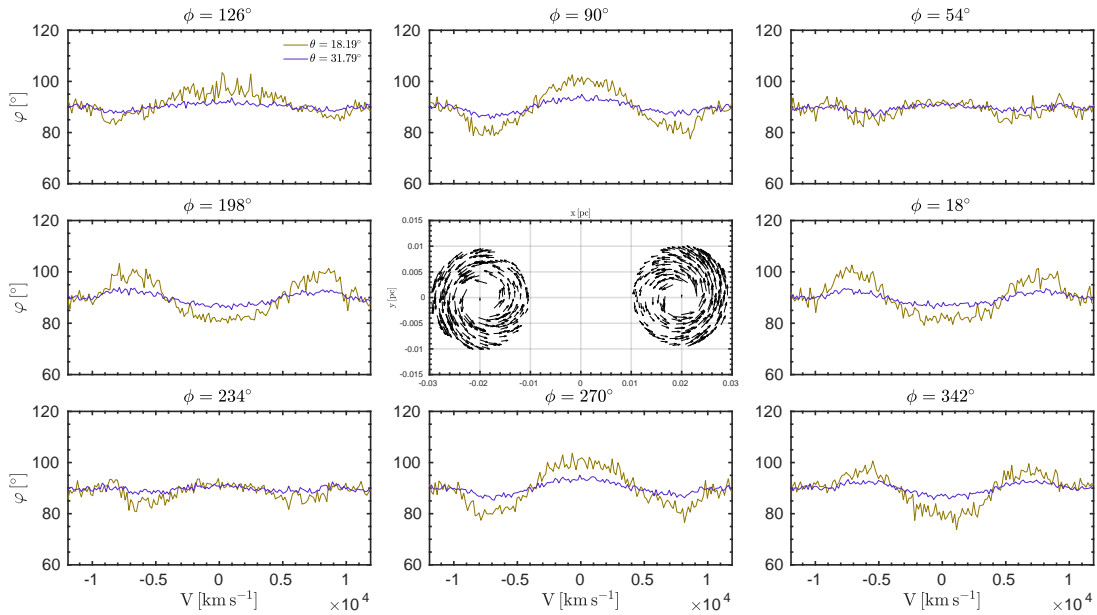
Figure A.1: Simulated profiles of φ across the line profile for two viewing inclinations i when observed from different azimuthal angles ϕ. Geometry and kinematics of the model is in the center for clarity. Credits: Savić et al. (2019).
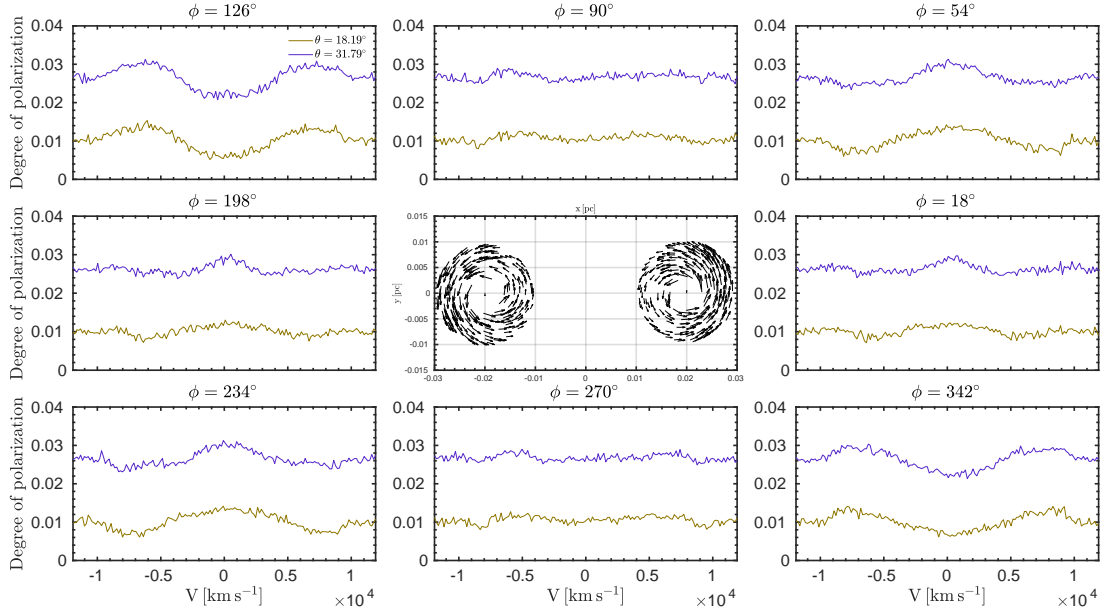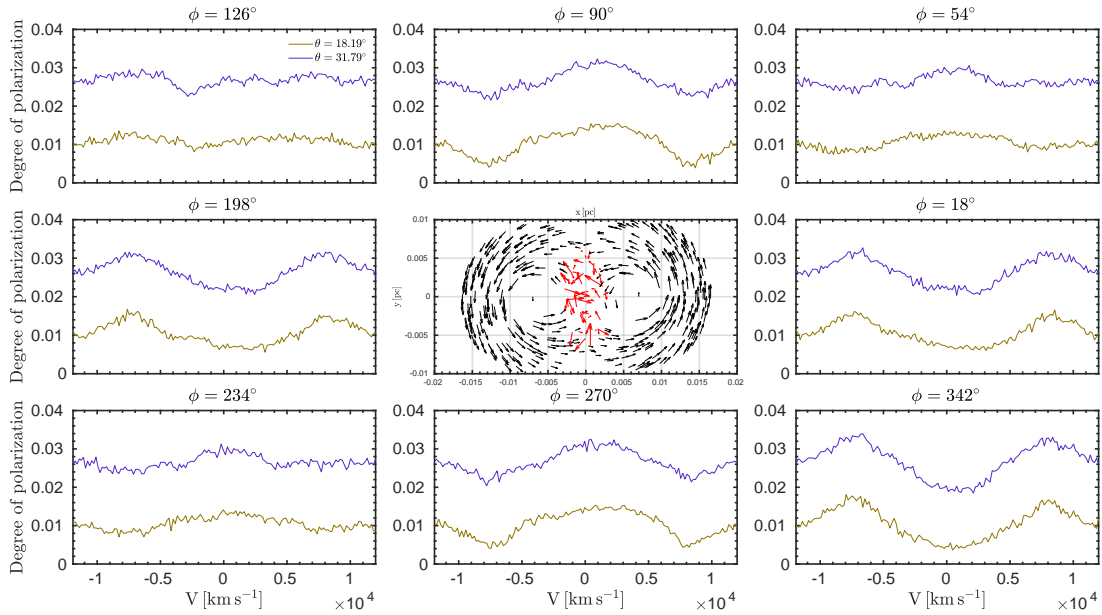
Figure A.2: Same as figure A.1, but for p. Credits: Savić et al. (2019).
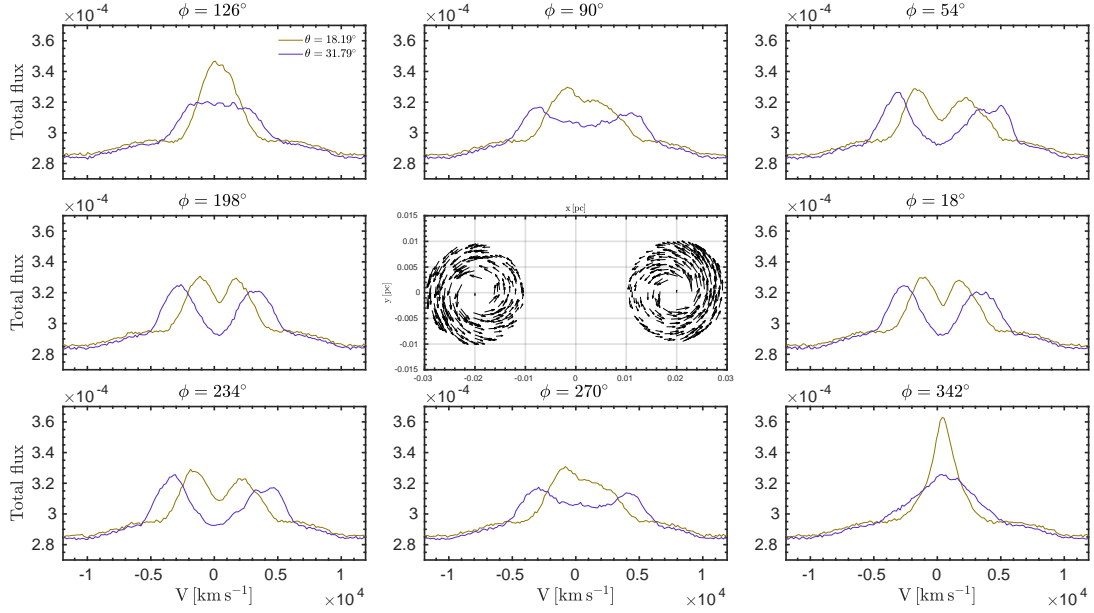
Figure A.3: Same as figure A.1, but for TF. Credits: Savić et al. (2019).
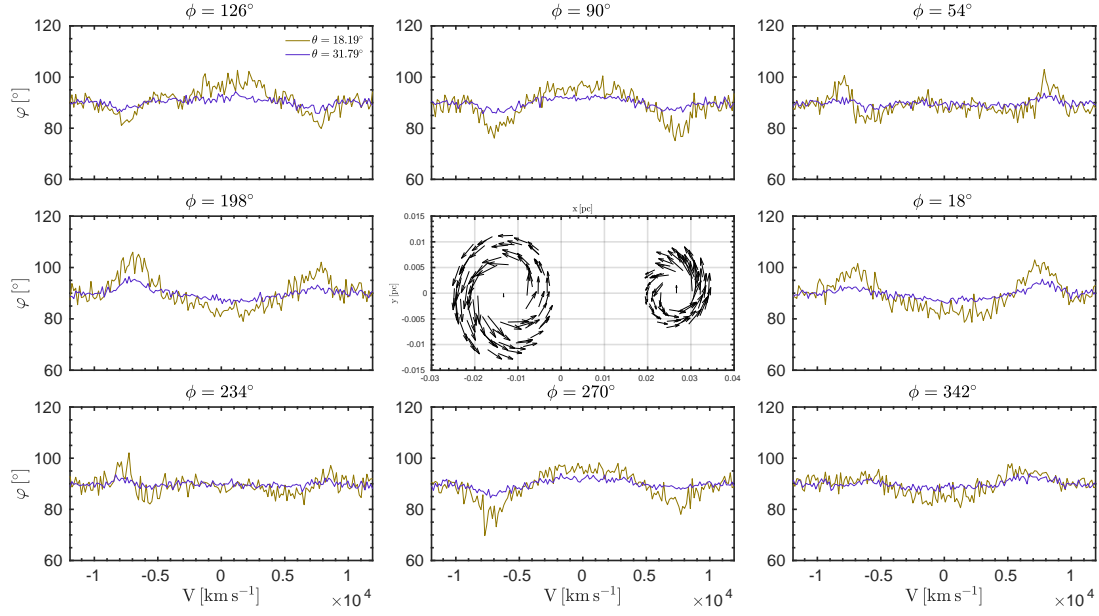
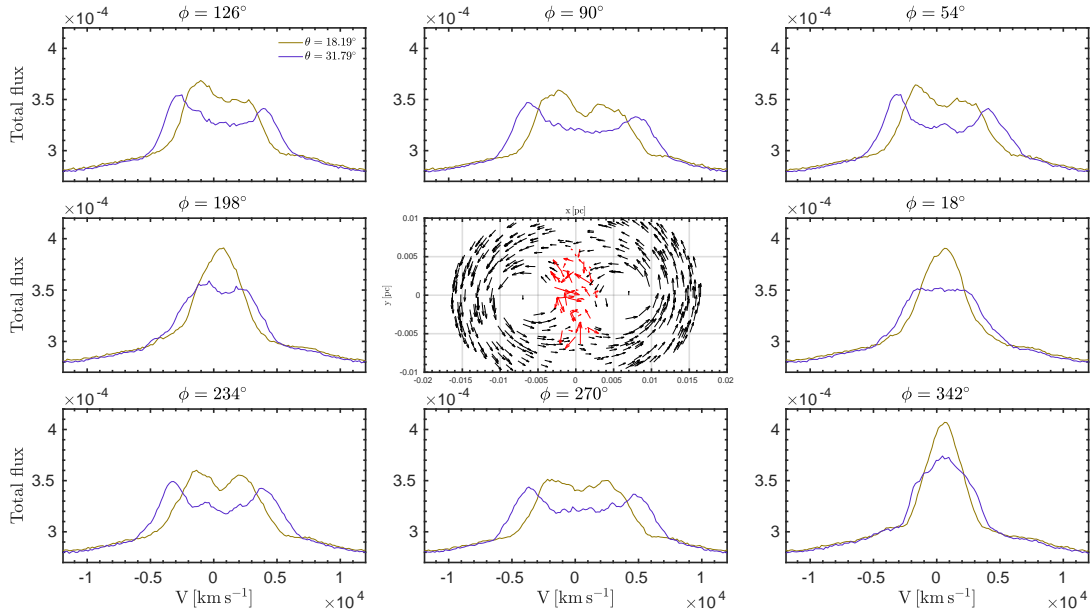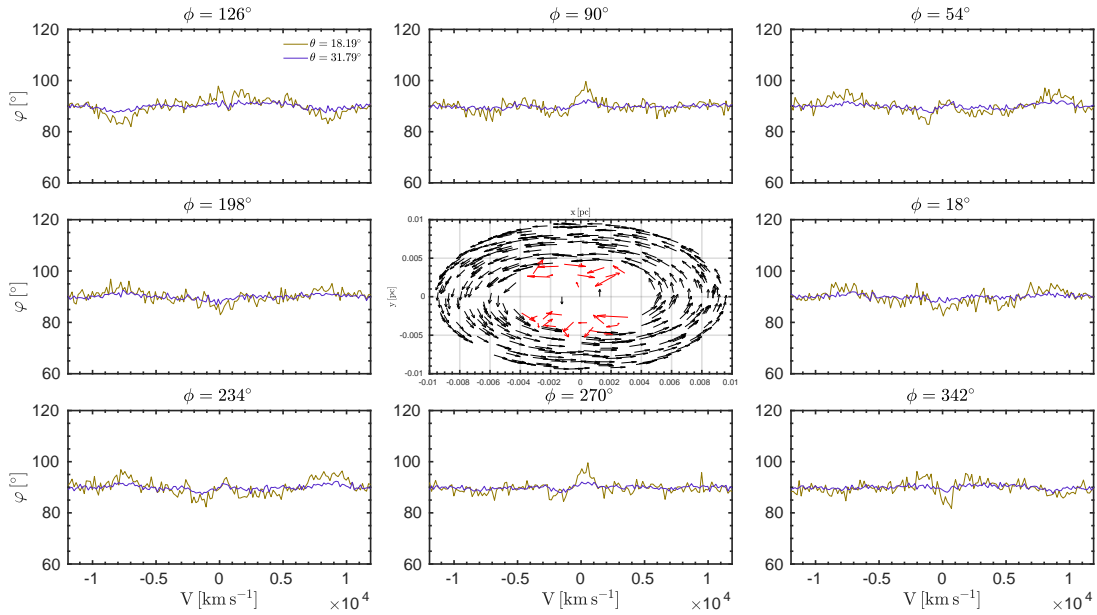**Figure A.4:** Same as figure A.1, but for $q = 0.5$. Credits: Savić et al. (2019).
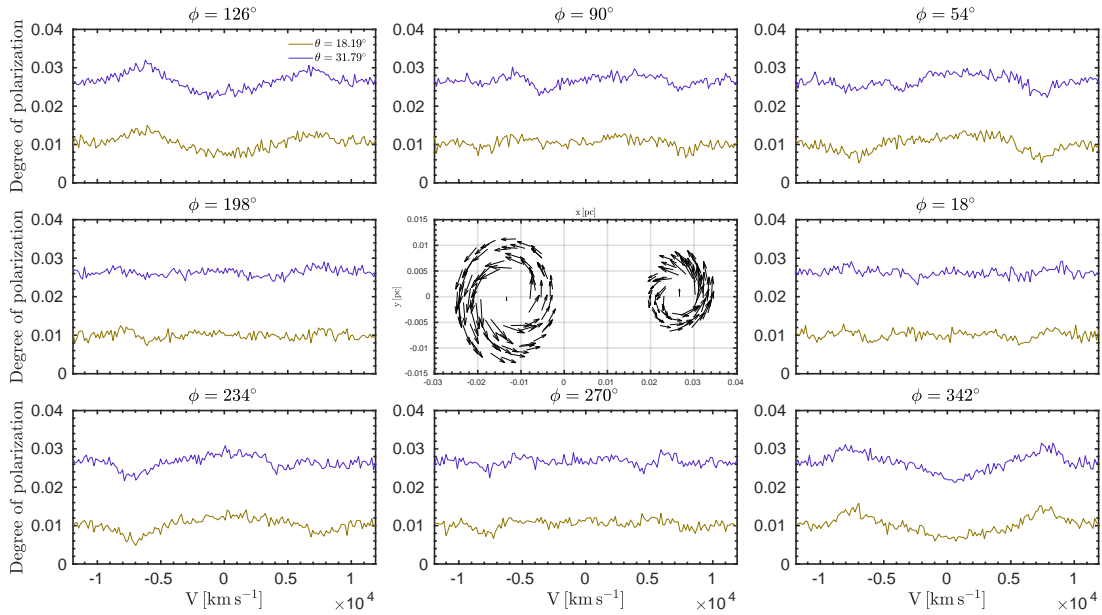
Figure A.5: Same as figure A.2, but for $q = 0.5$. Credits: Savić et al. (2019).
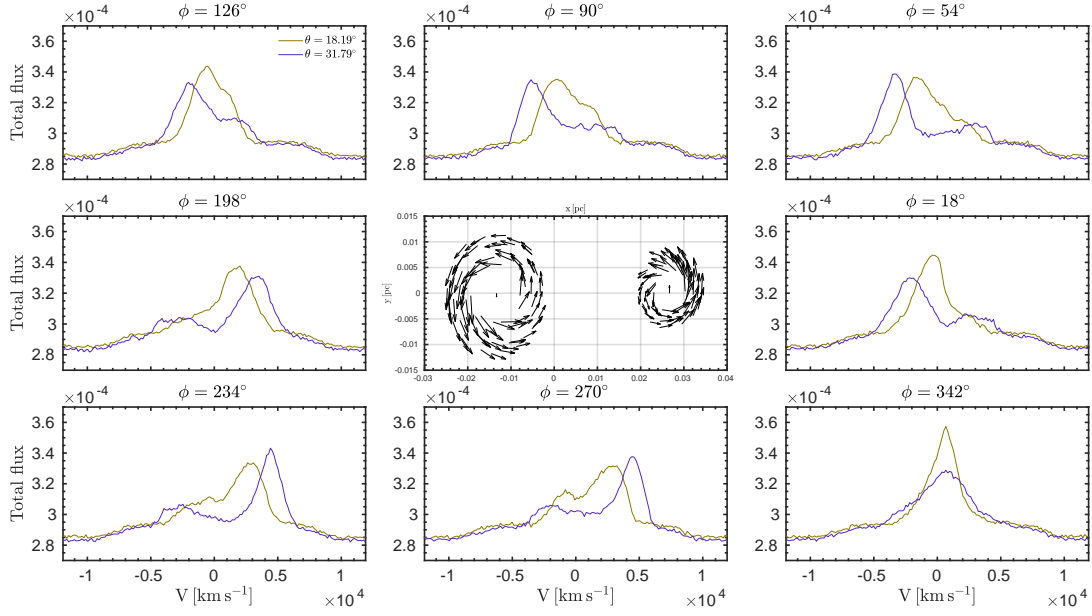
Figure A.6: Same as figure A.3, but for $q = 0.5$. Credits: Savić et al. (2019).
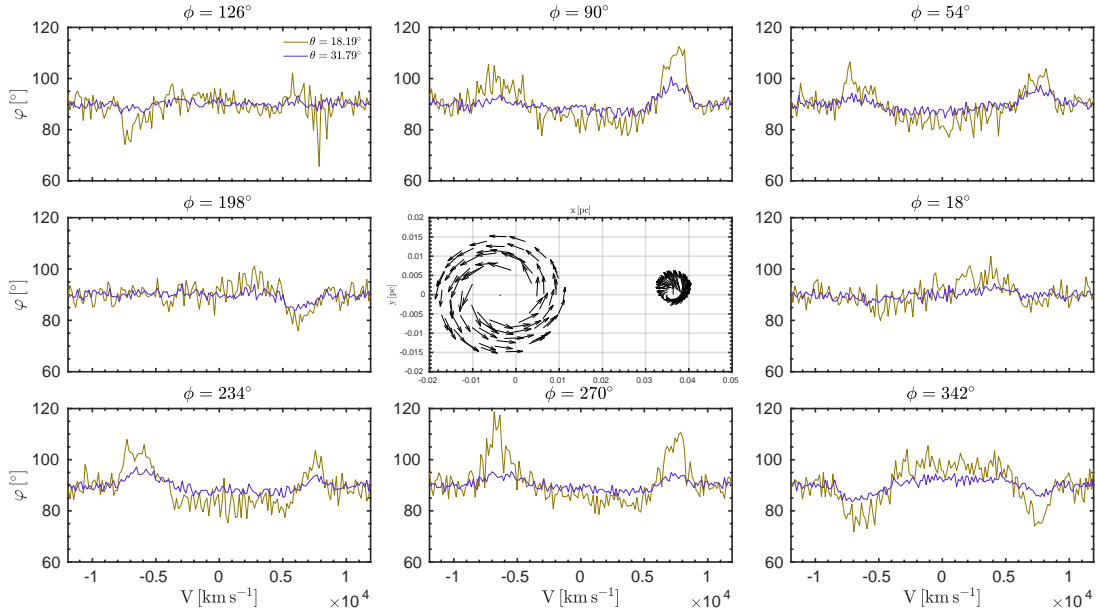
Figure A.7: Same as figure A.1, but for $q = 0.1$. Credits: Savić et al. (2019).
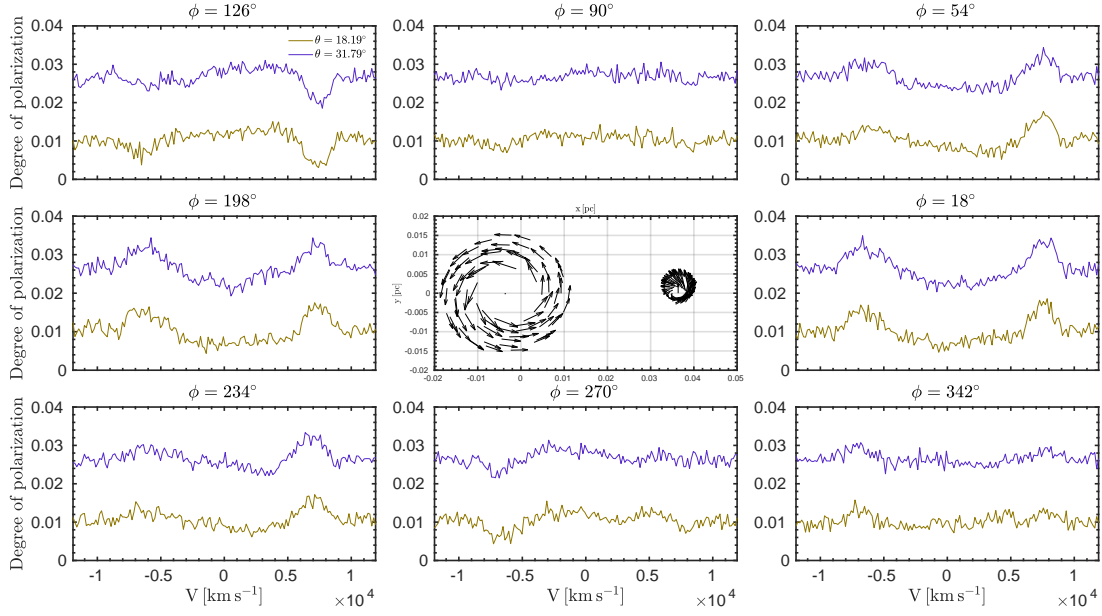
Figure A.8: Same as figure A.2, but for $q = 0.1$. Credits: Savić et al. (2019).
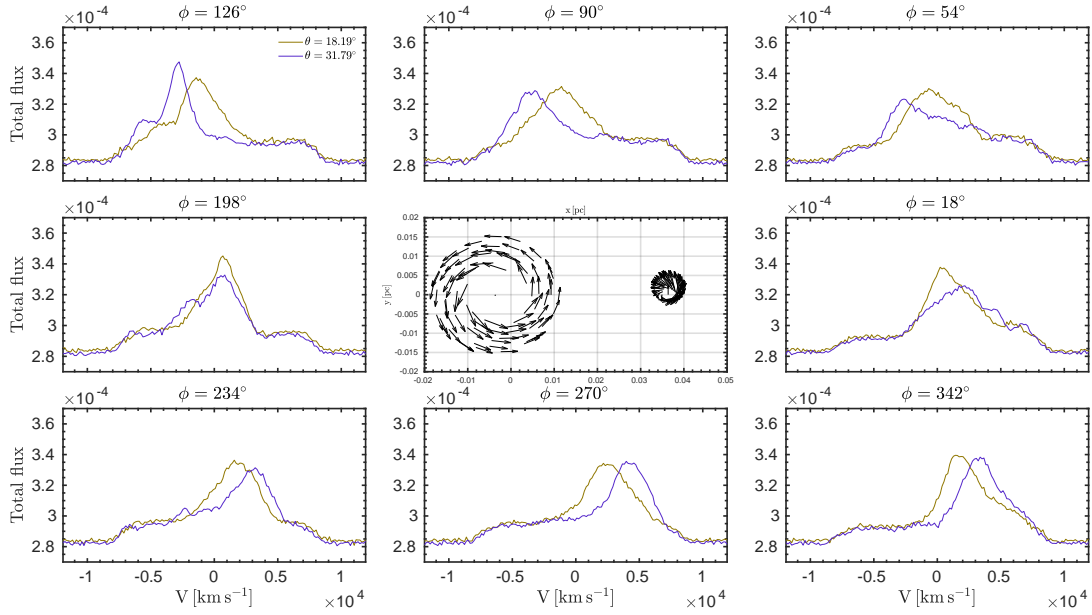
Figure A.9: Same as figure A.3, but for $q = 0.1$ Credits: Savić et al. (2019).
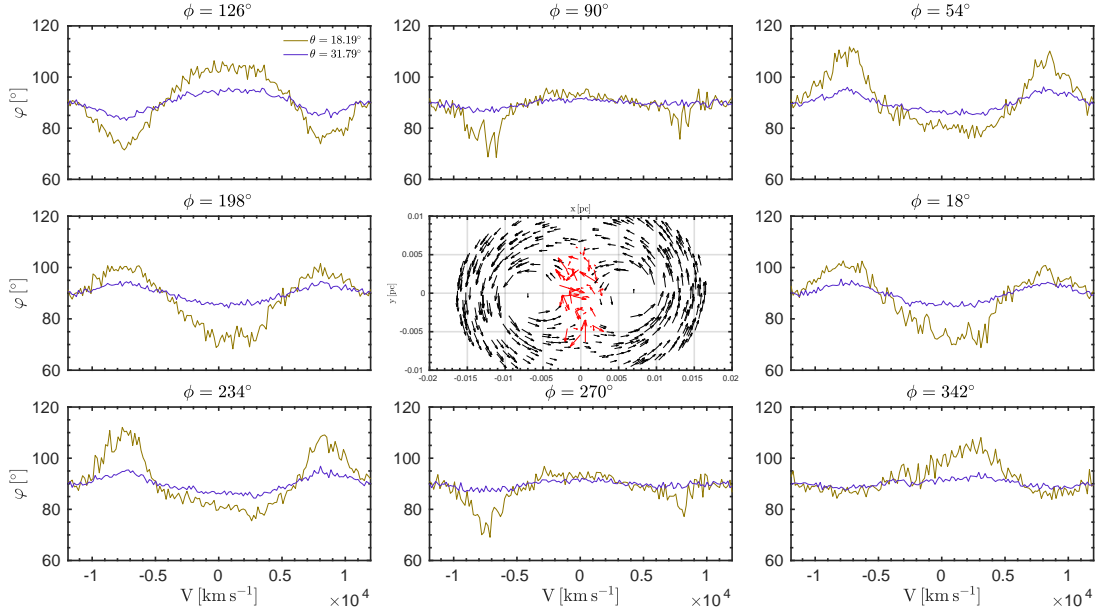
Figure A.10: Same as figure A.1, but for contact model. Credits: Savić et al. (2019).
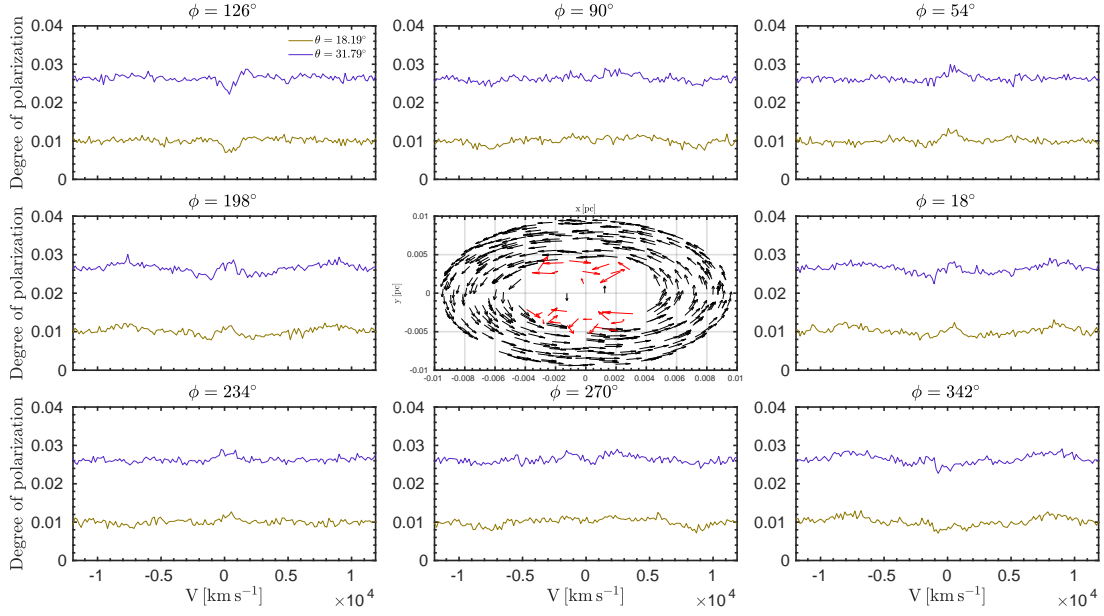

Figure A.11: Same as figure A.10, but for p. Credits: Savić et al. (2019).

Figure A.12: Same as figure A.10, but for TF. Credits: Savić et al. (2019).

Figure A.13: Same as figure A.1, but for mixed model. Credits: Savić et al. (2019).

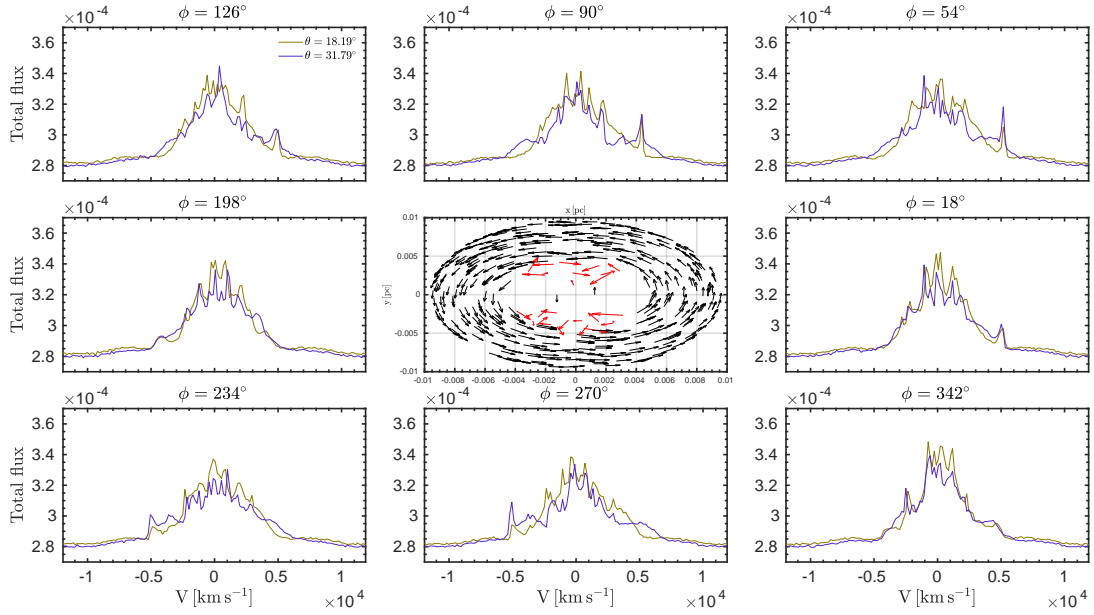**Figure A.14:** Same as figure A.13, but for p. Credits: Savić et al. (2019).

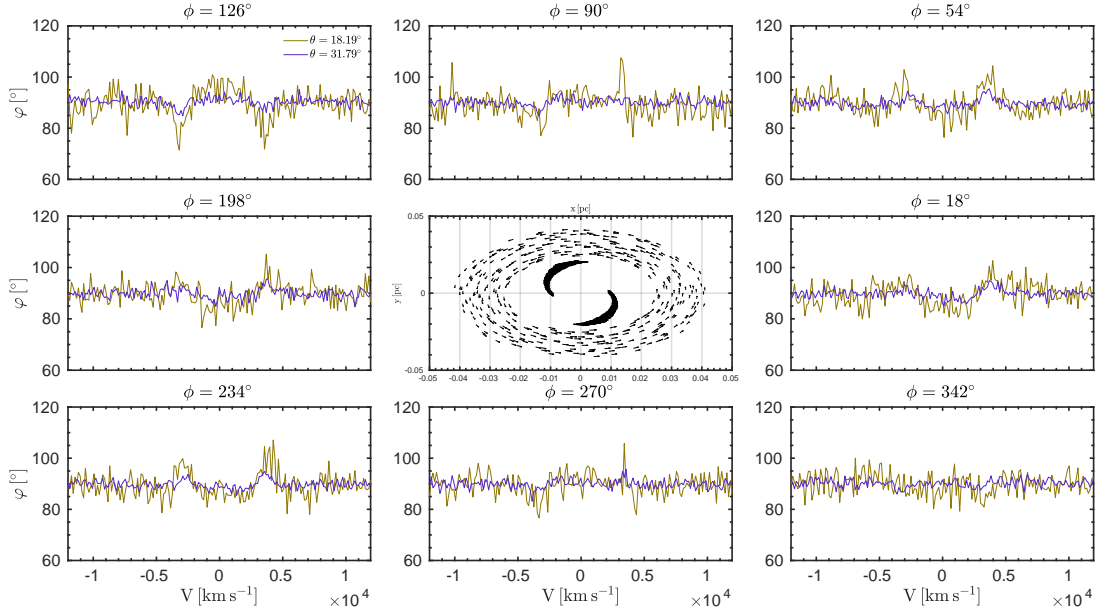**Figure A.15:** Same as figure A.13, but for TF. Credits: Savić et al. (2019).

Figure A.16: Profiles of φ across the line profile. Credits: Savić et al. (2019).
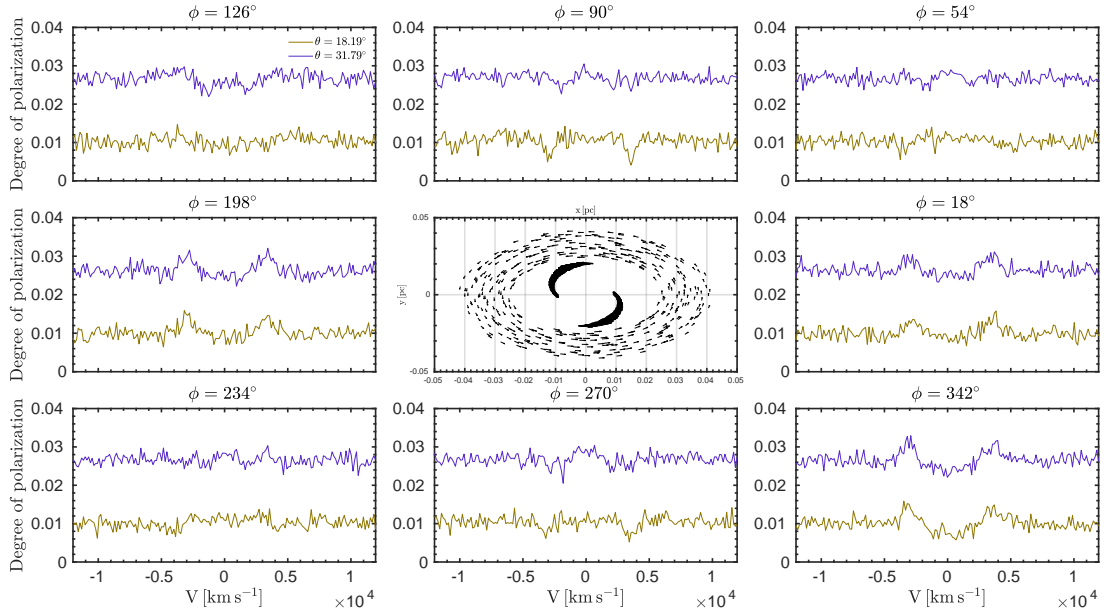

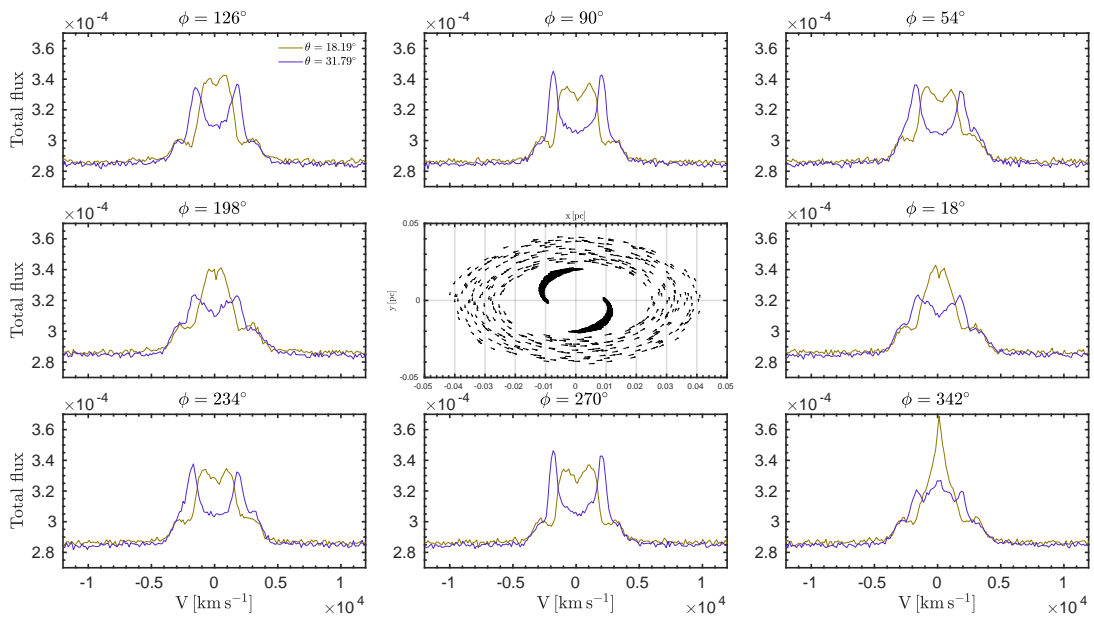**Figure A.17:** Profiles of p across the line profile. Credits: Savić et al. (2019).

Figure A.18: Profiles of TF across the line profile. Credits: Savić et al. (2019).

Bibliography

Aartsen, M. G., Ackermann, M., Adams, J., et al. 2014, Phys. Rev. Lett., 113, 101101

Abbott, B. P., Abbott, R., Abbott, T. D., et al. 2016, Physical Review Letters, 116, 061102

Abdo, A. A., Ackermann, M., Agudo, I., et al. 2010, ApJ, 716, 30

Afanasiev, V. L. & Amirkhanyan, V. R. 2012, Astrophysical Bulletin, 67, 438

Afanasiev, V. L., Borisov, N. V., Gnedin, Y. N., et al. 2011, Astronomy Letters, 37, 302

Afanasiev, V. L., Dodonov, S. N., Khrapov, S. S., Mustsevoi, V. V., & Moiseev, A. V. 2007, Astrophysical Bulletin, 62, 15

Afanasiev, V. L. & Moiseev, A. V. 2005, Astronomy Letters, 31, 194

Afanasiev, V. L. & Popović, L. Č. 2015, ApJ, 800, L35

Afanasiev, V. L., Popović, L. Č., & Shapovalova, A. I. 2019, MNRAS, 482, 4985

Afanasiev, V. L., Popović, L. Č., Shapovalova, A. I., Borisov, N. V., & Ilić, D. 2014, MNRAS, 440, 519

Afanasiev, V. L., Shapovalova, A. I., Popović, L. Č., & Borisov, N. V. 2015, MNRAS, 448, 2879

Aitken, D. K., Efstathiou, A., McCall, A., & Hough, J. H. 2002, MNRAS, 329, 647

Alexandroff, R., Strauss, M. A., Greene, J. E., et al. 2013, MNRAS, 435, 3306

Andreani, P., Cristiani, S., Grazian, A., La Franca, F., & Goldschmidt, P. 2003, AJ, 125, 444

Angel, J. R. P. & Stockman, H. S. 1980, ARA&A, 18, 321

Angel, J. R. P., Stockman, H. S., Woolf, N. J., Beaver, E. A., & Martin, P. G. 1976, ApJ, 206, L5

Antonucci, R. 1993, ARA&A, 31, 473

Antonucci, R. 2012, Astronomical and Astrophysical Transactions, 27, 557

Antonucci, R. R. J. 1982, Nature, 299, 605

Antonucci, R. R. J. 1983, Nature, 303, 158

Antonucci, R. R. J. 1984, ApJ, 278, 499

Antonucci, R. R. J. & Miller, J. S. 1985, ApJ, 297, 621

Appenzeller, I. 1968, ApJ, 151, 769

Appenzeller, I. & Hiltner, W. A. 1967, ApJ, 149, L17

Asmus, D., Hönig, S. F., & Gandhi, P. 2016, ApJ, 822, 109

Assef, R. J., Stern, D., Noirot, G., et al. 2018, ApJS, 234, 23

Atanacković-Vukmanović, O., Crivellari, L., & Simonneau, E. 1997, ApJ, 487, 735

Bañados, E., Venemans, B. P., Mazzucchelli, C., et al. 2018, Nature, 553, 473

Baes, M. & Camps, P. 2015, Astronomy and Computing, 12, 33

Baes, M., Verstappen, J., De Looze, I., et al. 2011, ApJS, 196, 22

Bahcall, J. N., Kirhakos, S., Schneider, D. P., et al. 1995, ApJ, 452, L91

Bahcall, J. N., Kozlovsky, B.-Z., & Salpeter, E. E. 1972, ApJ, 171, 467

Balbus, S. A. & Hawley, J. F. 1998, Reviews of Modern Physics, 70, 1

Baldi, R. D., Capetti, A., Robinson, A., Laor, A., & Behar, E. 2016, MNRAS, 458, L69

Baldwin, J., Ferland, G., Korista, K., & Verner, D. 1995, ApJ, 455, L119

Baldwin, J. A., Phillips, M. M., & Terlevich, R. 1981, PASP, 93, 5

Bambi, C. 2018, Annalen der Physik, 530, 1700430

Barniol Duran, R., Tchekhovskoy, A., & Giannios, D. 2017, MNRAS, 469, 4957

Barvainis, R. 1987, ApJ, 320, 537

Baskin, A. & Laor, A. 2005, MNRAS, 356, 1029

Baskin, A. & Laor, A. 2018, MNRAS, 474, 1970

Beckert, T. & Duschl, W. J. 2004, A&A, 426, 445

Beckmann, V. & Shrader, C. R. 2012, Active Galactic Nuclei (Wiley-VCH)

Begelman, M. C., Blandford, R. D., & Rees, M. J. 1980, Nature, 287, 307

Belczynski, K., Bulik, T., Fryer, C. L., et al. 2010, ApJ, 714, 1217

Bell, A. R. 1978, MNRAS, 182, 147

Bennert, N., Falcke, H., Schulz, H., Wilson, A. S., & Wills, B. J. 2002, ApJ, 574, L105

Bentz, M. C., Denney, K. D., Cackett, E. M., et al. 2006, ApJ, 651, 775

Bentz, M. C., Denney, K. D., Grier, C. J., et al. 2013, ApJ, 767, 149

Bentz, M. C. & Katz, S. 2015, PASP, 127, 67

Beskin, G. M. & Karpov, S. V. 2005, A&A, 440, 223

Bianchi, L., Shiao, B., & Thilker, D. 2017, The Astrophysical Journal Supplement Series, 230, 24

Bianchi, S., Corral, A., Panessa, F., et al. 2008, MNRAS, 385, 195

Blandford, R., Meier, D., & Readhead, A. 2018, arXiv e-prints, arXiv:1812.06025

Blandford, R. D. & McKee, C. F. 1982, ApJ, 255, 419

Blandford, R. D. & Payne, D. G. 1982, MNRAS, 199, 883

Blandford, R. D. & Znajek, R. L. 1977, MNRAS, 179, 433

Blustin, A. J., Branduardi-Raymont, G., Behar, E., et al. 2002, A&A, 392, 453

Boccardi, B., Krichbaum, T. P., Ros, E., & Zensus, J. A. 2017, A&A Rev., 25, 4

Bogdanović, T., Reynolds, C. S., & Miller, M. C. 2007, ApJ, 661, L147

Bohren, C. F. & Huffman, D. R. 1983, Absorption and scattering of light by small particles (Wiley, 1983)

Bolcar, M. R., Crooke, J., Hylan, J. E., et al. 2018, in Society of Photo-Optical Instrumentation Engineers (SPIE) Conference Series, Vol. 10698, Proc. SPIE, 106980O

Boller, T. 2001, in Astronomical Society of the Pacific Conference Series, Vol. 251, New Century of X-ray Astronomy, ed. H. Inoue & H. Kunieda, 112

Bon, E., Gavrilović, N., La Mura, G., & Popović, L. Č. 2009a, New A Rev., 53, 121

Bon, E., Jovanović, P., Marziani, P., et al. 2012, ApJ, 759, 118

Bon, E., Popović, L. Č., Gavrilović, N., La Mura, G., & Mediavilla, E. 2009b, MNRAS, 400, 924

Bon, E., Popović, L. Č., Ilić, D., & Mediavilla, E. 2006, New A Rev., 50, 716

Born, M. & Wolf, E. 2013, Principles of optics: electromagnetic theory of propagation, interference and diffraction of light (Elsevier)

Boroson, T. A. & Lauer, T. R. 2009, Nature, 458, 53

Brightman, M. & Nandra, K. 2011, MNRAS, 413, 1206

Brotherton, M. S. 1995, in Bulletin of the American Astronomical Society, Vol. 27, American Astronomical Society Meeting Abstracts, 1450

Brotherton, M. S., Green, R. F., Kriss, G. A., et al. 2002, ApJ, 565, 800

Brusa, M., Civano, F., Comastri, A., et al. 2010, ApJ, 716, 348

Burbidge, G. R., Burbidge, E. M., & Sandage, A. R. 1963, Reviews of Modern Physics, 35, 947

Burbidge, G. R., Crowne, A. H., & Smith, H. E. 1977, ApJS, 33, 113

Burtscher, L., Meisenheimer, K., Tristram, K. R. W., et al. 2013, A&A, 558, A149

Campitiello, S., Ghisellini, G., Sbarrato, T., & Calderone, G. 2018, A&A, 612, A59

Camps, P. & Baes, M. 2015, Astronomy and Computing, 9, 20

Camps, P., Misselt, K., Bianchi, S., et al. 2015, A&A, 580, A87

Capriotti, E., Foltz, C., & Byard, P. 1979, ApJ, 230, 681

Chandrasekhar, S. 1931, MNRAS, 91, 456

Chandrasekhar, S. 1960, Radiative transfer, Dover Books on Intermediate and Advanced Mathematics (Dover Publications)

Chartas, G., Kochanek, C. S., Dai, X., Poindexter, S., & Garmire, G. 2009, ApJ, 693, 174

Chen, K. & Halpern, J. P. 1989, ApJ, 344, 115

Chen, K., Halpern, J. P., & Filippenko, A. V. 1989, ApJ, 339, 742

Chmyreva, L., Beskin, G., & Karpov, S. 2017, Contributions of the Astronomical Observatory Skalnate Pleso, 47, 137

Clautice, D., Perlman, E. S., Georganopoulos, M., et al. 2016, ApJ, 826, 109

Clavel, J., Reichert, G. A., Alloin, D., et al. 1991, ApJ, 366, 64

Colbert, E. J. M. & Mushotzky, R. F. 1999, ApJ, 519, 89

Coleman, H. H. & Shields, G. A. 1990, ApJ, 363, 415

Collinson, J. S., Ward, M. J., Landt, H., et al. 2017, MNRAS, 465, 358

Contopoulos, G. & Jappel, A. 1974, Transactions of the International Astronomical Union, Volume_XVB: Proceedings of the Fifteenth General Assembly, Sydney 1973 and Extraordinary Assembly, Poland 1973. (Springer Netherlands)

Corbett, E. A., Robinson, A., Axon, D. J., & Young, S. 2000, MNRAS, 319, 685

Corbett, E. A., Robinson, A., Axon, D. J., Young, S., & Hough, J. H. 1998, MNRAS, 296, 721

Courvoisier, T. J. L., Robson, E. I., Blecha, A., et al. 1990, A&A, 234, 73

Courvoisier, T. J.-L., Turner, M. J. L., Robson, E. I., et al. 1987, A&A, 176, 197

Crenshaw, D. M., Kraemer, S. B., Gabel, J. R., et al. 2003, ApJ, 594, 116

Cuadra, J., Armitage, P. J., Alexander, R. D., & Begelman, M. C. 2009, MNRAS, 393, 1423

Curtis, H. D. 1918, Publications of Lick Observatory, 13, 9

Czerny, B. & Hryniewicz, K. 2011, A&A, 525, L8

de Vaucouleurs, G. 1959, Handbuch der Physik, 53, 275

de Vaucouleurs, G., de Vaucouleurs, A., Corwin, Jr., H. G., et al. 1991, S&T, 82, 621

Devore, J. L. 2011, Probability and Statistics for Engineering and the Sciences (Cengage learning)

Di Matteo, T., Celotti, A., & Fabian, A. C. 1999, MNRAS, 304, 809

Dibai, E. A. & Shakhovskoi, N. M. 1966, Astronomicheskij Tsirkulyar, 375, 1

Dombrovskii, V. A. & Gagen-Torn, V. A. 1968, Astrophysics, 4, 163

Dotti, M., Ruszkowski, M., Paredi, L., et al. 2009, MNRAS, 396, 1640

Dotti, M., Volonteri, M., Perego, A., et al. 2010, MNRAS, 402, 682

Dovčiak, M., Karas, V., & Matt, G. 2004, MNRAS, 355, 1005

Draine, B. T. 1984, ApJ, 277, L71

Draine, B. T. 2003, ARA&A, 41, 241

Draine, B. T. & Lee, H. M. 1984, ApJ, 285, 89

Du, P., Lu, K.-X., Hu, C., et al. 2016, ApJ, 820, 27

Du, P. & Wang, J.-M. 2019, arXiv e-prints, arXiv:1909.06735

Du, P., Zhang, Z.-X., Wang, K., et al. 2018, ApJ, 856, 6

Edge, D. O., Shakeshaft, J. R., McAdam, W. B., Baldwin, J. E., & Archer, S. 1959, MmRAS, 68, 37

Efstathiou, A., McCall, A., & Hough, J. H. 1997, MNRAS, 285, 102

Einstein, A. 1916, Annalen der Physik, 354, 769

Elitzur, M. 2006, New A Rev., 50, 728

Elitzur, M. 2012, ApJ, 747, L33

Elitzur, M. & Ho, L. C. 2009, ApJ, 701, L91

Elitzur, M. & Shlosman, I. 2006, ApJ, 648, L101

Emmering, R. T., Blandford, R. D., & Shlosman, I. 1992, ApJ, 385, 460

Eracleous, M., Boroson, T. A., Halpern, J. P., & Liu, J. 2012, ApJS, 201, 23

Eracleous, M. & Halpern, J. P. 1994, ApJS, 90, 1

Eracleous, M. & Halpern, J. P. 2003, ApJ, 599, 886

Eracleous, M., Lewis, K. T., & Flohic, H. M. L. G. 2009, New A Rev., 53, 133

Event Horizon Telescope Collaboration, Akiyama, K., Alberdi, A., et al. 2019a, ApJ, 875, L2

Event Horizon Telescope Collaboration, Akiyama, K., Alberdi, A., et al. 2019b, ApJ, 875, L1

Event Horizon Telescope Collaboration, Akiyama, K., Alberdi, A., et al. 2019c, ApJ, 875, L6

Fabian, A. C. 2012, ARA&A, 50, 455

Fabian, A. C., Zoghbi, A., Ross, R. R., et al. 2009, Nature, 459, 540

Fanaroff, B. L. & Riley, J. M. 1974, MNRAS, 167, 31P

Fano, U. 1949, Journal of the Optical Society of America (1917-1983), 39, 859

Fath, E. A. 1909a, Lick Observatory Bulletin, 5, 71

Fath, E. A. 1909b, Popular Astronomy, 17, 504

Feautrier, P. 1964, Comptes Rendus Academie des Sciences (serie non specifiee), 258, 3189

Ferrarese, L. & Ford, H. 2005, Space Sci. Rev., 116, 523

Ferrarese, L., Pogge, R. W., Peterson, B. M., et al. 2001, ApJ, 555, L79

Fischer, T. C., Crenshaw, D. M., Kraemer, S. B., & Schmitt, H. R. 2013, ApJS, 209, 1

Fitch, W. S., Pacholczyk, A. G., & Weymann, R. J. 1967, ApJ, 150, L67

Frank, J., King, A., & Raine, D. J. 2002, Accretion Power in Astrophysics: Third Edition (Cambridge University Press), 398

Freitas, I. C., Riffel, R. A., Storchi-Bergmann, T., et al. 2018, MNRAS, 476, 2760

Fritz, J., Franceschini, A., & Hatziminaoglou, E. 2006, MNRAS, 366, 767

Fukumura, K., Tombesi, F., Kazanas, D., et al. 2015, ApJ, 805, 17

Gabel, J. R., Crenshaw, D. M., Kraemer, S. B., et al. 2003, ApJ, 583, 178

Gaensler, B., Agudo, I., Akahori, T., et al. 2015, in Advancing Astrophysics with the Square Kilometre Array (AASKA14), 103

Gaskell, C. M. 1982, ApJ, 263, 79

Gaskell, C. M. 1983, in Liege International Astrophysical Colloquia, Vol. 24, Liege International Astrophysical Colloquia, ed. J.-P. Swings, 473–477

Gaskell, C. M. 1988, in Lecture Notes in Physics, Berlin Springer Verlag, Vol. 307, Active Galactic Nuclei, ed. H. R. Miller & P. J. Wiita, 61

Gaskell, C. M. 1996, ApJ, 464, L107

Gaskell, C. M. 2009, New A Rev., 53, 140

Gaskell, C. M., Goosmann, R. W., Merkulova, N. I., Shakhovskoy, N. M., & Shoji, M. 2012, ApJ, 749, 148

Gaskell, C. M. & Klimek, E. S. 2003, Astronomical and Astrophysical Transactions, 22, 661

Gaskell, C. M. & Sparke, L. S. 1986, ApJ, 305, 175

Gebhardt, K., Bender, R., Bower, G., et al. 2000, ApJ, 539, L13

Gebhardt, K., Rich, R. M., & Ho, L. C. 2002, ApJ, 578, L41

Gebhardt, K., Rich, R. M., & Ho, L. C. 2005, ApJ, 634, 1093

Genzel, R., Eisenhauer, F., & Gillessen, S. 2010, Reviews of Modern Physics, 82, 3121

Ghisellini, G. 2013, Radiative Processes in High Energy Astrophysics, Vol. 873 (Springer)

Goad, M. & Wanders, I. 1996, ApJ, 469, 113

Gofford, J., Reeves, J. N., Tombesi, F., et al. 2013, MNRAS, 430, 60

Goldstein, D. 2003, Polarized light (Taylor & Francis)

Goodrich, R. W. & Miller, J. S. 1994, ApJ, 434, 82

Goosmann, R. W. & Gaskell, C. M. 2007, A&A, 465, 129

Goosmann, R. W., Gaskell, C. M., & Marin, F. 2014, Advances in Space Research, 54, 1341

Gordon, K. D., Baes, M., Bianchi, S., et al. 2017, A&A, 603, A114

Gordon, K. D., Misselt, K. A., Witt, A. N., & Clayton, G. C. 2001, ApJ, 551, 269

Graham, M. J., Djorgovski, S. G., Stern, D., et al. 2015, MNRAS, 453, 1562

GRAVITY Collaboration, Dexter, J., Shangguan, J., et al. 2019, arXiv e-prints, arXiv:1910.00593

Gravity Collaboration, Sturm, E., Dexter, J., et al. 2018, Nature, 563, 657

Greenhill, L. J., Gwinn, C. R., Antonucci, R., & Barvainis, R. 1996, ApJ, 472, L21

Greenstein, J. L. & Schmidt, M. 1964, ApJ, 140, 1

Grier, C. J., Martini, P., Watson, L. C., et al. 2013, ApJ, 773, 90

Grier, C. J., Peterson, B. M., Pogge, R. W., et al. 2012, ApJ, 755, 60

Grier, C. J., Shen, Y., Horne, K., et al. 2019, arXiv e-prints, arXiv:1904.03199

Grier, C. J., Trump, J. R., Shen, Y., et al. 2017, ApJ, 851, 21

Gu, M., Cao, X., & Jiang, D. R. 2001, MNRAS, 327, 1111

Harper, D. A., Runyan, M. C., Dowell, C. D., et al. 2018, Journal of Astronomical Instrumentation, 7, 1840008

Hecht, E. 2016, Optics (Pearson Education)

Heckman, T. M. & Best, P. N. 2014, ARA&A, 52, 589

Heckman, T. M. & Kauffmann, G. 2011, Science, 333, 182

Herrnstein, J. R., Moran, J. M., Greenhill, L. J., & Trotter, A. S. 2005, ApJ, 629, 719

Hertz, H. 1888, Annalen der Physik, 270, 551

Hickox, R. C. & Alexander, D. M. 2018, ARA&A, 56, 625

Ho, L. C. 2008, ARA&A, 46, 475

Ho, L. C., Filippenko, A. V., & Sargent, W. L. W. 1997, ApJ, 487, 568

Hönig, S. F. 2019, arXiv e-prints, arXiv:1909.08639

Hönig, S. F. & Beckert, T. 2007, MNRAS, 380, 1172

Hönig, S. F. & Kishimoto, M. 2010, A&A, 523, A27

Hough, J. 2006, Astronomy and Geophysics, 47, 3.31

Hoyle, F. & Fowler, W. A. 1963, MNRAS, 125, 169

Hryniewicz, K. & Czerny, B. 2012, Mem. Soc. Astron. Italiana, 83, 146

Hubble, E. P. 1922, ApJ, 56

Hubble, E. P. 1926, ApJ, 64

Hutsemékers, D., Agís González, B., Sluse, D., Ramos Almeida, C., & Acosta Pulido, J.-A. 2017, A&A, 604, L3

Ilić, D., La Mura, G., Popović, L. Č., et al. 2007, in IAU Symposium, Vol. 238, Black Holes from Stars to Galaxies – Across the Range of Masses, ed. V. Karas & G. Matt, 383–384

Ilić, D., Popović, L. Č., Bon, E., Mediavilla, E. G., & Chavushyan, V. H. 2006, MNRAS, 371, 1610

Ilić, D., Popović, L. Č., La Mura, G., Ciroi, S., & Rafanelli, P. 2012, A&A, 543, A142

Ishibashi, W. & Courvoisier, T. J.-L. 2010, A&A, 512, A58

Ivezić, Ž. 2017, in IAU Symposium, Vol. 324, New Frontiers in Black Hole Astrophysics, ed. A. Gomboc, 330–337

Jackson, J. D. 1962, Classical Electrodynamics (John Wiley & Sons)

Jones, R. C. 1941, Journal of the Optical Society of America (1917-1983), 31, 488

Jones, R. C. 1942, Journal of the Optical Society of America (1917-1983), 32, 486

Jovanović, P. 2012, New A Rev., 56, 37

Kadler, M., Krauß, F., Mannheim, K., et al. 2016, Nature Physics, 12, 807

Kaspi, S., Brandt, W. N., George, I. M., et al. 2002, ApJ, 574, 643

Kaspi, S., Maoz, D., Netzer, H., et al. 2005, ApJ, 629, 61

Kaspi, S., Smith, P. S., Netzer, H., et al. 2000, ApJ, 533, 631

Kay, L. E. 1990, in BAAS, Vol. 22, 1267

Keel, W. C. 1980, AJ, 85, 198

Keller, C. U. 2002, in Astrophysical Spectropolarimetry, ed. J. Trujillo-Bueno, F. Moreno-Insertis, & F. Sánchez, 303–354

Kellermann, K. I., Sramek, R. A., Schmidt, M., Green, R. F., & Shaffer, D. B. 1994, AJ, 108, 1163

Kerr, R. P. 1963, Physical Review Letters, 11, 237

Khlopov, M. Y. 2010, Research in Astronomy and Astrophysics, 10, 495

Kim, J. Y., Krichbaum, T. P., Lu, R. S., et al. 2018, A&A, 616, A188

King, A. & Pounds, K. 2015, ARA&A, 53, 115

Kishimoto, M., Antonucci, R., Blaes, O., et al. 2008, Nature, 454, 492

Kishimoto, M., Hönig, S. F., Antonucci, R., et al. 2011, A&A, 536, A78

Kishimoto, M., Hönig, S. F., Beckert, T., & Weigelt, G. 2007, A&A, 476, 713

Kislat, F., Clark, B., Beilicke, M., & Krawczynski, H. 2015, Astroparticle Physics, 68, 45

Klein, O. & Nishina, T. 1929, Zeitschrift fur Physik, 52, 853

Kolokolova, L., Hough, J., & Levasseur-Regourd, A.-C. 2015, Polarimetry of Stars and Planetary Systems (Cambridge University Press)

Kormendy, J. & Ho, L. C. 2013, ARA&A, 51, 511

Kormendy, J. & Richstone, D. 1995, ARA&A, 33, 581

Koshida, S., Minezaki, T., Yoshii, Y., et al. 2014, ApJ, 788, 159

Koss, M., Trakhtenbrot, B., Ricci, C., et al. 2017, ApJ, 850, 74

Kovačević, A. B., Pérez-Hernández, E., Popović, L. Č., et al. 2018, MNRAS, 475, 2051

Kovačević, A. B., Popović, L. Č., Simić, S., & Ilić, D. 2019, ApJ, 871, 32

Kraemer, S. B., Tombesi, F., & Bottorff, M. C. 2018, ApJ, 852, 35

Krips, M., Eckart, A., Neri, R., et al. 2006, A&A, 446, 113

Kristian, J. 1973, ApJ, 179, L61

Krolik, J. H. & Begelman, M. C. 1988, ApJ, 329, 702

Krumpe, M., Miyaji, T., & Coil, A. L. 2010, ApJ, 713, 558

Lacy, M., Ridgway, S. E., Gates, E. L., et al. 2013, The Astrophysical Journal Supplement Series, 208, 24

Lacy, M., Ridgway, S. E., Sajina, A., et al. 2015, ApJ, 802, 102

Laha, S., Guainazzi, M., Dewangan, G. C., Chakravorty, S., & Kembhavi, A. K. 2014, MNRAS, 441, 2613

Landau, L. & Lifshitz, E. 1969, Mechanics, Ch. VII (Oxford: Pergamon Press)

Laor, A. 2000, ApJ, 543, L111

Laor, A. 2006, ApJ, 643, 112

Laor, A. & Netzer, H. 1989, MNRAS, 238, 897

Latimer, P., Pyle, B. E., Moore, C., & Brunsting, A. 1978, Appl. Opt., 17, 3152

Lazarian, A. & Hoang, T. 2019, ApJ, 883, 122

Lewis, K. T., Eracleous, M., & Storchi-Bergmann, T. 2010, ApJS, 187, 416

Li, Y.-R., Wang, J.-M., Ho, L. C., et al. 2016, ApJ, 822, 4

Lira, P., Goosmann, R. W., Kishimoto, M., & Cartier, R. 2019, arXiv e-prints, arXiv:1906.08718

Lister, M. L., Cohen, M. H., Homan, D. C., et al. 2009, AJ, 138, 1874

López-Gonzaga, N., Burtscher, L., Tristram, K. R. W., Meisenheimer, K., & Schartmann, M. 2016, A&A, 591, A47

Lopez-Rodriguez, E., Packham, C., Jones, T. J., et al. 2015, MNRAS, 452, 1902

Lynden-Bell, D. 1969, Nature, 223, 690

Lynden-Bell, D. 1978, Phys. Scr, 17, 185

Lyubarsky, Y. 2009, ApJ, 698, 1570

MacAlpine, G. M. 2003, in Revista Mexicana de Astronomia y Astrofisica Conference Series, Vol. 18, Revista Mexicana de Astronomia y Astrofisica Conference Series, ed. M. Reyes-Ruiz & E. Vázquez-Semadeni, 63–68

MacFadyen, A. I. & Milosavljević, M. 2008, ApJ, 672, 83

Madau, P. 1988, ApJ, 327, 116

Malizia, A., Landi, R., Molina, M., et al. 2016, MNRAS, 460, 19

Malkan, M. A. 1984, ApJ, 287, 555

Marin, F. 2014, MNRAS, 441, 551

Marin, F. 2017, A&A, 607, A40

Marin, F. 2018a, MNRAS, 479, 3142

Marin, F. 2018b, A&A, 615, A171

Marin, F., Charlot, S., Hutsemékers, D., et al. 2018, in SF2A-2018: Proceedings of the Annual meeting of the French Society of Astronomy and Astrophysics, Di

Marin, F. & Goosmann, R. W. 2014, in SF2A-2014: Proceedings of the Annual meeting of the French Society of Astronomy and Astrophysics, ed. J. Ballet, F. Martins, F. Bournaud, R. Monier, & C. Reylé, 103–108

Marin, F., Goosmann, R. W., & Gaskell, C. M. 2015, A&A, 577, A66

Marin, F., Goosmann, R. W., Gaskell, C. M., Porquet, D., & Dovčiak, M. 2012, A&A, 548, A121

Marin, F., Goosmann, R. W., & Petrucci, P.-O. 2016, A&A, 591, A23

Marinucci, A., Bianchi, S., Matt, G., et al. 2016, MNRAS, 456, L94

Markarian, B. E. 1967, Astrofizika, 3, 24

Markowitz, A. G., Krumpe, M., & Nikutta, R. 2014, MNRAS, 439, 1403

Martin, P. G., Thompson, I. B., Maza, J., & Angel, J. R. P. 1983, ApJ, 266, 470

Martínez-Sansigre, A., Rawlings, S., Lacy, M., et al. 2006, MNRAS, 370, 1479

Marziani, P., Sulentic, J. W., Dultzin-Hacyan, D., Calvani, M., & Moles, M. 1996, ApJS, 104, 37

Mathews, W. G. & Wampler, E. J. 1985, PASP, 97, 966

Mathis, J. S., Rumpl, W., & Nordsieck, K. H. 1977, ApJ, 217, 425

Matsumoto, M. & Nishimura, T. 1998, ACM Transactions on Modeling and Computer Simulation (TOMACS), 8, 3

Matthews, T., Bolton, J., Greenstein, J., Münch, G., & Sandage, A. 1961, Sky and Telescope, 21, 148

Matthews, T. A. & Sandage, A. R. 1963, ApJ, 138, 30

Maxwell, J. C. 1873, A treatise on electricity and magnetism, Clarendon Press

Mayer, L., Kazantzidis, S., Escala, A., & Callegari, S. 2010, Nature, 466, 1082

McClintock, J. E., Shafee, R., Narayan, R., et al. 2006, ApJ, 652, 518

McHardy, I. M., Gunn, K. F., Uttley, P., & Goad, M. R. 2005, MNRAS, 359, 1469

McHardy, I. M., Papadakis, I. E., Uttley, P., Page, M. J., & Mason, K. O. 2004, MNRAS, 348, 783

Meier, D. L., Koide, S., & Uchida, Y. 2001, Science, 291, 84

Mejía-Restrepo, J. E., Trakhtenbrot, B., Lira, P., Netzer, H., & Capellupo, D. M. 2016, MNRAS, 460, 187

Meyer, L., Ghez, A. M., Schödel, R., et al. 2012, Science, 338, 84

Meyers, K. A. & Peterson, B. M. 1985, PASP, 97, 734

Mihalas, D. 1978, Stellar atmospheres /2nd edition/ (San Francisco, WH Freeman and Co.)

Miller, J. S. & Goodrich, R. W. 1990, ApJ, 355, 456

Miller, K. A. & Stone, J. M. 1999, in Bulletin of the American Astronomical Society, Vol. 31, American Astronomical Society Meeting Abstracts, 1510

Miller, M. C. & Krolik, J. H. 2013, ApJ, 774, 43

Milosavljević, M. & Merritt, D. 2003, in American Institute of Physics Conference Series, Vol. 686, The Astrophysics of Gravitational Wave Sources, ed. J. M. Centrella, 201–210

Miyoshi, M., Moran, J., Herrnstein, J., et al. 1995, Nature, 373, 127

Mohr, P. J., Newell, D. B., & Taylor, B. N. 2016, Rev. Mod. Phys., 88, 035009

Moore, R. L. & Stockman, H. S. 1981, ApJ, 243, 60

Mor, R. & Netzer, H. 2012, MNRAS, 420, 526

Mortlock, D. J., Warren, S. J., Venemans, B. P., et al. 2011, Nature, 474, 616

Müller-Sánchez, F., Prieto, M. A., Hicks, E. K. S., et al. 2011, ApJ, 739, 69

Nandra, K. & Pounds, K. A. 1994, MNRAS, 268, 405

Narayan, R. & McClintock, J. E. 2008, New A Rev., 51, 733

Natale, G., Popescu, C. C., Tuffs, R. J., & Semionov, D. 2014, MNRAS, 438, 3137

Nenkova, M., Sirocky, M. M., Ivezić, Ž., & Elitzur, M. 2008a, ApJ, 685, 147

Nenkova, M., Sirocky, M. M., Nikutta, R., Ivezić, Ž., & Elitzur, M. 2008b, ApJ, 685, 160

Netzer, H. 1987, MNRAS, 225, 55

Netzer, H. 1990, in Active Galactic Nuclei, ed. R. D. Blandford, H. Netzer, L. Woltjer, T. J.-L. Courvoisier, & M. Mayor, 57–160

Netzer, H. 2013, The Physics and Evolution of Active Galactic Nuclei (Cambridge University Press)

Netzer, H. 2015, ARA&A, 53, 365

Netzer, H., Brotherton, M. S., Wills, B. J., et al. 1995, ApJ, 448, 27

Netzer, H. & Laor, A. 1993, ApJ, 404, L51

Newman, E. T., Couch, E., Chinnapared, K., et al. 1965, Journal of Mathematical Physics, 6, 918

Nguyen, K. & Bogdanović, T. 2016, ApJ, 828, 68

Noble, S. C., Mundim, B. C., Nakano, H., et al. 2012, ApJ, 755, 51

Nomura, M. & Ohsuga, K. 2017, MNRAS, 465, 2873

Nordström, G. 1918, Koninklijke Nederlandse Akademie van Wetenschappen Proceedings Series B Physical Sciences, 20, 1238

Novikov, I. D. & Thorne, K. S. 1973, in Black Holes (Les Astres Occlus), ed. C. Dewitt & B. S. Dewitt (Gordon and Breach, N.Y.), 343–450

O'Connell, D. J. K., ed. 1971, Study week on nuclei of galaxies

Onken, C. A., Ferrarese, L., Merritt, D., et al. 2004, ApJ, 615, 645

Oppenheimer, J. R. & Volkoff, G. M. 1939, Physical Review, 55, 374

Osterbrock, D. E. 1978, Proceedings of the National Academy of Science, 75, 540

Osterbrock, D. E. 1989, Astrophysics of gaseous nebulae and active galactic nuclei (University Science Books)

Osterbrock, D. E. & Ferland, G. J. 2006, Astrophysics of gaseous nebulae and active galactic nuclei (University Science Books)

Pacholczyk, A. G. & Weymann, R. 1968, AJ, 73, 836

Padovani, P. 2011, MNRAS, 411, 1547

Padovani, P. 2017a, Frontiers in Astronomy and Space Sciences, 4, 35

Padovani, P. 2017b, Nature Astronomy, 1, 0194

Page, K. L., Reeves, J. N., O'Brien, P. T., & Turner, M. J. L. 2005, MNRAS, 364, 195

Pâris, I., Petitjean, P., Aubourg, É., et al. 2018, A&A, 613, A51

Parke III, N. G. 1949, Journal of Mathematics and Physics, 28, 131

Penston, M. V. & Perez, E. 1984, MNRAS, 211, 33P

Peterson, B. M. 1993, PASP, 105, 247

Peterson, B. M. 2006, in Lecture Notes in Physics, Berlin Springer Verlag, Vol. 693, Physics of Active Galactic Nuclei at all Scales, ed. D. Alloin, 77

Peterson, B. M. 2014, Space Sci. Rev., 183, 253

Peterson, B. M., Denney, K. D., De Rosa, G., et al. 2013, ApJ, 779, 109

Peterson, B. M., Ferrarese, L., Gilbert, K. M., et al. 2004, ApJ, 613, 682

Peterson, B. M., McHardy, I. M., Wilkes, B. J., et al. 2000, ApJ, 542, 161

Pier, E. A. & Krolik, J. H. 1992, ApJ, 401, 99

Pier, E. A. & Krolik, J. H. 1993, ApJ, 418, 673

Piotrovich, M. Y., Gnedin, Y. N., Natsvlishvili, T. M., & Buliga, S. D. 2017, Ap&SS, 362, 110

Piotrovich, M. Y., Gnedin, Y. N., Silant'ev, N. A., Natsvlishvili, T. M., & Buliga, S. D. 2015, MNRAS, 454, 1157

Plebanski, J. 1960, Physical Review, 118, 1396

Popović, L. Č. 2003, ApJ, 599, 140

Popovic, L. C. 2006, Serbian Astronomical Journal, 173 [astro-ph/0612712]

Popović, L. Č. 2012, New A Rev., 56, 74

Popović, L. Č. & Ilić, D. 2017, Aktivna galaktička jezgra (Matematički fakultet Univerziteta u Beogradu)

Popović, L. Č., Jovanović, P., Mediavilla, E., et al. 2006, ApJ, 637, 620

Popović, L. Č., Kovačević-Dojčinović, J., & Marčeta-Mandić, S. 2019, MNRAS, 484, 3180

Popović, L. Č., Mediavilla, E., Bon, E., & Ilić, D. 2004, A&A, 423, 909

Popovic, L. C., Mediavilla, E. G., & Pavlovic, R. 2000, Serbian Astronomical Journal, 162, 1

Popovic, L. C., Vince, I., Atanackovic-Vukmanovic, O., & Kubicela, A. 1995, A&A, 293, 309

Porquet, D., Reeves, J. N., O'Brien, P., & Brinkmann, W. 2004, A&A, 422, 85

Postnov, K. A. & Yungelson, L. R. 2014, Living Reviews in Relativity, 17, 3

Pounds, K. A. & King, A. R. 2013, MNRAS, 433, 1369

Pounds, K. A., Reeves, J. N., King, A. R., et al. 2003, MNRAS, 345, 705

Prieto, M. A., Reunanen, J., Tristram, K. R. W., et al. 2010, MNRAS, 402, 724

Ramos Almeida, C. & Ricci, C. 2017, Nature Astronomy, 1, 679

Rani, P., Stalin, C. S., & Rakshit, S. 2017, MNRAS, 466, 3309

Reeves, J. N., O'Brien, P. T., & Ward, M. J. 2003, ApJ, 593, L65

Reeves, J. N., Porquet, D., Braito, V., et al. 2013, ApJ, 776, 99

Reissner, H. 1916, Annalen der Physik, 355, 106

Ricci, C., Trakhtenbrot, B., Koss, M. J., et al. 2017a, ApJS, 233, 17

Ricci, C., Trakhtenbrot, B., Koss, M. J., et al. 2017b, Nature, 549, 488

Richards, G. T., Myers, A. D., Gray, A. G., et al. 2009, ApJS, 180, 67

Robinson, A., Young, S., Axon, D. J., Kharb, P., & Smith, J. E. 2010, ApJ, 717, L122

Rojas Lobos, P. A., Goosmann, R. W., Marin, F., & Savić, D. 2018, A&A, 611, A39

Romero, G. E., Boettcher, M., Markoff, S., & Tavecchio, F. 2017, Space Sci. Rev., 207, 5

Runnoe, J. C., Brotherton, M. S., & Shang, Z. 2012, MNRAS, 427, 1800

Rybicki, G. B. & Lightman, A. P. 1979, Radiative processes in astrophysics (Wiley)

Ryle, M., Smith, F. G., & Elsmore, B. 1950, MNRAS, 110, 508

Salpeter, E. E. 1964, ApJ, 140, 796

Sasaki, M., Suyama, T., Tanaka, T., & Yokoyama, S. 2018, Classical and Quantum Gravity, 35, 063001

Savić, D. 2019, International Journal of Cosmology, 1, 50

Savić, D., Goosmann, R., Popović, L. Č., Marin, F., & Afanasiev, V. L. 2018, A&A, 614, A120

Savić, D., Marin, F., & Popović, L. Č. 2019, A&A, 623, A56

Schartmann, M., Wada, K., Prieto, M. A., Burkert, A., & Tristram, K. R. W. 2014, MNRAS, 445, 3878

Schmidt, M. 1963, Nature, 197, 1040

Schmidt, M. & Green, R. F. 1983, ApJ, 269, 352

Schmidt, M. & Matthews, T. A. 1964, ApJ, 139, 781

Schmidt, T. 1965, ZAp, 62, 217

Schmitt, H. R., Donley, J. L., Antonucci, R. R. J., Hutchings, J. B., & Kinney, A. L. 2003a, ApJS, 148, 327

Schmitt, H. R., Donley, J. L., Antonucci, R. R. J., et al. 2003b, ApJ, 597, 768

Schwarzschild, K. 1916, Sitzungsberichte der Königlich Preußischen Akademie der Wissenschaften (Berlin), 1916, Seite 189-196

Serkowski, K., Mathewson, D. S., & Ford, V. L. 1975, ApJ, 196, 261

Sesar, B., Ivezić, Ž., Lupton, R. H., et al. 2007, AJ, 134, 2236

Seyfert, C. K. 1943, ApJ, 97, 28

Shablovinskaya, E. S. & Afanasiev, V. L. 2019, MNRAS, 482, 4322

Shakura, N. I. & Sunyaev, R. A. 1973, A&A, 24, 337

Shannon, R. M., Ravi, V., Lentati, L. T., et al. 2015, Science, 349, 1522

Shapiro, S. L. & Teukolsky, S. A. 1991, Phys. Rev. Lett., 66, 994

Shapovalova, A. I., Popović, L. Č., Burenkov, A. N., et al. 2010, A&A, 509, A106

Shapovalova, A. I., Popović, L. Č., Chavushyan, V. H., et al. 2016, ApJS, 222, 25

Shapovalova, A. I., Popović, L. Č., Collin, S., et al. 2008, A&A, 486, 99

Shemmer, O., Netzer, H., Maiolino, R., et al. 2004, ApJ, 614, 547

Shen, Y., Horne, K., Grier, C. J., et al. 2016, ApJ, 818, 30

Shen, Y. & Loeb, A. 2010, ApJ, 725, 249

Shi, J.-M. & Krolik, J. H. 2015, ApJ, 807, 131

Shields, G. A. 1978, Nature, 272, 706

Shields, G. A. 1999, PASP, 111, 661

Shuder, J. M. 1982, ApJ, 259, 48

Simić, S. & Popović, L. Č. 2016, Ap&SS, 361, 59

Smailagić, M. & Bon, E. 2015, Journal of Astrophysics and Astronomy, 36, 513

Smith, J. E., Robinson, A., Alexander, D. M., et al. 2004, MNRAS, 350, 140

Smith, J. E., Robinson, A., Young, S., Axon, D. J., & Corbett, E. A. 2005, MNRAS, 359, 846

Smith, J. E., Young, S., Robinson, A., et al. 2002, MNRAS, 335, 773

Songsheng, Y.-Y. & Wang, J.-M. 2018, MNRAS, 473, L1

Stalevski, M., Asmus, D., & Tristram, K. R. W. 2017, MNRAS, 472, 3854

Stalevski, M., Fritz, J., Baes, M., Nakos, T., & Popović, L. Č. 2012, MNRAS, 420, 2756

Stalevski, M., Ricci, C., Ueda, Y., et al. 2016, MNRAS, 458, 2288

Stalevski, M., Tristram, K. R. W., & Asmus, D. 2019, MNRAS, 484, 3334

Steinacker, J., Baes, M., & Gordon, K. D. 2013, ARA&A, 51, 63

Stockman, H. S., Angel, J. R. P., & Miley, G. K. 1979, ApJ, 227, L55

Stockman, H. S., Moore, R. L., & Angel, J. R. P. 1984, ApJ, 279, 485

Stokes, G. G. 1851, Transactions of the Cambridge Philosophical Society, 9, 399

Storchi-Bergmann, T., Dall'Agnol de Oliveira, B., Longo Micchi, L. F., et al. 2018, ApJ, 868, 14

Strateva, I. V., Strauss, M. A., Hao, L., et al. 2003, AJ, 126, 1720

Suganuma, M., Yoshii, Y., Kobayashi, Y., et al. 2006, ApJ, 639, 46

Sulentic, J. W., Marziani, P., & Dultzin-Hacyan, D. 2000, ARA&A, 38, 521

Sunyaev, R. A. & Titarchuk, L. G. 1980, A&A, 86, 121

Tadhunter, C. & Tsvetanov, Z. 1989, Nature, 341, 422

Thomson, R. C., Mackay, C. D., & Wright, A. E. 1993, Nature, 365, 133

Thum, C., Agudo, I., Molina, S. N., et al. 2018, MNRAS, 473, 2506

Tinbergen, J. 1996, Astronomical Polarimetry (Cambridge University Press)

Toba, Y., Oyabu, S., Matsuhara, H., et al. 2014, ApJ, 788, 45

Tombesi, F., Cappi, M., Reeves, J. N., & Braito, V. 2012, MNRAS, 422, L1

Tombesi, F., Cappi, M., Reeves, J. N., et al. 2011, ApJ, 742, 44

Tombesi, F., Cappi, M., Reeves, J. N., et al. 2010, A&A, 521, A57

Tran, H. D., Miller, J. S., & Kay, L. E. 1992, ApJ, 397, 452

Tristram, K. R. W., Meisenheimer, K., Jaffe, W., et al. 2007, A&A, 474, 837

Trouille, L., Barger, A. J., & Tremonti, C. 2011, ApJ, 742, 46

Trujillo-Bueno, J., Moreno-Insertis, F., & Sanchez Martinez, F. 2002, Astrophysical
    Spectropolarimetry (Cambridge University Press)

Urrutia, T., Lacy, M., Spoon, H., et al. 2012, ApJ, 757, 125

Urry, C. M. & Padovani, P. 1995, PASP, 107, 803

Vazquez, B., Galianni, P., Richmond, M., et al. 2015, ApJ, 801, 127

Véron-Cetty, M. P. & Véron, P. 2001, A&A, 375, 791

Vika, M., Driver, S. P., Graham, A. W., & Liske, J. 2009, MNRAS, 400, 1451

Vila, G. S., Romero, G. E., & Casco, N. A. 2012, A&A, 538, A97

Vlahakis, N. & Königl, A. 2004, ApJ, 605, 656

Volonteri, M., Haardt, F., & Madau, P. 2003a, ApJ, 582, 559

Volonteri, M., Madau, P., & Haardt, F. 2003b, ApJ, 593, 661

Wada, K. 2012, ApJ, 758, 66

Wada, K., Schartmann, M., & Meijerink, R. 2016, ApJ, 828, L19

Walker, S. A., Fabian, A. C., Russell, H. R., & Sanders, J. S. 2014, MNRAS, 442, 2809

Walter, R. & Courvoisier, T. J.-L. 1992, A&A, 266, 57

Wang, J.-M. & Netzer, H. 2003, A&A, 398, 927

Weisskopf, M. C., Ramsey, B., O'Dell, S. L., et al. 2016, Results in Physics, 6, 1179

Whiteoak, J. B. 1966, ZAp, 64, 181

Whitney, B. A. 2011, Bulletin of the Astronomical Society of India, 39, 101

Wightman, A. 1948, Physical Review, 74, 1813

Woo, J.-H. & Urry, C. M. 2002, ApJ, 579, 530

Woo, J.-H., Yoon, Y., Park, S., Park, D., & Kim, S. C. 2015, ApJ, 801, 38

Yuan, S., Strauss, M. A., & Zakamska, N. L. 2016, MNRAS, 462, 1603

Zasov, A. V. & Postnov, K. A. 2006, General astrophysics (Vek Fryazino)

Zel'dovich, Y. B. & Novikov, I. D. 1964, Soviet Physics Doklady, 9, 246

Zhang, S. N., Feroci, M., Santangelo, A., et al. 2016, in Society of Photo-Optical
    Instrumentation Engineers (SPIE) Conference Series, Vol. 9905, Proc. SPIE, 99051Q

Zheng, W., Binette, L., & Sulentic, J. W. 1990, ApJ, 365, 115

Zu, Y., Kochanek, C. S., & Peterson, B. M. 2011, ApJ, 735, 80

Zuo, W., Wu, X.-B., Fan, X., et al. 2015, ApJ, 799, 189

Biography

Đorđe Savić was born in 1990 in Kragujevac, where he finished the elementary and high school. Bachelor studies in astronomy and astrophysics he enrolled at the University of Belgrade, Faculty of mathematics in school 2009/10. year. He graduated in 2013 with an average mark of 9.65. During the basic studies he was awarded in 2012, 2013 and 2014 for the remarkable success achieved during the course of study. In November 2013 he was received the prize "Prof. dr Zaharije Brkić" awarded for the best graduate student of astronomy in the previous school year. Master studies of astronomy and astrophysics he enrolled in the school year 2013/14 year. On 7 October 2014, he defended his master thesis under the title "Stability of mass transfer in close binary systems with white dwarfs as components", which he gained title Master Astronomer. He started joint PhD in 2014/15 at the Faculty of Mathematics and in 2015/16 at the University of Strasbourg under the supervision of Prof. dr Luka Č. Popović and dr René Goosmann. From 2014 to 2018, he was involved as a teaching assistant on the subject "Spectroscopy of Astrophysical Plasma", for the Erasmus mundus master program in astronomy – Astromundus. Starting with the 1st of March 2015, he is employed at the Astronomical Observatory in Belgrade as junior research assistant. He co-authored four papers in the prominent international journals, as well as a number of conference contributions.

Прилог 1.

Изјава о ауторству

Потписани-а   <u>Ђорђе Савић</u>

број индекса   <u>2012/2014</u>
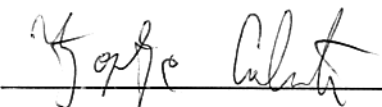
Изјављујем

да је докторска дисертација под насловом

<u>Мерење маса црних рупа код активних галактичких језгара</u>
<u>помоћу поларизације у широким емисионим линијама</u>

- резултат сопственог истраживачког рада,
- да предложена дисертација у целини ни у деловима није била предложена за добијање било које дипломе према студијским програмима других високошколских установа,
- да су резултати коректно наведени и
- да нисам кршио/ла ауторска права и користио интелектуалну својину других лица.

Потпис докторанда

У Београду, <u>02. 09. 2019.</u>

Прилог 2.

Изјава о истоветности штампане и електронске верзије докторског рада

Име и презиме аутора Ђорђе Савић

Број индекса 2012/2014

Студијски програм Астрономија и астрофизика

Наслов рада Мерење маса црних рупа код активних галактичких језгара помоћу поларизације у широким емисионим линијама

Ментор Проф. др Лука Ч. Поповић, др René Goosmann

др Jean-Marie Hameury
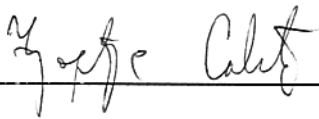
Потписани/а Ђорђе Савић

Изјављујем да је штампана верзија мог докторског рада истоветна електронској верзији коју сам предао/ла за објављивање на порталу **Дигиталног репозиторијума Универзитета у Београду.**

Дозвољавам да се објаве моји лични подаци везани за добијање академског звања доктора наука, као што су име и презиме, година и место рођења и датум одбране рада.

Ови лични подаци могу се објавити на мрежним страницама дигиталне библиотеке, у електронском каталогу и у публикацијама Универзитета у Београду.

Потпис докторанда

У Београду, 02. 09. 2019.

Прилог 3.

Изјава о коришћењу

Овлашћујем Универзитетску библиотеку „Светозар Марковић" да у Дигитални репозиторијум Универзитета у Београду унесе моју докторску дисертацију под насловом:

Мерење маса црних рупа код активних галактичких језгара
помоћу поларизације у широким емисионим линијама

која је моје ауторско дело.

Дисертацију са свим прилозима предао/ла сам у електронском формату погодном за трајно архивирање.
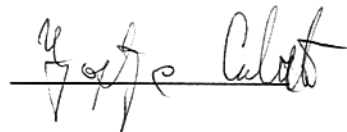
Моју докторску дисертацију похрањену у Дигитални репозиторијум Универзитета у Београду могу да користе сви који поштују одредбе садржане у одабраном типу лиценце Креативне заједнице (Creative Commons) за коју сам се одлучио/ла.

1. Ауторство

2. Ауторство - некомерцијално

3. Ауторство – некомерцијално – без прераде

4. Ауторство – некомерцијално – делити под истим условима

5. Ауторство – без прераде

6. Ауторство – делити под истим условима

(Молимо да заокружите само једну од шест понуђених лиценци, кратак опис лиценци дат је на полеђини листа).

Потпис докторанда

У Београду, 02. 09. 2019.

1. Ауторство - Дозвољавате умножавање, дистрибуцију и јавно саопштавање дела, и прераде, ако се наведе име аутора на начин одређен од стране аутора или даваоца лиценце, чак и у комерцијалне сврхе. Ово је најслободнија од свих лиценци.

2. Ауторство – некомерцијално. Дозвољавате умножавање, дистрибуцију и јавно саопштавање дела, и прераде, ако се наведе име аутора на начин одређен од стране аутора или даваоца лиценце. Ова лиценца не дозвољава комерцијалну употребу дела.

3. Ауторство - некомерцијално – без прераде. Дозвољавате умножавање, дистрибуцију и јавно саопштавање дела, без промена, преобликовања или употребе дела у свом делу, ако се наведе име аутора на начин одређен од стране аутора или даваоца лиценце. Ова лиценца не дозвољава комерцијалну употребу дела. У односу на све остале лиценце, овом лиценцом се ограничава највећи обим права коришћења дела.

4. Ауторство - некомерцијално – делити под истим условима. Дозвољавате умножавање, дистрибуцију и јавно саопштавање дела, и прераде, ако се наведе име аутора на начин одређен од стране аутора или даваоца лиценце и ако се прерада дистрибуира под истом или сличном лиценцом. Ова лиценца не дозвољава комерцијалну употребу дела и прерада.

5. Ауторство – без прераде. Дозвољавате умножавање, дистрибуцију и јавно саопштавање дела, без промена, преобликовања или употребе дела у свом делу, ако се наведе име аутора на начин одређен од стране аутора или даваоца лиценце. Ова лиценца дозвољава комерцијалну употребу дела.

6. Ауторство - делити под истим условима. Дозвољавате умножавање, дистрибуцију и јавно саопштавање дела, и прераде, ако се наведе име аутора на начин одређен од стране аутора или даваоца лиценце и ако се прерада дистрибуира под истом или сличном лиценцом. Ова лиценца дозвољава комерцијалну употребу дела и прерада. Слична је софтверским лиценцама, односно лиценцама отвореног кода.